Quality Control Mechanisms of Molecular Chaperones in the Folding and Degradation of Client Proteins

by

Eric Tse

A dissertation submitted in partial fulfillment
of the requirements for the degree of
Doctor of Philosophy
(Biological Chemistry)
in the University of Michigan
2018

Doctoral Committee:

      Associate Professor, Daniel Southworth, University of California at San Francisco, co-chair
      Professor Philip C. Andrews, co-chair
      Professor Ursula Jakob
      Professor Yoichi Osawa
      Associate Professor Zhaohui Xu

Eric Tse
2018
orvvdom@umich.edu
ORCHID: 0000-0002-8351-4722

Dedication

This thesis is dedicated to my parents Hue M. Vuong and Patrick Tse, for raising me to be a skeptic. They eventually granted me the freedom to pursue my love for science and technology, and their constant love and support have helped keep me sane and make me feel like I have a home somewhere. This work would not have been possible without them.

Preface

This thesis compiles published and unpublished work on the biochemical and structural characterization of pro-folding and pro-degradation functions of molecular chaperone proteins. Heat shock protein 70 (Hsp70) as well as the small heat shock proteins (sHsps) Hsp27 and αB crystallin (HSPB5), are of interest for their roles in protein homeostasis. In addition, a thioredoxin peroxidase, peroxiredoxin (Prx), was examined for its additional functions as a protein chaperone. The thesis begins with an introduction section, detailing the biochemical and structural insights and outstanding questions that motivate the study of these various chaperone systems. In addition, I give a brief overview of electron microscopy, of one of the main technologies utilized in my thesis work. In Chapter 1, human Hsp70 is studied together with the C-terminus of Hsp70 Interacting Protein (CHIP), an E3 ubiquitin ligase to characterize a pro-degradation pathway dependent on the Hsp70 and its ability to target microtubule binding protein tau (MAPT or tau) to become polyubiquitinated. This work was done in collaboration with the Andrews lab at University of Michigan and is currently being formatted into a manuscript in preparation for submission. Next in Chapter 2, in collaboration with the Gestwicki lab at UCSF, another Hsp70 co-chaperone, a nucleotide exchange factor BAG3, is studied together with Hsp70 and the sHsp Hsp27 as an example of the coordination between the Hsp70 and the sHsp systems in facilitating protein refolding. This work has been published as Rauch JN, **Tse E**, Freilich R, Mok SA, Makley LN, Southworth DR, Gestwicki JE., *BAG3 Is a Modular, Scaffolding Protein that physically Links Heat Shock Protein 70 (Hsp70) to the Small Heat Shock Proteins* J Mol Biol. 2017 Jan 6;429(1):128-141. Chapter 3 focuses on another sHsp system αB crystallin or HSPB5 and its ability to delay aggregation, triggered in a response to changes in pH. This work is due to collaboration with the Klevit lab at the University of Washington, and was published as Rajagopal, P. **Tse, E**. Borst, A. J. Delbecq, S. P. Shi, L. Southworth, D. R. Klevit, R. E., *A conserved histidine modulates HSPB5 structure to trigger chaperone activity in response to stress-related acidosis* Elife, 2015. 4. Chapter 4 describes work with the Jakob lab at the University of Michigan on the Prx decamer form which is capable of preventing protein aggregation in the presence of heat stress. Parts of this work have been published in Teixeira, F. Castro, H. Cruz, T. **Tse, E**. Koldewey, P. Southworth, D. R. Tomas, A. M. Jakob, U., *Mitochondrial peroxiredoxin functions as crucial chaperone reservoir in Leishmania infantum* Proc Natl Acad Sci U S A, 2015. 112(7): p. E616-24 and an additional manuscript is currently in preparation. In Chapter 5 we summarize the conclusions of the observations made on the various pro-folding and pro-degradation pathways as well as provide an outlook on the future directions of the works presented.

Table of Contents

Chapter 1) Hsp70 Dependent Triage Mechanisms Use CHIP E3 Ubiquitin Ligase to Facilitate Poly-ubiquitination of Tau

Chapter 2) BAG3 Is a Modular, Scaffolding Protein that physically Links Heat Shock Protein 70 (Hsp70) to the Small Heat Shock Proteins

List of Figures

Abstract

Molecular chaperones are essential proteins that assist in the folding of substrate 'client' proteins to adopt their functionally active three-dimensional structures. The process of protein folding in the cell occurs in a highly concentrated crowded cellular environment among various other macromolecules and amidst various cell stresses which result in issues of aberrant protein folding into toxic species and aggregates. Thus, to counteract these stressors, cells have evolved a complex network of chaperone proteins to maintain protein homeostasis, or proteostasis. Hsp70 is an essential molecular chaperone that acts on clients important for a wide variety of cellular functions. Hsp70 can facilitate refolding of clients to regain their function. However, it can also target client proteins to proteasomal degradation. Turnover of aberrantly folded or aggregation prone proteins such as tau implicates Hsp70 in various pathologies including neurodegenerative diseases.

Another class of protein chaperones, termed 'holdases', act to delay protein aggregation. The small heat shock proteins (sHSP) systems possess such activity, binding to non-native conformations of clients. sHsps such as Hsp27 and αB crystallin exist as distributions of large oligomeric species that respond dynamically to pH and temperature stresses. Recent studies have demonstrated oligomeric rearrangements occur for sHsps to protect client proteins. A major outstanding question is how do these oligomeric assemblies' complex structures sense cell stress or protein unfolding or aggregation. In addition to sensing cell stress, sHsps and holdase chaperones are also capable of bridging with the activities of other classes of chaperones, including the Hsp70 chaperone system. Hsp70 functions in concert with a network of co-chaperone proteins which diversify its protein folding capabilities. BAG3 is a nucleotide exchange factor (NEF) that facilitates the exchange of ADP and ATP in Hsp70. In addition, interactions with sHsp family chaperones have emerged, making it a promising target in elucidating the link between these two functionally distinct chaperone systems.

The overall theme to my thesis work has been to characterize protein homeostasis achieved through pro-folding and pro-degradation pathways. A major focus of my thesis concerns the ability of Hsp70 to work in concert with the CHIP E3 ubiquitin ligase to target tau for polyubiquitination in a chaperone dependent manner, thus facilitating protein turnover. Another focus has been on a pro-folding function of chaperones, the so-called holdase function, where I have explored the structural rearrangements of the sHsp αB crystallin as well as another multifunctional chaperone, peroxiredoxin, and how these conformational changes and oligomeric rearrangements trigger with external stress and correlate with activation of chaperone activity. This thesis also explores the cooperation between sHsps and Hsp70 to

facilitate protein refolding, where I characterize rearrangements that occur in the Hsp27 oligomer distribution modulated by BAG3, and its implications on Hsp70 binding. One of the major techniques utilized in my thesis work is electron microscopy, obtaining structural information of protein complexes, from obtaining low resolution size distributions of sHsp oligomers to pushing resolution of Hsp70 in complex with CHIP beyond quaternary structural information to sub-nanometer resolution of the peroxiredoxin in its active chaperone form in complex with substrate. EM has provided useful information to corroborate biochemical assays that characterize when chaperones protect, refold or degrade client substrates. Altogether, this work has examined a wide spectrum of chaperone activities, providing support for emerging views on chaperone oligomer holdase activity as well as direct evidence of Hsp70 mediated ubiquitination of its important client tau. These studies serve as a foundation for future work on obtaining the structural basis of the decision process where chaperone proteins decide the fate of their client substrates.

Introduction- Quality Control Mechanisms of Molecular Chaperones in the Folding and Degradation of Client Proteins

- **0.1 The Hsp70 chaperone cycle- conformational dynamics in facilitating client refolding**

Heat shock protein 70 (Hsp70) is a molecular chaperone capable of binding to partially misfolded proteins, making it essential to the folding of nascent polypeptides, functioning by binding and refolding unfolded proteins and preventing of aggregation of toxic species [1-3]. Two major families of Hsp70 are of particular interest, namely the constitutively expressed Hsc70 and the heat induced Hsp70 of which most of my studies focus on the Hsp70 isoform. Hsp70 carries out its function by repeated cycles of binding and release of client substrates, resulting from ATP hydrolysis at the Hsp70 N-terminal nucleotide binding domain (NBD) [4-7]. Hsp70 binds to solvent exposed hydrophobic patches at its C-terminal substrate binding domain (SBD), acting as both a holdase to prevent aggregation as well as aiding protein refolding (Figure 0.1). Because Hsp70 binds to short hydrophobic sequences, the clientele for Hsp70 is vast because it isn't restricted by shape or size of the client protein [8, 9]. And unlike typical holdase chaperones, Hsp70 allows proteins to renature and obtain their functional three-dimensional structure as in the case with the model substrate luciferase [10, 11].
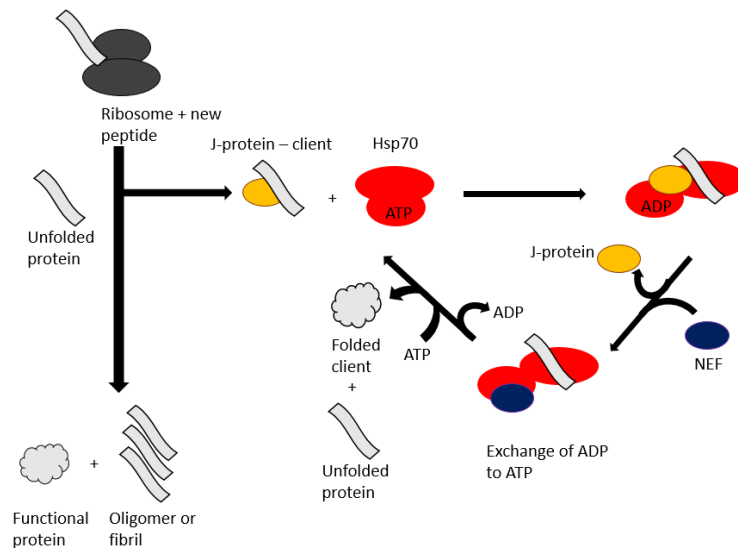
Figure 0.1 Hsp70 chaperone cycle. Two major conformations for Hsp70 have been extensively characterized, a high client affinity ADP state and a low client affinity ATP state. Co-chaperones such as J-proteins or other chaperone systems such as the small heat shock proteins (sHsps) are thought to intercept unfolded proteins or nascent polypeptides holding them in a folding competent state to be handed off to the Hsp70 system. After J-proteins accelerate the rate of ATP hydrolysis Hsp70 enters a high client affinity ADP state. When ADP is displaced by ATP, catalyzed by the assistance of co-chaperones known as nucleotide exchange factors, (NEFs), Hsp70 returns to its low client affinity state and releases the client for a chance to refold on its own or reenter the Hsp70 chaperone cycle. In this process Hsp70 repeatedly binds and releases client proteins and facilitates the folding and refolding of clients

Hsp70 function is further modified by its interaction with protein partners called co-chaperones that alter the function of the protein chaperone complex. These co-chaperones interact with Hsp70 at its NBD or the C-terminal consensus motif IEEVD in higher eukaryotes [12]. The network of co-chaperones vary in functional effects , from different modulators of Hsp70's intrinsic ATPase activity as in J-proteins, to nucleotide exchange factors (NEFs) that exchange ADP for ATP [13]. In addition, the IEEVD motif interacts with tetratricopeptide (TPR) domain containing proteins which include a wide array of functions from protein phosphatases to E3 ubiquitin ligases [14]. Because these sites of interaction are often shared between co-chaperones, competition between these various proteins adds another layer of complexity to the already complicated Hsp70 cycle. These interactions expand the repertoire of Hsp70 function to include protein trafficking to organelles, signal transduction, and proteasomal degradation [15].

- **0.1.1 Structure and Function of Hsp70**

As mentioned above, Hsp70 consists of two major domains, the N-terminal nucleotide binding domain and the C-terminal substrate binding domain, linked together by a flexible linker. The chaperone function of Hsp70 occurs through client interactions in its SBD, which in turn is modulated by the nucleotide state of the NBD, communicating allosterically to give two distinct structural and functional conformations, the ATP and ADP states [16, 17]. In the ATP conformation client affinity has been reported at K_d 1-10 µM, with fast on-off rates for client proteins, compared to when bound to ADP, those same clients were reported at binding affinities of K_d 1-10 mM [19, 20].

The 45 kDa NBD consists of a two-lobe v-cleft structure. Each lobe of the NBD is subdivided into two subdomains (IA, IB, IIA, IIB) and form a nucleotide binding cleft in which ATP hydrolysis occurs (Figure 0.2). Subdomains of the NBD undergo continuous dynamic structural changes in response to nucleotide binding [4, 5, 21], as well as co-chaperone binding such as NEF or J-proteins [2].

The SBD is composed of a 25kDa β-sheet subdomain and a 10 kDa α-helical lid [16, 17] (Figure 0.2). In the ADP bound state, there are two sets of four stranded twisted β-sheets which, together with the loops connecting the β strands, make contact with the peptide backbone of peptide substrates. The α-helical lid domain forms hydrophobic faces that pack together with substrate and the β-sheet subdomain to form a hydrophobic core surrounding the client, closing the substrate binding pocket [22].
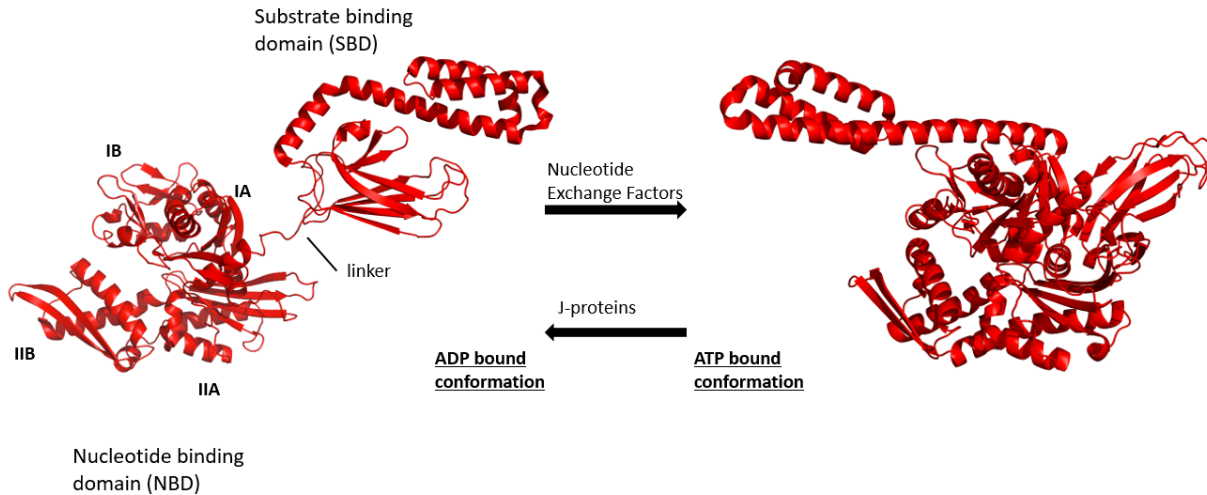
Figure 0.2 Hsp70 domain organization. Hsp70 consists of two domains, a nucleotide binding domain (NBD) and a substrate binding domain (SBD) connected by a flexible linker in the ADP state. When ADP is displaced by ATP, catalyzed by the assistance of co-chaperones known as nucleotide exchange factors, Hsp70 undergoes a dramatic conformational change where the α helical lid of the SBD folds back and the linker, along with many other areas of the SBD form extensive contacts with the NBD, in a low client affinity state. J-proteins accelerate the rate of ATP hydrolysis returning it to the high client affinity ADP state.

Various structural rearrangements in the NBD cause important interactions to occur between the NBD and the flexible linker which connects to the SBD [23]. This linker confers interdomain allostery, where information regarding the nucleotide state of Hsp70 is transmitted between the two domains [24]. Depending on the NBD nucleotide state the linker ranges from flexible when bound to ADP and structured when bound to ATP, evidenced by accessibility in proteolytic digest and hydrogen-deuterium exchange. The full length Hsp70 structure has been determined for the bacterial homologue DnaK in both the ADP and ATP bound states and has served as guides for the investigation of human Hsp70 structure [17, 22, 25]. These structures provide direct evidence of the role of the interdomain linker in allostery. In the ADP state, the linker region exists as a dynamic random coil whereas upon ATP binding the linker becomes buried between subdomain IA and IIA of the NBD and thus propagate structural changes through the linker into the SBD.

Binding of ATP transmits conformational changes through the linker to the SBD, most remarkably causing a complete opening between the α-helical lid and the β-sheet subdomain of the SBD [8] (Figure 0.2). In the ATP state, Hsp70 exists in a low affinity state for clients, unable to form the hydrophobic binding pocket. Affinity for the substrate decreases by an order of 100 to 1000, with faster on/off rates [18]. Substrate binding reciprocally increases Hsp70 rate of ATP hydrolysis, which will cause Hsp70 to cycle back to its ADP conformation.

3

Cycling between the ATP and ADP states has been shown to be a major factor in facilitating the refolding activity of Hsp70, driving the continued cycling of binding and release of clients [26]. Mutations made in the NBD are capable of impairing Hsp70 folding function by limiting the ATP turnover [21, 27]. However, certain mutations have been found to impair nucleotide hydrolysis without impacting Hsp70 capacity to refold proteins, implying other cellular factors are at play tuning Hsp70 driven folding [28]. Studies have shown that client retention on Hsp70, where the cycle of client release and nucleotide hydrolysis is interrupted, promotes degradation of clients through the ubiquitin-proteasome pathway [29]. Given the diverse nature of client proteins and the complex network of co-chaperones that work in concert, the cycling of Hsp70 states behaves as a process of protein triage rather than a process dedicated to refolding.

Thus, questions focus on how Hsp70 directs protein folding and degradation remains paramount to understanding proteostasis, which require understanding of Hsp70 interactions with co-chaperones and clients during this triage process. Limited structural information is available for the full length Hsp70 bound to clients and co-chaperones due to the dynamic nature of the Hsp70 chaperone cycle. Crystal structures have elucidated how the NBD interact with J-proteins [30] and NEFs [13], and NMR has proven a powerful tool in determining conformational changes that occur with substrate binding in the context of the full length Hsp70 [9]. However, structural studies have been restricted to truncations of the bacterial homologue DnaK which lack the c-terminal IEEVD responsible for interactions with the E3 ubiquitin ligase linking Hsp70 to the proteasome in eukaryotes. Recently, studies utilizing electron microscopy have been able to elucidate the structures of chaperone complexes with client, presenting a lucrative direction in which to study multi-chaperone complexes [31, 32]. Structural and biochemical studies utilizing the full length human Hsp70, co-chaperones and clients are needed to understand proteostasis pathways and the triage process.

- **0.1.2 Co-chaperones diversify Hsp70 chaperone structure and function**

The major families of co-chaperones bind to distinct yet potentially overlapping interaction surfaces on Hsp70, including the C-terminus IEEVD motif, C-terminal lid domain and various regions along the NBD [2]. The J protein co-chaperones, such as Hsp40, bind Hsp70 at NBD subdomain IIA to accelerate the rate of ATP hydrolysis [30, 33]. The NEF co-chaperones, such as BAG3, bind lobes IB and IIB, opening the nucleotide binding cleft and facilitate the release of ADP [34]. By accelerating nucleotide exchange on Hsp70 to return to the ATP state, NEFs cause substrate release from Hsp70 for a new cycle of client binding. TPR domain containing co-chaperones bind Hsp70's C-terminus and include the C-terminus of

Hsp70 binding protein (CHIP) an E3 ubiquitin ligase, linking the Hsp70 chaperone system to the proteasomal degradation of client proteins [35].

NMR studies on interactions of Hsc70 with CHIP have indicated that the flexible nature of the C-terminus of Hsc70 allows for a loose tethered complex to allow CHIP to accommodate the extended and heterogenous nature of unfolded clients and space to recruit other enzymes of the ubiquitin proteasome pathway [36]. Other modes of binding have also been discovered for Hsc70 where additional contacts between the CHIP TPR and the lid region of Hsc70 have been shown to be important for their interaction as well as the ubiquitination of clients [37]. This suggests that although in solution the complex remains flexible, additional contacts may bring the chaperones and client into closer proximity for productive ubiquitination. The interactions between Hsp70 c-terminus and TPR containing co-chaperones and with other chaperone systems such as Hsp90 have been aided by the use of chemical crosslinking to stabilize these multi-protein complexes to obtain structural information on the low energy states in the protein folding cycle [31, 38]. Thus, major efforts are being made to elucidate the nature of the vast combinations of chaperones, co-chaperones and clients as well as pushing the resolution limit to obtain information beyond their quaternary structures.

- **0.1.3 Significance of Hsp70 in neurodegenerative diseases**

Disruption of proteostasis causes protein misfolding diseases, including Alzheimer's, Parkinson's and other neurodegenerative disorders [3, 39]. These pathologies exhibit a propensity to form protein aggregate species in neurons, spurred by patterns of unfolding, post-translational modification and mutations [40, 41]. It has been shown that the decline of various chaperone systems, such as Hsp70 and Hsp90, leads to the advance of neurodegeneration in mouse and neuronal cell culture models [42, 43]. Upregulation of Hsp70 has been shown to counteract neurodegenerative pathologies and small molecules that promote Hsp70 client binding have also been shown to promote turnover of aggregation prone clients such as tau protein [29, 44, 45]. The role of ubiquitination has been essential in linking Hsp70 chaperone activity to lowering cellular levels of tau [45]. Thus, elucidation of the mechanism of client ubiquitination serves as another step towards uncovering the process of Hsp70 triage of clients.

- **0.1.4 The E3 ubiquitin ligase CHIP- maintaining balance and proteostasis**

The pathway to proteasomal degradation begins with the process of poly-ubiquitination, which consists of the formation of a poly-ubiquitin chain linked to a lysine of the target substrate [46]. The small 76 amino acid polypeptide ubiquitin is built into a chain of ubiquitin proteins, utilizing the carboxy terminus

5

of ubiquitin to form an isopeptide bond with the substrate and specific lysines on ubiquitin to assemble additional subunits. This serves as a post translational modification which then can target the substrate to the proteasome, on its own or in concert with other factors that disassemble or unfold the client. Inhibition of the proteasome has allowed identification of the various patterns of linkages that occur to promote degradation, such as the K48 or K11 [47]. Other lysines have been identified in poly-ubiquitin chains, such as the K63, but are involved in signaling and have been shown to be protect substrate from proteasomal degradation.
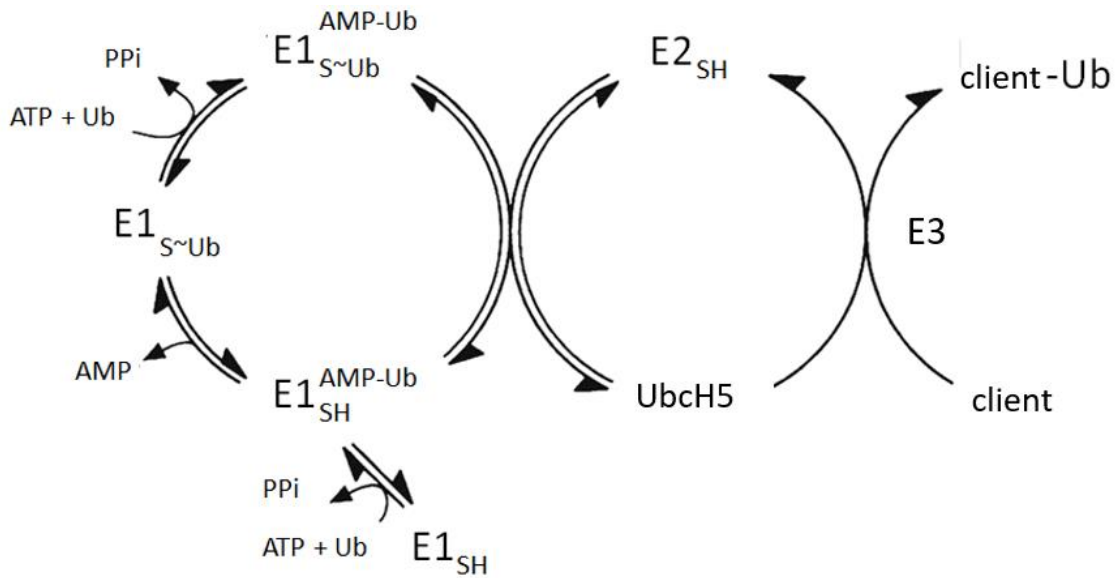
Figure 0.3 The ubiquitin-proteasome pathway. Proteins are directed to the proteasome protease by the post-translational modification of ubiquitin-chain conjugation, a complex energy dependent process that transfers a series of ubiquitin molecules onto a lysine of a target molecule. Ubiquitin is transferred between an E1 activating enzyme and E2 conjugating enzyme as well as an E3 ligase enzyme which catalyzes the final step either directly or indirectly. The ability of protein chaperones such as Hsp70 and Hsp90 to direct client ubiquitination allows for chaperones to both maintain a pool of functional protein as well as degrade them, facilitating protein turnover.

Transfer of ubiquitin involves a very complex chain of events carried out through three major classes of enzymes (Figure 0.3). An E1 activation enzyme first forms a high energy thioester bond between the E1 and ubiquitin though the use of ATP. The ubiquitin is then transferred to a second enzyme termed the E2 conjugation enzymes where it is poised for transfer onto the substrate. This is catalyzed through the third class called E3 ligase enzymes, which either acts as a catalyst or scaffold between the E2 and the substrate (the RING family of E3 enzymes) or as an additional receptor of ubiquitin where it is transferred first to the E3 before the substrate (HECT or RBR) [48]. These multi-tiered steps serve as checkpoints for substrate recognition and regulation.

An additional level of substrate selectivity is seen with the proteostasis chaperone machinery, namely the Hsp70, Hsp90 and CHIP proteins [49, 50]. CHIP acts as a RING class E3 ubiquitin ligase, and has been shown to selectively ubiquitinate clients bound to chaperone [35]. The structure of CHIP has been solved and reveals three domains responsible for its function in facilitating the protein degradation aspect of proteostasis [51, 52] (Figure 0.4). CHIP consists of an N-terminal tetratricopeptide domain (TPR) responsible for interactions with the EEVD motifs of Hsp70 and Hsp90, a middle helical hairpin domain which allows CHIP dimerization and a U-box domain, structurally related to the RING E3 domains. Dimerization of CHIP has been shown to be essential for its ability to ubiquitinate substrate [53]. This raises the questions of the function of having two TPR domains and two U-box domains in the mechanism of chaperone bound client ubiquitination. Structural studies have suggested that the restricted area and binding surfaces of the U-box domain for E2 enzymes allows for one U-box accessible for recruitment [54].
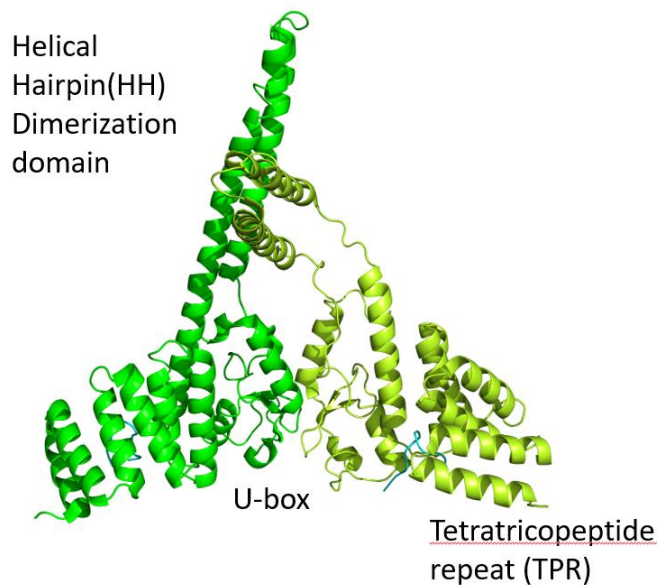
Figure 0.4 Crystal structure of murine CHIP. CHIP exists in solution as an obligate homodimer, essential for its function in ubiquitin transfer. In addition it contains the canonical tetratricopeptide repeat domain responsible for interactions with Hsp70 and Hsp90 EEVD motifs.

The affinity of CHIP for Hsp70 is greater than for Hsp90 or Hsc70, demonstrating preferential and varying capacities for ubiquitination to occur in the different chaperone systems [14]. These layers of regulation make it essential to understand the biochemical and structural properties of various chaperone:E3 complexes. Work detailing the Hsp70:CHIP interaction is discussed in chapter 1.

- **0.1.5 The nucleotide exchange factor BAG3 – bridging multiple chaperone systems**

Another significant co-chaperone aiding in the function of Hsp70 are NEF enzymes such as the Bcl-2associated AnthanoGene (BAG) proteins. NEFs bind to the NBD of Hsp70 and facilitate the exchange of ADP for ATP to allow continued cycling of nucleotide states [55]. The families of human NEF proteins are numerous and differentially expressed, and have been implicated in various disease states including Alzheimer's disease [56]. Of particular interest in my thesis is the BAG family of proteins, namely BAG3 which contains multiple binding motifs that in addition to acting as an Hsp70 NEF can interact with other chaperone systems [13].

BAG proteins consist of a C-terminal BAG domain which is capable of binding the bottom of the two lobes of the Hsp70 NBD, IB and IIB (Figure 0.1), to open the nucleotide binding pocket [34]. The BAG domain has been characterized as a three-helix bundle, but efforts to solve the structure of the N-terminal regions have proved elusive. This is due to the variability and flexibility of the domains that have been classified for the various BAG proteins [26]. BAG3 is one of the largest enzymes of the BAG family, containing many distinct protein-protein interaction domains [57, 58] (Figure 0.5). Its WW domain facilitates binding with PPxY motifs of clients, multiple PXXP motifs allow interactions with SH3 domains and two IPV motifs are responsible for binding with members of the sHSP chaperone family [59]. Though the structural characterization of BAG3 itself is challenging, the ability of these many domains to act as a scaffold was of great interest as to how BAG3 can modify the structure and function of chaperone complexes and for instance influence cell processes such as autophagy [57]. In chapter 2, a study on the BAG3 co-chaperone explores the Hsp70 pro-folding functions and the structural implications this protein has on bridging the Hsp70 and sHsp systems.

- **0.2 Tau- a model Hsp70 client implicated in protein folding diseases and neurodegeneration**

The accumulation of the microtubule-associated protein Tau (MAPT or tau) in neurofibrillary tangles (NFTs) is a hallmark of various neurodegenerative diseases, including Alzheimer's disease, frontotemporal dementia and chronic traumatic encephalopathy [39]. Hsp70 has been shown to affect the rate of tau accumulation, engaging tau at various pathological events [60]. However, structural modifications that occur to tau in route to its toxic oligomeric or aggregate species have been difficult to characterize owing to its intrinsic disorder [61].

Effective therapies directly targeting the tau protein are currently lacking. The molecular mechanisms regulating tau stability are not yet clear, therefore one focus of tauopathy treatment has been to

accelerate tau clearance, its degradation via the ubiquitin-proteasome pathway to alleviate the accumulation of potentially toxic species [29]. This has been shown to promote the viability of neurons as well as survival rates in mouse, drosophila and neuronal cell models [62-64].

- **0.2.1 Structural modifications of tau protein and disease**

Tau has six isoforms in humans, with the 0N4R the most common isoform in the central nervous system of the adult mouse brain [65]. The 0N4R name indicates the number of N-terminal inserts and microtubule binding repeat domains (R). The varying ratios of isoforms play a role in the propensity for NFTs to form in neurons, however the cellular levels of the 0N4R isoform make it of particular interest in neurodegenerative pathologies. Paired helical filaments (PHFs), the subunits that assemble into NFTs, have been characterized structurally and consist of tau heavily modified by post-translational modifications [66, 67].
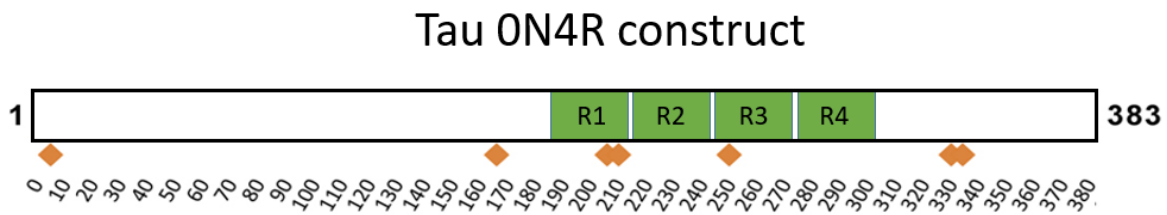
Figure 0.5 Structural elements of tau. The microtubule binding repeat domains confer tau the ability to stabilize microtubules and axonal cytoskeletal elements. Hsp70 binding sites, marked with diamonds, have also been mapped to this region by the Gestwicki and Dickey labs. Tau is an intrinsically disordered protein when not bound to protein partners and adopts mostly random inconsistent structures. Tau is found to aggregate in various neuropathologies and protein chaperones are thought to prevent this.

Tau can be phosphorylated multiple sites and hyperphosphorylation, or near saturation of these sites, is observed in NFTs and disease states [41, 68]. However, the physiological functions of tau phosphorylation or how it may contribute to neurodegenerative pathology are not completely understood. Ubiquitination is commonly found as post-translational modifications, and site and linkage specificity has been shown to accelerate turnover or protect tau from degradation [69]. The mechanism of how tau becomes ubiquitinated and targeted for degradation before forming into PHFs remains an important question underlying tau proteostasis.

- **0.2.2 Regulation of tau homeostasis by protein chaperones**

Underlying the observation that depletion of tau leads to increased viability [42, 62], studies on how the protein chaperone systems affect tau have shown that Hsp70 directly impacts the prevention of tau

aggregation as well as degradation [70]. Hsp70 has been shown to bind to the microtubule binding repeats of tau, preventing the formation of PHFs and assisting tau function in the binding and stabilization of axonal microtubules [29, 71]. Increasing affinity of Hsp70 for client suggests that the overall time Hsp70 spends bound to tau is a major determinant of cellular levels of tau, where specifically the stress inducible isoform Hsp72 or HSPA1A has been shown to better promote client ubiquitination and degradation over Hsc70 or other chaperones such as Hsp90 [72-74]. Thus, Hsp70 acts on a critical stage of tau pathology although the direct interaction is unknown. Because of the connection of Hsp70 to the proteasome through CHIP, the direct interaction between Hsp70 and CHIP is an important regulatory process in facilitating triage for tau proteostasis. To further investigate mechanisms which can be chemically probed to enhance tau turnover, Chapter 1 describes a study of the molecular events that take place during tau poly-ubiquitination.

- **0.3 Small heat shock proteins - oligomeric assemblies stalling client aggregation**

Small heat shock proteins (sHSPs) are a class of ATP independent protein chaperones that function in binding and stabilizing unfolded or aggregation prone client proteins [11]. Their primary function has been characterized as delaying protein aggregation, where protein refolding has typically been attributed to the assistance of other chaperone systems such as Hsp70. Usually consisting of small molecular weight species, sHsps exist as oligomers in solution of variable size and shape [75]. Studies have shown that upon activation, structural changes occur that alter the multimeric assemblies to form distinct 'activated' chaperones that protect exposed hydrophobic patches of unfolding or aggregating clients [76]. Thus, sHsps act as a reservoir of chaperones that serve as a buffer against protein aggregation, potentially connecting various chaperone families [13, 59]. Characterizing how this crosstalk occurs as well as what triggers the activation of sHsps is an outstanding question that will be further explored in chapters 2 and 3.

- **0.3.1 sHSP nucleotide independent holdase functions increase cell viability**

sHSPs participate in many biological processes, including the cell cycle, cell differentiation, stress response, and apoptosis [77]. Mutations of sHsp have been implicated in various diseases in development and peripheral nervous system pathologies [78]. Diseases such as cardiomyopathy, motor neuron diseases and cataracts have directly linked sHsp function to stabilizing various cytoskeletal elements as well as preventing protein aggregation [79-81]. One class of sHsps, Hsp27 or HSPB1, has been shown to alleviate the toxic effects of protein aggregates such as amyloid β *in vitro*, revealed to

bind to the oligomeric amyloid β and cause formation of larger aggregates without disrupting the secondary structure of the client proteins [82], demonstrating the varied structures of the holdase clients and the ambiguity of what constitutes toxic species to the cell. Another sHsp, αB crystallin or HSPB5, is directly involved in the buffering of stress in eye lens fiber cells, where high protein concentrations are necessary to provide adequate refractive index [81]. The environment causes pH stress relative to other cells where HSPB5 is expressed and may be a factor activating its holdase function [83]. Given the wide breadth of processes sHsp affects in the cell, the oligomeric distribution of sHsp proteins is one method of regulation and diversifying sHsp function. Although the general effect of slowing aggregation has been known, it has been difficult to characterize a structural mechanism in which they protect clients. Another major outstanding question is how binding partners and the chemical stressors modulate and activate sHsp oligomeric distribution.

- **0.3.2 The ensemble of structural states for the sHSP, αB crystallin (HSPB5)**

HSPB5 is an example of a sHsp existing as multimeric assemblies in solution, consisting of oligomers of very small gene products [84]. It shares many architectural features common among sHsps, including a conserved central α crystallin domain (ACD) which is flanked by variable N- and C-terminal regions. The basic HSPB5 subunit or protomer exists as an anti-parallel homodimer, with the ACD domains forming a dimer interface [85] (Figure 0.6). Structures of the core ACD dimer reveal an 8 β sheet stranded structure and is very similar between different classes of sHsps and across different species [75]. Within the variable regions, the C-terminus contains short sequence motifs of isoleucines, "IXI/V", that have been observed to bind to the ACD of neighboring dimers, forming interdimer contacts important for oligomeric assemblies of protomers [86]. HSPB5 assembles into a distribution of oligomeric states that undergo dynamic structural rearrangements and subunit exchange into different sized oligomers ranging from dimers to 40-mers [87]. Because of the lack of structural information regarding the unstructured variable regions, and the heterogeneity of the distribution of oligomers in solution, it has been challenging to obtain high resolution information on the arrangement of protomers and the protomer structures within the oligomers. Which forms of HSPB5 oligomers are active remains a central question.
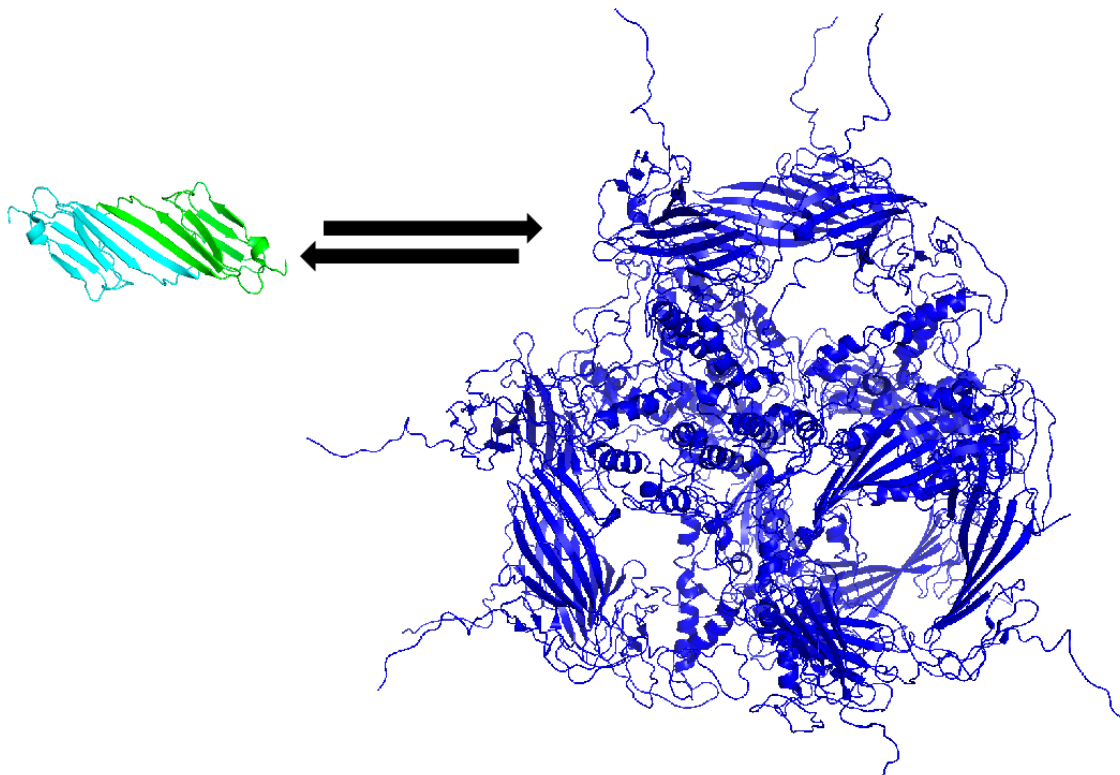
Figure 0.6 HSPB5 building blocks of higher order oligomers. The solution NMR structure of the HSPB5 dimer is represented in light blue and green, with an extensive β sheet interface describing the α-crystallin domains across between each monomer. Although it is not clear what exactly the building blocks are for many sHsp proteins, models have been proposed for symmetric assemblies of oligomers that reflect their average molecular weight in solution, such as the 24mer HSPB5. Because of the importance of the C-terminal IXI/V motif and the variable N-terminus, this particular model proposed by the Klevit lab has many random coils joining inter-dimer contacts as well as extend out into solution due to their non-structured nature.

HSPB5 and other sHsp proteins must engage in heteromeric interactions with their clients [76]. As mentioned previously, the diverse clientele that engage with sHsp proteins makes many modes of client modes possible. In support of this notion, one study demonstrated that a mixture of sHsps and clients in cell lysate demonstrated much better capacity to prevent aggregation than with individual recombinant substrates, illustrating the importance of the client structure. The dynamic nature of protomer exchange in sHsp oligomers on their own has also been shown to be dependent on stress conditions, as well as post-translational modifications [88]. However, it is unclear how these cellular stressors and changes affect the oligomeric distributions of sHsp species and how they protect clients. In chapter 3, these

questions of how the individual HSPB5 dimers react to pH stress are analyzed and the effects on oligomeric distribution and subsequent client binding are assessed.

- **0.4 Peroxiredoxin - emerging chaperone activities for multi-functional proteins**

Peroxiredoxins (Prxs) are highly conserved and ubiquitous peroxidases that are essential for antioxidant protection and cell signaling and relatively recently characterized as holdase chaperones [89]. Typical 2-Cys-Prxs are obligate homodimers of two inverted subunits that rely on two cysteines for hydroperoxide detoxification: the peroxidatic cysteine (Cp), which interacts directly with peroxides, and the resolving cysteine (Cr), which condenses with the oxidized Cp of the other subunit by forming a disulfide bond (Figure 0.7). The disulfide bond subsequently is regenerated by a thiol-containing oxidoreductase, such as thioredoxin or another member of the thioredoxin family [90].
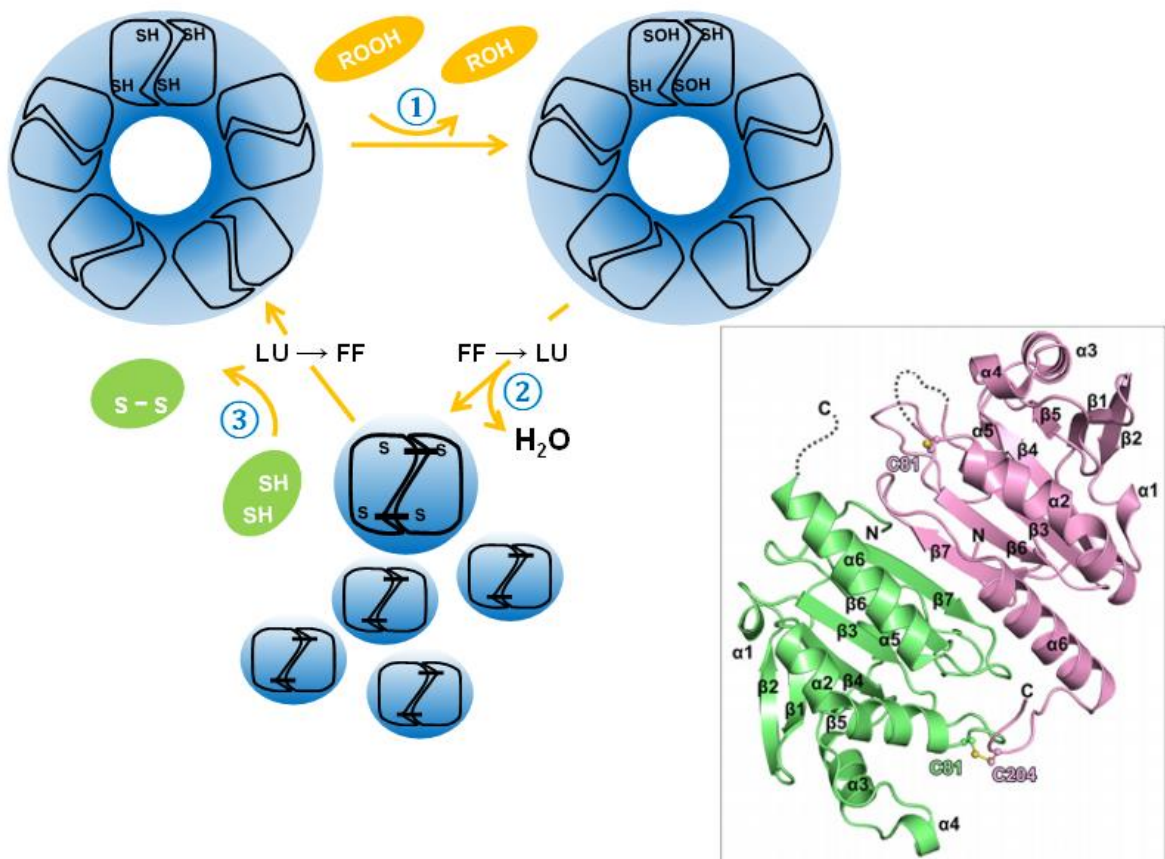
Figure 0.7 Peroxiredoxin function in protecting against oxidative stress. Members of 2-cys-peroxiredoxin family are obligate homodimers that are responsible for the clearance of a majority of peroxides produced for instance in the mitochondria. There are two active sites in each dimer responsible for the peroxidase activity, once oxidized it must become reduced by a thiol containing oxidoreductase to begin the next cycle. The *Leishmania infantum* mTXNPx uses tryparedoxin for this role hence the name. This figure was generated by Filipa Teixeira from Ursula Jakob's lab.

2-Cys-Prxs have been studied extensively in regard to their role in the detoxification of reactive oxygen and nitrogen species [91]. They also have been implicated in other biological activities, including H_2O_2 signaling, protein oxidation, and chaperoning functions under stress conditions [92]. The chaperone activity of 2-Cys-Prxs was first reported in 2004, when Jang et al. [93] proposed that peroxide-mediated overoxidation of the active cysteine Cp in yeast cytosolic 2-Cys-Prx (Tsa 1) inactivates the peroxidase function and triggers its conversion into high molecular weight oligomers that prevent *in vitro* protein aggregation.

- **0.4.1 Cell stress triggers various modifications to Prx structure and function**

Various conditions have been characterized that act as a functional switch converting Prx from a peroxidase to a holdase chaperone, including heavy oxidative stress, heat or site-specific post-translational modification [94-96]. These stimuli trigger structural changes in Prx that cause the homodimeric proteins to noncovalently associate into ring like decameric or dodecameric structures [97]. Reports have shown that the dimer-decamer conversion regulate the efficiency of peroxidase catalytic activity and chaperone activity, however the exact nature of the higher molecular weight species and which forms are active antioxidants or chaperones is unclear. It has been proposed that oxidative stress causes the shutdown of peroxidase activity with the overoxidation of disulfides to sulfenic acid, and causes structural changes that result in the stacking of decameric Prx [98]. Stress conditions such as pH has been shown to promote the formation of higher molecular weight species, with unfolding of the C-terminal domains which protrude from the outer Prx ring as putative substrate interaction sites [96, 99, 100]. Major questions remain of how the decameric Prx can account for some of these active high molecular weight species and their chaperone activity in the presence of heat shock.
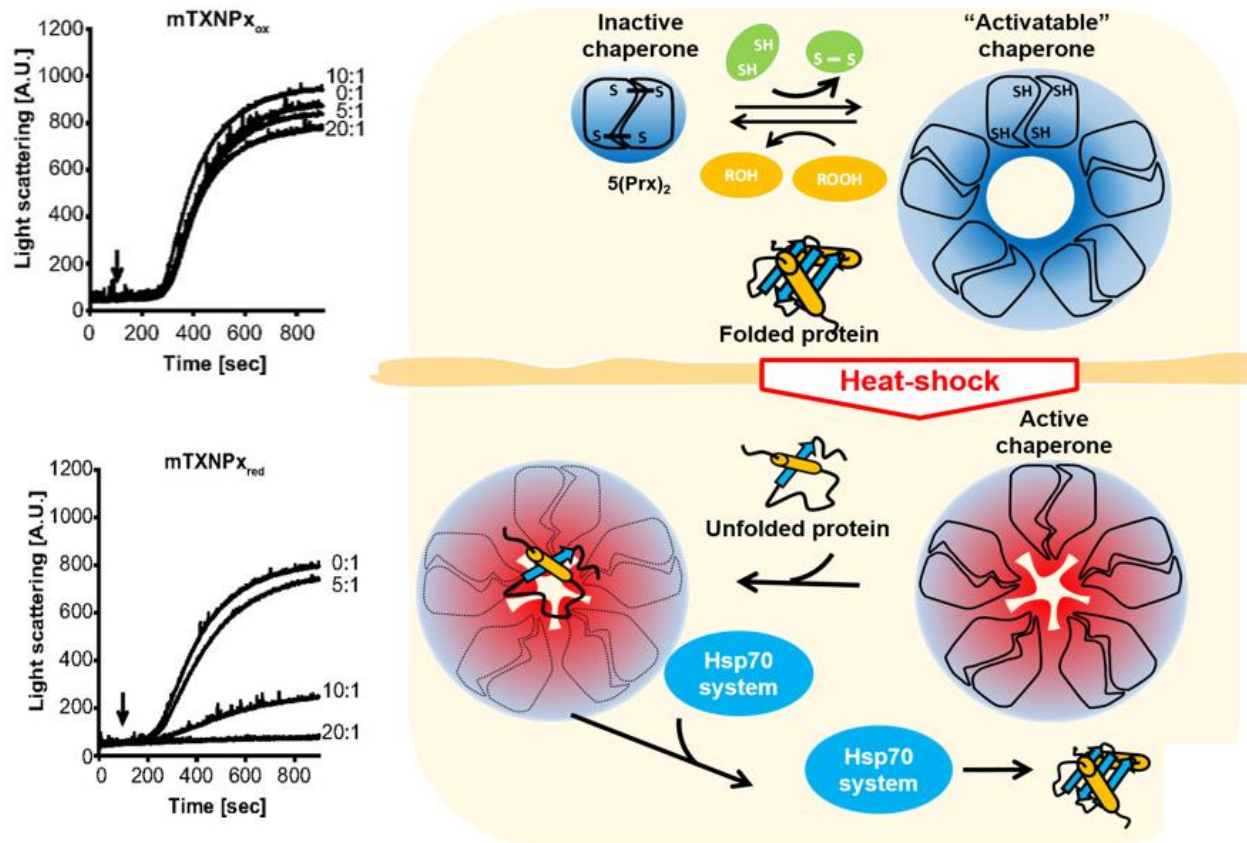
Figure 0.8 Chaperone activity of *Leishmania infantum* mTXNPx. The Jakob Lab has shown that heat shock activates a chaperone function in this mTXNPx molecule, using luciferase as a model substrate that aggregates over time during heat stress (top left panel, increased light scattering), however mTXNPx, specifically in the the reduced decamer form, is capable of preventing aggregation. This figure was generated by Filipa Teixeira from Ursula Jakob's lab.

Of particular interest is work by Castro et. al, detailing the relevance of another 2-Cys-Prx family protein, mitochondrial tryparedoxin-peroxidase (mTXNPx) in its ability to act as a chaperone to allow survival of a protozoan parasite [101]. The parasite *Leishmania Infantum* has a digenic life cycle, where it must survive between the cells of invertebrates (insects) and mammals and thus two different ambient temperatures (Figure 0.8). It was demonstrated that the mTXNPx deficient parasites were much more sensitive to temperature shifting from 25 °C and 37 °C, the transition from insect to mammalian hosts [94]. Through mutagenesis of mTXNPx abolishing its peroxidase activity, it was suggested that an alternative function of mTXNPx was responsible for ensuring viability of the parasite. Using this model system, we were able characterize a chaperone mechanism of a Prx class enzyme dependent on the specific decamer form of mTXNPx, presenting a case study on the importance of protein folding in the face of stressors such as heat shock. The published mechanism of temperature-sensitive activation, as

15

well as further studies into the structure of the client bound chaperone complex and their binding interface is presented in chapter 4.

- **0.5 Electron microscopy: a powerful technique providing structural information from both high and low resolutions**

In my thesis work, I use the term electron microscopy (EM) generally to refer to the practice of single particle analysis of protein molecules embed in heavy metal stain (negative stain EM) or vitrified ice (cryo-EM) [102-104]. A very basic overview of how these techniques allow the visualization of protein structure follows. By subjecting the immobilized proteins to high vacuum and an incident electron beam, an electron microscope, through the use of symmetric magnetic fields, can reconverge the diffracted electrons to obtain a two-dimensional image of the particles, an electron micrograph containing particles in various orientations (Figure 0.9). 2D projections correlate with the 3D object they represent described by the central section theorem [105], which states that the fourier transforms of the 2D projections are 'central slices' through the origin of the fourier transform of the 3D object. The fundamental goal of electron microscopy aims to determine a complete 3D fourier representation of the object by assigning for each projection the pose, or orientation parameters relating the 2D projections to one another by rotational and translational shifts, so that the reverse fourier transform can be used to recover the 3D object in real space.

In practice, the process of determining 3D structure from cryo-EM is very challenging, with one of its most fundamental issues arising from the intrinsically noisy images owing to the physics involved in electron diffraction by proteins [106, 107]. Solutions to these issues have steadily advanced over the decades. Freezing proteins in solution at liquid nitrogen temperatures has helped alleviate the amount of radiation damage incurred by electron exposure, and the use of liquid ethane to trap proteins in non-crystalline or vitreous ice has allowed imaging of proteins with low background signal [103, 108]. This, alongside the development of specialized hardware of more coherent electron sources, more powerful and stable microscopes, has made electron microscopy into a routine procedure for determination of protein structure [109, 110] .
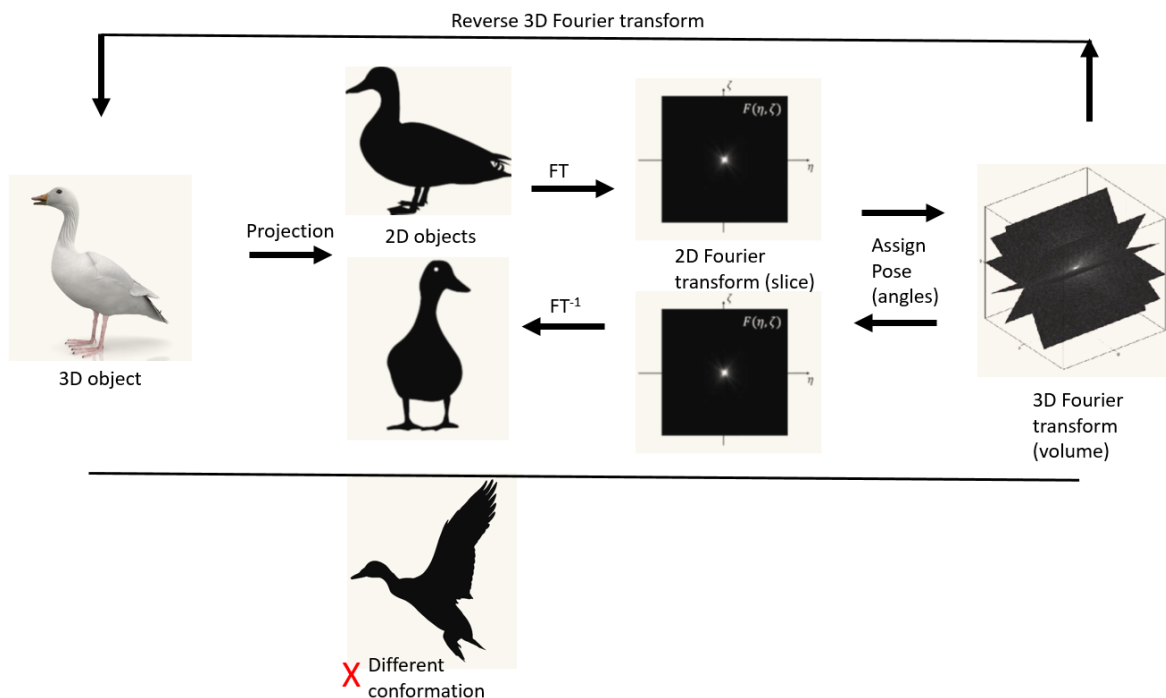
Figure 0.9 Simplified schematic for structural determination by EM. From an electron microscope, one can obtain 2D projections of the 3D object of interest such as protein particles. In an ideal scenario, we can prepare the protein sample suspended in random orientations and thus obtain multiple projections of the same object. Care must be taken to remove projections that are of a different object or conformation. Any 3D or 2D object can be represented in Fourier space, by calculating the Fourier transform of something in spatial coordinates one can obtain a representation of that object in terms the frequencies which in this case reflect spatial frequency of contrast. The main problem of EM is the assignment of pose, or the orientation of each Fourier slice, because one must have some idea of the 3D object to project this test model and match each projection to the best orientation of the test model.

The past decade in particular has seen major advances that have directly contributed to the cryo-EM studies I have carried out in my thesis in chapters 1 and 4. The development of semiconductor detectors, termed 'direct detectors', has succeeded the use of CCD technology [111]. These cameras have the ability to precisely count electrons at any given position on the detector and has both greatly improved the resolution and signal of electron micrographs and enables the ability to split an image exposure into short subframes in order to realign each subframe to account for any movements induced by the electron beam or instabilities in the microscope [112]. Recent efforts in the development of 'phase-plates' have also gained traction, and is further detailed as a future direction in chapter 5 [113]. This technology can be simplified as a method to obtain better contrast for smaller protein particles, an issue that generally limits the ability of cryo-EM to resolve higher resolution information for particles on the order of 300 kDa or smaller [114].

Development of software to handle the complex problem of assigning the pose for each 2D projection has been an ongoing effort [115, 116] . A developer of one popular and robust software package, Sjors Scheres, has described two major hurdles in solving the structure through EM: data such as orientation parameters are not experimentally observed and the dataset is finite without a unique solution [117]. With these issues in mind, the RELION software package has proven to be very effective in establishing a pipeline to solving 3D structure. Taking classical approaches of bootstrap refinement of orientation parameters, it utilizes marginalization and Bayesian statistic approaches to weight noisy particle images by the likelihood of pose being correct. This software package has been instrumental in obtaining 3D information from cryo-EM. Software for the automation of image acquisition from an electron microscope has also allowed a greater throughput in obtaining enough EM data to overcome the issues of noise and has been extremely helpful in pushing the resolution of cryo-EM structures. In addition, optimization of software to run these calculations utilizing GPUs have sped up the ability to process EM-data [118]. I have placed much effort in understanding and establishing automation and processing of EM data in my graduate career, and these developments are further detailed as exciting future directions in chapter 5.

Negative stain EM has also been an effective and high throughput method to analyze structural information of various protein complexes in my graduate work. Because of the challenges presented earlier on producing a unique, high resolution solution through cryo-EM, it is not always feasible to determine structure for every protein sample. Negative stain EM has advantages in the overall time spent and consistency of sample preparation can allow immediate visualization [104]. This low-resolution technique embeds protein sample in heavy metal stain, such as uranyl formate, producing high contrast between stain and protein to allow visualization of quaternary structure. Useful structural information can be obtained about the overall conformations that occur with biochemical conditions.

- **0.6 Notes**

Section 0.4 of this introduction is adapted from the publication Teixeira, F. Castro, H. Cruz, T. **Tse, E**. Koldewey, P. Southworth, D. R. Tomas, A. M. Jakob, U., Proc Natl Acad Sci U S A, 2015. **112**(7): p. E616-24. Motivations behind the Prx project biochemistry and guidance provided by Filipa Teixeira and Ursula Jakob.

- **0.7 References**

1. Saibil, H., *Chaperone machines for protein folding, unfolding and disaggregation.* Nat Rev Mol Cell Biol, 2013. **14**(10): p. 630-42.
2. Zuiderweg, E.R., L.E. Hightower, and J.E. Gestwicki, *The remarkable multivalency of the Hsp70 chaperones.* Cell Stress Chaperones, 2017. **22**(2): p. 173-189.
3. Hartl, F.U., A. Bracher, and M. Hayer-Hartl, *Molecular chaperones in protein folding and proteostasis.* Nature, 2011. **475**(7356): p. 324-32.
4. Wilbanks, S.M., C. DeLuca-Flaherty, and D.B. McKay, *Structural basis of the 70-kilodalton heat shock cognate protein ATP hydrolytic activity. I. Kinetic analyses of active site mutants.* J Biol Chem, 1994. **269**(17): p. 12893-8.
5. Flaherty, K.M., et al., *Structural basis of the 70-kilodalton heat shock cognate protein ATP hydrolytic activity. II. Structure of the active site with ADP or ATP bound to wild type and mutant ATPase fragment.* J Biol Chem, 1994. **269**(17): p. 12899-907.
6. Zuiderweg, E.R., et al., *Allostery in the Hsp70 chaperone proteins.* Top Curr Chem, 2013. **328**: p. 99-153.
7. Mayer, M.P., *Hsp70 chaperone dynamics and molecular mechanism.* Trends in Biochemical Sciences, 2013. **38**(10): p. 507-514.
8. Zhuravleva, A. and L.M. Gierasch, *Substrate-binding domain conformational dynamics mediate Hsp70 allostery.* Proc Natl Acad Sci U S A, 2015. **112**(22): p. E2865-73.
9. Alderson, T.R., J.H. Kim, and J.L. Markley, *Dynamical structures of Hsp70 and Hsp70–Hsp40 complexes.* Structure (London, England : 1993), 2016. **24**(7): p. 1014-1030.
10. Mayer, M.P., et al., *Multistep mechanism of substrate binding determines chaperone activity of Hsp70.* Nat Struct Biol, 2000. **7**(7): p. 586-93.
11. Carra, S., et al., *The growing world of small heat shock proteins: from structure to functions.* Cell Stress Chaperones, 2017. **22**(4): p. 601-611.
12. Scheufler, C., et al., *Structure of TPR domain-peptide complexes: critical elements in the assembly of the Hsp70-Hsp90 multichaperone machine.* Cell, 2000. **101**(2): p. 199-210.
13. Rauch, J.N. and J.E. Gestwicki, *Binding of human nucleotide exchange factors to heat shock protein 70 (Hsp70) generates functionally distinct complexes in vitro.* J Biol Chem, 2014. **289**(3): p. 1402-14.
14. Stankiewicz, M., et al., *CHIP participates in protein triage decisions by preferentially ubiquitinating Hsp70-bound substrates.* FEBS J, 2010. **277**(16): p. 3353-67.
15. Clerico, E.M., et al., *How hsp70 molecular machines interact with their substrates to mediate diverse physiological functions.* J Mol Biol, 2015. **427**(7): p. 1575-88.
16. Bertelsen, E.B., et al., *Solution conformation of wild-type E. coli Hsp70 (DnaK) chaperone complexed with ADP and substrate.* Proc Natl Acad Sci U S A, 2009. **106**(21): p. 8471-6.
17. Kityk, R., et al., *Structure and dynamics of the ATP-bound open conformation of Hsp70 chaperones.* Mol Cell, 2012. **48**(6): p. 863-74.
18. Schmid, D., et al., *Kinetics of molecular chaperone action.* Science, 1994. **263**(5149): p. 971-3.
19. Burkart, V., et al., *High affinity binding of hydrophobic and autoantigenic regions of proinsulin to the 70 kDa chaperone DnaK.* BMC Biochemistry, 2010. **11**: p. 44-44.
20. Fourie, A.M., J.F. Sambrook, and M.J. Gething, *Common and divergent peptide binding specificities of hsp70 molecular chaperones.* J Biol Chem, 1994. **269**(48): p. 30470-8.
21. Barthel, T.K., J. Zhang, and G.C. Walker, *ATPase-defective derivatives of Escherichia coli DnaK that behave differently with respect to ATP-induced conformational change and peptide release.* J Bacteriol, 2001. **183**(19): p. 5482-90.

22.   Qi, R., et al., *Allosteric opening of the polypeptide-binding site when an Hsp70 binds ATP.* Nat Struct Mol Biol, 2013. **20**(7): p. 900-7.
23.   Vogel, M., M.P. Mayer, and B. Bukau, *Allosteric regulation of Hsp70 chaperones involves a conserved interdomain linker.* J Biol Chem, 2006. **281**(50): p. 38705-11.
24.   Swain, J.F., et al., *Hsp70 chaperone ligands control domain association via an allosteric mechanism mediated by the interdomain linker.* Mol Cell, 2007. **26**(1): p. 27-39.
25.   Zhuravleva, A., E.M. Clerico, and L.M. Gierasch, *An interdomain energetic tug-of-war creates the allosterically active state in Hsp70 molecular chaperones.* Cell, 2012. **151**(6): p. 1296-307.
26.   Mayer, M.P. and B. Bukau, *Hsp70 chaperones: cellular functions and molecular mechanism.* Cell Mol Life Sci, 2005. **62**(6): p. 670-84.
27.   O'Brien, M.C., K.M. Flaherty, and D.B. McKay, *Lysine 71 of the chaperone protein Hsc70 Is essential for ATP hydrolysis.* J Biol Chem, 1996. **271**(27): p. 15874-8.
28.   Johnson, E.R. and D.B. McKay, *Mapping the role of active site residues for transducing an ATP-induced conformational change in the bovine 70-kDa heat shock cognate protein.* Biochemistry, 1999. **38**(33): p. 10823-30.
29.   Young, Z.T., et al., *Stabilizing the Hsp70-Tau Complex Promotes Turnover in Models of Tauopathy.* Cell Chem Biol, 2016. **23**(8): p. 992-1001.
30.   Kampinga, H.H. and E.A. Craig, *The HSP70 chaperone machinery: J proteins as drivers of functional specificity.* Nat Rev Mol Cell Biol, 2010. **11**(8): p. 579-92.
31.   Kirschke, E., et al., *Glucocorticoid receptor function regulated by coordinated action of the Hsp90 and Hsp70 chaperone cycles.* Cell, 2014. **157**(7): p. 1685-97.
32.   Alvira, S., et al., *Structural characterization of the substrate transfer mechanism in Hsp70/Hsp90 folding machinery mediated by Hop.* Nat Commun, 2014. **5**: p. 5484.
33.   Ahmad, A., et al., *Heat shock protein 70 kDa chaperone/DnaJ cochaperone complex employs an unusual dynamic interface.* Proc Natl Acad Sci U S A, 2011. **108**(47): p. 18966-71.
34.   Sondermann, H., et al., *Structure of a Bag/Hsc70 complex: convergent functional evolution of Hsp70 nucleotide exchange factors.* Science, 2001. **291**(5508): p. 1553-7.
35.   Connell, P., et al., *The co-chaperone CHIP regulates protein triage decisions mediated by heat-shock proteins.* Nat Cell Biol, 2001. **3**(1): p. 93-6.
36.   Smith, M.C., et al., *The E3 ubiquitin ligase CHIP and the molecular chaperone Hsc70 form a dynamic, tethered complex.* Biochemistry, 2013. **52**(32): p. 5354-64.
37.   Zhang, H., et al., *A bipartite interaction between Hsp70 and CHIP regulates ubiquitination of chaperoned client proteins.* Structure, 2015. **23**(3): p. 472-82.
38.   Ebong, I.O., et al., *Heterogeneity and dynamics in the assembly of the heat shock protein 90 chaperone complexes.* Proc Natl Acad Sci U S A, 2011. **108**(44): p. 17939-44.
39.   Morimoto, R.I., *Proteotoxic stress and inducible chaperone networks in neurodegenerative disease and aging.* Genes Dev, 2008. **22**(11): p. 1427-38.
40.   Cook, C., et al., *Acetylation of the KXGS motifs in tau is a critical determinant in modulation of tau aggregation and clearance.* Hum Mol Genet, 2014. **23**(1): p. 104-16.
41.   Hanger, D.P., B.H. Anderton, and W. Noble, *Tau phosphorylation: the therapeutic challenge for neurodegenerative disease.* Trends in Molecular Medicine, 2009. **15**(3): p. 112-119.
42.   Ramsden, M., et al., *Age-dependent neurofibrillary tangle formation, neuron loss, and memory impairment in a mouse model of human tauopathy (P301L).* J Neurosci, 2005. **25**(46): p. 10637-47.
43.   Jinwal, U.K., et al., *The Hsp90 cochaperone, FKBP51, increases Tau stability and polymerizes microtubules.* J Neurosci, 2010. **30**(2): p. 591-9.
44.   Wang, A.M., et al., *Activation of Hsp70 reduces neurotoxicity by promoting polyglutamine protein degradation.* Nat Chem Biol, 2013. **9**(2): p. 112-8.

45. Fontaine, S.N., et al., *The active Hsc70/tau complex can be exploited to enhance tau turnover without damaging microtubule dynamics.* Hum Mol Genet, 2015. **24**(14): p. 3971-81.

46. Kleiger, G. and T. Mayor, *Perilous journey: a tour of the ubiquitin–proteasome system.* Trends in cell biology, 2014. **24**(6): p. 352-359.

47. Komander, D. and M. Rape, *The ubiquitin code.* Annu Rev Biochem, 2012. **81**: p. 203-29.

48. Kamadurai, H.B., et al., *Mechanism of ubiquitin ligation and lysine prioritization by a HECT E3.* Elife, 2013. **2**: p. e00828.

49. Pratt, W.B., et al., *Proposal for a role of the Hsp90/Hsp70-based chaperone machinery in making triage decisions when proteins undergo oxidative and toxic damage.* Exp Biol Med (Maywood), 2010. **235**(3): p. 278-89.

50. Thompson, A.D., et al., *Analysis of the tau-associated proteome reveals that exchange of Hsp70 for Hsp90 is involved in tau degradation.* ACS Chem Biol, 2012. **7**(10): p. 1677-86.

51. Zhang, M., et al., *Chaperoned ubiquitylation--crystal structures of the CHIP U box E3 ubiquitin ligase and a CHIP-Ubc13-Uev1a complex.* Mol Cell, 2005. **20**(4): p. 525-38.

52. Xu, Z., et al., *Structure and interactions of the helical and U-box domains of CHIP, the C terminus of HSP70 interacting protein.* Biochemistry, 2006. **45**(15): p. 4749-59.

53. Nikolay, R., et al., *Dimerization of the human E3 ligase CHIP via a coiled-coil domain is essential for its activity.* J Biol Chem, 2004. **279**(4): p. 2673-8.

54. Graf, C., et al., *Insights into the conformational dynamics of the E3 ubiquitin ligase CHIP in complex with chaperones and E2 enzymes.* Biochemistry, 2010. **49**(10): p. 2121-9.

55. Takayama, S., Z. Xie, and J.C. Reed, *An evolutionarily conserved family of Hsp70/Hsc70 molecular chaperone regulators.* J Biol Chem, 1999. **274**(2): p. 781-6.

56. Carrettiero, D.C., et al., *The cochaperone BAG2 sweeps paired helical filament- insoluble tau from the microtubule.* J Neurosci, 2009. **29**(7): p. 2151-61.

57. Gamerdinger, M., et al., *Protein quality control during aging involves recruitment of the macroautophagy pathway by BAG3.* EMBO J, 2009. **28**(7): p. 889-901.

58. Xu, Z., et al., *14-3-3 protein targets misfolded chaperone-associated proteins to aggresomes.* J Cell Sci, 2013. **126**(Pt 18): p. 4173-86.

59. Seidel, K., et al., *The HSPB8-BAG3 chaperone complex is upregulated in astrocytes in the human brain affected by protein aggregation diseases.* Neuropathol Appl Neurobiol, 2012. **38**(1): p. 39-53.

60. Miyata, Y., et al., *Molecular chaperones and regulation of tau quality control: strategies for drug discovery in tauopathies.* Future Med Chem, 2011. **3**(12): p. 1523-37.

61. Narayanan, R.L., et al., *Automatic assignment of the intrinsically disordered protein Tau with 441-residues.* J Am Chem Soc, 2010. **132**(34): p. 11906-7.

62. Santacruz, K., et al., *Tau suppression in a neurodegenerative mouse model improves memory function.* Science, 2005. **309**(5733): p. 476-81.

63. Augustinack, J.C., et al., *Specific tau phosphorylation sites correlate with severity of neuronal cytopathology in Alzheimer's disease.* Acta Neuropathol, 2002. **103**(1): p. 26-35.

64. Huang, Y., Z. Wu, and B. Zhou, *hSOD1 promotes tau phosphorylation and toxicity in the Drosophila model.* J Alzheimers Dis, 2015. **45**(1): p. 235-44.

65. Ballatore, C., V.M. Lee, and J.Q. Trojanowski, *Tau-mediated neurodegeneration in Alzheimer's disease and related disorders.* Nat Rev Neurosci, 2007. **8**(9): p. 663-72.

66. Coppola, G., et al., *Evidence for a role of the rare p.A152T variant in MAPT in increasing the risk for FTD-spectrum and Alzheimer's diseases.* Hum Mol Genet, 2012. **21**(15): p. 3500-12.

67. Shahpasand, K., et al., *Regulation of mitochondrial transport and inter-microtubule spacing by tau phosphorylation at the sites hyperphosphorylated in Alzheimer's disease.* J Neurosci, 2012. **32**(7): p. 2430-41.

68.   Fitzpatrick, A.W.P., et al., *Cryo-EM structures of tau filaments from Alzheimer's disease.* Nature, 2017. **547**(7662): p. 185-190.

69.   Dickey, C.A., et al., *Deletion of the ubiquitin ligase CHIP leads to the accumulation, but not the aggregation, of both endogenous phospho- and caspase-3-cleaved tau species.* J Neurosci, 2006. **26**(26): p. 6985-96.

70.   Jinwal, U.K., et al., *Imbalance of Hsp70 family variants fosters tau accumulation.* FASEB J, 2013. **27**(4): p. 1450-9.

71.   Otvos, L., Jr., et al., *Monoclonal antibody PHF-1 recognizes tau protein phosphorylated at serine residues 396 and 404.* J Neurosci Res, 1994. **39**(6): p. 669-73.

72.   Dickey, C.A., et al., *The high-affinity HSP90-CHIP complex recognizes and selectively degrades phosphorylated tau client proteins.* J Clin Invest, 2007. **117**(3): p. 648-58.

73.   Abisambra, J., et al., *Allosteric heat shock protein 70 inhibitors rapidly rescue synaptic plasticity deficits by reducing aberrant tau.* Biol Psychiatry, 2013. **74**(5): p. 367-74.

74.   Jinwal, U.K., et al., *Chemical manipulation of hsp70 ATPase activity regulates tau stability.* J Neurosci, 2009. **29**(39): p. 12079-88.

75.   Delbecq, S.P. and R.E. Klevit, *One size does not fit all: the oligomeric states of alphaB crystallin.* FEBS Lett, 2013. **587**(8): p. 1073-80.

76.   Mymrikov, E.V., et al., *The Chaperone Activity and Substrate Spectrum of Human Small Heat Shock Proteins.* J Biol Chem, 2017. **292**(2): p. 672-684.

77.   Haslbeck, M. and E. Vierling, *A First Line of Stress Defense: Small Heat Shock Proteins and Their Function in Protein Homeostasis.* Journal of Molecular Biology, 2015. **427**(7): p. 1537-1548.

78.   Giese, K.C. and E. Vierling, *Mutants in a small heat shock protein that affect the oligomeric state. Analysis and allele-specific suppression.* J Biol Chem, 2004. **279**(31): p. 32674-83.

79.   Vicart, P., et al., *A missense mutation in the alphaB-crystallin chaperone gene causes a desmin-related myopathy.* Nat Genet, 1998. **20**(1): p. 92-5.

80.   Goldstein, L.E., et al., *Cytosolic beta-amyloid deposition and supranuclear cataracts in lenses from people with Alzheimer's disease.* Lancet, 2003. **361**(9365): p. 1258-65.

81.   Nahomi, R.B., et al., *Chaperone peptides of alpha-crystallin inhibit epithelial cell apoptosis, protein insolubilization, and opacification in experimental cataracts.* J Biol Chem, 2013. **288**(18): p. 13022-35.

82.   Wilhelmus, M.M., et al., *Specific association of small heat shock proteins with the pathological hallmarks of Alzheimer's disease brains.* Neuropathol Appl Neurobiol, 2006. **32**(2): p. 119-30.

83.   McVicar, N., et al., *Quantitative tissue pH measurement during cerebral ischemia using amine and amide concentration-independent detection (AACID) with MRI.* J Cereb Blood Flow Metab, 2014. **34**(4): p. 690-8.

84.   Horwitz, J., *Alpha crystallin: the quest for a homogeneous quaternary structure.* Exp Eye Res, 2009. **88**(2): p. 190-4.

85.   van Montfort, R.L., et al., *Crystal structure and assembly of a eukaryotic small heat shock protein.* Nat Struct Biol, 2001. **8**(12): p. 1025-30.

86.   Taylor, R.P. and I.J. Benjamin, *Small heat shock proteins: a new classification scheme in mammals.* J Mol Cell Cardiol, 2005. **38**(3): p. 433-44.

87.   Braun, N., et al., *Multiple molecular architectures of the eye lens chaperone alphaB-crystallin elucidated by a triple hybrid approach.* Proc Natl Acad Sci U S A, 2011. **108**(51): p. 20491-6.

88.   Miesbauer, L.R., et al., *Post-translational modifications of water-soluble human lens crystallins from young adults.* J Biol Chem, 1994. **269**(17): p. 12494-502.

89.   Hall, A., P.A. Karplus, and L.B. Poole, *Typical 2-Cys peroxiredoxins--structures, mechanisms and functions.* FEBS J, 2009. **276**(9): p. 2469-77.

90.   Chae, H.Z., S.J. Chung, and S.G. Rhee, *Thioredoxin-dependent peroxide reductase from yeast.* J Biol Chem, 1994. **269**(44): p. 27670-8.

91.   Winterbourn, C.C., *Reconciling the chemistry and biology of reactive oxygen species.* Nat Chem Biol, 2008. **4**(5): p. 278-86.

92.   Rhee, S.G. and H.A. Woo, *Multiple functions of peroxiredoxins: peroxidases, sensors and regulators of the intracellular messenger H(2)O(2), and protein chaperones.* Antioxid Redox Signal, 2011. **15**(3): p. 781-94.

93.   Jang, H.H., et al., *Two Enzymes in One: Two Yeast Peroxiredoxins Display Oxidative Stress-Dependent Switching from a Peroxidase to a Molecular Chaperone Function.* Cell, 2004. **117**(5): p. 625-635.

94.   Castro, H., et al., *Leishmania mitochondrial peroxiredoxin plays a crucial peroxidase-unrelated role during infection: insight into its novel chaperone activity.* PLoS Pathog, 2011. **7**(10): p. e1002325.

95.   Saccoccia, F., et al., *Moonlighting by different stressors: Crystal structure of the chaperone species of a 2-Cys peroxiredoxin.* Structure(London, England:1993), 2012. **20**(3): p. 429-439.

96.   Angelucci, F., et al., *Switching between the Alternative Structures and Functions of a 2-Cys Peroxiredoxin, by Site-Directed Mutagenesis.* Journal of Molecular Biology, 2013. **425**(22): p. 4556-4568.

97.   Hall, A., et al., *Structure-based Insights into the Catalytic Power and Conformational Dexterity of Peroxiredoxins.* Antioxidants & Redox Signaling, 2011. **15**(3): p. 795-815.

98.   Trujillo, M., et al., *Kinetics of peroxiredoxins and their role in the decomposition of peroxynitrite.* Subcell Biochem, 2007. **44**: p. 83-113.

99.   Khoshouei, M., et al., *Volta phase plate cryo-EM of the small protein complex Prx3.* Nature Communications, 2016. **7**: p. 10534.

100.   Jang, H.H., et al., *Phosphorylation and concomitant structural changes in human 2-Cys peroxiredoxin isotype I differentially regulate its peroxidase and molecular chaperone functions.* FEBS Lett, 2006. **580**(1): p. 351-5.

101.   Morais, M.A.B., et al., *How pH Modulates the Dimer-Decamer Interconversion of 2-Cys Peroxiredoxins from the Prx1 Subfamily.* The Journal of Biological Chemistry, 2015. **290**(13): p. 8582-8590.

102.   Dobro, M.J., et al., *Chapter Three - Plunge Freezing for Electron Cryomicroscopy*, in *Methods in Enzymology*, J.J. Grant, Editor. 2010, Academic Press. p. 63-82.

103.   McDowall, A.W., et al., *Electron microscopy of frozen hydrated sections of vitreous ice and vitrified biological samples.* J Microsc, 1983. **131**(Pt 1): p. 1-9.

104.   Ohi, M., et al., *Negative Staining and Image Classification - Powerful Tools in Modern Electron Microscopy.* Biol Proced Online, 2004. **6**: p. 23-34.

105.   Penczek, P.A., *Image restoration in cryo-electron microscopy.* Methods Enzymol, 2010. **482**: p. 35-72.

106.   Grant, T. and N. Grigorieff, *Measuring the optimal exposure for single particle cryo-EM using a 2.6 A reconstruction of rotavirus VP6.* Elife, 2015. **4**: p. e06980.

107.   Wade, R.H., *A brief look at imaging and contrast transfer* Ultramicroscopy, 1992. **46**: p. 145-156

108.   Stark, H., F. Zemlin, and C. Boettcher, *Electron Radiation Damage to Protein Crystals of Bacteriorhodopsin at Different Temperatures.* Ultramicroscopy, 1996. **63**(2): p. 75-79.

109.   Sun, J. and H. Li, *Chapter Ten - How to Operate a Cryo-Electron Microscope*, in *Methods in Enzymology*, J.J. Grant, Editor. 2010, Academic Press. p. 231-249.

110.   Suloway, C., et al., *Automated molecular microscopy: the new Leginon system.* Journal of structural biology, 2005. **151**(1): p. 41-60.

111. McMullan, G., et al., *Comparison of optimal performance at 300keV of three direct electron detectors for use in low dose electron microscopy.* Ultramicroscopy, 2014. **147**: p. 156-63.

112. Rosenzweig, R., et al., *Promiscuous binding by Hsp70 results in conformational heterogeneity and fuzzy chaperone-substrate ensembles.* eLife, 2017. **6**: p. e28030.

113. Danev, R., D. Tegunov, and W. Baumeister, *Using the Volta phase plate with defocus for cryo-EM single particle analysis.* eLife, 2017. **6**: p. e23006.

114. Tarazona, M.P. and E. Saiz, *Combination of SEC/MALS experimental procedures and theoretical analysis for studying the solution properties of macromolecules.* Journal of Biochemical and Biophysical Methods, 2003. **56**(1): p. 95-116.

115. Tang, G., et al., *EMAN2: an extensible image processing suite for electron microscopy.* J Struct Biol, 2007. **157**(1): p. 38-46.

116. Shaikh, T.R., et al., *SPIDER image processing for single-particle reconstruction of biological macromolecules from electron micrographs.* Nat. Protocols, 2008. **3**(12): p. 1941-1974.

117. Scheres, S.H.W., *A Bayesian View on Cryo-EM Structure Determination.* Journal of Molecular Biology, 2012. **415**(2): p. 406-418.

118. Kimanius, D., et al., *Accelerated cryo-EM structure determination with parallelisation using GPUs in RELION-2.* Elife, 2016. **5**.

Chapter 1

Hsp70 Dependent Triage Mechanisms of CHIP E3 Ubiquitin Ligase Facilitate Poly-ubiquitination of Tau

- **1.1 Abstract**

Heat shock protein 70 (Hsp70) is a ubiquitous molecular chaperone that is essential in cellular protein homeostasis, or proteostasis, binding to exposed hydrophobic patches of client substrate to protect proteins from aggregation and facilitate refolding. This process is described by two major conformations of Hsp70 where its N-terminal nucleotide-binding domain (NBD) and C-terminal substrate binding domain (SBD) rely on allosteric communication to couple ATP hydrolysis with substrate binding. Alternation between a high affinity ADP state and a low affinity ATP state constitutes a cycle of client binding and release essential for its foldase activity. In addition, Hsp70 has been shown to interact with the CHIP (C-terminus of Hsp70 Interacting Protein), an E3 ubiquitin ligase, to promote client ubiquitination, and proteasomal degradation, leading to protein turnover. How this process of triage occurs or how Hsp70 directs ubiquitination is not clearly understood. To better understand Hsp70 dependent ubiquitination, we examined the role of nucleotide binding on CHIP recruitment and identified the formation of an ADP-specific Hsp70:CHIP tetramer complex. Utilizing a pathologically important client protein tau, we found that conditions that favor Hsp70 recruitment of CHIP result in the Hsp70 dependent poly-ubiquitination of tau, suggesting the importance of Hsp70 in homeostasis of tau that precedes development of pathological forms of tau. In addition, we found evidence that Hsp70, CHIP and tau must remain associated for efficient poly-ubiquitination to occur. These studies show direct evidence for how slowing down the Hsp70 chaperone cycle in the ADP state promotes client turnover, suggesting a mechanism where conditions that favor Hsp70 dwell time on clients allows sufficient time for CHIP binding and poly-ubiquitination. We characterized the structure of the Hsp70:CHIP complex utilizing cryo-EM and mass spectrometry, revealing a W-shaped architecture that positions Hsp70 SBD and CHIP U-box domain for efficient ubiquitin transfer. By identification of crosslinks in the Hsp70:CHIP as well as the Hsp70:CHIP:tau complex we are able to validate our cryo-EM structure as well as examine the changes in interaction surfaces when these proteins bind together. Overall, we provide a structural model that describes the binding events that poise Hsp70 bound tau for ubiquitination.

- **1.2 Introduction**

Heat shock protein 70 (Hsp70) is a molecular chaperone capable of binding to partially misfolded proteins, making it an essential component in folding of nascent polypeptides, binding and refolding unfolded proteins and preventing of aggregation of toxic species [1, 2]. It carries out its function by repeated cycles of binding and release of its client substrates, resulting from ATP hydrolysis [3]. Hsp70 consists of two major domains, the N-terminal nucleotide binding domain (NBD) and the C-terminal substrate binding domain (SBD), joined together by a flexible linker. The chaperone function of Hsp70 occurs through client binding at the SBD modulated allosterically by the nucleotide state of the NBD, characterized by distinct ATP and ADP conformations [4, 5]. In the ATP conformation, Hsp70 has fast on-off rates for client proteins, resulting in overall low substrate affinity [6]. When bound to ADP, Hsp70 possesses much higher substrate affinity, with model client peptides reported at K_d 1-10 µM [7, 8]. Hsp70 binds to solvent exposed hydrophobic patches, acting as both a holdase to prevent aggregation as well as allow protein refolding [9]. Because Hsp70 binds to short hydrophobic sequences, the clientele for Hsp70 is vast because it isn't restricted by shape or size of the client protein [10].

An important client of Hsp70 is the microtubule-associated protein Tau (MAPT or tau) [11]. The accumulation of tau in neurofibrillary tangles (NFTs) is a hallmark of various neurodegenerative diseases, including Alzheimer's disease, frontotemporal dementia and chronic traumatic encephalopathy [12-14]. The molecular mechanisms regulating tau stability are not yet clear, therefore one focus of tauopathy treatment has been to accelerate tau clearance via ubiquitin-dependent degradation by the proteasome [15]. This has been shown to promote the viability of neurons as well as survival rates in mouse, drosophila and neuronal cell models [16]. Hsp70 has been shown to interact with tau, promoting its stability or facilitating its degradation in conjunction with the CHIP E3 ubiquitin ligase [17, 18]. However, structural modifications that occur to tau en route to its toxic oligomeric or aggregate species have been difficult to characterize owing to its intrinsic disorder [19]. Studies on how the protein chaperone systems affect tau have shown that Hsp70 directly impacts the prevention of tau aggregation as well as degradation [20]. Hsp70 has been shown to bind to the microtubule binding repeats of tau, preventing the formation of PHFs and assisting tau function in the binding and stabilization of axonal microtubules [17]. Studies using small molecules increasing the affinity of Hsp70 for client suggest that the overall time Hsp70 spends bound to tau is a major determinant of cellular levels of tau [21]. The stress inducible isoform Hsp72 or HSPA1A has also been shown to better promote client ubiquitination and degradation than the Hsc70 isoform or other chaperones such as Hsp90 [17].

Although it is clear that Hsp70 is critical for the turnover of tau, direct evidence of the mechanism by which Hsp70 directs tau or general client ubiquitination is lacking.

Tetratricopeptide (TPR) domain containing co-chaperones bind Hsp70's C-terminus and include the C-terminus of Hsp70 binding protein (CHIP) an E3 ubiquitin ligase [22, 23], linking the Hsp70 chaperone system to the proteasomal degradation of client proteins [24, 25]. CHIP acts as a RING class E3 ubiquitin ligase, and has been shown to selectively ubiquitinate clients bound to chaperone [26]. The structure of CHIP has been solved and reveals three domains responsible for its function in facilitating the protein degradation aspect of proteostasis [23]. CHIP consists of a N-terminal tetratricopeptide domain (TPR) responsible for interactions with the EEVD motifs of Hsp70 and Hsp90, a middle helical hairpin domain which allows CHIP dimerization and a U-box domain, structurally related to the RING E3 domains. Dimerization of CHIP has been shown to be essential for its ability to ubiquitinate substrate [27]. This raises the questions of the function of having two TPR domains and two U-box domains in the mechanism of chaperone bound client ubiquitination. Structural studies have suggested that the restricted area and binding surfaces of the U-box domain for E2 enzymes allows for one U-box accessible for recruitment [23]. Adding to the complexity, the affinity of CHIP for Hsp70 is greater than for Hsp90 or Hsc70, demonstrating preferential and varying capacities for ubiquitination to occur in the different chaperone systems [28]. These layers of regulation make it essential to understand the biochemical and structural properties of various chaperone:E3 complexes. NMR studies have demonstrated that the flexibility of the Hsp70:CHIP interaction is an important feature of this interaction, making an exact structure difficult to obtain [25]. However a crystal structure now exists for fragments of CHIP and Hsp70 the Hsc70:CHIP complex describing CHIP TPR and the C-terminus of Hsp70 demonstrating that specific interactions between Hsp70 and CHIP describe low energy states that are important for the binding between these two proteins [24, 25]. Previous structural studies characterizing the full-length Hsp70 have focused on the *Escherichia coli* ortholog DNAK, which lacks the C-terminal IEEVD motif. Further structural studies are needed to clarify the mechanism of Hsp70 binding to CHIP and how it directs client ubiquitination.

In this study, we establish conditions regulating the interaction of human proteins Hsp70, HSPA1A, and CHIP, revealing that the specific ADP conformation of CHIP stabilizes a 2:2 Hsp70:CHIP complex. Formation of this complex becomes less efficient in conditions that favor the ATP form of Hsp70 and that the tetramer formation is mediated by the IEEVD:TPR interaction. We also found that the ADP form of Hsp70 favored both the binding of tau as well as the formation of a Hsp70:CHIP:tau ternary complex.

To test the downstream effects of the formation of this ternary complex, we reconstituted an *in vitro* poly-ubiquitination assay to show Hsp70 dependent ubiquitination of tau, and demonstrate that though ATP is required for ubiquitination, conditions that would drive Hsp70 equilibrium towards its ADP state result in more efficient poly-ubiquitination. This raises the possibility of the Hsp70:CHIP tetramer complex playing a role in client ubiquitination. In collaboration with the lab of Phil Andrews at the University of Michigan, we use mass spectrometry to validate native contacts between Hsp70 and CHIP as well as identify regions of flexibility. We are also able to obtain crosslinking map with the Hsp70:CHIP:tau ternary complex and observe changes in the structure of tau upon chaperone binding as well as displacement of some of the lid region-TPR contacts by tau supporting a model where Hsp70 positions the substrate near the U-box. Finally we report a cryo-EM structure of the Hsp70:CHIP complex and propose a model for its quaternary structure based on our biochemical evidence. These results show that the binding between Hsp70, CHIP and tau allows productive ubiquitination to occur and we provide a structural model that brings together the client with the ubiquitin transfer machinery suggesting how multi-valent Hsp70 binding events to tau push it towards a high efficiency state for CHIP ubiquitination as a mechanism for protein triage.

- **1.3 Results**

- **1.3.1 Hsp70:CHIP form an ADP-specific tetramer complex**

Previous studies identified that Hsp70 and CHIP bind via the canonical EEVD:TPR interaction with a K_d of 0.95 µM [29]. CHIP has also been reported to have higher affinities for Hsp70 c-termini peptides at 0.51 µM, making it unclear how the nucleotide dependent conformations of the full length Hsp70 affects its interaction with CHIP [30]. Hsp70:CHIP complex formation was investigated using size exclusion chromatography in tandem with multi-angle light scattering (SEC-MALS). This method obtains an average molecular weight (Mw_{avg}) value for proteins across an elution fraction, independent of their shape [31]. The Mw_{avg} for the CHIP elution was determined to be ~75 kDa, corresponding to a dimer species based on the 35 kDa molecular weight of the monomer, calculated from the sequence (Mw_{calc}) (Figure 1.1A and Table 1.1). This is in agreement with the known dimerization of the HH and U-box domains [23]. Purified Hsp70 elutes in a similar position, but with a Mw_{avg} of ~100 kDa, potentially corresponding to a mix of monomeric and dimeric species based on a Mw_{calc} of 70 kDa for the monomer (Figure 1.1A and Table 1.1). Notably, Hsp70 has previously been characterized to exist in both monomer and dimer forms [32, 33].
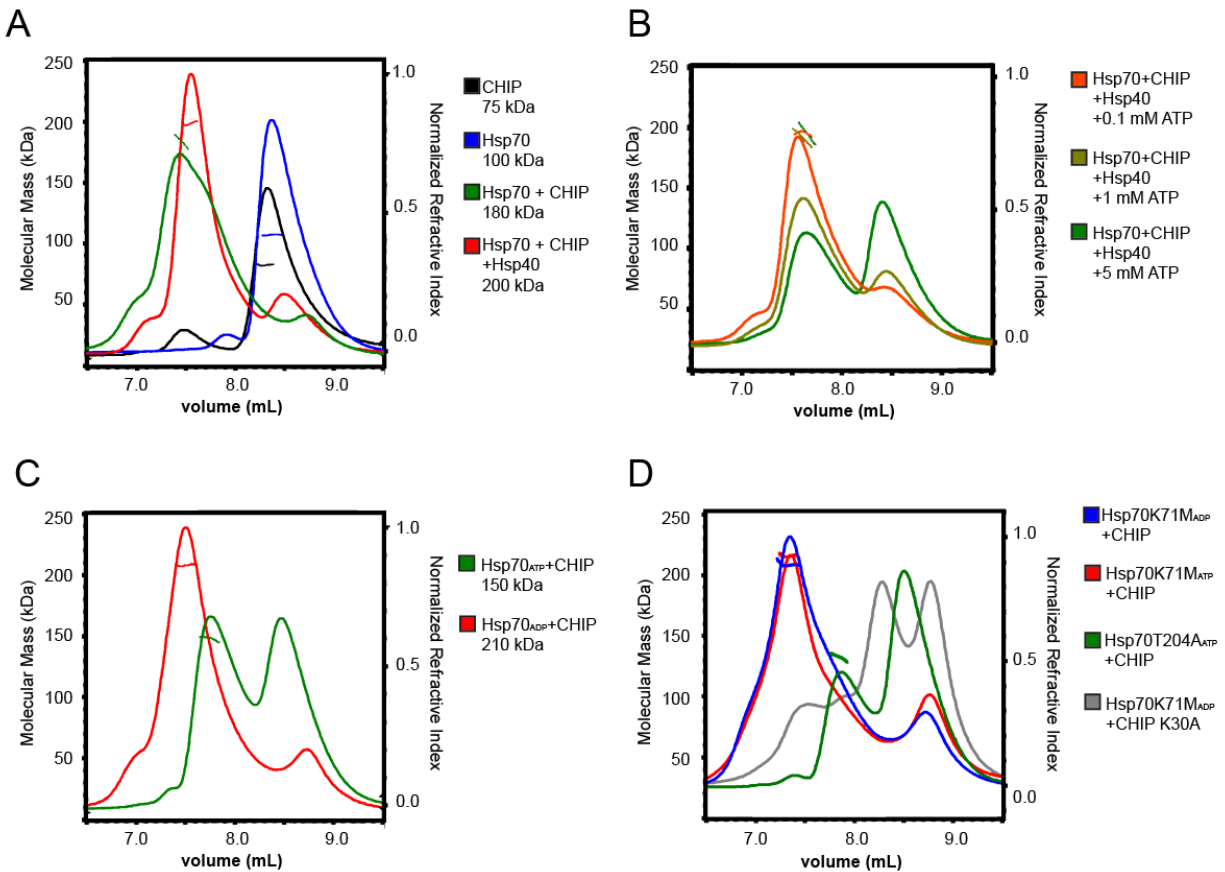
Figure 1.1 Binding with the TPR of CHIP is dependent on the nucleotide state of Hsp70. CHIP and Hsp70 were analyzed by SEC-MALS, showing both the elution profile of the protein samples (refractive index, right Y-axis) with Mw_{avg} (Horizontal traces beneath peaks corresponding to left Y-axis). A) Incubation of CHIP and Hsp70 result in a leftward shift compared to elution profiles of either protein alone (green vs blue and black), the presence of substoichiometric Hsp40 results in Mw_{avg} improving in homogeneity (red, consistent Mw_{avg} value across peak). B) After forming the Hsp70:CHIP complex using the conditions in A (red trace), titration of increasing amount of ATP causes complex dissociation. C) Hsp70:CHIP was prepared without Hsp40 in the presence of 5mM ATP (green) or ADP (red) showing stable complex formation in saturating ADP conditions. D) Hsp70K71M, in which nucleotide hydrolysis activity is abolished and allostery between NBD and SBD are decoupled, exists primarily in the ADP conformation [34, 35], and can form a stable complex with CHIP regardless of nucleotide present (red and blue). This is in contrast to the T204A mutation which also ablates ATPase activity but has been used to characterize Hsp70 structure in the ATP conformation [34, 36].

Following incubation of equimolar Hsp70 and CHIP a broad peak is observed that is shifted substantially from the Hsp70 and CHIP peaks (Figure 1.1A). The Mw_{avg} for this peak was determined to be 140 kDa, indicating Hsp70 and CHIP form a complex. Gel analysis confirmed that both Hsp70 and CHIP were equally present in the corresponding fraction (Figure 1.2). While the Mw_{calc} of Hsp70:CHIP with a 1:2 stoichiometry is ~140kDa, the broad peak shape indicated potential dissociation of the complex and multiple species may be present.
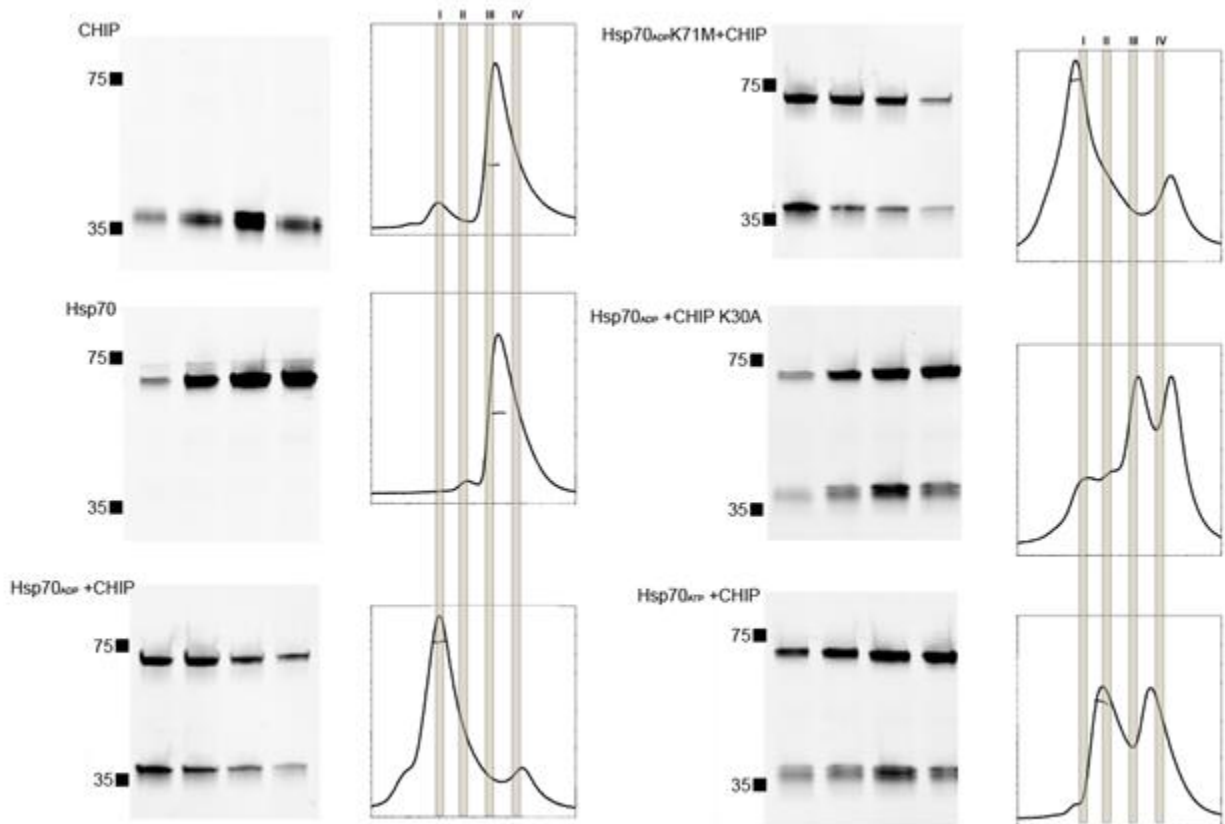
Figure 1.2 SEC profiles and SDS-PAGE analysis of SEC fractions. SEC experiments for the Hsp70:CHIP complexes under various conditions were performed and fractions were collected at the same positions for each SEC run and analyzed by SYPRO ruby protein gel stain (Invitrogen).

We surmised that Hsp70 may exist in both ATP- and ADP-bound states in the purified sample, thereby resulting in altered interactions with CHIP due to different conformations or dimerization [37]. Therefore, Hsp70 and CHIP were incubated with a sub-stoichiometric amount of Hsp40 to catalyze ATP hydrolysis and convert Hsp70 to the ADP state. SEC-MALS analysis of this sample revealed Hsp70:CHIP elutes primarily as a large mono-dispersed peak with a Mw_{avg} of 200 kDa, indicating a tetrameric complex based on the 210 kDa Mw_{calc} (Figure 1.1A). Analysis of Hsp70 alone following incubation with Hsp40 revealed an elution shift and a ~70kDa Mw_{avg}, supporting an Hsp40-driven conversion to a monomeric, ADP-state (Figure 1.3).
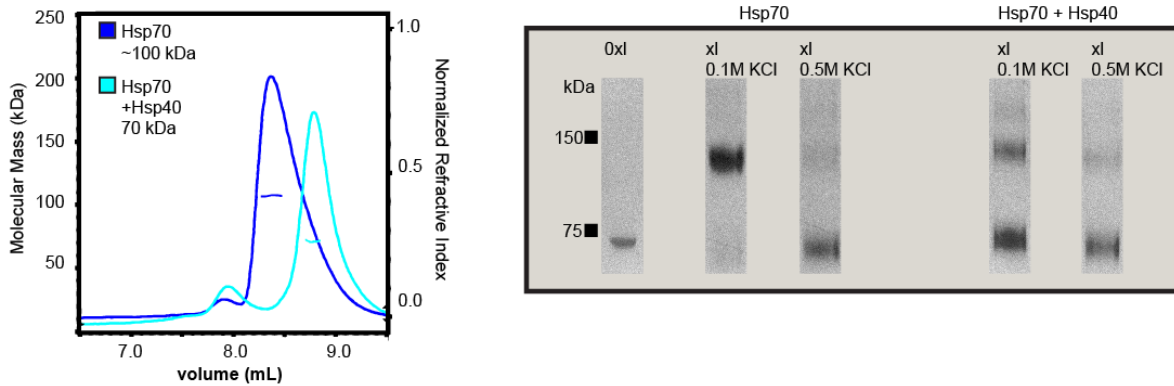
Figure 1.3 Hsp70 conformational changes from nucleotide binding. By SEC-MALS we observe differences in Hsp70 depending on the nucleotide state. After our protein purification protocol, Hsp70 remains in an ATP bound state, evidenced by the change in elution profile and Mw_{avg} upon incubation with Hsp40 which accelerates Hsp70 ATPase activity (left). Glutaraldehyde crosslinking reveals that Hsp70 has a higher propensity to form dimers in the ATP state compared to when incubated with Hsp40 (right panel, compare xl 0.1M KCl conditions). These interactions are transient since dimer formation is reduced under high salt concentrations (right panel, 0.5M KCl lanes) [32].

To further explore the nucleotide specificity, Hsp70 was purified following incubation with Hsp40 to form the ADP-state (Hsp70$_{ADP}$) and tested for interaction with CHIP. With 5 mM ADP present, Hsp70$_{ADP}$ and CHIP co-elute with a Mw_{avg} of 210 kDa, indicating a tetrameric species (Figure 1.1C, 1.2). However, when Hsp70$_{ADP}$ is incubated with increasing amounts of ATP (0.1-5mM), which would cause nucleotide exchange, the peak corresponding to the 210 kDa species reduces substantially, while the peak for the unbound proteins increases, indicating a loss of the tetrameric complex.

Established Hsp70 ATPase mutants, K71M [34, 35] and T204A [34, 36] were also tested for interaction with CHIP. Strikingly, Hsp70-K71M and CHIP co-elute with a 210 kDa Mw_{avg} in the presence of saturating amounts of either ATP or ADP, indicating an Hsp70:CHIP tetramer complex is stabilized independently of the bound nucleotide for this mutant (Figure 1.1D, 1.2). In comparison, T204A shows a reduced Mw_{avg} in the presence of either ATP or ADP, indicating the tetrameric complex is destabilized. An increase in size is identified with ADP relative to ATP for T204A, suggesting some tetramer complex is formed, however, this is reduced in comparison to wt and K71M under the same conditions. Notably, the K71M mutation is proposed to decouple allosteric communication between the NBD and SBD and favor the ADP-state conformation [34, 35, 38], while the T204A mutation likely favors ATP state [34, 36, 39]. The CHIP TPR mutation, K30A, was also tested and showed a substantially reduced binding to wt Hsp70$_{ADP}$, indicating the complex is indeed stabilized via the EEVD:TPR interaction (Figure 1.1D). Overall, these data demonstrate that CHIP interaction specifically favors the ADP-state conformation of Hsp70, with the TPR domains contributing to the formation of a stable tetramer complex.

- **1.3.2 The ADP specific Hsp70:CHIP complex can stably interact with client protein tau**

Cellular levels of tau have been shown to be regulated by Hsp70 isoforms, where the inducible Hsp70 can facilitate tau clearance. Previous studies established that Hsp70 and CHIP reduce levels of tau in various cell models [18, 40, 41], however the molecular mechanism is not well-understood. Thus we sought to characterize whether the ADP-specific Hsp70:Chip tetramer complex we identified binds and ubiquitinates tau. For these studies, we focused on the 0N4R human tau isoform, which has previously been established to be ubiquitinated by CHIP [42, 43]. *In vitro*, tau is soluble and unfolded when unbound to microtubules [19]. By SEC-MALS analysis, purified 0N4R tau elutes at 9.4 mL, with a Mw_{avg} of 55kDa, indicating a primarily monomeric form, based on the Mw_{calc} of 45kDa (Figure 1.4A, C). A tail is identified on the right side of the elution peak and a lower Mw smear is observed in the corresponding fractions indicating additional species are present, likely due to minor degradation. Binding and complex formation with Hsp70 in the ATP and ADP states was then tested. In the presence of saturating ATP, no elution shift was observed following incubation with tau compared to Hsp70-ATP alone, however Hsp70 and tau co-elute in the peak (compare Figures 1.4A and 1.1A and Figures 1.2 and 1.4C). Following incubation with saturating ADP, resulting in conversation of Hsp70 to the ADP state, a substantial change in the elution profile was identified, and a broad, predominant peak is observed eluting at 8.8 mL with a 160 kDa Mw_{avg}, indicating the formation of a larger complex (Figure 1.4A). Both Hsp70 and tau are present in this peak, and considering the Mw_{calc} for Hsp70:tau is 115 kDa, the stoichiometry is likely greater than 1:1 (Table 1.1). A substantial amount of Hsp70 is present in the peak compared to tau (Figure 1.4C) and multiple Hsp70 binding sites on tau have been previously characterized [17]. Thus, we conclude that 2 or more Hsp70s are likely bound to tau in the elution peak. Indeed, when fractions from this peak are crosslinked and analyzed by SDS-PAGE and western blot, distinct higher molecular weight bands are observed above a 1:1 complex (Figure 1.4D). These results identify that tau binding by Hsp70 is specific for the ADP-state, supporting a native Hsp70-substrate interaction, and the resulting complex is stable and likely multi-valent for Hsp70.
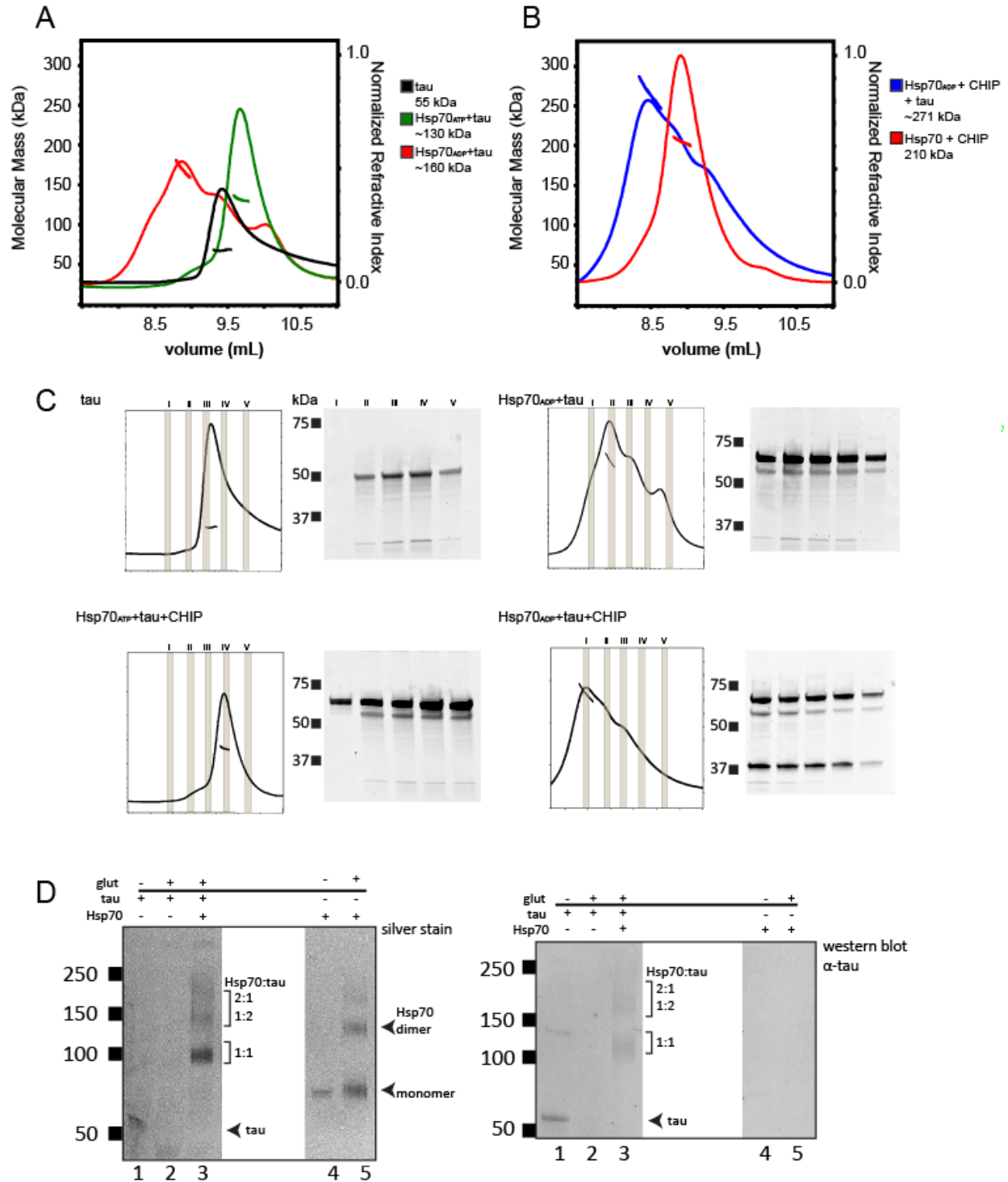
Figure 1.4 Detection of Hsp70 client tau binding and the formation of a Hsp70:CHIP:tau ternary complex. A) SEC-MALS analysis for Hsp70 binding with tau show that in the presence of ADP, we are able to detect a stable complex by SEC with a Mw$_{avg}$ suggesting multiple Hsp70 binding to tau. B) The inclusion of tau shows complex formation with higher Mw$_{avg}$ than the 210 kDa Hsp70:CHIP complex, suggesting the binding of all three protein components. C) SEC profiles and SDS-PAGE analysis of peak fractions show co-elution of Hsp70:tau and Hsp70:CHIP:tau complexes. D) Glutaraldehyde crosslinking of tau indicate the presence of higher order Mw species in solution that show multi-valent Hsp70 binding to a tau molecule.

To determine whether the Hsp70:CHIP tetramer complex we identified interacts with tau, all three proteins were incubated together in equimolar concentrations and analyzed by SEC-MALS. Compared to Hsp70$_{ADP}$:CHIP, a predominant peak is identified that elutes earlier with a Mw$_{avg}$ of ~270 kDa (Figure 1.4B, C). All three proteins are present in fractions, indicating the presence of a stable Hsp70:CHIP:tau ternary complex. Although there is variability in the Mw$_{avg}$, indicated by the slope of the Mw calculation across the peak, 270 kDa corresponds approximately to an Hsp70:CHIP tetramer bound to 1 tau molecule. Based on the broad shoulder to the right of the main peak there is likely a substantial presence of the Hsp70:CHIP tetramer and Hsp70:tau complexes. Different ratios of the proteins were tested during the incubation but did not improve the homogeneity or increase the Mw$_{avg}$ of the ternary complex (data not shown). No changes in the elution were observed when CHIP and tau were incubated together, indicating CHIP and tau do not form a complex in the absence of Hsp70 (data not shown). Overall these results indicate that the ADP-specific Hsp70:CHIP tetramer complex forms stable interactions with the tau substrate, and potentially one molecule of tau could be making dual interactions across the two Hsp70 molecules.

	Mw$_{calc}$ (kDa)	elution volume (mL)
Hsp70$_{ADP}$	70 kDa	10.1 mL
CHIP	70 kDa	10.0 mL
tau	60 kDa	9.4 mL
2Hsp70$_{ADP}$ + 2CHIP	210 kDa	8.9 mL
Hsp70$_{ADP}$ + tau	130 kDa	8.9 mL
2Hsp70$_{ADP}$ + 1tau + 2CHIP	270 kDa	8.4 mL

Table 1.1 Mw$_{calc}$ was obtained from the primary sequences of the proteins used for our experiments and their combination in various stoichiometries. Relative elution volumes are compared, listing from experiments run on the KW-804 (Shodex) column.

- **1.3.3 Tau ubiquitination occurs in an Hsp70 dependent mechanism**

To investigate the events following association of the Hsp70:CHIP:tau ternary complex, we designed a ubiquitination assay to measure tau ubiquitination in conditions that favor Hsp70 association with CHIP. When we added ubiquitin, E1 and E2 enzymes to a mixture of pre-formed Hsp70:CHIP:tau complex under the conditions used for SEC-MALS, we found that tau poly-ubiquitination occurred only in the presence of Hsp70 (Figure 1.5A). Since ubiquitination requires the presence of ATP for conjugation to substrates [44], Hsp70 is expected to exist in both ADP and ATP conformations under our assay conditions. Therefore to further test our observations of nucleotide dependent CHIP recruitment, the Hsp70 K71M and T204A mutants were used. We found that in the presence of only ATP, where

previously the Hsp70 K71M but not the T204A mutant was shown to stably associate with CHIP (Figure 1.1D), ubiquitination of tau was robust with the K71M mutation in contrast to the reduced ubiquitination in the T204A mutant (Figure 1.5B), suggesting that it is possible for the tetramer form of Hsp70:CHIP to be involved during tau ubiquitination.
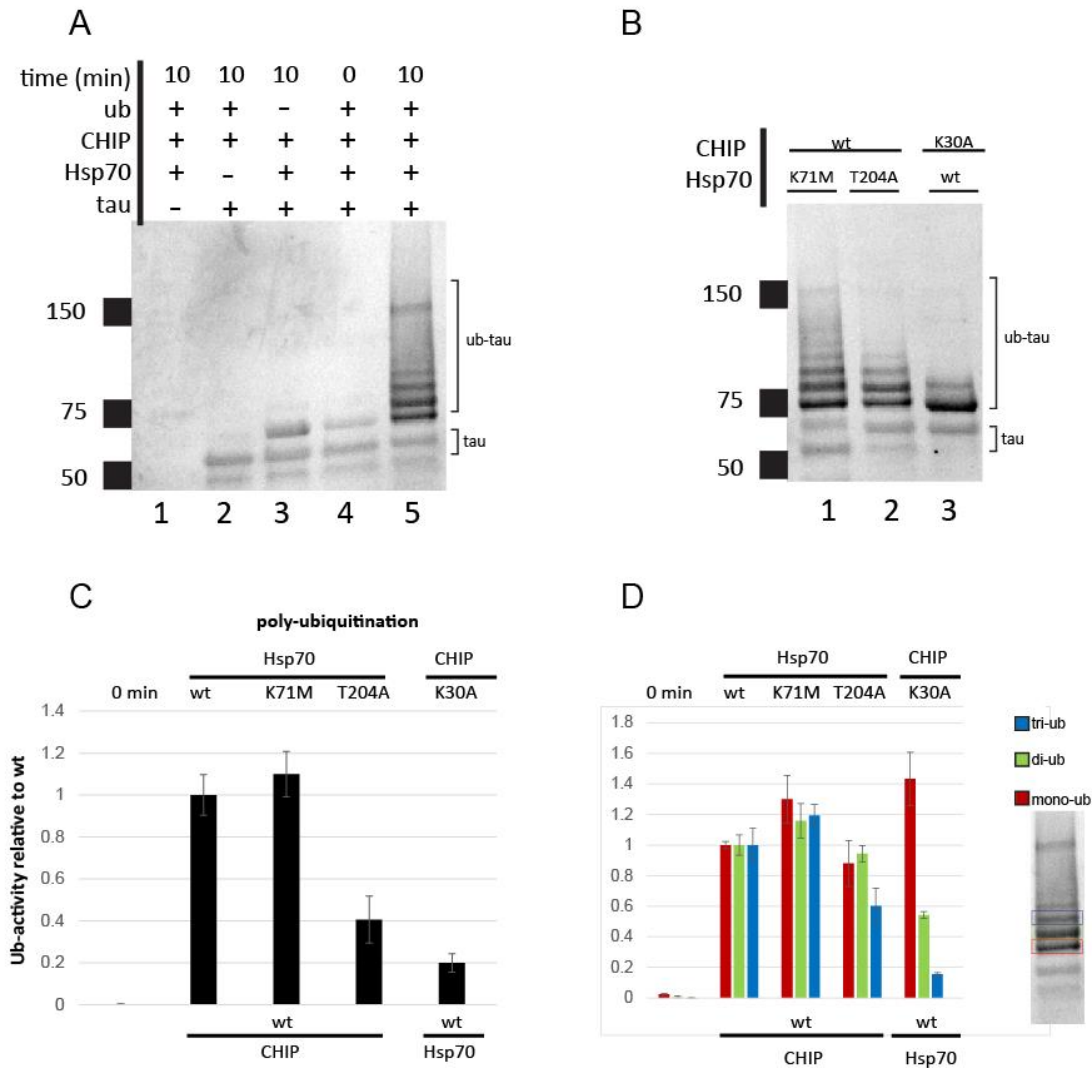
Figure 1.5 Ubiquitination of tau proceeds through CHIP in an Hsp70 dependent manner. A) *In vitro* ubiquitination assay system analyzed by αtau western blotting in the presence of wheat E1, UbcH5c E2, CHIP and tau in the presence or absence of Hsp70. Following a 10 minute reaction, only in the presence of Hsp70 do we get efficient poly-ubiquitination of tau. B) 10 minute ubiquitination reactions carried out using various mutants of Hsp70 and CHIP, show that the K71M mutant promotes poly-ubiquitination compared to the Hsp70T204A mutant and CHIPK30A mutant which decrease the ability for Hsp70 to bind CHIP. C) Quantitation of fluorescent signal of western blots in A and B, accounting for the area of the blot above the mono-ubiquitinated tau band. D) Signal intensities specific to the mono- di- and tri- ubiquitin bands show more drastic decrease in signal for the Hsp70T204A and CHIPK30A conditions to add multiple ubiquitins.

The decrease in signal seemed to occur more noticeably in the upper bands corresponding to poly-ubiquitinated tau, thus we quantified the fluorescent intensities of these higher order bands as ratios relative to the wildtype ubiquitination signal, normalized by the signal present for tau at the zero time point. We see that there are large differences in processive ubiquitination upon destabilizing the Hsp70:CHIP interaction (Figure 1.5C). Furthermore the ratios of signals for the bands for mono-, di- and tri- ubiquitinated tau show that as more ubiquitin is added to the chain, the more pronounced the effect of destabilizing the Hsp70:CHIP interaction becomes (Figure 1.5D). This points to a model in which conditions where Hsp70 can simultaneously bind client and recruit CHIP allows for increased efficiency in adding multiple ubiquitins onto client, resulting in protein turnover.

To further test the effects of client retention on Hsp70 dependent ubiquitination, we combined a competition experiment with our ubiquitination assay. Utilizing a synthetic substrate peptide that has been well characterized to bind to the Hsp70 SBD with a K_d of ~10 μM [7, 8], we compared the untreated ubiquitination reaction with conditions where we incubate Hsp70, CHIP, and tau at 10 uM, 1mM ADP and the NRLLLTG peptide at an excess 50 μM or 100 μM. This peptide would, in theory, compete for occupancy of the Hsp70 SBD with tau. Under these conditions, we observe decreased poly-ubiquitination in the presence of peptide (Figure 1.6 compare green and blue lanes). Previous studies have shown that utilizing peptide concentrations 2-3 times above that of Hsp70 was enough to see extensive changes in binding via the SBD [45], thus we expect competition with tau binding and ubiquitination. However, when we pre-incubate the Hsp70:CHIP:tau complex without peptide, and it is subsequently added at the start of the ubiquitination reaction, we find that under ADP binding conditions, poly-ubiquitination appears to be restored comparing these 10 minute ubiquitination reactions (Figure 1.6, compare blue and red lanes).

These reaction conditions were replicated and show that the NRLLLTG peptide competition is consistent and only occurs when it is pre-incubated together with tau, CHIP and Hsp70 (Figure 1.7). This suggests that the slow client off-rate in the Hsp70:CHIP:tau complex allows for poly-ubiquitination to occur, substrate peptide is unable to displace tau suggesting that Hsp70 cycling does not occur during poly-ubiquitination.
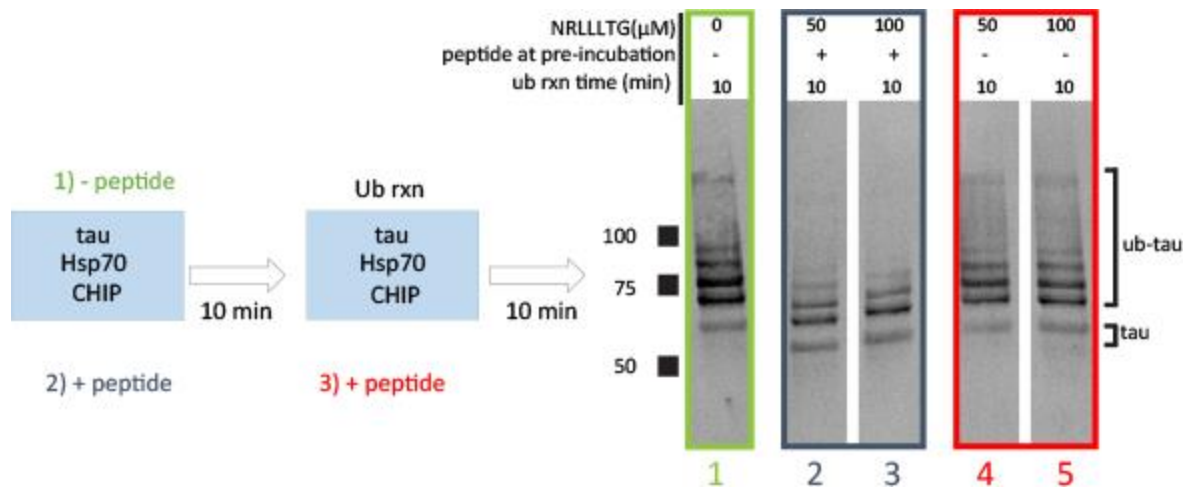
Figure 1.6 Hsp70 substrate peptide inhibition of substrate binding and effects on client ubiquitination. Western blots of 10 minute ubiquitination assay, carried out on samples where no peptide was added (green), 50 or 100 µM peptide was added (blue) and 50 or 100 µM peptide was added after Hsp70:CHIP:tau complexes were pre-formed (red).

This is in agreement with our previous analysis of Hsp70 mutants, where the efficient poly-ubiquitination is carried out by the Hsp70K71M mutant which remains in the ADP conformation and does not cycle between nucleotide states. Together, these results suggest a model where the ADP state of Hsp70 or slowing down the Hsp70 chaperone cycle promotes ubiquitination of tau.
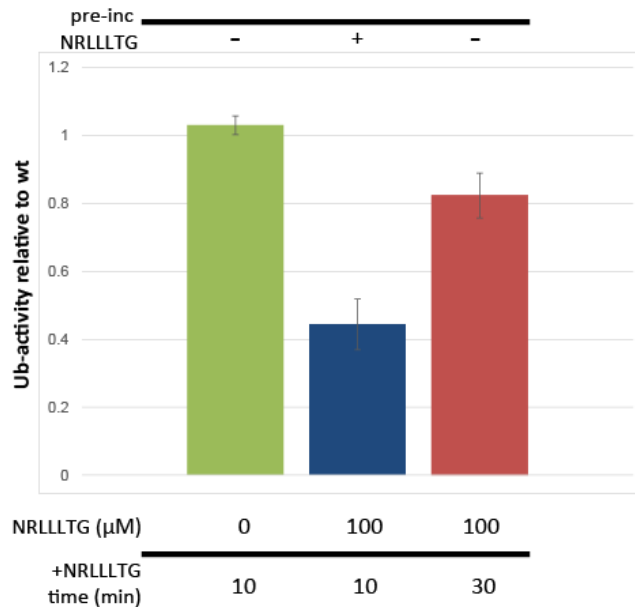
Figure 1.7 Quantitation of the fluorescence intensities of the competition-ubiquitination assays, where NRLLLTG peptide was absent (green), added together with tau (blue), or added after tau (red), using 100 µM peptide and carrying out the pre-incubation period for 10 minutes and ubiquitination for 10 minutes

- **1.3.4 Hsp70:CHIP crosslinking maps reveal structural changes upon client binding**

In order to obtain structural data of the Hsp70:CHIP complex we utilized cryo-EM and a lysine reactive crosslinker (bis-succinimidyl 1,4 diazabicyclo[2.2.2]octane) designated as 'DC4' [46]. These crosslinkers have standard linker arms with reactive NHS esters but a central connecting domain containing one or more quaternary cyclic amines. We sought to stabilize a low energy state of the Hsp70:CHIP heterotetramer to observe the interactions between the Hsp70 SBD and CHIP U-box domains. By obtaining crosslink identities we would be able to map the connectivity between the two proteins, since the unique MS2 pattern of crosslinked peptides allows them to be easily identified and subsequent MS3 identifies the component peptides.
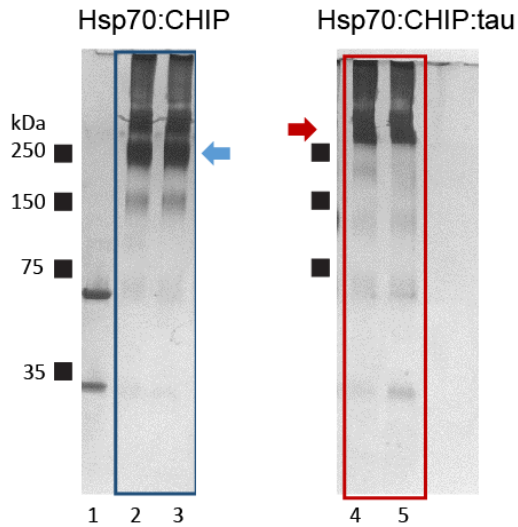
Figure 1.8 DC4 crosslinking profiles. The appearance and amount of protein present in the higher molecular weight bands is dependent on concentration of protein and crosslinker. Bands corresponding to uncrosslinked Hsp70 and tau (lane 1) are greatly diminished as the protein shifts to species at ~140, ~210 and higher Mw (lanes 2 and 3). Hsp70:CHIP:tau crosslinked into a band distinct from the ~200 kDa band of Hsp70:CHIP (lanes 4 and 5) and western blotting demonstrated that tau was present in the complex (data not shown).

We demonstrated that reconstituted Hsp70 dimer, the CHIP dimer, and the Hsp70:CHIP complex, crosslink with DC4 efficiently, resulting in 70, 140 and 210 kDa bands by SDS-PAGE (Figure 1.8). After optimizing conditions to produce mostly crosslinked Hsp70:CHIP we subjected the samples through an additional SEC purification to remove higher molecular weight species to isolate the 200 kDa band of proteins.

Because the DC4 has specific cleavage products and fragmentation patterns within the crosslinker moiety in matrix-assisted laser desorption ionization (MALDI) mass spectrometry, we sought to identify

the peptides crosslinked between Hsp70 and CHIP [46]. With the help of Angela Walker, Loli Piersimoni and Phil Andrews, we performed trypsin digestion and tandem liquid chromatography and mass spectrometry (MALDI-TOF-TOF) to identify the crosslinked regions. Oversampling of crosslink sites identified many intra-subunit crosslinks that were consistent with the structures of the individual proteins [4, 5, 23] (Figure 1.9A). In the Hsp70:CHIP dataset, certain lysines exhibited patterns of crosslinking with multiple residues, indicating inconsistency in its structure or position. These hyperconnected residues indicate flexibility in the region of the lysine [47]. Residue K417 of Hsp70 resides within the linker region suggesting this crosslinking profile to be consistent with the ADP conformation of Hsp70 when it is flexible rather than when docked into the NBD in the ATP form [48]. Lysine K131 of CHIP is present at the helical hairpin domain of CHIP, and exhibits hyperconnectivity to the Hsp70 molecule, indicating flexibility in this dimerization domain region which have had conflicting reports on its structure [22, 23]. Substantially different patterns of crosslinked peptides and dead-end peptides were observed between the Hsp70, CHIP and Hsp70:CHIP datasets, providing additional validation that they were crosslinked in complex (data not shown). In the crosslinking profile of the Hsp70:CHIP complex, we observe that most of the crosslinks are made in the TPR region of CHIP and the C-terminus of Hsp70, consistent with known interactions [25] (Figure 1.9A).

Furthermore, we were able to obtain a crosslinked client bound Hsp70:CHIP:tau ternary complex for analysis by mass spectrometry (Figure 1.9B). The crosslinking profile of the ternary complex shows consistency with known interactions among the three proteins, maintaining the Hsp70 C-terminus interactions with the CHIP N-terminal TPR domain, as well as showing areas in the Hsp70 substrate binding domain interacting with the microtubule repeat domains in tau [17]. Comparison of the crosslink profiles between the Hsp70:CHIP and Hsp70:CHIP:tau complexes reveal that contacts between Hsp70 SBD and CHIP TPR are displaced by new contacts between Hsp70 and tau, thus it may be possible that tau is brought to the space previously occupied by the Hsp70 SBD near the CHIP U-box. We also observed that upon complex formation, tau becomes relatively rigid, evidenced by the larger number of crosslinks observed for shorter distances in primary sequence of tau (Figure 1.9C). This is in contrast to the crosslink map of tau on its own, where it has more freedom to sample conformations that allow lysines to reach each other separated by more amino acids (Figure 1.9D). This suggests that when tau is bound to Hsp70 and CHIP it adopts a unique extended form that is protected from making crosslinks with itself. These results suggest a model where tau is bound to the Hsp70:CHIP complex to restrict its conformations, making it more rigid and extended to allow space for E2 conjugating enzymes to be recruited for productive poly-ubiquitination of tau
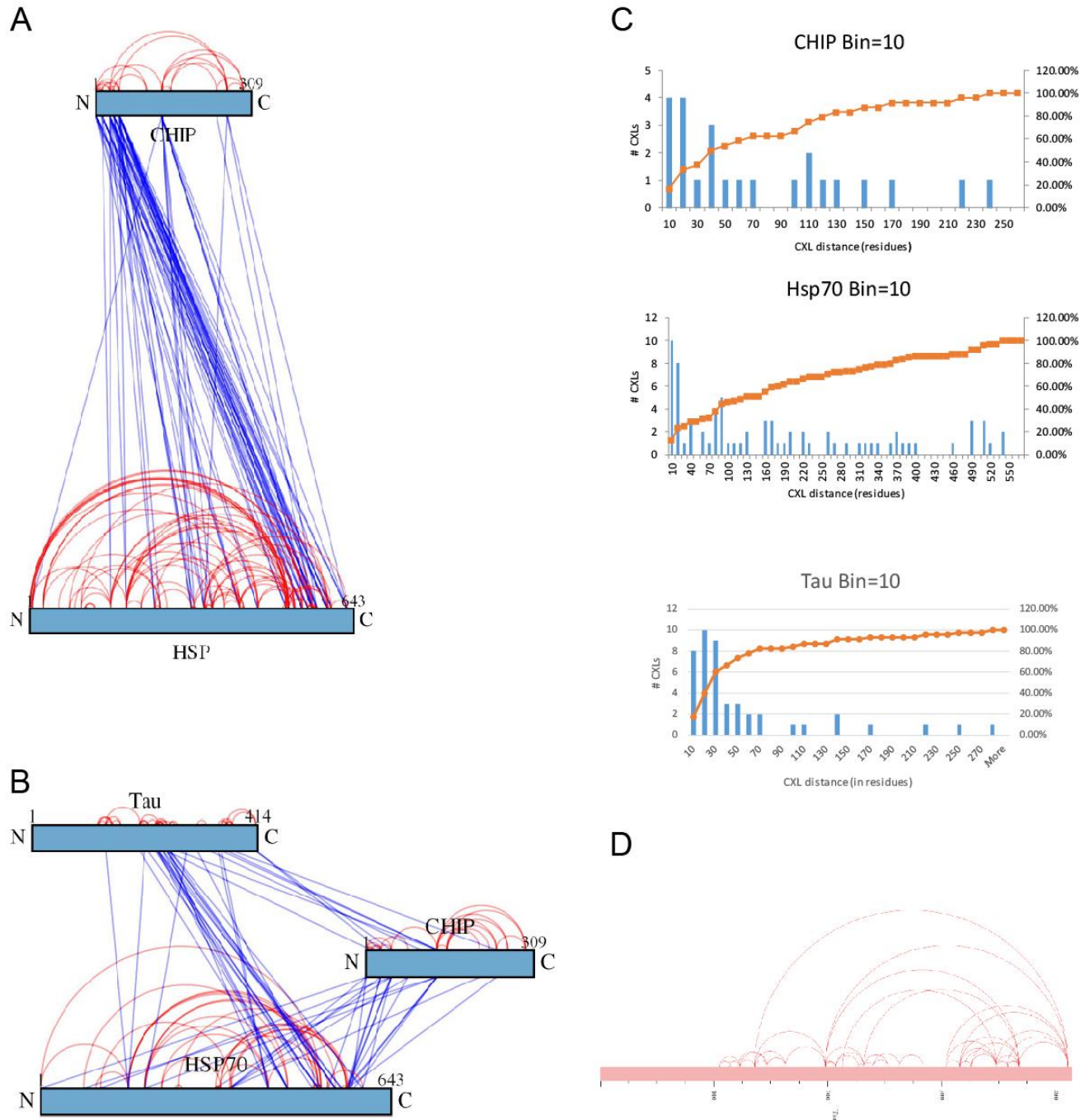
Figure 1.9 Mass spectrometry identification of DC4 crosslinked peptides for the Hsp70:CHIP and Hsp70:CHIP:tau complexes. A) Linkage map of crosslinked peptides in the Hsp70:CHIP complex mapping extensively the N-terminus of CHIP with the C-terminus of Hsp70, each line represents the identification of doublets in the MS/MS spectra indicating the fragmentation of the DC4 between crosslinked peptides [46]. Component peptides were identified using a standard database search. B) Linkage map of the Hsp70:CHIP:tau complex revealing the interactions between the microtubule repeats in the center of the tau molecule with the Hsp70 SBD, and displacement of some of the contacts in the lid region of Hsp70 with CHIP. C) Histogram tabulating the number of crosslinks identified in the ternary complex that had lengths corresponding to distances in the primary amino acid sequence between the linked residues. D) Crosslink map of tau on its own exhibiting longer range crosslinks. These experiments were performed by Angela Walker Loli Piersimoni. Figures were created by Phil Andrews.

40

- **1.3.5 Hsp70:CHIP cryo-EM structure and proposed arrangement of quaternary structure**

We were also able to use the DC4 crosslinked Hsp70:CHIP samples for cryo-EM. We observed homogeneous globular particles in vitrified ice, amenable to single particle reconstruction (Figure 1.10A). A low resolution 3D reconstruction was obtained from 141,196 particles selected from over 3000 electron micrographs out of an initial 250,000 raw particles recorded on a K2 camera (Gatan) in a Titan Krios microscope (FEI) (Figure 1.10B). An initial model was generated using results from 3D classification on negatively stained Hsp70:CHIP complex particles and was similar to the ab initio SGD procedure within RELION (see methods). Projections of the 3D model show consistency with the reference-free class averages. We docked the known crystal structures of the CHIP dimer (2C2L) as well as the NMR RDC refined crystal structure of the DNAK ADP (4KHO) structure into our model, in order to obtain a rough estimate if our volume could account for the mass of the components, positioning the CHIP dimer in the center and 2 Hsp70 monomers on either flank (Figure 1.10C). In this arrangement, contacts between the lid region of Hsp70 and CHIP are maintained supporting our MS crosslinking data. Density is present for both NDB and SBDs for the Hsp70 molecules. The TPR and U-box domains of CHIP are accounted for, however the helical hairpin dimerization domain seems to be unresolved, which was suggested by the crosslink hyperconnectivity of K131 of CHIP (Figure 1.9).

It has been shown that the Hsp70 binds to model client peptides locking the peptides in extended conformations to form a hydrophobic core surrounding the client, closing the substrate binding pocket [45]. This suggests that the 2Hsp70:1tau complex can be accounted for when recruiting CHIP and the E2 enzymes for poly-ubiquitination. Limitations to the resolution of our cryo-EM structure could be due in part to the use of the lysine reactive crosslinker, which performs non-specific lysine crosslinks across the protein complex. We have recently begun cryo-EM characterization of the native Hsp70:CHIP complex and demonstrate that the reference-free 2D averages for both datasets show very similar features (Figure 1.10D). Our goal will be to obtain a high resolution cryo-EM structure of the uncrosslinked complex and compare it with the crosslinking profiles obtainable by mass spectrometry to corroborate the interactions between Hsp70:CHIP and further extend these comparisons to the client bound Hsp70:CHIP:tau complex.
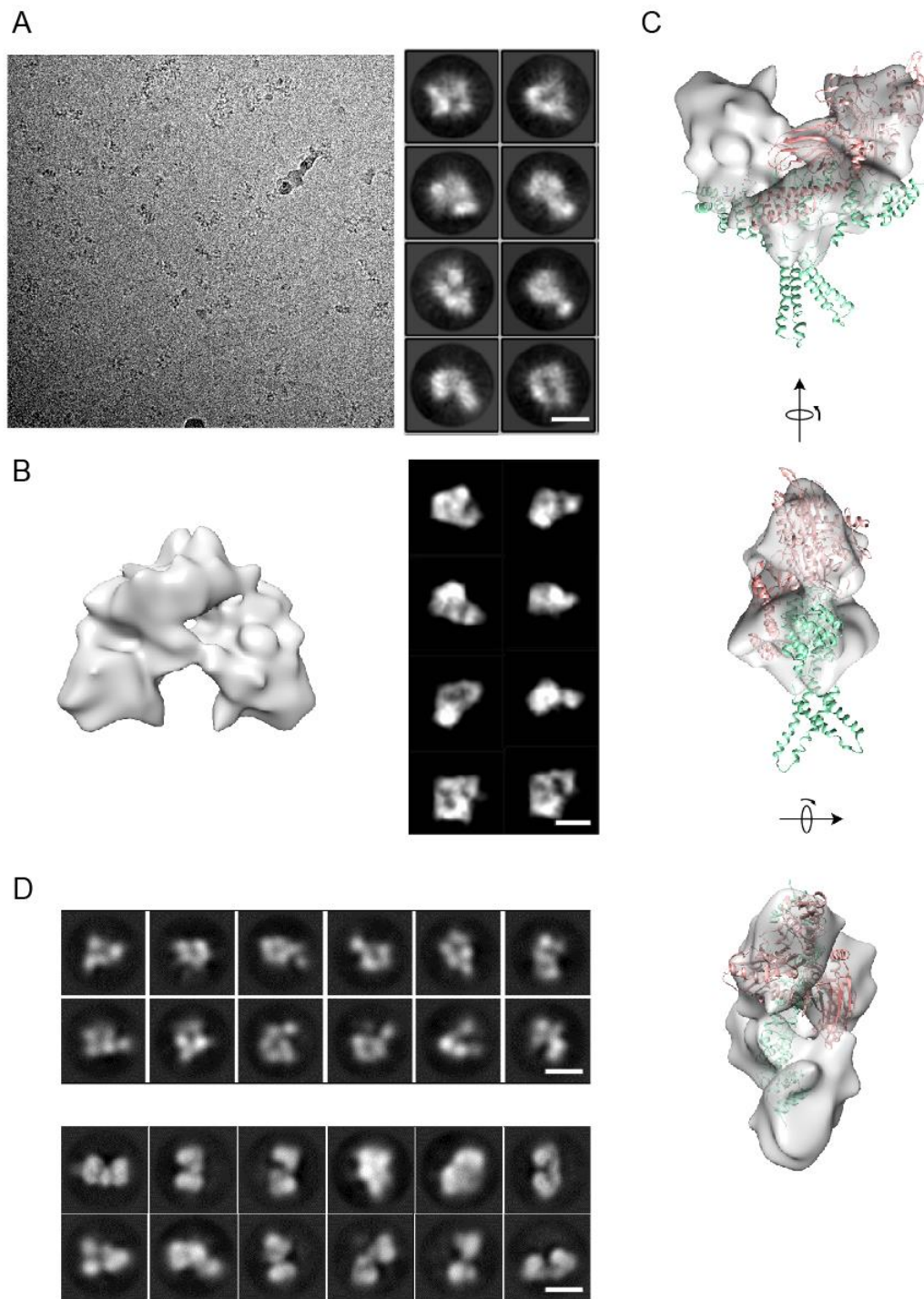
Figure 1.10 Cryo-EM of the Hsp70:CHIP complex. A) Example electron micrograph (left) of globular particles resulting in the reference free class averages that show internal features generated by RELION (right) (scale bar:10nm). B) 3D reconstruction of the cryo-EM dataset, limitations in improving the resolution remain an issue, however projections from this model are consistent with 2D averages. C) Crystal structures for Hsp70 (4KHO) and CHIP (2C2L) were docked into the volume to explore possible arrangements of the proteins in complex. D) 2D class averages of a non-crosslinked native Hsp70:CHIP dataset (bottom) show similar features to views seen in the DC4 crosslinked averages.

- **1.4 Discussion**

Hsp70 has been implicated in the regulation of tau, preventing aggregation or improving its turnover [17, 21, 43]. We have been able to directly demonstrate the ability of Hsp70 to direct tau ubiquitination through the CHIP E3 ubiquitin ligase and discover that the nucleotide state of Hsp70 plays a critical role in the ubiquitination of tau for proteasomal degradation (see Figure 1.5). ATP is required for the transfer of ubiquitin to clients or substrates in the cell and it likely that Hsp70 exists in an equilibrium between conformational states. Thus, it may be unclear whether the formation of the stable 210 kDa Hsp70:CHIP complex is necessary for Hsp70 driven ubiquitination. However, one important observation from this study is that the efficiency of ubiquitination is enhanced in conditions that favor the Hsp70 ADP state and the Hsp70:CHIP complex (see Figures 1.1 and 1.5). Pushing the equilibrium of Hsp70 conformations to either state would act as the switch regulating client ubiquitination. Both binding and ubiquitination of tau were enhanced in conditions that favored the formation of a stable 210 kDa Hsp70:CHIP complex.

Because ATP is required for ubiquitin transfer we used the Hsp70K71M mutant to demonstrate the impact of protein conformation on client ubiquitination. Because the K71M mutant does not hydrolyze ATP and is allosterically decoupled from transitioning between conformational states, even in the presence of ATP, this mutant can be described as non-cycling, unable to repeatedly bind and release client [34, 38]. We supported this notion by designing a peptide inhibition aspect to our ubiquitination assay (Figure 1.6). We observed that when the Hsp70:CHIP:tau complex has pre-formed, the Hsp70 substrate peptide was unable to compete for the SBD. This suggests that during ubiquitination, Hsp70 is not actively going through its conformational cycle. This is interesting because it implies that Hsp70 molecules that are not actively folding client perhaps make the switch to triage. This has been observed before in studies where inhibition of the Hsp70 chaperone cycle promotes tau clearance [18, 21]. In addition, mutations of the Hsp70 that have been engineered to resemble the ADP conformation have been shown to bind to client and direct tau towards proteasomal degradation [43]. We can propose a model where the 210 kDa complex represents the most efficient form of the chaperone that can facilitate client ubiquitination, and that the cellular energy levels or factors that cause protein folding to slow the cycling of Hsp70 would then open the pathway for client degradation. Further studies will be needed to clarify the relationship between the stalling of the Hsp70 client binding and release with the formation of the 210kDa complex.

We were also able to observe evidence of higher molecular weight species based on the Mw_{avg} for the formation of Hsp70:tau complex (Figure 1.4). This implies the existence of a bivalent Hsp70 bound tau

molecule. In line with our model of client stalling it would be interesting to see if the formation of these tau molecules with multi-valent Hsp70 are a sign of stress that push these complexes towards high efficiency in ubiquitination. Previous studies on DnaK have shown that under certain conditions, multiple simultaneous binding events to a single client can be observed with the presence of the Hsp40 homologue DnaJ and ATP [49]. For our system, it could be possible that the conditions for multiple Hsp70 binding are due to a stalling of Hsp70 cycling, promoting the ADP conformation where tau binding and CHIP binding are observed. In the conditions tested that allowed a larger proportion of Hsp70 in the ATP form, we saw a decrease in the Mw_{calc} of these particles, suggesting that the Hsp70:tau and Hsp70:CHIP complexes are falling apart and that both CHIP TPRs fail to engage molecules of Hsp70. This suggests that the 210 kDa Hsp70:CHIP complex is important and perhaps somehow related with the multiple binding of Hsp70s on a single tau client. We saw evidence of this in our MS linkage maps of the Hsp70:CHIP:tau complex, where there was a loss of flexibility in tau upon chaperone binding (Figure 1.9), suggesting that it may be possible for a single tau to be held rigid across two Hsp70 molecules and that would enable the recruitment of CHIP.

Further details in the molecular events or significance of having two TPR domains or two Hsp70 molecules on a client will require higher resolution structural information. Shorter crosslinks will enable us to obtain higher resolution, akin to a shorter FRET probe, to measure short range contacts and map areas of relative rigidity [46]. Comparative crosslinking using heavy isotope labelled crosslinkers will also be helpful in discerning quantitatively the change of the binding interface when transitioning between the client-bound chaperone complexes (work to be done in collaboration with Phil Andrews). This will help us determine if there is an order of events that occur between Hsp70, CHIP and tau that allows for subsequent ubiquitination. Binding assays for SEC-MALS showed that on the order of bulk solution of molecules, order of addition had no effect on the SEC profiles or MALS results (data not shown). However on the molecular level there may be a role for certain binding interfaces to form or be excluded when Hsp70 performs protein triage. Finally the most direct and turns out most challenging pathway is direct structure determination for this chaperone:co-chaperone complex. With high resolution cryo-EM the goal is to directly visualize potential tau binding interfaces and whether it could exist across two Hsp70 molecules brought together by CHIP.

All this data leads us to a model where stalling of Hsp70 foldase activity of repeated cycles of binding allows for Hsp70 to accumulate on client proteins, where a tau molecule or perhaps any client at risk of unfolding or aggregation becomes targeted for proteasomal degradation instead of refolding. Under

stress conditions, the need to turnover proteins reducing cellular levels of tau or other aggregation prone species could be a form of defense to maintain proteostasis. Structural as well as further biochemical studies can be aimed at investigating the significance of multiple Hsp70 binding events on clients or the dual Hsp70 binding events that occur on CHIP.
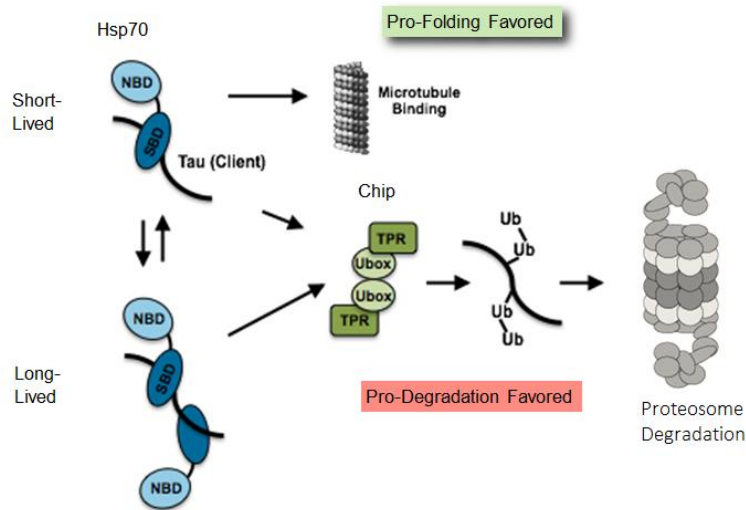
- **1.5 Methods**

- Recombinant Protein Purification

CHIP was obtained from a pET151 vector containing the human CHIP gene from the Agard lab at UCSF, containing a 6x His tag separated from the CHIP by a TEV cleavage site and expressed in BL-21 E. coli cells. After growth of several liters of cells in Luria Bertani broth, optical density was checked until about 0.8 OD relative to uncultured media before adding to a final concentration of 500 µM IPTG for induction of protein expression. Following overnight incubation at 18 °C, cells were treated with a protease inhibitor cocktail (Roche) and pelleted at 5,000xg on a Sorvall centrifuge and lysed using an Emulsiflex high pressure homogenizer (Avestin). After high speed centrifugation of the cell debris at 40,000xg, the supernatant was treated with Ni-NTA beads to affinity purify the His-tagged CHIP. Following elution with 200mM imidazole buffer, the sample was buffer exchanged into SEC buffer (100mM KCl, 40mM HEPES pH 7.4, 5mM MgCl2, 7mM BME) overnight and digested with TEV protease. The sample was subsequently subjected to size exclusion chromatography on a superdex 200 16/600 column (GE healthcare). Fractions containing the protein were confirmed by SDS-PAGE and pooled fractions were subjected to buffer exchange into a SEC buffer with 5% glycerol for flash freezing and storage.

Hsp70 human isoform HSPA1A was expressed in a baculovirus expression vector system with a TEV cleavable His-tagged N-term modified by the Center for Chemical Genomics at the LSI. After induction, growth, and recovery of the cells, they were subjected to a purification protocol identical to that of CHIP. Generation of the T204A, K71M mutants of Hsp70 and the K30A mutant CHIP was carried out using QuikChange site-directed mutagenesis (Agilent) and confirmed by DNA sequencing. The 0N4R tau construct was cloned into a pET28 vector by the Gestwicki lab at UCSF, and used to transform BL-21 cells for E. coli expression. This construct was also His-tagged and followed the same purification protocol as the Hsp70 and CHIP methods, with the addition of a cation exchange chromatography step between affinity purification and SEC, using a HiTrap SP (GE healthcare).

- Size exclusion chromatography in tandem with multi-angle light scattering (SEC-MALS)

Hsp70:CHIP, Hsp70:tau, Hsp70:CHIP:tau and individual protein components were prepared for analysis by SEC-MALS by first incubating the proteins alone or together at equimolar ratios, generally at 10 μM protein concentration, in a SEC buffer in the presence of either ADP or ATP at the concentrations listed, with 5mM nucleotide considered 'saturating' conditions. Hsp40, when used, is present in substoichiometric amounts, typically 1/10 of the concentration of Hsp70. After 30 minutes, the samples were filtered and injected for SEC-MALS analysis and fractionation. The Mw_{avg} of complexes were determined by separation using a WTC-050S5 SEC column (Wyatt Technology Corporation) with an Akta micro (GE Healthcare) and analysis with a DAWN HELEOS II MALS detector equipped with a WyattQELS DLS, and Optilab rEX differential refractive index detector using ASTRA VI software (Wyatt Technology Corporation). The Mw_{avg} was determined from the Raleigh ratio calculated by measuring the static light scattering and corresponding protein concentration of a selected peak. Bovine serum albumin served as a calibration standard. Light scattering data and calculations were performed using the ASTRA software package (Wyatt Technology Corporation).

- Ubiquitination assays

Protein concentrations were optimized to produce tau ubiquitination that showed appreciable signal by western blot using an Alexa-488 tagged secondary antibody (ThermoFisher). This meant using 1 μM concentration of proteins in order to avoid overloading the gel and giving too high of a fluorescent signal. E1 and E2 enzyme was generously provided by the Klevit lab at the University of Washington. Ubiquitin protein was purchased from Sigma. E1 enzyme from wheat was used at 0.2 μM. To adjust the rates of ubiquitination to observe differences between the mutant proteins and conditions, the

concentration of E2 enzyme was adjusted, with the final working concentration ending up at 4 μM. Excess amount of ubiquitin was used at 40 μM. E1, E2, ubiquitin and ATP were first incubated together with the aim of reaching saturating levels of E2-ub to adjust for the variability due to the initial E1, E2 transfer steps. We also incubated Hsp70, CHIP and tau together for 30 minutes at 10 μM concentration to replicate conditions in which binding was observed by SEC-MALS. The ternary complex solution was then diluted to a final working concentration of 1 μM along with the concentrations of the E1, E2 and ubiquitin as previously described. Reactions were always split with one reaction containing no ubiquitin and immediately boiled at 100 °C for 2 minutes to mark the zero time point. Time was recorded following dilution and addition of the E1, E2-ub mixture, with 10 minute time points typically being when the reaction would be stopped by adding SDS loading dye, reducing agent and heat for 2 minutes. Samples were analyzed by SDS-PAGE and transferred to PVDF membranes for western blot analysis, using an mouse α tau monoclonal antibody (Santa Cruz) and an Alexa-488 α mouse antibody and developed on a Typhoon Tio imager (GE healthcare). Subsequent quantification of intensities were obtained using the ImageQuant software.

For peptide competition assays, we first established that incubating Hsp70, CHIP, tau and NRLLLTG peptide together resulted in the interference of tau binding by titration of the peptide, manifested by decreased poly-ubiquitination. Hsp70, CHIP and tau were then either preincubated together with the NRLLLTG peptide at the indicated concentrations or were first preincubated without peptide for 10 minutes before its addition.

- Cryo-EM

Samples for cryo-EM were prepared on C-FLAT holey carbon grids (EMS) in SEC buffer with a Vitrobot (FEI Co.). Data was collected on a Titan Krios microscope (FEI co.) operated at 300 kV on a K2 direct electron detector with a 1.0 Å pixel size. 8 second exposures with 0.2s/frame rate and a dose of 50 e/Å2 were used in electron counting mode. 3583 Micrographs were collected for the dc4 crosslinked Hsp70:CHIP dataset and 1518 micrographs were collected for the native Hsp70:CHIP complex, utilizing Leginon automated data collection software [50]. Micrograph movie files were output and Motioncor2 program was used to perform gain normalization and patch-based motion correction [51], after which CTFFIND4 was used to estimate CTF parameters for the corrected micrographs [52]. The DoG picker program was used for automated particle picking. RELION was used to do multiple rounds of reference-free 2D averaging to remove images that did not correspond to protein particles to result in a final particle count of 141,196 and 145,125 for the DC4 crosslinked Hsp70:CHIP and the native complex

respectively. 3D Refinement of the Dc4 crosslinked dataset has been performed using an initial model generated from negative stain EM class averages used to bootstrap refinement against a sphere, as well as an initial model produced by the stochastic gradient descent algorithms in RELION [53]. Initial models were low pass filtered to 60 Å yielded a final structure at 12 Å resolution after B factor sharpening.

- DC4 crosslinking in preparation for mass spectrometry and cryo-EM

Complex formation was performed identical to the preparation used for SEC-MALS experiments. The Hsp70:CHIP and Hsp70:CHIP:tau complexes were then diluted to a concentration of 1 µM protein to avoid high concentrations of high molecular weight complexes due to crowding. We used 1 mM DC4 concentrations in balancing the amount of crosslinked ~200kDa product while reducing the high molecular weight protein smear. At 1 µM concentrations we were able to find distinct bands between 210 and 250kDa for the Hsp70:CHIP. The Hsp70:CHIP:tau complex produced a higher molecular weight band compared to the binary complex. The samples were then concentrated and injected on an S200pc column (GE healthcare) for additional purification removing the high molecular weight species. Samples were subsequently analyzed by cryo-EM and mass spectrometry. Trypsin digestion, mass spectrometry and data analysis for identification of crosslinked peptides were carried out as described in a previous publication [46].

- **1.6 References**

1.   Alderson, T.R., J.H. Kim, and J.L. Markley, *Dynamical structures of Hsp70 and Hsp70–Hsp40 complexes.* Structure (London, England : 1993), 2016. **24**(7): p. 1014-1030.
2.   Mayer, M.P., *Hsp70 chaperone dynamics and molecular mechanism.* Trends in Biochemical Sciences, 2013. **38**(10): p. 507-514.
3.   Clerico, E.M., et al., *How hsp70 molecular machines interact with their substrates to mediate diverse physiological functions.* J Mol Biol, 2015. **427**(7): p. 1575-88.
4.   Bertelsen, E.B., et al., *Solution conformation of wild-type E. coli Hsp70 (DnaK) chaperone complexed with ADP and substrate.* Proc Natl Acad Sci U S A, 2009. **106**(21): p. 8471-6.
5.   Kityk, R., et al., *Structure and dynamics of the ATP-bound open conformation of Hsp70 chaperones.* Mol Cell, 2012. **48**(6): p. 863-74.
6.   Qi, R., et al., *Allosteric opening of the polypeptide-binding site when an Hsp70 binds ATP.* Nat Struct Mol Biol, 2013. **20**(7): p. 900-7.
7.   Fourie, A.M., J.F. Sambrook, and M.J. Gething, *Common and divergent peptide binding specificities of hsp70 molecular chaperones.* J Biol Chem, 1994. **269**(48): p. 30470-8.
8.   Ricci, L. and K.P. Williams, *Development of fluorescence polarization assays for the molecular chaperone Hsp70 family members: Hsp72 and DnaK.* Curr Chem Genomics, 2008. **2**: p. 90-5.
9.   Rosenzweig, R., et al., *Promiscuous binding by Hsp70 results in conformational heterogeneity and fuzzy chaperone-substrate ensembles.* eLife, 2017. **6**: p. e28030.
10.   Mayer, M.P., et al., *Multistep mechanism of substrate binding determines chaperone activity of Hsp70.* Nat Struct Biol, 2000. **7**(7): p. 586-93.

11.   Jinwal, U.K., et al., *Chemical manipulation of hsp70 ATPase activity regulates tau stability.* J Neurosci, 2009. **29**(39): p. 12079-88.
12.   Morimoto, R.I., *Proteotoxic stress and inducible chaperone networks in neurodegenerative disease and aging.* Genes Dev, 2008. **22**(11): p. 1427-38.
13.   Augustinack, J.C., et al., *Specific tau phosphorylation sites correlate with severity of neuronal cytopathology in Alzheimer's disease.* Acta Neuropathol, 2002. **103**(1): p. 26-35.
14.   Ballatore, C., V.M. Lee, and J.Q. Trojanowski, *Tau-mediated neurodegeneration in Alzheimer's disease and related disorders.* Nat Rev Neurosci, 2007. **8**(9): p. 663-72.
15.   Miyata, Y., et al., *Molecular chaperones and regulation of tau quality control: strategies for drug discovery in tauopathies.* Future Med Chem, 2011. **3**(12): p. 1523-37.
16.   Santacruz, K., et al., *Tau suppression in a neurodegenerative mouse model improves memory function.* Science, 2005. **309**(5733): p. 476-81.
17.   Jinwal, U.K., et al., *Imbalance of Hsp70 family variants fosters tau accumulation.* FASEB J, 2013. **27**(4): p. 1450-9.
18.   Fontaine, S.N., et al., *The active Hsc70/tau complex can be exploited to enhance tau turnover without damaging microtubule dynamics.* Hum Mol Genet, 2015. **24**(14): p. 3971-81.
19.   Narayanan, R.L., et al., *Automatic assignment of the intrinsically disordered protein Tau with 441-residues.* J Am Chem Soc, 2010. **132**(34): p. 11906-7.
20.   Thompson, A.D., et al., *Analysis of the tau-associated proteome reveals that exchange of Hsp70 for Hsp90 is involved in tau degradation.* ACS Chem Biol, 2012. **7**(10): p. 1677-86.
21.   Young, Z.T., et al., *Stabilizing the Hsp70-Tau Complex Promotes Turnover in Models of Tauopathy.* Cell Chem Biol, 2016. **23**(8): p. 992-1001.
22.   Xu, Z., et al., *Structure and interactions of the helical and U-box domains of CHIP, the C terminus of HSP70 interacting protein.* Biochemistry, 2006. **45**(15): p. 4749-59.
23.   Zhang, M., et al., *Chaperoned ubiquitylation--crystal structures of the CHIP U box E3 ubiquitin ligase and a CHIP-Ubc13-Uev1a complex.* Mol Cell, 2005. **20**(4): p. 525-38.
24.   Zhang, H., et al., *A bipartite interaction between Hsp70 and CHIP regulates ubiquitination of chaperoned client proteins.* Structure, 2015. **23**(3): p. 472-82.
25.   Smith, M.C., et al., *The E3 ubiquitin ligase CHIP and the molecular chaperone Hsc70 form a dynamic, tethered complex.* Biochemistry, 2013. **52**(32): p. 5354-64.
26.   Murata, S., et al., *CHIP is a chaperone-dependent E3 ligase that ubiquitylates unfolded protein.* EMBO Rep, 2001. **2**(12): p. 1133-8.
27.   Nikolay, R., et al., *Dimerization of the human E3 ligase CHIP via a coiled-coil domain is essential for its activity.* J Biol Chem, 2004. **279**(4): p. 2673-8.
28.   Stankiewicz, M., et al., *CHIP participates in protein triage decisions by preferentially ubiquitinating Hsp70-bound substrates.* FEBS J, 2010. **277**(16): p. 3353-67.
29.   Graf, C., et al., *Insights into the conformational dynamics of the E3 ubiquitin ligase CHIP in complex with chaperones and E2 enzymes.* Biochemistry, 2010. **49**(10): p. 2121-9.
30.   Assimon, V.A., D.R. Southworth, and J.E. Gestwicki, *Specific Binding of Tetratricopeptide Repeat Proteins to Heat Shock Protein 70 (Hsp70) and Heat Shock Protein 90 (Hsp90) Is Regulated by Affinity and Phosphorylation.* Biochemistry, 2015. **54**(48): p. 7120-31.
31.   Tarazona, M.P. and E. Saiz, *Combination of SEC/MALS experimental procedures and theoretical analysis for studying the solution properties of macromolecules.* Journal of Biochemical and Biophysical Methods, 2003. **56**(1): p. 95-116.
32.   Morgner, N., et al., *Hsp70 forms antiparallel dimers stabilized by post-translational modifications to position clients for transfer to Hsp90.* Cell Rep, 2015. **11**(5): p. 759-69.

33.   Thompson, A.D., et al., *Visualization and functional analysis of the oligomeric states of Escherichia coli heat shock protein 70 (Hsp70/DnaK).* Cell Stress Chaperones, 2012. **17**(3): p. 313-27.

34.   Barthel, T.K., J. Zhang, and G.C. Walker, *ATPase-defective derivatives of Escherichia coli DnaK that behave differently with respect to ATP-induced conformational change and peptide release.* J Bacteriol, 2001. **183**(19): p. 5482-90.

35.   O'Brien, M.C., K.M. Flaherty, and D.B. McKay, *Lysine 71 of the chaperone protein Hsc70 Is essential for ATP hydrolysis.* J Biol Chem, 1996. **271**(27): p. 15874-8.

36.   Johnson, E.R. and D.B. McKay, *Mapping the role of active site residues for transducing an ATP-induced conformational change in the bovine 70-kDa heat shock cognate protein.* Biochemistry, 1999. **38**(33): p. 10823-30.

37.   Zhuravleva, A., E.M. Clerico, and L.M. Gierasch, *An interdomain energetic tug-of-war creates the allosterically active state in Hsp70 molecular chaperones.* Cell, 2012. **151**(6): p. 1296-307.

38.   Vogel, M., M.P. Mayer, and B. Bukau, *Allosteric regulation of Hsp70 chaperones involves a conserved interdomain linker.* J Biol Chem, 2006. **281**(50): p. 38705-11.

39.   McCarty, J.S. and G.C. Walker, *DnaK as a thermometer: threonine-199 is site of autophosphorylation and is critical for ATPase activity.* Proc Natl Acad Sci U S A, 1991. **88**(21): p. 9513-7.

40.   Abisambra, J., et al., *Allosteric heat shock protein 70 inhibitors rapidly rescue synaptic plasticity deficits by reducing aberrant tau.* Biol Psychiatry, 2013. **74**(5): p. 367-74.

41.   Saidi, L.J., et al., *Carboxy terminus heat shock protein 70 interacting protein reduces tau-associated degenerative changes.* J Alzheimers Dis, 2015. **44**(3): p. 937-47.

42.   Dickey, C.A., et al., *Deletion of the ubiquitin ligase CHIP leads to the accumulation, but not the aggregation, of both endogenous phospho- and caspase-3-cleaved tau species.* J Neurosci, 2006. **26**(26): p. 6985-96.

43.   Fontaine, S.N., et al., *Isoform-selective Genetic Inhibition of Constitutive Cytosolic Hsp70 Activity Promotes Client Tau Degradation Using an Altered Co-chaperone Complement.* J Biol Chem, 2015. **290**(21): p. 13115-27.

44.   Kleiger, G. and T. Mayor, *Perilous journey: a tour of the ubiquitin–proteasome system.* Trends in cell biology, 2014. **24**(6): p. 352-359.

45.   Stevens, S.Y., et al., *The solution structure of the bacterial HSP70 chaperone protein domain DnaK(393-507) in complex with the peptide NRLLLTG.* Protein Sci, 2003. **12**(11): p. 2588-96.

46.   Clifford-Nunn, B., H.D. Showalter, and P.C. Andrews, *Quaternary diamines as mass spectrometry cleavable crosslinkers for protein interactions.* J Am Soc Mass Spectrom, 2012. **23**(2): p. 201-12.

47.   Phillips, A.S., et al., *Conformational dynamics of alpha-synuclein: insights from mass spectrometry.* Analyst, 2015. **140**(9): p. 3070-81.

48.   Zhuravleva, A. and L.M. Gierasch, *Substrate-binding domain conformational dynamics mediate Hsp70 allostery.* Proc Natl Acad Sci U S A, 2015. **112**(22): p. E2865-73.

49.   Noguchi, A., et al., *DnaJ-promoted binding of DnaK to multiple sites on sigma32 in the presence of ATP.* J Bacteriol, 2014. **196**(9): p. 1694-703.

50.   Suloway, C., et al., *Automated molecular microscopy: the new Leginon system.* Journal of structural biology, 2005. **151**(1): p. 41-60.

51.   Zheng, S., et al., *Anisotropic Correction of Beam-induced Motion for Improved Single-particle Electron Cryo-microscopy.* bioRxiv, 2016.

52.   Rohou, A. and N. Grigorieff, *CTFFIND4: Fast and accurate defocus estimation from electron micrographs.* Journal of Structural Biology, 2015. **192**(2): p. 216-221.

53.   Scheres, S.H.W., *A Bayesian View on Cryo-EM Structure Determination.* Journal of Molecular Biology, 2012. **415**(2): p. 406-418.

Chapter 2

BAG3 Is a Modular, Scaffolding Protein that physically Links Heat Shock Protein 70 (Hsp70) to the

Small Heat Shock Proteins

- **2.1 Abstract**

Small heat shock proteins (sHsps) are a family of ATP-independent molecular chaperones that are important for binding and stabilizing unfolded proteins. In this task, the sHsps have been proposed to coordinate with ATP-dependent chaperones, including heat shock protein 70 (Hsp70). However, it is not yet clear how these two important components of the chaperone network are linked. In collaboration with the lab of Jason Gestwicki at UCSF, we report that the Hsp70 co-chaperone, BAG3, is a modular, scaffolding factor to bring together sHsps and Hsp70s. Using domain deletions and point mutations, we found that BAG3 uses both of its IPV motifs to interact with sHsps, including Hsp27 (HspB1), αB-crystallin (HspB5), Hsp22 (HspB8), and Hsp20 (HspB6). BAG3 does not appear to be a passive scaffolding factor; rather, its binding promoted de-oligomerization of Hsp27, likely by competing for the self-interactions that normally stabilize large oligomers. BAG3 bound to Hsp70 at the same time as Hsp22, Hsp27, or αB-crystallin, suggesting that it might physically bring the chaperone families together into a complex. Indeed, addition of BAG3 coordinated the ability of Hsp22 and Hsp70 to refold denatured luciferase in vitro. Together, these results suggest that BAG3 physically and functionally links Hsp70 and sHsps.

- **2.2 Introduction**

The mammalian genome contains multiple classes of molecular chaperones that are named according to their approximate size, including heat shock protein 90 (Hsp90), heat shock protein 70 (Hsp70), heat shock protein 40 (Hsp40), and the small heat shock proteins (sHsps) [1]. Each of the categories of chaperones appears to be partly dedicated to individual aspects of protein quality control [2]. For example, Hsp70 and Hsp90 are ATPases that use nucleotide hydrolysis to regulate reversible binding to unfolded or partially folded proteins, stabilizing many "clients" and favoring their folding and/or

---

[1] My contributions to this chapter were the SEC-MALS and EM analysis. Contributions by the members of the Klevit lab are indicated in the figure legends

trafficking [3,4]. Other chaperones, such as the Hsp40s, appear to recruit specific clients to the Hsp70 and Hsp90 systems [5]. The importance of having multiple, non-overlapping categories of chaperones is highlighted by their incredible conservation across all kingdoms of life [6–8].

Together, the chaperones constitute a network that maintains global protein folding and function [1]. Within the chaperone network, many of the major chaperones make physical interactions with each other. For example, the prokaryotic orthologs of Hsp70 and Hsp90 directly bind to each other [9,10], as do the orthologs of Hsp70 and Hsp110 [11]. In mammals, Hsp70s are physically linked to the Hsp90s, but through the scaffolding protein, HOP (Hsc70–Hsp90 organizing factor). HOP is required for the Hsp70/Hsp90-mediated activation of steroid hormone receptors [12–15], perhaps by facilitating client transfer between the chaperones [16,17]. Thus, the mammalian chaperone network appears to be held together, in part, by protein–protein interactions between chaperones and scaffolding proteins. This feature might allow unfolded clients to be protected by a closely knit series of physically interacting factors, possibly limiting their exposure to bystander proteins.

Within the chaperone network, sHsps are a large and enigmatic class [18]. In humans, there are 10 members of the sHsp family, denoted HSPB1 through HSPB10 [19]. Unlike other molecular chaperone families, such as Hsp70 or Hsp90, sHsps do not possess enzymatic activity; instead, sHsps function as "holdases," a term that refers to their ability to bind and stabilize denatured or non-native proteins against aggregation [20,21]. Individual sHsps range in size from 12 to 43 kDa and they are defined by the presence of a conserved α-crystallin domain. In each sHsp, the α-crystallin domain that is flanked by variable, disordered N- and C-terminal domains that contain phosphorylation sites and may bind to clients [22]. The structure of the α-crystallin domain of Hsp27 has been solved by NMR and it features an anti-parallel beta-sheet that mediates stable dimerization [23–25]. In addition, the α-crystallin domain contains two highly conserved beta sheets, termed β4–β8, that form a hydrophobic groove. In some sHsps, such as Hsp27 and α-crystallin, an IXI motif in the C-terminus binds to this groove and stabilizes higher order oligomers [26–29] Specifically, the IXI motif from one unit of the sHsp seems to reach back onto the β4–β8 groove of another. This groove can even support hetero-oligomers between different sHsp family members [30,31]. The oligomers are typically polydisperse and range in size from ~ 12 to 40 dimer subunits [30,32,33].

The method by which sHsps bind and stabilize clients is still being explored. One model suggests that the sHsp oligomers dissociate in the presence of clients, and then re-form into a new oligomeric form containing bound client [34,35]. This idea is supported by electron microscopy (EM) [20,36] and mass

spectrometry studies [37–39]. It has also been shown that smaller oligomers of sHsp are more potent

holdases in vitro[39,40] and that even fragments of sHsps can still bind clients [41]. These observations

suggest that smaller oligomers might be better able to bind clients. In cells, phosphorylation of some

sHsps forces larger oligomers into smaller ones, perhaps providing a way for cell stress signaling to

increase chaperone function [39,42,43]. Similarly, some sHsps can also sense pH [44,45], adjusting their

structure to protect clients.

One major gap in our understanding of the chaperone network is how the sHsps link to the other major

components. This question is important because sHsps lack the enzymatic activity that appears to be

required for active remodeling or refolding by the other categories of chaperones. Rather, sHsps have

been proposed to work in conjunction with other chaperone systems, including Hsp70, in cells [46,47].

In this model, sHsp oligomers might interact with clients and keep them in a state that is competent for

re-folding by Hsp70.

Bcl-2-associated anthanogene-3 (BAG3) is a stress-inducible, 61-kDa protein that is characterized by the

presence of multiple protein–protein interaction motifs (Figure 2.1A), separated by long regions of

predicted disorder. BAG3 is a member of the BAG family of co-chaperones (BAG1–5), which are

characterized by a conserved BAG domain. The BAG domain is well known to bind the nucleotide-

binding domain (NBD) of members of the Hsp70 family [48,49]. This protein–protein interaction helps

release ADP from the chaperone to facilitate nucleotide cycling. BAG3 binds to Hsp70 tighter than BAG1

or BAG2 [50], and it is the most potent nucleotide exchange factor, suggesting that it is a functionally

important partner for Hsp70s. Outside of the BAG domain, the members of the BAG family have a

variety of other motifs that are not shared. For example, BAG3 contains a WW domain that has been

shown to be important for binding PPxY motif proteins, such as RAPGEF6 [51] and SYNPO2 [52]. The

PXXP region of BAG3 has been implicated in interactions with SH3 domain-containing proteins, including

Src [53] and PLC-γ [54], an interaction that might link BAG3 and Hsp70 to signaling pathways. Finally,

and most importantly for this study, BAG3 contains two IPV motifs separated by ~ 100 aa in its N-

terminus. BAG3 has been proposed to interact with sHsps through its IPV motifs [55–57], possibly

mimicking the intra-molecular interactions that normally occur between the IXI motif and the β4–β8

grooves.

Based on these interactions, it seemed plausible that BAG3 could be a scaffolding protein that physically

links sHsps to the Hsp70 system. To test this model in vitro, we generated a suite of BAG3 constructs

with individual domains mutated or deleted. We found that BAG3 interacts with multiple members of

the sHsp family using both of its IPV motifs. Interestingly, we found that BAG3 binding was not passive; rather it disrupts the Hsp27 oligomers, as judged by chromatography and EM. This finding suggests that BAG3 might actively remodel sHsps, potentially activating them or changing their interactions with clients. Indeed, we found that BAG3 could coordinate the ability of Hsp22 and Hsp70 to refold denatured luciferase. Finally, we were able to show that BAG3 can bridge the two chaperone families at the same time and that this physical interaction is dependent on the IPV and BAG domains of BAG3. Based on these data, we propose that BAG3 is the link between these two important components of the chaperone network.

- **2.3 Results**

- **2.3.1 BAG3 binds multiple sHsps**

	Hsp27	Hsp27-3D	Hsp27c	α-crystallin	Hsp20	Hsp22
K$_D$ (μM)	8.7 ± 2.2	3.5 ± 1.7	0.49 ± 0.06	5.0 ± 0.6	1.2 ± 0.7	1.2 ± 0.3
N	1.7 ± 0.2	1.9 ± 0.2	2.0 ± 0.1	1.8 ± 0.1	1.9 ± 0.2	2.0 ± 0.05
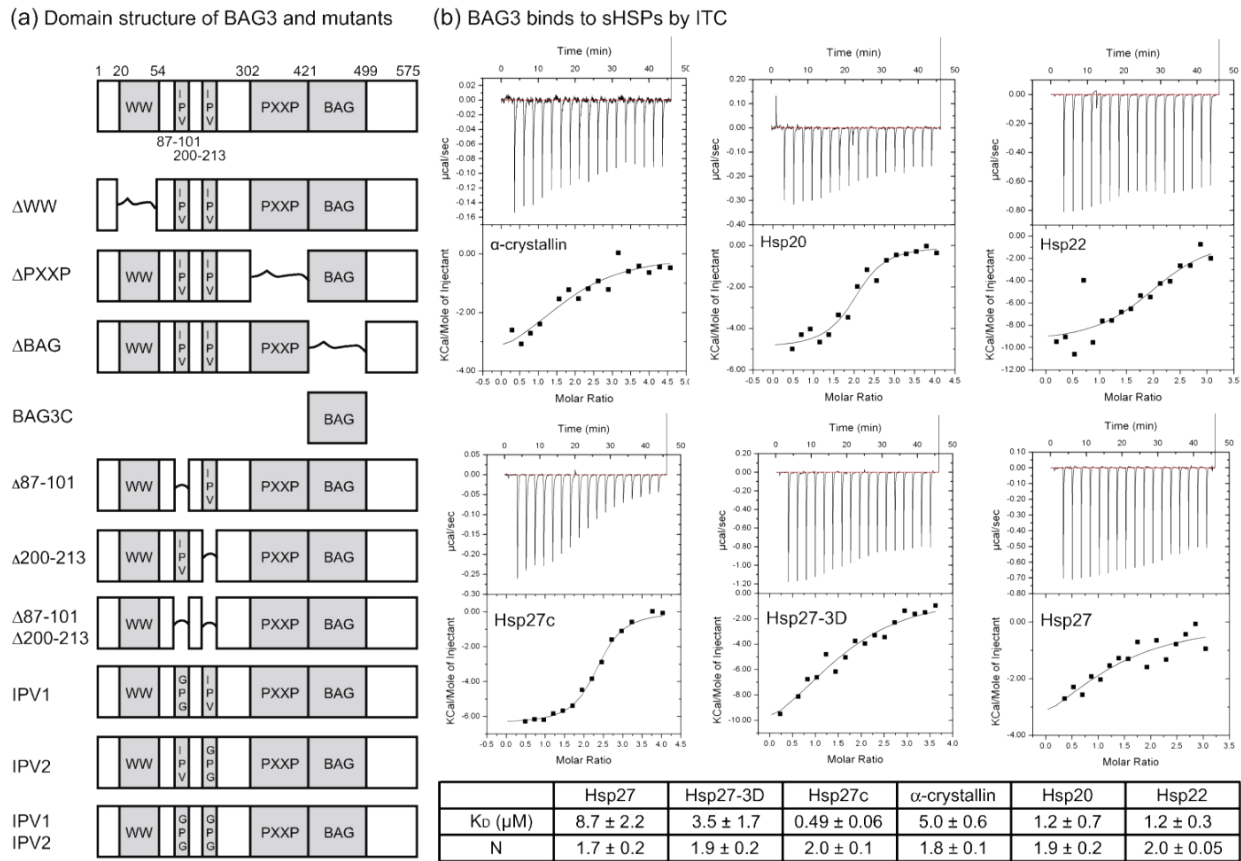
Figure 2.1 BAG3 binds to sHsps. A) Schematic of the domain architecture of BAG3, plus the deletions and point mutations used in this study. Deleted domains are indicated by a connecting line. B) ITC results confirm the relative affinities of BAG3 for sHsps. Results are representative of experiments performed in triplicate. Error is SEM. These experiments and figures were performed and created by Rauch JN (Gestwicki laboratory, UCSF).

To study the interactions with BAG3, we selected four members of the sHsp family that are ubiquitously expressed in all human tissues [19]: Hsp27 (HSPB1), α-crystallin (HSPB5), Hsp20 (HSPB6), and Hsp22 (HSPB8). Of these proteins, Hsp20, Hsp22, and α-crystallin have been reported to interact with BAG3 by co-immunoprecipitation and pulldown studies [55,57]; however, the affinities of these interactions were not known. Therefore, we employed isothermal titration calorimetry (ITC) to better understand them (Figure 2.1B). Interestingly, BAG3 bound tightest to Hsp22 (1.2 ± 0.3 μM) and Hsp20 (1.2 ± 0.7 μM), In contrast, BAG3 had a relatively weaker affinity for Hsp27 (8.7 ± 2.2 μM) and α-crystallin (5.0 ± 0.6 μM). Because of the possibility of competing interactions and the structural heterogeneity of the sHsps, the reported K_d values are best used as relative values. Regardless, these results support the idea that BAG3 uses IPV motifs to interact with sHsps because Hsp22 and Hsp20 lack their own IXI motifs and primarily exists as dimers or tetramers in solution [56,58], while Hsp27 and αB-crystallin have IXI motifs and form larger oligomers.

To better understand whether BAG3 might compete with the IXI motifs, we studied the interaction of BAG3 with two Hsp27 variants. Hsp27-3D is a triple phospho-mimetic mutant that forms smaller oligomers in solution [39], while Hsp27c is a truncated form that contains only the core α-crystallin domain and is exclusively a dimer in solution [25]. We found that Hsp27c bound with the tightest affinity (K_d ~ 0.49 ± 0.06 μM), followed by Hsp27-3D (3.5 ± 1.7 μM), and then Hsp27 (8.7 ± 2.2 μM). These results suggest that larger Hsp27 oligomers may have the weakest affinity for BAG3, while dimers bind the tightest. We hypothesize that this difference is because of competition between IXI motifs in the sHSPs and IPV motifs in BAG3 (see below). Furthermore, the ITC results suggested that the stoichiometry of each of the sHsp:BAG3 interactions is approximately 2:1 (Figure 2.1B). This was an intriguing result because BAG3 contains two IPV motifs, so it could potentially interact with both of the conserved β4–β8 grooves on either side of a sHsp dimer.

- **2.3.2 BAG3 uses IPV motifs to interact with the β4–β8 region**

To address this question more definitively, we prepared labeled Hsp27c and examined binding to BAG3 by [15]N–[1]N heteronuclear single quantum coherence NMR. We observed selective chemical shift perturbations (CSPs) in the β4–β8 region (Figure 2.2), consistent with the idea that BAG3 competes with the native IXI motifs. Furthermore, mutation of valine to alanine in a short IPV-containing peptide weakened its apparent affinity, showing that the IPV was important. Next, we generated BAG3 variants in which individual domains were systematically deleted.

(A) Full length BAG3 binds to Hsp27c in the β4-β8 region.
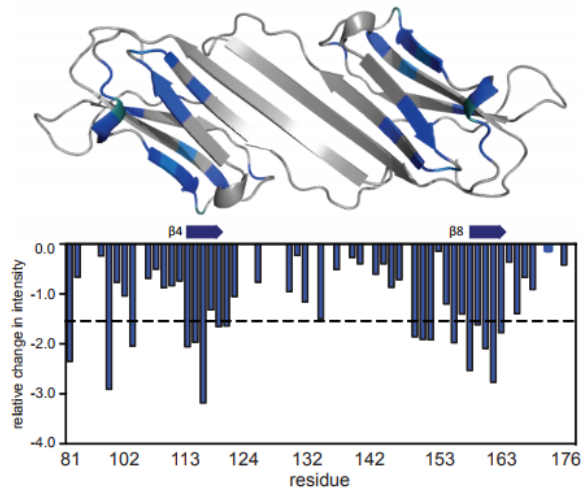
(C) IPV peptide, but not an IPA control, binds the β4-β8 region.
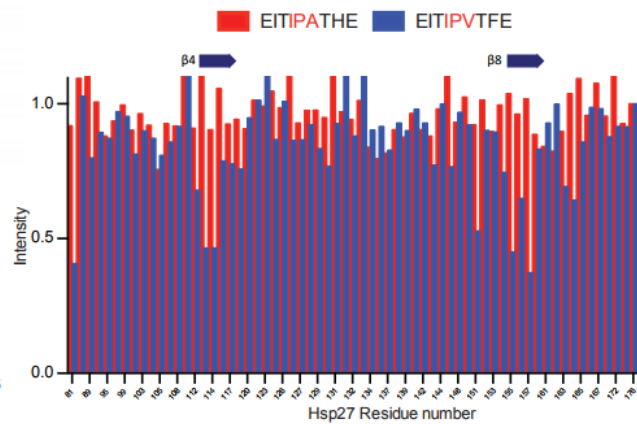
(B) IPV peptide binds the β4-β8 region.
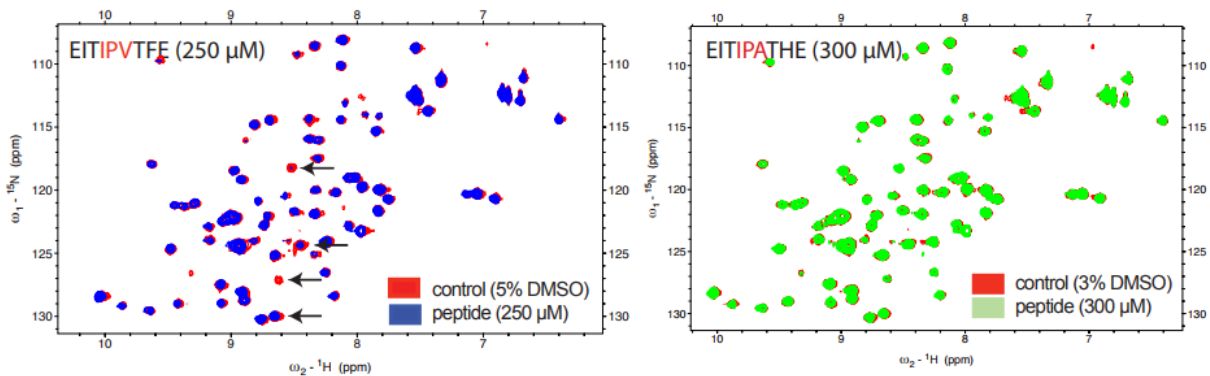
Figure 2.2 The IPV motif interacts with the expected β4-β8 region of Hsp27c. A) Titration of full length BAG3 into labeled Hsp27c revealed chemical shift perturbations (CSPs) in the β4-β8 region. CSPs greater than two standard deviations were colored blue on PDB 2N3J. Concentrations: Hsp27c (200 µM), Bag3 (100 µM). B) Titration of an IPV peptide confirms the interaction site. IPV peptide: EITIPVTFE (250 µM), 5% DMSO. IPA peptide: EITIPATHE (300 µM) 3% DMSO, 1mM EDTA. Due to solubility limits for the BAG3-derived peptides, sequences from Hsp27 were used. C) Comparison of the peak intensities from addition of the IPV and IPA peptides. Methods: HSQC spectra were acquired at 30 °C on a 600 MHz Bruker Avance III spectrometer equipped with cryoprobe, running Topspin version 2.1. Spectra were acquired on samples containing 200 µM Hsp27c in 50 mM sodium phosphate, pH 7.5, 100 mM NaCl and the results were compared to solvent controls. 256 scans were acquired per t1 value and spectral widths of 1500 Hz and 9615 Hz were used in the ^{1}H and ^{15}N dimensions, respectively. Processing and spectral visualization were performed using rNMR and Sparky. These experiments and figures were performed and created by Rauch JN (Gestwicki laboratory, UCSF).

These deletions included the BAG3 variants: ΔWW, Δ87–101, Δ200–213, Δ87–101, and Δ200–213, ΔPXXP, ΔBAG, and BAG3C (Figure 2.1A). The truncations Δ87–101, Δ200–213, Δ87–101, and Δ200–213 removed the first IPV motif, the second IPV motif or both, respectively, while the other truncations removed known domains involved in other protein–protein interactions. Finally, BAG3C was composed of only the BAG domain, so we could use it to understand the role of this region. We assayed the truncated proteins for binding to Hsp27c using ITC (Figure 2.3) and found that the ΔWW, ΔPXXP, or

ΔBAG proteins bound with approximately the same affinity as full length (~ 0.5 to 0.7 μM). BAG3C construct did not bind to Hsp27c, as expected. These results are consistent with the role of IPV motifs in binding to sHsps, and they suggest that other domains are not involved. More interestingly, we found that deletion of individual IPV motifs (Δ87–101, Δ200–213) or mutation of the first IPV motif to GPG (named as IPV1) weakened affinity by at least 2-fold (~ 1 to 2 μM). The mutation or deletion of individual IPV motifs also reduced the stoichiometry (N) of the interaction from 2:1 to approximately 1:1 (Figure 2.3B). When both IPV motifs were deleted (Δ87–101 and Δ200–213) or mutated (IPV1 and IPV2 to GPG), binding was abolished. The simplest explanation for these results is that BAG3 uses both of its IPV motifs to engage the Hsp27c dimer.

To explore whether this bi-dentate binding mode might be conserved in the interaction with other sHsps, we measured binding of each of the BAG3 mutants to Hsp27, αB-crystallin, Hsp22, and Hsp20 using a flow cytometry protein interaction assay (FCPIA). Consistent with the results obtained using Hsp27c, deletion or mutation of one IPV motif weakened the apparent binding affinity (typically by about 2-fold) for each of the full-length sHsps. Removing both IPV motifs prevented measurable binding to Hsp27, HSP27-3D, Hsp20, and αB-crystallin (K_d > 50 μM) and weakened the affinity for Hsp27c and Hsp22 by more than 25-fold (K_d ~ 10 to 20 μM). Replacing both IPV motifs with GPG had a similar effect; binding to Hsp27, HSP27-3D, and αB-crystallin was unmeasurable (K_d > 50 μM) and the affinity for Hsp27c, Hsp20, and Hsp22 was weakened (K_d ~ 3 μM). Together, these results suggest that BAG3 uses both of its IPV motifs to interact with sHsps. These interactions do not necessarily have to involve two IPV motifs binding to a single dimer, especially in the context of the more complex, polydisperse sHsp oligomers.
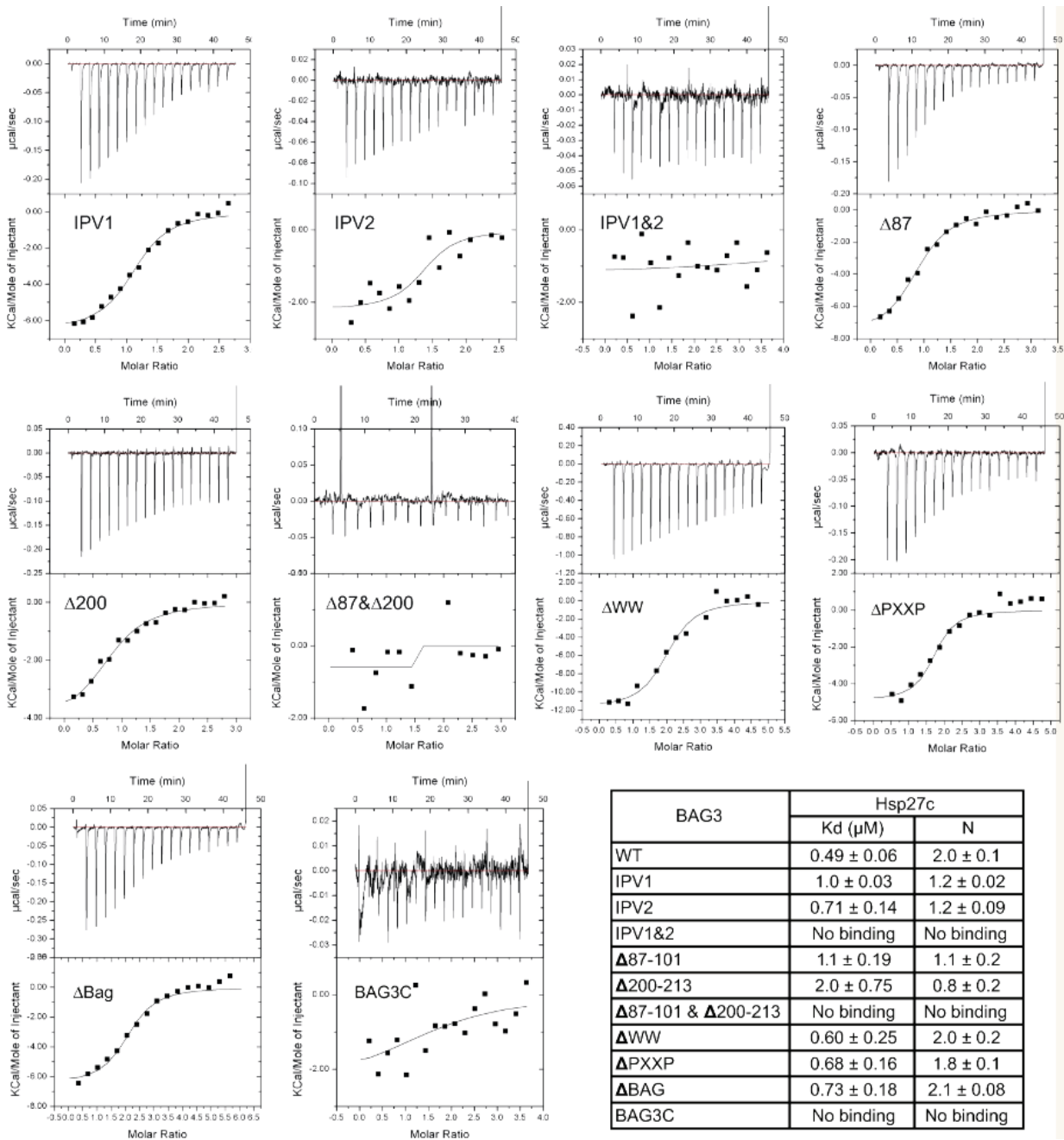
Figure 2.3 BAG3 uses both IPV motifs to bind sHsps. Deletions and point mutations in BAG3 reveal that the IPV motifs are important for binding to Hsp27c, using ITC. Experiments were performed in duplicate and the error bars are SEM. These experiments and figures were performed and created by Rauch JN (Gestwicki laboratory, UCSF).

- ### 2.3.3 BAG3 reduces the size of Hsp27 oligomers

Knowing that BAG3 uses its IPV motifs to interact with sHsps and that sHsps also use their IXI motifs to regulate their oligomer size, we wondered if BAG3 could disrupt sHsp oligomers. To test this hypothesis, we first used size exclusion chromatography with multi-angle light scattering (SEC-MALS). This technique

58

allows molecular weight determination of a sample based on the intensity of light scattering as a function of angle. In these experiments, we focused on Hsp27 because it is known to form large oligomers that can be visualized by EM (see below) [44]. Injection of Hsp27 (30 μM) alone yielded an SEC-MALS trace with an average mass of 425 kDa (Figure 2.4A). This mass corresponds to ~ 18 monomeric subunits, which is consistent with literature values [59]. In addition, the Hsp27 peak was broad (mass range 390–470 kDa), suggesting a polydisperse ensemble of oligomers that has been observed previously [60]. Adding BAG3 to this sample effectively reduced the apparent oligomer size from 425 kDa to 330 kDa (Figure 2.4A). This change represents a predicted drop in average subunit size from approximately 18 monomers to ~ 14 monomers, supporting the hypothesis that BAG3 can disassemble oligomers of Hsp27. Importantly, this estimate is a conservative upper bound because
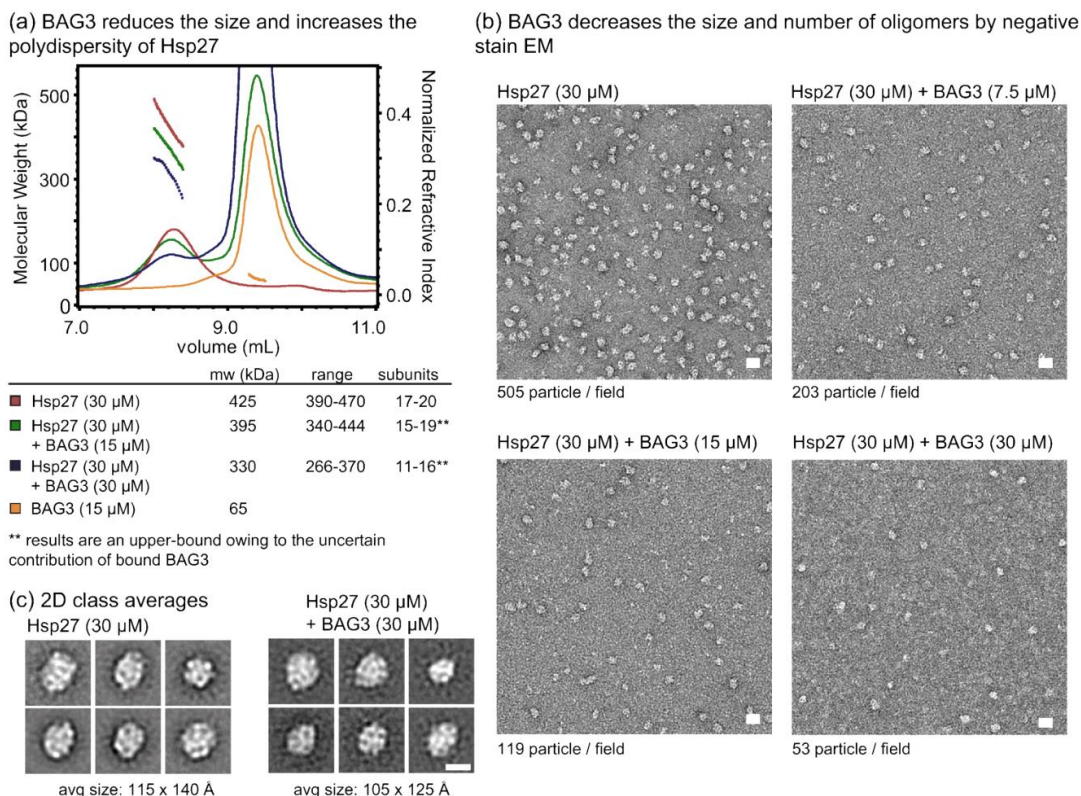
Figure 2.4 BAG3 binding reduces the size of Hsp27 oligomers. A) Hsp27 (30 μM) was incubated with increasing concentrations of BAG3 and the mixtures were analyzed by SEC-MALS. BAG3 reduced the average molecular weight of the Hsp27 peak and increased the polydispersity of the samples. Experiments were repeated in duplicate and average MW is reported with SEM. Importantly, the estimate of the number of Hsp27 subunits within the complex does not include the contributed mass of bound BAG3 because the stoichiometry is not yet clear, so it should be considered a conservative upper bound. B) 2D class averages of oligomer particles show a modest decrease in the average particle size. Scale bar is 10 nm. C) BAG3 decreases the number of Hsp27 oligomers, as measured by negative stain EM. Scale bar is 20 nm.

59

BAG3 is also likely to contribute to the apparent molecular mass. If, based on the ITC results, we assume a 2:1 stoichiometry, then the oligomers would be composed of ~ 6 monomers. Although a definitive conclusion is difficult, owing to the heterogeneity of the samples, the qualitative conclusion is that BAG3 disrupts the Hsp27 oligomers.

To test this idea in a different way, we used EM. We found that oligomers of Hsp27 are visible using negative stain EM, with an average size of 115 × 140 Å (Figure 2.4B). Importantly, we expect that smaller oligomers, such as dimers, are "invisible" by this method because they do not readily accumulate stain. In fact, this feature allowed us to ask whether BAG3 could convert samples of Hsp27 into a smaller oligomer size by two approaches. In the first, we examined all of the visible particles and measured their dimensions to see if BAG3 could favor smaller structures. Indeed, we found that the Hsp27 particle size decreased to 105 × 125 Å when treated with 30 µM BAG3 (Figure 2.4B). Next, we counted the total number of visible Hsp27 particles in the grids to estimate whether BAG3 was lowering the number of oligomers. Small oligomers and dimers of Hsp27 would not be expected to retain stain and, therefore, would not be visible by this method. Strikingly, we found that the total number of visible particles was strongly reduced by BAG3 in a dose-dependent manner (Figure 2.4C). Specifically, the average number of oligomers observed in micrographs of Hsp27 alone was 505 particles/field. With increasing amounts of BAG3 at a constant concentration of Hsp27 (30 µM), the number of large particles was drastically decreased: 203 in the presence of 7.5 µM BAG3, 119 in the presence of 15 µM BAG3, and only 53 oligomer particles in the presence of 30 µM BAG3. At this time, the exact stoichiometry of the Hsp27–BAG3 complexes and the size distribution of treated samples are not clear. However, these results point to a model in which competition for IXI motifs during binding to BAG3 is not static—it results in a decrease in average Hsp27 oligomer size.

- **2.3.4 BAG domain is essential for Hsp70 nucleotide exchange factor function**

BAG3 forms a tight interaction with the NBD of Hsp70 (K_d ~ 10 nM) to stimulate ADP release [50]. While it is known that this process requires the BAG domain, it was not yet clear if other regions of BAG3, especially the IPV motifs, might contribute to Hsp70 binding. To explore this idea, we measured binding of the BAG3 deletion mutants to Hsp70. Using FCPIA, we first confirmed that ΔBAG can no longer bind to Hsp70 (Figure 2.5A), consistent with the literature. This result was also confirmed by ITC (Figure 2.5B). The other deletions or mutations had a less dramatic effect on the BAG3–Hsp70 affinity (typically less than 2-fold reduction), suggesting that the majority of the binding energy originates from the BAG domain.

To verify this finding in a different platform, we turned to a nucleotide release assay. In this assay, Hsp70 is loaded with a fluorescent ATP analog and then the ability of BAG3 to release the tracer is measured by fluorescence polarization [50]. We found that all of the domain deletion constructs were approximately equivalent in their ability to promote nucleotide release from Hsp70 (Figure 2.5), with the exception of the ΔBAG construct. Together, these results point to a model in which the BAG domain interaction with Hsp70's NBD is largely "insulated" from other parts of BAG3, including the IPV motifs.

(a) The BAG domain is required for tight binding to Hsp70's NBD by FCPIA
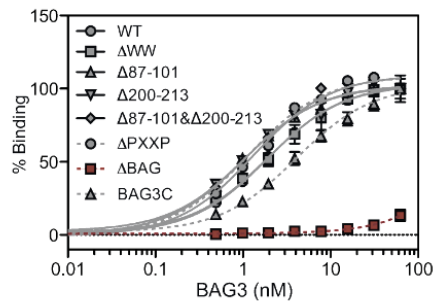
(b) The BAG domain is required for tight binding to Hsp70's NBD by ITC

BAG3	NBDL	
	K$_D$ (nM)	N
WT	13 ± 4.3	0.9 ± 0.01
ΔWW	10 ± 6.0	0.9 ± 0.01
Δ87-101	5.9 ± 3.0	1.0 ± 0.01
Δ200-213	7.5 ± 2.0	0.9 ± 0.004
Δ87-101 & Δ200-213	23 ± 11	0.9 ± 0.02
ΔPXXP	28 ± 13	0.9 ± 0.04
ΔBAG	No Binding	No Binding
BAG3C	32 ± 12	1.0 ± 0.02

(c) The BAG domain is required for release of fluorescent nucleotide from Hsp70 NBD
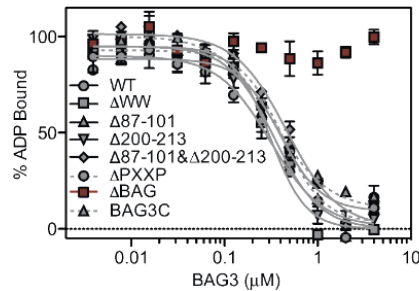
Figure 2.5 BAG3 binds Hsp70 through its BAG domain and stimulates client release. Binding of labeled BAG3 to immobilized Hsp70 by A) FCPIA and B) ITC. Results are the average of experiments performed in triplicate. Error bars represent EM. C) BAG3 releases fluorescent nucleotide from Hsp70 NBD. Deletion of the BAG domain blocks this activity. Results are the average of experiments performed in triplicate. Error is SEM. These experiments and figures were performed and created by Rauch JN (Gestwicki laboratory, UCSF).

- **2.3.5 Hsp70–BAG3–sHsp form a ternary complex**

After characterizing the individual, binary interactions between BAG3–sHsp and BAG3–Hsp70, we set out to determine if a ternary Hsp70–BAG3–sHsp complex could be formed. The results of the binding studies thus far suggested that BAG3 could be a modular scaffolding protein, leading to the prediction that binding to Hsp70 would not impact binding to sHsps and vice versa. To ask this question, we immobilized Hsp22, α-crystallin or Hsp27 on streptavidin beads, incubated them with a constant concentration of Alexa 647-labeled BAG3 (50 nM), and then added increasing amounts of Alexa 488-labeled Hsp70NBD (Figure 2.6A). Unfortunately, we were not able to immobilize sufficient levels of Hsp20 for this study. If Hsp70NBD could compete with sHsp for binding to BAG3, we would expect to see a decrease in Alexa 647 signal upon titration. However, we observed no decrease in fluorescence in the presence of Hsp70NBD (Figure 2.6A, top). Moreover, since we labeled BAG3 and Hsp70NBD with fluorophores that have distinct spectral properties, we were also able to confirm that both proteins were bound at the same time by monitoring the increase in Alexa 488 signal (Figure 2.6A, bottom). Lending further support to the idea of a modular interaction, the apparent affinity of the Hsp70NBD–BAG3 interaction (~ 15 nM) was unchanged in the presence of Hsp22, α-crystallin, or Hsp27, when compared to the binary interaction. These findings suggest that sHsps and Hsp70 do not interfere with (or promote) binding to the other partner. In important control studies, we found that Hsp70NBD did not bind Hsp22, α-crystallin, or Hsp27 in the absence of BAG3 (Figure 2.6A). Thus, Bag3 appears to be a modular scaffolding protein for the two chaperone families.

To confirm this idea, we analyzed solutions of Hsp70, BAG3, Hsp22, or a mixture of the three by SEC. Hsp22 was chosen for this experiment because of its tight affinity (see Figure 2.1B) and its relatively homogeneous oligomer size distribution on SEC (Figure 2.6B). Also, ATP (1 mM) was added to favor tight binding of Hsc70NBD to BAG3. Other sHsps were too heterogeneous in this platform to allow conclusions. However, we found that Hsp70, BAG3, and Hsp22 were clearly distinguished from each other on the SEC traces when injected individually (Figure 2.6B). Moreover, pre-incubation of these components showed a conversion to a higher-order complex (Figure 2.6B). All three proteins were part of this complex, as judged by collecting fractions and subjecting them to SDS-PAGE. Thus, BAG3 appears to be an adapter protein that links Hsp22, and likely other sHSPs, to Hsp70.

(a) BAG3 binds sHsp and Hsp70 at the same time
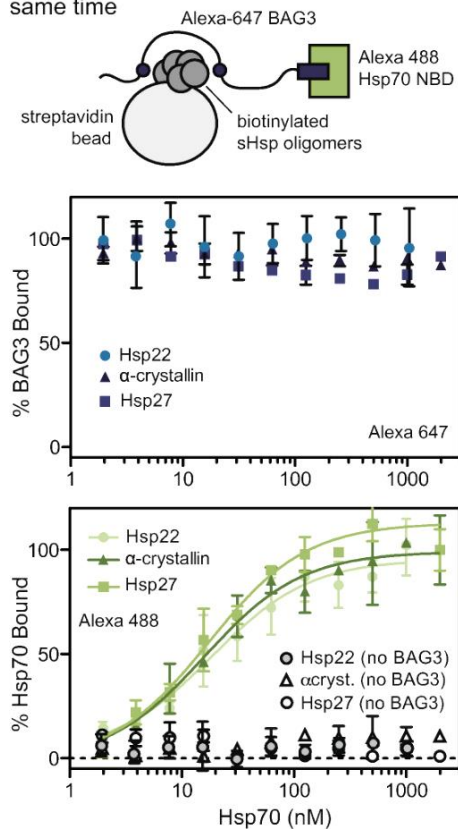
(b) BAG3, Hsp22 and Hsp70 form a ternary complex
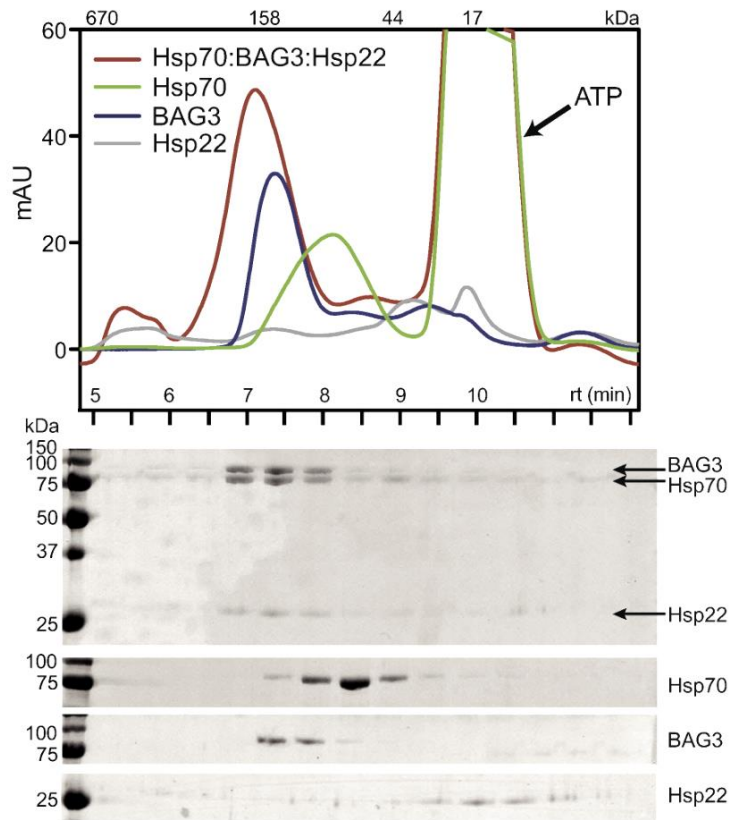
Figure 2.6 BAG3 stabilizes a ternary complex with Hsp70. (a) Alexa Fluor 488-labeled Hsp70 NBD was titrated against a solution of Alexa Fluor 647-labeled BAG3 in the presence of sHsp- (α-crystallin, Hsp27, or Hsp22) coated beads. Binding was detected using a flow cytometer. Experiments were performed in triplicate and error is SEM. A schematic of binding experiment is shown. Note that the sHsp oligomer size is heterogeneous. (b) SEC and SDS-PAGE analysis of a solution of Hsp22 (6 μM), BAG3 (12 μM), and Hsp70 (6 μM) or solutions of individual components. In all experiments, ATP was added (1 mM) to favor tight binding of Hsp70 to BAG3. These experiments and figures were performed and created by Rauch JN (Gestwicki laboratory, UCSF).

- **2.3.6 Hsp22 promotes the co-chaperone activity of BAG3 in vitro**

To explore possible functional implications of the ternary complex, we measured two chaperone activities of Hsp70: ATP turnover and firefly luciferase refolding. ATPase activity is typically measured using a colorimetric, malachite green assay, while refolding activity is measured by treating denatured firefly luciferase with chaperones and monitoring the recovery of luminescence. It is known that substoichiometric concentrations of BAG3 promote Hsp70's nucleotide turnover because it overcomes the rate-limiting step in cycling. Likewise, low levels of BAG3 are thought to balance the binding-and-release of luciferase in the refolding assay, increasing the yield of re-folded enzyme. However, in both assays, higher concentrations of BAG3 seem to stall Hsp70, such that it converts from being a stimulator into an apparent inhibitor [50].

Using these assays, we varied the concentration of both BAG3 and Hsp22, holding the levels of Hsc70 (1 µM) constant. Importantly, we found that Hsp22 had no significant effect on either ATPase activity or luciferase refolding in the absence of BAG3 (Figure 2.7A and B), so this sHsp was ideal for these experiments. In the ATPase assay, we observed a striking ability of Hsp22 to promote the activity of BAG3 (Figure 2.7A). For example, at 0.5 µM of Hsp22, BAG3 became a potent suppressor of cycling. At 2 µM, this effect was even more pronounced, allowing BAG3 to be a strong inhibitor at concentrations at which it was normally inactive (e.g., 0.125 µM; Figure 2.7A). We noted a trend of Hsp22 to modestly promote the ability of low levels of BAG3 to activate turnover when the Hsp22 was also present at low concentrations (0.125 and 0.0625 µM of Hsp22; Figure 2.7A); however, this trend was not statistically significant (p value > 0.01).
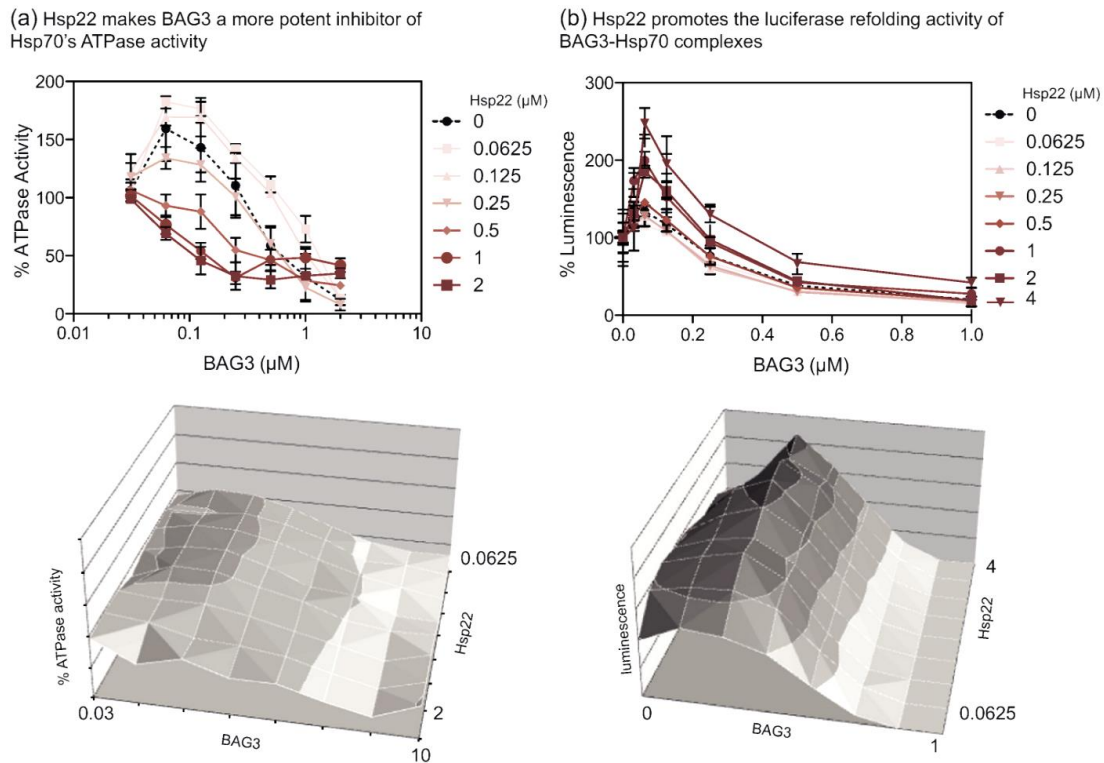
Figure 2.7 Hsp22 affects the chaperone functions of Hsp70 through BAG3. (a) The ATPase activity of Hsp70 was measured by malachite green assays. Addition of BAG3 suppresses ATPase activity, consistent with previous reports. Hsp22 promotes this activity and makes BAG3 more effective at lower concentrations. Results are the average of at least three independent experiments performed in triplicate. Error bars represent SD. Importantly, Hsp22 has no effect on Hsp70's ATPase activity in the absence of BAG3. (b) Hsp22 coordinates with Hsp70–BAG3 to refold denatured luciferase. Titration of BAG3 into Hsp70 initially promotes luciferase refolding, but it then becomes inhibitory at higher concentrations. Addition of Hsp22 promotes luciferase refolding. Results are the average of at least three independent experiments performed in triplicate. The error bars represent SD. In both A and B, the results are shown as a two- and three-dimensional display of the same data. These experiments and figures were performed and created by Rauch JN (Gestwicki laboratory, UCSF).

The possible effects of BAG3 and Hsp22 on luciferase refolding were measured using a similar approach. Chaperone-mediated refolding of firefly luciferase requires a careful balance of client binding and release, which eventually favors the folded, enzymatically active state. We observed that titration of Hsp22 into the Hsc70–BAG3 system strongly promoted the refolding of luciferase, with luminescence increased by 2- to 3-fold when Hsp22 was above 1 μM (Figure 2.7B). Again, this activation was highly dependent on coordination with BAG3, because Hsp22 was unable to promote refolding in the absence of BAG3 or at high concentrations of BAG3. These results suggest that BAG3 regulates the chaperone functions of Hsc70 and Hsp22 in the context of refolding damaged luciferase.

- **2.4 Discussion**

Using pulldowns, BAG3 had been reported to interact with some sHsps through its IPV motifs [56,57]. Using NMR, we first confirmed that BAG3 binds the conserved β4–β8 region of the core crystallin domain, where the IXI motifs normally reside (see Figure 2.2). Furthermore, deleting or mutating either of the IPV motifs of BAG3 weakened binding to Hsp27, Hsp20, Hsp22, and αB-crystallin and deleting or mutating them both largely abolished binding (see Figure 2.1). These results suggest that BAG3 uses both of its IPV motifs to engage the two β4–β8 grooves. In the simplest case (such as Hsp27c), such an interaction could occur through a "clamp-like" mechanism, with both of the IPV motifs making contact within a single dimer. There is a sufficient distance between the IPV motifs (~ 100 aa; see Figure 2.1A) to allow for such an interaction and the 2:1 stoichiometry, calculated from ITC, is supportive. However, the sHsps that form larger oligomers, such as those formed by full-length Hsp27 or αB-crystallin, may interact with BAG3 in a more complex way. Indeed, it seems likely that a single BAG3 might use both IPV motifs to bind β4–β8 regions in nearby protomers within the oligomer, which are not necessarily part of a single homodimer.

One important implication of this model is that BAG3 might be expected to inhibit oligomerization of some sHsps. Specifically, it is known that the IXI motifs of some sHsps are important in linking dimers together into higher order oligomers. This idea is supported by the fact that Hsp20 and Hsp22 both lack their own IXI motifs and have reported to form relatively smaller oligomers in solution [56,58]. Indeed, we found that incubation of full-length Hsp27 with BAG3 leads to an overall decrease in both oligomer size and frequency, as judged by SEC-MALS and EM. Thus, BAG3 does not appear to be a "passive" scaffolding protein. Rather, its interactions with sHsps compete for IXI binding and partially disrupt quaternary structure. As we observed in the luciferase refolding experiments (see Figure 2.7), this structural change may have functional implications. It is important to note that interactions outside the

IXI motifs also contribute to the formation of higher-order oligomers, so it seems unlikely that BAG3 could convert oligomers to an entirely dimeric state.

Hsp70 and the sHsps constitute an ancient system for protecting proteins under conditions of proteotoxic stress. sHsps are capable of binding and stabilizing unfolded/denatured proteins and keeping them in a refolding-competent form [21]. Due to their lack of intrinsic refolding ability, sHsps must then collaborate with ATP-powered refolding systems, such as the Hsp70 system [61]. Indeed, it has been shown both in vitro and in vivo that sHsp substrates can be refolded by the Hsp70 chaperone system [62–65]. However, a mechanistic understanding of how sHsps might communicate with the Hsp70 system has been elusive, especially for the mammalian systems.

Using FCPIA and SEC, we found that BAG3 could bind to Hsp70 at the same time as Hsp27, Hsp22, and αB-crystallin. Multiple pieces of evidence suggest that the strength of the two protein–protein interactions within this ternary complex (e.g., BAG3–Hsp70, BAG3–sHsp) is not influenced by the other. For example, the apparent affinity of the BAG3 interaction with Hsp27, Hsp22, and αB-crystallin was not significantly different in the presence of Hsp70 (see Figure 2.4). Moreover, deletion of the BAG domain or the IPV motifs from BAG3 did not impact binding to the other partner (see Figs. 2 and 4). Thus, it appears that BAG3 is a modular scaffolding protein that physically links sHsps to Hsp70. In this way, BAG3 may act like the scaffolding protein, HOP, which coordinates the Hsp70–Hsp90 axis [66]. In that system, HOP is thought to organizing "hand-off" of partially folded clients, such as nuclear hormone receptors, between the chaperones. We speculate that the mammalian chaperone network may contain additional examples of such scaffolding proteins.

Because smaller oligomers of Hsp27 and α-crystallin had been shown to be more potent chaperones [39,40] and we found that BAG3 could compete for the IXI motifs that help hold together oligomers (see Figure 2.4), we wondered whether BAG3 might promote sHsp chaperone activity. Furthermore, BAG3 is well known to regulate Hsp70's chaperone function through its BAG domain interactions, so it might be expected to coordinate the activities of both sHsps and Hsp70s. Indeed, we found that the combination of BAG3, Hsp22, and Hsp70 (at the proper ratio) was a potent refolding machine (see Figure 2.7). The mechanistic details of this process are not yet known and it remains to be seen whether this ternary complex could be functionally important in cells and animals. Yet, these results suggest that BAG3 is both a physical and functional link between the sHsps and Hsp70s. In this way, BAG3 is not a "passive" scaffolding protein, but one that remodels the activity of its chaperone partners.

BAG3 binds to Hsp70 with an affinity of ~ 13 nM (see Figure 2.5) in the ATP state, while its affinity for sHsps is between ~ 8700 and 350 nM (see Figure 2.1). Although there is much to learn about how "client" proteins, expression level and post-translational modifications might impact these apparent affinity constants in the cell, it is interesting that BAG3 has a tighter affinity for Hsp70 than sHsps. This observation suggests that BAG3 and Hsp70 form a relatively more stable pair, which might only transiently coordinate with sHsps.

BAG3 is the only stress-inducible member of the BAG family, so we propose that its unique scaffolding function may be especially important during conditions that favor protein unfolding and aggregation. In this scenario, the stress-inducible expression of BAG3 might bring together sHsps with Hsp70s, while simultaneously "activating" both systems. It is clear that other stress-inducible mechanisms, such as phosphorylation of sHsps [42,43], also contribute to adaptive proteostasis. However, the expression of BAG3 may also play a role in this process through its ability to coordinate two major components of the chaperone network.

- **2.5 Methods**

- Cloning and recombinant protein production

All domain deletion constructs were subcloned from the BAG3 pMCSG7 parent vector and confirmed with DNA sequencing. Mutations were constructed using standard mutagenesis protocols. Constructs for Hsp27, Hsp27c, Hsp27-3D, and α-crystallin were all received from the Klevit laboratory. Hsp22 was a kind gift from Jean-Marc Fontaine, and Hsp20 was received from the Conklin laboratory and subsequently cloned into the pMCSG7 vector. All constructs were transformed into BL21(DE3) cells and single colonies were used to inoculate TB medium containing ampicillin (50 μg/mL). Cultures were grown at 37 °C for 5 h, cooled to 20 °C and induced overnight with 200 μM IPTG. BAG3 full length and IPV mutants were purified as previously described [50]. BAG3 deletion constructs were pelleted and re-suspended in His-binding buffer (50 mM Tris, 300 mM NaCl, 10 mM imidazole [pH 8.0]) + 3 M Urea. Samples were sonicated and then applied to the Ni-NTA resin. After Ni-NTA columns, all proteins were subjected to TEV cleavage overnight, concentrated and applied to a Superdex S200 (GE Healthcare) size exclusion column in BAG buffer (25 mM Hepes, 5 mM MgCl2, 150 mM KCl [pH 7.5]). Hsp72 and Hsp72NBD were purified as described elsewhere [67]. sHsp in plasmids containing an N-terminal His tag (Hsp27-3D, α-crystallin, Hsp22, and Hsp20) were all purified using a His column and subsequent SEC on a Superdex S200 in BAG buffer or phosphate-buffered saline, as previously reported [33]. Hsp27 and

Hsp27c were in tagless vectors, so they were purified using a two-step ammonium sulfate precipitation followed by MonoQ and SEC. Briefly, ammonium sulfate was added to a final concentration of 16.9% (w/v), centrifuged, pellet discarded, and then an additional 16.9% (w/v) ammonium sulfate was added to the supernatant to precipitate the protein from solution. Precipitated protein was brought up and dialyzed into MonoQ Buffer A (20 mM Tris, pH 8.0) overnight, followed by a MonoQ column (0–1 M NaCl gradient), and finally an SEC on a Superdex S75 (Hsp27c) or Superdex S200 (GE Healthcare) equilibrated in 50 mM sodium phosphate and 100 mM NaCl (pH 7.5) buffer. Throughout the manuscript, the concentration of sHSPs is reported based on effective monomer concentration and not oligomer concentration.

- ITC

BAG3 constructs, Hsp72NBD, and sHsps were dialyzed overnight against ITC buffer (25 mM Hepes, 5 mM MgCl2, 100 mM KCl [pH 7.5]). Concentrations were determined using a BCA Assay (Thermo Scientific), and the experiment was performed with a MicroCal VP-ITC (GE Healthcare) at 25 °C. Hsp72NBD (100 µM) or indicated sHsp (200 µM) in the syringe was titrated into a 10-µM cell solution of BAG3 protein. Calorimetric parameters were calculated using Origin® 7.0 software and fit with a one-site binding model.

- FCPIA

The assay procedure was adopted from previous reports [50]. Briefly, biotinylated Hsp70 was immobilized (1 h at room temperature) on streptavidin-coated polystyrene beads (Spherotech). After immobilization, beads were washed to remove any unbound protein and then incubated with labeled BAG3 proteins at the indicated concentrations. Binding was detected using an Accuri™ C6 flow cytometer to measure median bead-associated fluorescence. Beads capped with biocytin were used as a negative control, and non-specific binding to beads was subtracted from signal.

For ternary complex formation experiments, Hsp27 or α-crystallin was immobilized on beads with constant concentration (50 nM) of Alexa 647-labeled BAG3 present. Increasing concentrations of Alexa 488-labeled Hsp72 NBD were titrated against the sHsp–BAG3 solution and fluorescence was measured using an Accuri™ C6 flow cytometer. Again, beads capped with biocytin were used as a negative control, and non-specific binding to beads was subtracted from signal.

- Nucleotide release assay

A fluorescent ATP analog, N6-(6-Amino)hexyl-ATP-5-FAM (Jena Bioscience) was used to measure BAG3-induced nucleotide dissociation from Hsp72, as previously described [50]. In black, round-bottom, low-volume 384-well plates (Corning), 1 μM Hsp72 and 20 nM N6-(6-Amino)hexyl-ATP-5-FAM were incubated with varying concentrations of BAG3 protein for 10 min at room temperature in assay buffer (100 mM Tris, 20 mM KCl, 6 mM MgCl2 [pH 7.4]). After incubation, fluorescence polarization was measured (excitation: 485 nm emission: 535 nm) using a SpectraMax M5 plate reader.

- SEC-MALS

Solutions of Hsp27 (15 μM) and BAG3 (either 15 or 30 μM) were pre-mixed and resolved by analytical SEC on a Shodex 804 column on an Ettan LC (GE Healthcare). Molecular weights were determined by multi-angle laser light scattering using an in-line DAWN HELEOS detector and an Optilab rEX differential refractive index detector (Wyatt Technology Corporation). The column was equilibrated overnight in BAG buffer prior to analysis. Samples were run at the indicated concentrations. Calculation of molecular weights was performed using the ASTRA software package (Wyatt Technology Corporation).

- SEC

Solutions of BAG3 (6 μM), Hsp72 (6 μM), Hsp22 (12 μM), or BAG3–Hsp72–Hsp22 (6 μM:6 μM:12 μM) were examined using a Superdex S200 (GE Healthcare) size exclusion column. Indicated fractions were collected and analyzed using SDS-PAGE analysis. Samples were separated using 4%–15% Tris–Tricine gels (Bio-Rad) and stained with Coomassie Blue. Image color was changed to grayscale for clarity.

- EM

Solutions of Hsp27 (30 μM) and BAG3 (7.5, 15, or 30 μM) were pre-incubated, diluted, and applied to a thin carbon-coated copper grid for negative staining using uranyl formate at pH ~ 6.0. Electron micrographs were collected on a Tecnai T12 Microscope (FEI) equipped with a LaB6 filament operated at 120 kV. Images were collected at 50,000 × magnification with a 2.2 Å/pixel spacing and 1.0–1.3 A defocus range on a 4k × 4k CCD camera (Gatan). Particle images were selected and extracted from micrographs, subsequently phase-corrected from the estimated CTF parameters using EMAN2 software. 2D reference free alignment and classification was then performed using the SPIDER software package. A set of 15 class averages representing ~ 1500 particles for each BAG3 concentration were used to measure the longest dimension observed as well as the distance perpendicular to obtain an average size of the particles.

- Chaperone assays

The steady-state ATPase activity of Hsc70 was measured by malachite green and the refolding of chemically denatured firefly luciferase was measured by recovered luminescence, as previously reported [50]. Hsc70 was used at 1 µM. DnaJA2 was used at 0.5 µM and ATP at 1 mM. In the ATPase experiments, results were normalized to the signal from Hsc70 and DnaJA2 with 30 nM BAG3 (100%). In the luciferase refolding experiments, results were normalized to the luminescence signal produced by addition of Hsc70 and DnaJA2 alone (100%). At these concentrations and incubation times, this value represents only ~ 40% of the total luminescence signal that can be recovered. We selected these conditions to allow for BAG3 and Hsp22 to have the possibility of further improving the refolding activity.

- **2.6 References**

1. F.U. Hartl, A. Bracher, M. Hayer-Hartl, *Molecular chaperones in protein folding and proteostasis* Nature, 475 (2011), pp. 324-332
2. V. Prahlad, R.I. Morimoto, *Integrating the stress response: lessons for neurodegenerative diseases from C. elegans* Trends Cell Biol., 19 (2009), pp. 52-61
3. E.R. Zuiderweg, E.B. Bertelsen, A. Rousaki, M.P. Mayer, J.E. Gestwicki, A. Ahmad*, Allostery in the Hsp70 chaperone proteins* Top. Curr. Chem., 328 (2013), pp. 99-153
4. K.A. Krukenberg, T.O. Street, L.A. Lavery, D.A. Agard *Conformational dynamics of the molecular chaperone Hsp90* Q. Rev. Biophys., 44 (2011), pp. 229-255
5. H.H. Kampinga, E.A. Craig *The HSP70 chaperone machinery: J proteins as drivers of functional specificity* Nat. Rev. Mol. Cell Biol., 11 (2010), pp. 579-592
6. H.H. Kampinga, J. Hageman, M.J. Vos, H. Kubota, R.M. Tanguay, E.A. Bruford, et al., *Guidelines for the nomenclature of the human heat shock proteins Cell Stress Chaperones*, 14 (2009), pp. 105-111
7. J.C. Bardwell, E.A. Craig *Major heat shock gene of Drosophila and the Escherichia coli heat-inducible dnaK gene are homologous* Proc. Natl. Acad. Sci. U. S. A., 81 (1984), pp. 848-852
8. W.R. Boorstein, T. Ziegelhoffer, E.A. Craig *Molecular evolution of the HSP70 multigene family* J. Mol. Evol., 38 (1994), pp. 1-17
9. O. Genest, J.R. Hoskins, A.N. Kravats, S.M. Doyle, S. Wickner *Hsp70 and Hsp90 of E. coli directly interact for collaboration in protein remodeling* J. Mol. Biol., 427 (2015), pp. 3877-3889
10. H. Nakamoto, K. Fujita, A. Ohtaki, S. Watanabe, S. Narumi, T. Maruyama, et al. *Physical interaction between bacterial heat shock protein (Hsp) 90 and Hsp70 chaperones mediates their cooperative action to refold denatured proteins* J. Biol. Chem., 289 (2014), pp. 6110-6119
11. F. Seyffer, E. Kummer, Y. Oguchi, J. Winkler, M. Kumar, R. Zahn, et al. *Hsp70 proteins bind Hsp100 regulatory M domains to activate AAA + disaggregase at aggregate surfaces* Nat. Struct. Mol. Biol., 19 (2012), pp. 1347-1355
12. A.B. Schmid, S. Lagleder, M.A. Grawert, A. Rohl, F. Hagn, S.K. Wandinger, et al. *The architecture of functional modules in the Hsp90 co-chaperone Sti1/Hop* EMBO J., 31 (2012), pp. 1506-1517

13.   E. Kirschke, D. Goswami, D. Southworth, P.R. Griffin, D.A. Agard *Glucocorticoid receptor function regulated by coordinated action of the Hsp90 and Hsp70 chaperone cycles* Cell, 157 (2014), pp. 1685-1697

14.   W.B. Pratt, Y. Morishima, M. Murphy, M. Harrell *Chaperoning of glucocorticoid receptors* Handb. Exp. Pharmacol. (2006), pp. 111-138

15.   B.D. Johnson, R.J. Schumacher, E.D. Ross, D.O. Toft *Hop modulates Hsp70/Hsp90 interactions in protein folding* J. Biol. Chem., 273 (1998), pp. 3679-3686

16.   H. Wegele, S.K. Wandinger, A.B. Schmid, J. Reinstein, J. Buchner *Substrate transfer from the chaperone Hsp70 to Hsp90* J. Mol. Biol., 356 (2006), pp. 802-811

17.   S. Alvira, J. Cuellar, A. Rohl, S. Yamamoto, H. Itoh, C. Alfonso, et al. *Structural characterization of the substrate transfer mechanism in Hsp70/Hsp90 folding machinery mediated by Hop* Nat. Commun., 5 (2014), p. 5484

18.   G. Morrow, L.E. Hightower, R.M. *Tanguay Small heat shock proteins: big folding machines* Cell Stress Chaperones, 20 (2015), pp. 207-212

19.   G. Kappe, E. Franck, P. Verschuure, W.C. Boelens, J.A. Leunissen, W.W. de Jong *The human genome encodes 10 alpha-crystallin-related small heat shock proteins: HspB1–10* Cell Stress Chaperones, 8 (2003), pp. 53-61

20.   E. Basha, G.J. Lee, L.A. Breci, A.C. Hausrath, N.R. Buan, K.C. Giese, et al. *The identity of proteins associated with a small heat shock protein during heat stress in vivo indicates that these chaperones protect a wide range of cellular functions* J. Biol. Chem., 279 (2004), pp. 7566-7575

21.   M. Haslbeck, E. Vierling A first line of stress defense: small heat shock proteins and their function in protein homeostasis J. Mol. Biol., 427 (2015), pp. 1537-1548

22.   A. Mainz, J. Peschek, M. Stavropoulou, K.C. Back, B. Bardiaux, S. Asami, et al. *The chaperone alphaB-crystallin uses different interfaces to capture an amorphous and an amyloid client* Nat. Struct. Mol. Biol., 22 (2015), pp. 898-905

23.   K.K. Kim, R. Kim, S.H. *Kim Crystal structure of a small heat-shock protein* Nature, 394 (1998), pp. 595-599

24.   R.L. van Montfort, E. Basha, K.L. Friedrich, C. Slingsby, E. Vierling *Crystal structure and assembly of a eukaryotic small heat shock protein* Nat. Struct. Biol., 8 (2001), pp. 1025-1030

25.   G.K. Hochberg, H. Ecroyd, C. Liu, D. Cox, D. Cascio, M.R. Sawaya, et al. *The structured core domain of alphaB-crystallin can prevent amyloid fibrillation and associated toxicity* Proc. Natl. Acad. Sci. U. S. A., 111 (2014), pp. E1562-E1570

26.   N. Braun, M. Zacharias, J. Peschek, A. Kastenmuller, J. Zou, M. Hanzlik, et al. *Multiple molecular architectures of the eye lens chaperone alphaB-crystallin elucidated by a triple hybrid approach* Proc. Natl. Acad. Sci. U. S. A., 108 (2011), pp. 20491-20496

27.   S.Y. Pasta, B. Raman, T. Ramakrishna, M. Rao Ch, *The IXI/V motif in the C-terminal extension of alpha-crystallins: alternative interactions and oligomeric assemblies* Mol. Vis., 10 (2004), pp. 655-662

28.   S. Jehle, B.S. Vollmar, B. Bardiaux, K.K. Dove, P. Rajagopal, T. Gonen, et al. *N-terminal domain of alphaB-crystallin provides a conformational switch for multimerization and structural heterogeneity* Proc. Natl. Acad. Sci. U. S. A., 108 (2011), pp. 6409-6414

29.   S. Studer, M. Obrist, N. Lentze, F. Narberhaus *A critical motif for oligomerization and chaperone activity of bacterial alpha-heat shock proteins* Eur. J. Biochem., 269 (2002), pp. 3578-3586

30. A.P. Arrigo *Human small heat shock proteins: protein interactomes of homo- and hetero-oligomeric complexes: an update* FEBS Lett., 587 (2013), pp. 1959-1969

31. M.P. Bova, H.S. McHaourab, Y. Han, B.K. Fung *Subunit exchange of small heat shock proteins. Analysis of oligomer formation of alphaA-crystallin and Hsp27 by fluorescence resonance energy transfer and site-directed truncations* J. Biol. Chem., 275 (2000), pp. 1035-1042

32. J.A. Aquilina, J.L. Benesch, O.A. Bateman, C. Slingsby, C.V. Robinson *Polydispersity of a mammalian chaperone: mass spectrometry reveals the population of oligomers in alphaB-crystallin* Proc. Natl. Acad. Sci. U. S. A., 100 (2003), pp. 10611-10616

33. L.N. Makley, K.A. McMenimen, B.T. DeVree, J.W. Goldman, B.N. McGlasson, P. Rajagopal, et al. *Pharmacological chaperone for alpha-crystallin partially restores transparency in cataract models* Science, 350 (2015), pp. 674-677

34. R. Shashidharamurthy, H.A. Koteiche, J. Dong, H.S. McHaourab *Mechanism of chaperone function in small heat shock proteins: dissociation of the HSP27 oligomer is required for recognition and binding of destabilized T4 lysozyme* J. Biol. Chem., 280 (2005), pp. 5281-5289

35. K.C. Giese, E. Vierling *Changes in oligomerization are essential for the chaperone activity of a small heat shock protein in vivo and in vitro* J. Biol. Chem., 277 (2002), pp. 46310-46318

36. T. Stromer, M. Ehrnsperger, M. Gaestel, J. Buchner *Analysis of the interaction of small heat shock proteins with unfolding proteins* J. Biol. Chem., 278 (2003), pp. 18015-18021

37. F. Sobott, J.L. Benesch, E. Vierling, C.V. Robinson *Subunit exchange of multimeric protein complexes. Real-time monitoring of subunit exchange between small heat shock proteins by using electrospray mass spectrometry* J. Biol. Chem., 277 (2002), pp. 38921-38929

38. F. Stengel, A.J. Baldwin, A.J. Painter, N. Jaya, E. Basha, L.E. Kay, et al *Quaternary dynamics and plasticity underlie small heat shock protein chaperone function* Proc. Natl. Acad. Sci. U. S. A., 107 (2010), pp. 2007-2012

39. B. Jovcevski, M.A. Kelly, A.P. Rote, T. Berg, H.Y. Gastall, J.L. Benesch, et al. *Phosphomimics destabilize Hsp27 oligomeric assemblies and enhance chaperone activity* Chem. Biol., 22 (2015), pp. 186-195

40. J. Peschek, N. Braun, J. Rohrberg, K.C. Back, T. Kriehuber, A. Kastenmuller, et al. *Regulated structural transitions unleash the chaperone activity of alphaB-crystallin* Proc. Natl. Acad. Sci. U. S. A., 110 (2013), pp. E3780-E3789

41. R.B. Nahomi, M.A. DiMauro, B. Wang, R.H. Nagaraj *Identification of peptides in human Hsp20 and Hsp27 that possess molecular chaperone and anti-apoptotic activities* Biochem. J., 465 (2015), pp. 115-125

42. A.P. Arrigo, B. Gibert *HspB1 dynamic phospho-oligomeric structure dependent interactome as cancer therapeutic target* Curr. Mol. Med., 12 (2012), pp. 1151-1163

43. M.J. Welsh, M. Gaestel *Small heat-shock protein family: function in health and disease* Ann. N. Y. Acad. Sci., 851 (1998), pp. 28-35

44. P. Rajagopal, E. Tse, A.J. Borst, S.P. Delbecq, L. Shi, D.R. Southworth, et al. *A conserved histidine modulates HSPB5 structure to trigger chaperone activity in response to stress-related acidosis* eLife, 4 (2015)

45. T. Fleckenstein, A. Kastenmuller, M.L. Stein, C. Peters, M. Daake, M. Krause, et al. *The chaperone activity of the developmental small heat shock protein Sip1 is regulated by pH-dependent conformational changes* Mol. Cell, 58 (2015), pp. 1067-1078

46. J. Winkler, J. Tyedmers, B. Bukau, A. Mogk *Chaperone networks in protein disaggregation and prion propagation* J. Struct. Biol., 179 (2012), pp. 152-160

47. S.K. Calderwood, J. Gong *Heat shock proteins promote cancer: it's a protection racket* Trends Biochem. Sci. (2016)

48. D. Brehmer, S. Rudiger, C.S. Gassler, D. Klostermeier, L. Packschies, J. Reinstein, et al. *Tuning of chaperone activity of Hsp70 proteins by modulation of nucleotide exchange* Nat. Struct. Biol., 8 (2001), pp. 427-432

49. H. Rampelt, M.P. Mayer, B. Bukau *Nucleotide exchange factors for Hsp70 chaperones* Methods Mol. Biol., 787 (2011), pp. 83-91

50. J.N. Rauch, J.E. Gestwicki *Binding of human nucleotide exchange factors to heat shock protein 70 (Hsp70) generates functionally distinct complexes in vitro* J. Biol. Chem., 289 (2014), pp. 1402-1414

51. M. Iwasaki, R. Tanaka, A. Hishiya, S. Homma, J.C. Reed, S. Takayama *BAG3 directly associates with guanine nucleotide exchange factor of Rap1, PDZGEF2, and regulates cell adhesion* Biochem. Biophys. Res. Commun., 400 (2010), pp. 413-418

52. A. Ulbricht, F.J. Eppler, V.E. Tapia, P.F. van der Ven, N. Hampe, N. Hersch, et al. *Cellular mechanotransduction relies on tension-induced and chaperone-assisted autophagy* Curr. Biol., 23 (2013), pp. 430-435

53. T.A. Colvin, V.L. Gabai, J. Gong, S.K. Calderwood, H. Li, S. Gummuluru, et al. *Hsp70–Bag3 interactions regulate cancer-related signaling* networks Cancer Res., 74 (2014), pp. 4731-4740

54. H. Doong, J. Price, Y.S. Kim, C. Gasbarre, J. Probst, L.A. Liotta, et al. *CAIR-1/BAG-3 forms an EGF-regulated ternary complex with phospholipase C-gamma and Hsp70/Hsc70* Oncogene, 19 (2000), pp. 4385-4395

55. M. Fuchs, D.J. Poirier, S.J. Seguin, H. Lambert, S. Carra, S.J. Charette, et al. Identification of the key structural motifs involved in HspB8/HspB6–Bag3 interaction Biochem. J., 425 (2010), pp. 245-255

56. S. Carra, S.J. Seguin, J. Landry *HspB8 and Bag3: a new chaperone complex targeting misfolded proteins to macroautophagy* Autophagy, 4 (2008), pp. 237-239

57. A. Hishiya, M.N. Salman, S. Carra, H.H. Kampinga, S. Takayama *BAG3 directly interacts with mutated alphaB-crystallin to suppress its aggregation and toxicity* PLoS One, 6 (2011), Article e16828

58. F.A. van de Klundert, R.H. Smulders, M.L. Gijsen, R.A. Lindner, R. Jaenicke, J.A. Carver, et al. *The mammalian small heat-shock protein Hsp20 forms dimers and is a poor chaperone* Eur. J. Biochem., 258 (1998), pp. 1014-1021

59. J.R. Theriault, H. Lambert, A.T. Chavez-Zobel, G. Charest, P. Lavigne, J. Landry *Essential role of the NH2-terminal WD/EPF motif in the phosphorylation-activated protective function of mammalian Hsp27* J. Biol. Chem., 279 (2004), pp. 23463-23471

60. J.A. Aquilina, J.L. Benesch, L.L. Ding, O. Yaron, J. Horwitz, C.V. Robinson *Subunit exchange of polydisperse proteins: mass spectrometry reveals consequences of alphaA-crystallin truncation* J. Biol. Chem., 280 (2005), pp. 14485-14491

61. M. Haslbeck, T. Franzmann, D. Weinfurtner, J. Buchner *Some like it hot: the structure and function of small heat-shock proteins* Nat. Struct. Mol. Biol., 12 (2005), pp. 842-846

62.	A. Mogk, C. Schlieker, K.L. Friedrich, H.J. Schonfeld, E. Vierling, B. Bukau *Refolding of substrates bound to small Hsps relies on a disaggregation reaction mediated most efficiently by ClpB/DnaK* J. Biol. Chem., 278 (2003), pp. 31033-31042

63.	G.J. Lee, A.M. Roseman, H.R. Saibil, E. Vierling *A small heat shock protein stably binds heat-denatured model substrates and can maintain a substrate in a folding-competent state* EMBO J., 16 (1997), pp. 659-671

64.	M. Ehrnsperger, S. Graber, M. Gaestel, J. Buchner *Binding of non-native protein to Hsp25 during heat shock creates a reservoir of folding intermediates for reactivation* EMBO J., 16 (1997), pp. 221-229

65.	G.J. Lee, E. Vierling *A small heat shock protein cooperates with heat shock protein 70 systems to reactivate a heat-denatured protein* Plant Physiol., 122 (2000), pp. 189-198

66.	S. Chen, D.F. Smithv *Hop as an adaptor in the heat shock protein 70 (Hsp70) and hsp90 chaperone machinery* J. Biol. Chem., 273 (1998), pp. 35194-35200

67.	A.D. Thompson, K.M. Scaglione, J. Prensner, A.T. Gillies, A. Chinnaiyan, H.L. Paulson, et al. *Analysis of the tau-associated proteome reveals that exchange of Hsp70 for Hsp90 is involved in tau degradation* ACS Chem. Biol., 7 (2012), pp. 1677-1686

Chapter 3

A conserved histidine modulates HSPB5 structure to trigger chaperone activity in response to stress-related acidosis

- **3.1 Abstract**

Small heat shock proteins (sHSPs) are essential 'holdase' chaperones that form large assemblies and respond dynamically to pH and temperature stresses to protect client proteins from aggregation. While the alpha-crystallin domain (ACD) dimer of sHSPs is the universal building block, how the ACD transmits structural changes in response to stress to promote holdase activity is unknown. In collaboration with the lab of Rachel Klevit at the University of Washington, we found that the dimer interface of HSPB5 is destabilized over physiological pHs and a conserved histidine (His-104) controls interface stability and oligomer structure in response to acidosis. Destabilization by pH or His-104 mutation shifts the ACD from dimer to monomer but also results in a large expansion of HSPB5 oligomer states. Remarkably, His-104 mutant-destabilized oligomers are efficient holdases that reorganize into structurally distinct client–bound complexes. Our data support a model for sHSP function wherein cell stress triggers small perturbations that alter the ACD building blocks to unleash a cryptic mode of chaperone action.

- **3.2 Introduction**

Cells have numerous strategies to cope with the consequences of stress conditions that lead to protein misfolding and aggregation. Ineffective resolution of protein misfolding and unmitigated protein aggregation can lead to formation of plaques, fibrils, and other aggregated species encountered in neurodegenerative diseases. Generally, ATP-dependent chaperones such as Hsp70 and Hsp90 assist with protein refolding, while ATP-independent chaperones known as small heat shock proteins (sHSPs) act as first responders by maintaining proteins in soluble forms to inhibit misfolding and to delay aggregation. Under transcriptional regulation of the heat shock factor, Hsf1, levels of sHSPs can rise to 1% of total

---

[2] My contributions to this chapter were the SEC-MALS and negative stain EM analysis of the global architecture of HSPB5 and client binding. Contributions by members of the Klevit lab (University of Washington) are indicated in the figure legends

cellular protein when conditions deviate from the norm, e.g. ischemia, hypoxia, oncogene activation, and chemotherapy [1]. sHSPs are found throughout prokaryotes and eukaryotes. There are ten sHSPs encoded in the human genome (HSPB1, HSPB2, etc), ranging in size from 15 to 25 kDa. Most, including the ubiquitously expressed human sHSP HSPB5, form large assemblies that exist as dynamic distributions of polydisperse oligomers whose properties are both temperature and pH dependent [2]. Which form or forms of an sHSP are active and how they function are central unanswered questions. In addition, how sHSPs interact with partly unfolded or aggregate-prone proteins ('clients') to prevent formation of aggregates remains enigmatic.

Some acute cellular stresses are associated with acidosis. For example, measurements in mouse brain following ischemic stroke showed a pH of 6.4 in ischemic tissue compared to a pH of 7.0 in normal tissue [3]. A decrease in cellular pH may give rise to destabilization of some proteins and/or a decrease in solubility for proteins with pI values between pH 6 and 7. Furthermore, the pH in normal eye lens fiber cells, which contain extremely high concentrations of the sHSPs HSPB4 and HSPB5 is ~6.5 [4, 5]. Such observations raise the question as to the nature and determinants of pH-dependent properties of sHSPs in general and HSPB5 in particular.

Here, we report how pH affects structural, biochemical, and functional properties of HSPB5 (also known as αB-crystallin). Like all sHSPs, HSPB5 has a conserved central α-crystallin domain (ACD) flanked by variable N- and C-terminal regions. We carried out investigations both on the HSPB5-ACD, which forms the dimeric building block found in all sHSPs, and on full-length oligomeric HSPB5. We find that ACD dimer stability decreases over a narrow physiologically relevant pH range and we have identified a conserved histidine residue that is largely responsible for the observed destabilization. Surprisingly, the histidine is not on the dimer interface but its mutation to glutamine or lysine partly or fully recapitulates low pH behavior both in the context of the ACD dimer and in oligomers. The mutant proteins allowed us to probe the consequences of dimer interface destabilization without additional complicating factors that arise when comparing experiments performed at differing pH. Mutations that destabilize the dimer interface produce extremely large oligomers that can rearrange to form long-lived complexes with a model client protein. Our studies unmask a cryptic mode of HSPB5/client interaction not previously detected using the wild-type protein under non-stress conditions. The results highlight mechanistic differences in the ways in which holdases work and suggest that HSPB5 has a repertoire of ways in which it can carry out its function.

- **3.3 Results**

- **3.3.1 NMR solution structure and ^{15}N relaxation reveal conformational plasticity in HSPB5-ACD**

As ACD dimers are the fundamental, stably folded building blocks of sHSP oligomers, we first sought to define their response to changes in pH over a physiologically relevant range. Although multiple structures have been solved for HSPB5-ACD, there are differences among them as well as differences in the conditions under which the structures were obtained (i.e., pH 4.6, 6.0, 7.5, 8.5, 9.0) [6]. We felt this situation necessitated structure determination under solution conditions relevant to our studies. The solution structure of HSPB5-ACD at pH 7.5, 22°C (Figure 3.1 A,B) was calculated from NMR data that included backbone and side chain chemical shifts, NOEs, and RDCs. As in all previously determined HSPB5-ACD dimer structures (PDB 2WJ7, 3L1G, 2KLR, 2Y22, 4M5S, and 4M5T), each subunit adopts a six-stranded β-sandwich structure and two ACDs form a dimer through anti-parallel alignment of their long β6+7 strands (Figure 3.1 A,B,C). A notable difference among solved sHSP ACD structures is that dimers appear in different alignments of the two β6+7 strands [6, 7]. In the solution structure reported here, the dimer interface places Glu117 across from Glu117' (Figure 3.1D). This register is observed in all but two of the available HSPB5-ACD structures and is also the predominant alignment observed in other metazoan sHSP ACD structures.
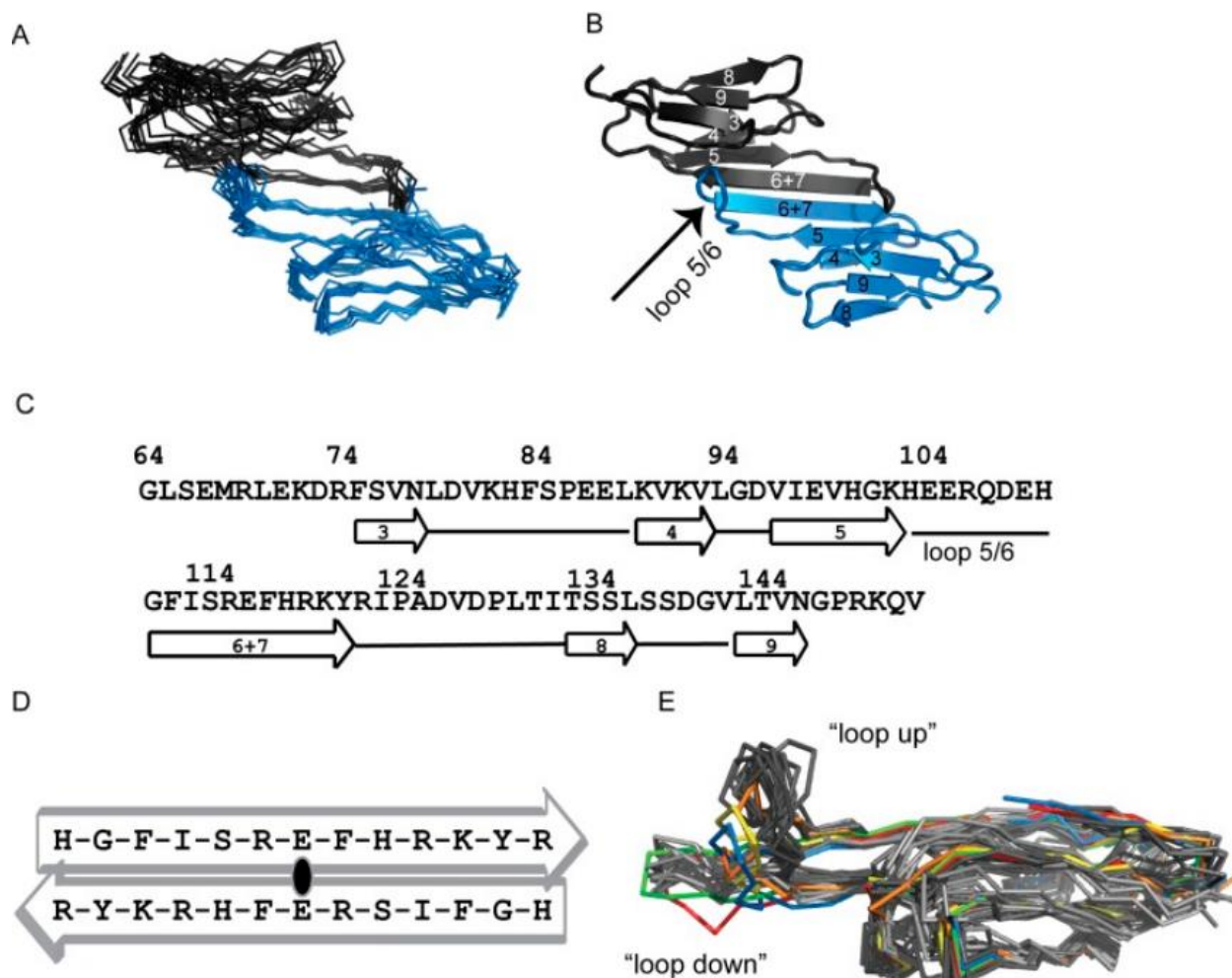
Figure 3.1 Solution structure ensemble of HSPB5-ACD at pH 7.5 is an anti-parallel dimer. A) Backbone traces of ten ACD structures determined by RosettaOligomer are aligned over all residues (RMSD of 1.4 Å). Subunits of the dimer are shown in blue and gray. B) Cartoon representation of one member of the HSPB5-ACD ensemble is shown. The six strands of the β-sandwich structure are labeled using previously defined nomenclature for ACD structures. The dimer is formed by antiparallel arrangement of the β6+7 strands at the interface. Loop 5/6 is highlighted in the blue subunit. (C) The sequence of the ACD construct for which the solution structure was solved is shown with elements of secondary structure highlighted. (D) The alignment of the β6+7 strands at the dimer interface, shown schematically, places Glu-117 across from Glu-117'. This alignment is called 'APII' in previous reports (Clark et al., 2011). (E) Overlay of protomers from all available HSPB5-ACD structures. All members of the solution NMR structure (this paper; PDB 2N0K) and the solid-state NMR structure (2KLR; Jehle et al., 2010) are shown in dark gray and light gray, respectively. Five crystal structures are shown: (1) 2WJ7 (yellow), (2) 3L1G (orange), (3) 4M5S (green), (4) 4M5T (red), and (5) 2Y22 (blue). These experiments and figures were performed and created by Rajagopal P (Klevit laboratory, University of Washington).

At the level of the protomers, the HSPB5-ACD structures are remarkably similar despite having been solved under significantly different conditions and by different techniques (Figure 3.1E). Two NMR ensembles (solution-state reported here and solid-state PDB 2KLR) and five crystal structures all overlay well with the exception of the loop that connects β5 and β6+7 (called Loop 5/6; residues His-104–Gly-112). Loop 5/6 curves upwards in our solution ensemble (pH 7.5) and in three crystal structures (2WJ7

[pH 9.0], 3L1G [pH 4.6], and 2Y22 [pH 8.6]). In the 'loop up' conformation, Loop 5/6 residues make contacts across the dimer interface to the other subunit. In contrast, Loop 5/6 curves slightly downwards in the solid-state NMR ensemble (2KLR; pH 7.5) and in two crystal structures (4M5S [pH 6.0]; 4M5T [pH 6.5]). Thus, among structures solved between pH 6.5 and 7.5, both loop conformations have been observed, suggesting that the loop is dynamic in the physiological pH range.

To investigate dynamic processes in the HSPB5-ACD, we performed ^{15}N relaxation measurements. A majority of backbone amide nitrogens have ^{15}N T2 values between 30 and 40 ms, but resonances in Loop 5/6 and the dimer interface have T2 < 30 ms, indicating they undergo a change in their environment in the millisecond timescale (data not shown). To better probe this time regime, we performed NMR ^{15}N relaxation-compensated CPMG relaxation dispersion measurements under the solution structure conditions (700 μM ACD at pH 7.5, 22°C). Examples of relaxation curves obtained from spectra collected at two magnetic field strengths (600 and 800 MHz) are shown in Figure 3.2A. Twenty resonances gave curves that could be analyzed; of these, half are well fit by a two-state model (χ_{red}^2; reduced chi-square < 10; Figure 3.2). This indicates that the ACD dimer is exchanging between a major species (i.e., the one revealed in the solution structure ensemble) and one or more minor species. The nature of the minor species will be discussed below. Values for k_{ex}, the rate of exchange, for individual resonances ranged between 760 s^{-1} and 1119 s^{-1}. The less than two-fold difference for the range of values obtained from fitting data for individual resonances suggests that the residues that exhibit exchange could be involved in the same dynamic phenomenon. The residues that undergo exchange are along the dimer interface and in Loop 5/6 (Figure 3.2B). These findings are consistent with the apparent plasticity of the dimer interface and Loop 5/6 inferred from crystal structures of the ACD dimer. Analysis of available HSPB5-ACD structures and NMR relaxation data combined indicate that (1) the HSPB5 protomer structure is retained over a wide pH range and (2) there are two regions of plasticity, namely the dimer interface and Loop 5/6.
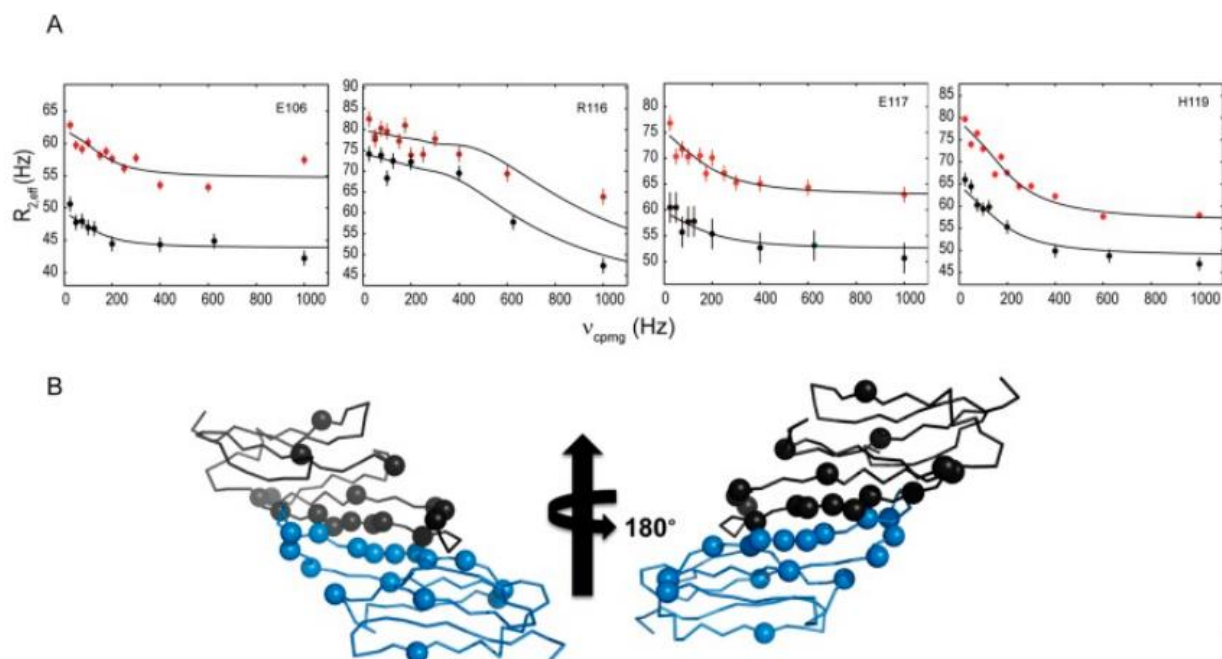
Figure 3.2 ^{15}N-CPMG relaxation dispersion experiments detect dimer-to-monomer exchange. A) Relaxation dispersion measurements reveal a two-state transition. Representative relaxation dispersion curves of ^{15}N transverse relaxation rate (R2,$_{eff}$) plotted as a function of field strength, (ν_{CPMG}) are shown (see Materials and methods for details). Data were recorded at static field strengths of 800 MHz (red) and 600 MHz (black) at pH 7.5 and 22°C. Values of k$_{ex}$, δω, and pb were extracted using the program, GUARDD. B) Backbone representation of HSPB5-ACD dimer is shown with the Cα atoms of exchanging residues that are well fit by a two-state model shown as spheres. Resonances showing relaxation rates in the range 760 s^{-1} to 1119 s^{-1} occur mainly at the dimer interface and in Loop 5/6. These experiments and figures were performed and created by Rajagopal P (Klevit laboratory, University of Washington).

- ### 3.3.2 HSPB5-ACD undergoes pH-dependent dimer dissociation

To assess thermodynamic stability of the ACD dimer, dimer–monomer dissociation constants were determined from isothermal titration calorimetry dilution measurements in which highly concentrated ACD was titrated into buffer. The resulting isotherms fit a simple dimer-monomer equilibrium model. We made measurements at two physiological pH values, pH 7.5 and pH 6.5 (25°C), and obtained dissociation constants of 2 ± 2 μM and 30 ± 16 μM, respectively. The value at pH 7.5 is in excellent agreement with the value of 2 μM inferred from tandem MS/MS measurements performed at the same pH [8]. The dimer is also destabilized by an increase in temperature, with a K$_D$ of 36 ± 2 μM at pH 7.5, 37°C. Thus, the HSPB5-ACD dimer is destabilized by either a decrease in pH from 7.5 to 6.5 or an increase in temperature from 25°C to 37°C.
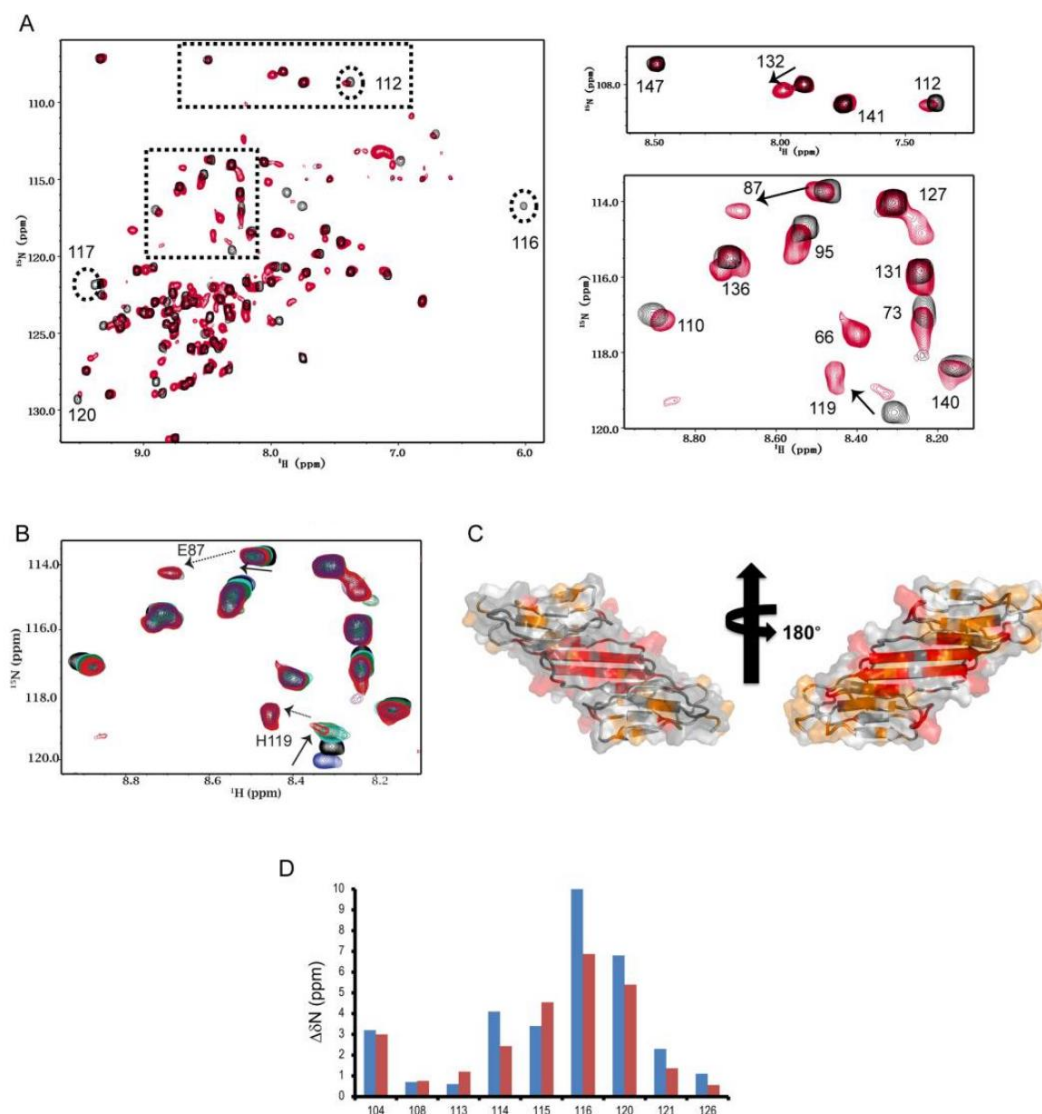
Figure 3.3 HSPB5-ACD undergoes a conformational transition between pH 7.5 and 6.5. A) ^1H-^{15}N HSQC spectra acquired on a 200 μM sample of HSPB5-ACD at pH 7.5 and 6.5 (22°C) reveal two states. Full spectra collected at pH 7.5 (black) and 6.5 (red) are overlaid (left). At pH 7.5, 82/85 non-proline residues are observed (residues G64, L65, and S139 are not detected due to fast exchange with H_2O). At pH 6.5, approximately ~65 additional peaks appear, indicating the presence of two conformations. Boxed regions shown on the right provide clear examples of peak doubling. Some resonances (labeled in the panel on the left) disappear from their original positions at pH 7.5 and their new positions could not be determined by inspection of the spectrum at pH 6.5. B) Example of a full pH titration series (spectra collected at pH 8.4 [blue], 7.5 [black], 7.0 [cyan], 6.7 [green], and 6.5 [red]). The behavior of the resonance of H119 as a function of pH illustrates two pH-dependent processes (see text). Its chemical shift is in fast exchange from pH 8.4 to 7.5 (solid arrow) and changes direction and is in slow exchange from pH 7.0 to 6.5 (dashed arrow). The region shown contains several other resonances that undergo slow-exchange transitions over the same pH range. C) Residues that undergo the slow exchange transition are highlighted in color on a surface representation of the ACD dimer. Residues with perturbations > 0.2 ppm are red; those with perturbations between 0.1 - 0.2 ppm are orange. D) Analysis of relaxation dispersion data yields the difference in ^{15}N chemical shift between the major and minor species ($\Delta\delta N_{calc}$). The values of $\Delta\delta N_{calc}$ (blue) are compared to the experimental values obtained from the difference of ^{15}N chemical shifts at pH 7.5 and 6.5, i.e., $\Delta\delta N^{(7.5-6.5)}$ (red), in the histogram. Concordance between these two parameters supports the notion that the minor form detected by relaxation dispersion experiments is the monomeric form of ACD that is populated at lower pH. These experiments and figures were performed and created by Rajagopal P (Klevit laboratory, University of Washington).

^{1}H, ^{15}N-HSQC spectra of HSPB5-ACD collected at pH 7.5 and 6.5 show extensive changes (Figure 3.3A). Furthermore, spectra collected between pH 7.0 and pH 6.0 had significant peak doubling which is mostly resolved at pH 6.0, making analysis of the pH-induced spectral changes based solely on existing resonance assignments at pH 7.5 [9] challenging. Therefore, we assigned the HSPB5-ACD spectum at pH 6.5 using standard triple resonance spectra collected at both pH 6.5 and pH 6.0 so that we could follow individual resonances through a pH titration series. An expanded region of the ^{1}H, ^{15}N HSQC pH series is shown in Figure 3.3B. In the absence of another pH-dependent process, resonances arising from residues that undergo a protonation/deprotonation event as a function of pH will shift in a continuous manner. Resonances from residues that are proximal to titrating residues will also show similar behavior. Such processes will appear in the so-called 'fast-exchange' NMR regime due to the rapid on/off rate of acidic protons. At pH values above 6.7, some resonances in the HSPB5-ACD spectrum exhibit fast-exchange pH behavior, consistent with protonation/deprotonation of ionizable groups. This behavior is illustrated by the resonance for His-119 in spectra collected at pH 6.7 and above (Figure 3.3B). At pH < 6.7, some resonances double and appear in a new position (for example, resonances labeled 87, 119, and 135 in Figure 3.3B). Such behavior exemplifies intermediate-to-slow exchange and is indicative of the existence of two states that interconvert slowly on the NMR timescale. The relative intensities of the peaks reflect the relative population of the two states, so a new species of HSPB5-ACD is increasingly populated as the pH decreases.

Spectral assignments at pH 7.5 and 6.5 allowed identification of residues most affected by the pH-dependent transition. The chemical shift difference between the 'high' pH form (pH 7.5) and the 'low' pH form (pH 6.5), $\Delta\delta$(pH7.5–pH6.5) was calculated for each NH resonance (see 'Materials and methods'). Resonances that exhibit large chemical shift perturbations (>0.2 ppm) and/or change trajectory during the titration mainly arise from two structural regions (colored red in Figure 3.3C): the dimer interface (residues F113–I124) and Loop 5/6. In light of the pH-dependent K_D values obtained by ITC, the dissociation of dimers to monomers is a likely source of the slow exchange process observed in NMR spectra below pH 7.

The above findings raised the possibility that the minor species detected by relaxation dispersion at pH 7.5 is an ACD monomer. In addition to the exchange rate, the fractional population of the minor species (pb = 1 − pa), and the chemical shift difference between the major and minor species for a given resonance ($\delta\omega$) can be extracted from analysis of relaxation dispersion data [10]. Seven resonances provided an estimate for the fractional population of the minor species, pb, as ~5%, in good agreement

with the value of 4% calculated from the K_D measured by ITC. We compared the predicted difference in ^{15}N chemical shift ($\delta\omega$) to the experimentally determined difference in chemical shifts between the ACD at pH 7.5 and at pH 6.5, $\Delta\delta N$(pH7.5- pH6.5). As seen in Figure 3.3D, there is remarkably close correspondence for dimer interface residues, supporting the notion that the minor species detected by relaxation dispersion at pH 7.5 is the same as the monomeric form populated as the pH decreases below 7.

Finally, we performed relaxation dispersion measurements at 37°C (pH 7.5) to determine the rates of association/dissociation at physiological temperature. For a dimer-to-monomer transition, the measured exchange rate will be concentration dependent:

$$\bullet \quad k_{ex}=k_{md}[\mathrm{monomer}]+k_{dm},$$

where k_{md} is the rate constant for monomer–dimer association and k_{dm} is the constant for dimer dissociation. We collected relaxation dispersion data at two protein concentrations (700 and 200 µM; pH 7.5, 37°C). Global fitting of relaxation dispersion data for residues in the dimer interface gave kex values of ~1500 s^{-1} and 460 s^{-1} at 700 and 200 µM HSPB5-ACD, respectively. The concentration dependence confirms that the observed exchange is due to dimer-monomer dissociation/association. Based on a K_D (=k_{dm}/k_{md}) of 36 µM, the concentration of ACD monomers at 700 µM ACD subunits is ~100 µM. This gives k_{md} = 1.1 × 107 M−1 s−1 (in the range for diffusion-controlled bimolecular association; [11]) and k_{dm} = 400 s−1. Thus, several NMR parameters plus ITC measurements provide a picture in which the long dimer interface dissociates at a rate of 400 s^{-1} at pH 7.5, 37°C and is destabilized as pH decreases below 7. Under the same conditions, full-length HSPB5 subunits in oligomers exchange much more slowly, at a rate of 10^{-3} s^{-1} [12]. Therefore, the rate at which subunits leave an oligomer is not determined by disruption of the ACD dimer and the results suggest that dimer interfaces within oligomers may break and reform many times during the residency of subunits within HSPB5 oligomers.
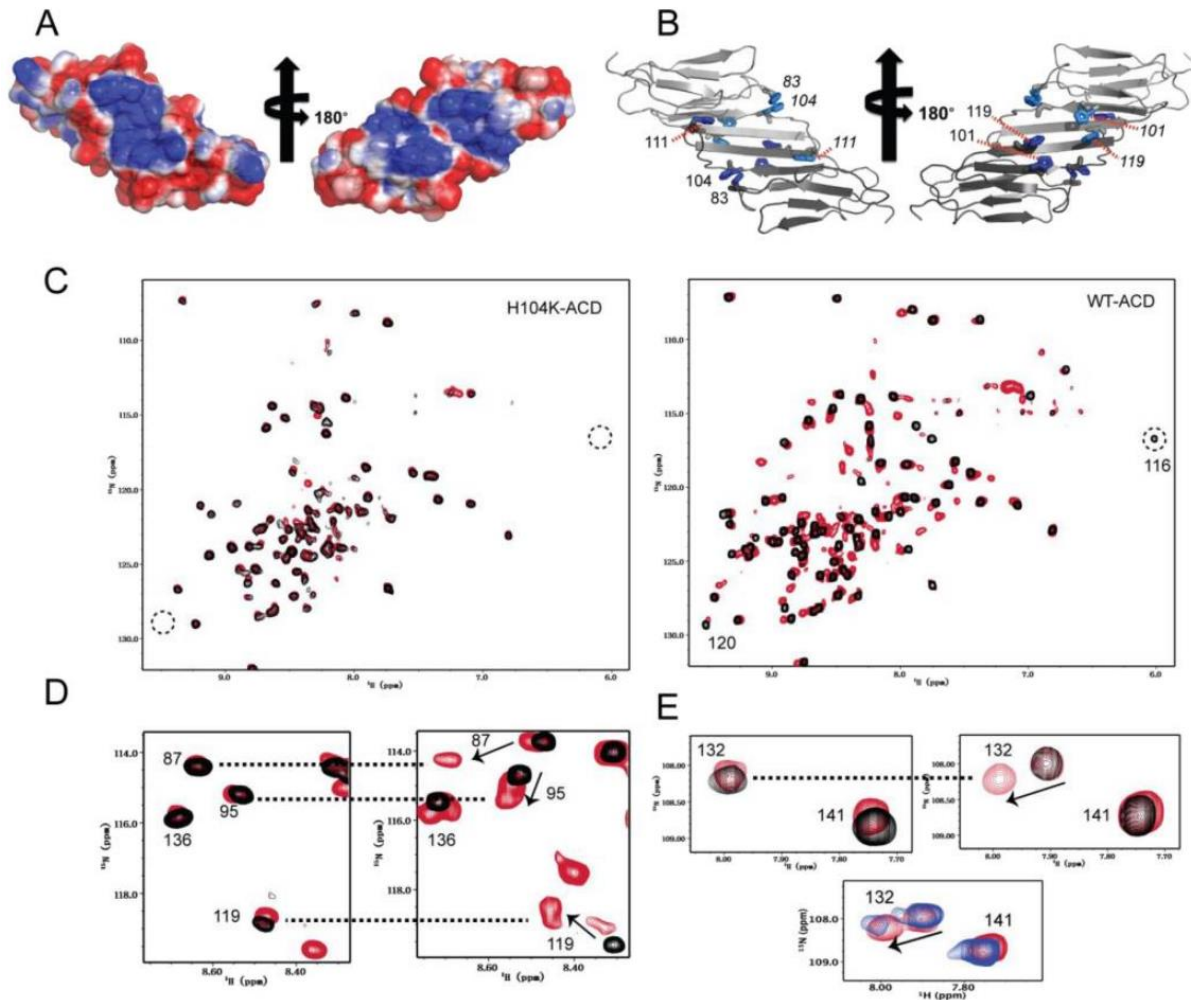
Figure 3.4 His-104 plays a key role in the dimer-monomer transition. A) The electrostatic surface of HSPB5-ACD at pH 7.5 (calculated using experimentally determined histidine pK_R values) reveals patches of positive (blue) and negative (red) charges that cross the dimer interface. B) The five histidines of HSPB5-ACD (blue and cyan sticks) occur as pairs and are located in proximity to the dimer interface. C) Mutation of His-104 shifts the dimer-monomer equilibrium as observed by NMR. Overlays of ^{1}H-^{15}N HSQC spectra at pH 7.5 (black) and pH 6.5 (red) are shown for H104K-ACD (left panel) and WT-ACD (right panel). A single set of peaks is observed in WT-ACD at pH 7.5, and peaks due to the monomer conformation appear as the pH is lowered. Peaks belonging to the dimer interface, e.g., R120 and R116 disappear from their original positions in WT-ACD at pH 6.5 and in H104K-ACD at both pH conditions (dotted circles). D, E) Expanded regions of ^{1}H-^{15}N HSQC spectra of WT-, H104K-, and H104Q-ACD. The same color scheme is used for WT- and H104K-ACD as in panel C; H104Q-ACD overlay is in blue (pH 7.5) and red (pH 6.5). D) Comparison of H104K-ACD (left panel) and WT-ACD (right panel). Dotted lines connect resonances in similar positions in H104K-ACD and WT-ACD. The example shows that the peaks for residues 87, 95, 119, and 136 have similar positions in H104K-ACD (at both pH values) as in WT-ACD at pH 6.5. E) Comparison of identical regions of spectra of H104K-ACD (top left panel), WT-ACD (top right panel), and H104Q-ACD (lower panel). Both forms (dimer and monomer) are observed in the H104Q-ACD spectrum at both pH values, whereas only peaks corresponding to the monomer are observed in H104K-ACD at both pH values. These experiments and figures were performed and created by Rajagopal P (Klevit laboratory, University of Washington).

- **3.3.3 A conserved histidine is responsible for destabilization of the HSPB5-ACD dimer**

The arrangement of the ACD dimer creates patches of positively and negatively charged surface that cross the dimer interface on both faces of the structure (Figure 3.4A). At pH 7.5 and 22°C where the dimer is more stable, the electrostatic forces are presumably in balance, but the high densities of like charges suggest the stability is tenuous. A protonation event or other rearrangement at or near the dimer interface may tip the balance and trigger dimer dissociation. HSPB5-ACD has a high histidine content, with five His residues out of 89 total residues, (5.6%, which is more than double the average His frequency across all proteomes). In the dimer structure, eight of ten histidine residues (five in each protomer) are located in pairs (two His-83/His-104 pairs and two His-101/His-119 pairs) and are concentrated towards the center of the dimer (Figure 3.4B). Overall, the organization and surface electrostatics suggested a possible role for histidine residues in triggering the pH-dependent dimer dissociation.

To identify candidate histidines, pKR values and tautomeric states were determined from NMR chemical shifts of imidazole ring nuclei (Nδ1, Nϵ2, Hδ2, and Hϵ1) measured as a function of pH. pK_R values were obtained for four of five His residues: His-101 and His-111 have low values of <6 and His-83 and His-119 have values of 6.6 and 7.7, respectively (Figure 3.4). A pK_R could not be determined for His-104 because its side chain resonances broaden and disappear at pH values below 7.5. Though His 104 is not positioned on the dimer interface, the behavior of its backbone NH resonance is similar to backbone NH resonances on the dimer interface undergoing exchange between dimer and monomer, indicating that it undergoes a change in environment as a result of the dimer-to-monomer transition. At pH 7.5 where its imidazole resonances are detectable, His-104 exists as the less common Nδ1H tautomer, while the other four His residues are in the more common Nϵ2H tautomer. A resonance is observed at a chemical shift of 12.4 ppm for the Nδ1H of His-104, indicating that it is hydrogen bonded. Among members of the solution ensemble, there are several potential H-bonding partners in proximity to His-104: the backbone carbonyls of His-83, Glu-105, and Glu-106 and side chain groups of Arg-107 and Arg-116 (Figure 3.4). Together, the data reveal that His-104 is in a specific conformation in the ACD dimer at pH 7.5 that is stabilized through an H-bond.

The sensitivity of His-104 resonances to the dimer-to-monomer transition suggested it as a prime candidate for the pH trigger. His-104 was substituted with either Gln or Lys and the mutant ACDs were

compared to WT-HSPB5-ACD. As discussed above (Figure 3.3A,B), peak doubling is observed in the spectrum of WT ACD below pH 7, with new peaks appearing at lower pH corresponding to ACD monomers. The ^{1}H-^{15}N HSQC spectrum of H104Q-ACD has peak doubling even at pH 7.5 and the two sets of peaks correspond to dimer and monomer peaks already assigned in the WT spectrum (Figure 3.4E, lower panel). The H104K-ACD HSQC spectrum has a single set of resonances under both pH conditions, but the peaks correspond to the monomer, even at pH 7.5 (Figure 3.4C–E). Thus, substitution of His-104 with glutamine destabilizes the dimer so that approximately equal populations are observed at pH 7.5 and NMR concentrations. Glutamine at position 104 would have difficulty mimicking the Nδ1H-bond formed by His-104. Substitution of His-104 with a positively charged lysine yields an ACD that is predominantly monomeric at pH 7.5. We did not determine K_D values for the mutants by dilution ITC experiments because the starting ACD concentration must be ten-fold above KD. Based on the relative populations of dimer and monomer peaks in the NMR spectra, we can estimate that the K_D for H104Q-ACD is ~100–500 µM (approximately equal populations of dimer and monomer at [ACD] = 200 µM) and the K_D for H104K-ACD is >1 mM (based on our inability to detect dimer resonances in samples containing 200 µM protein). Although only order-of-magnitude, these estimates reveal that substitution of His-104 with Gln or Lys destabilizes the dimer more than 100-fold. To ascertain whether the effect of mutating His-104 is specific, the other four His residues were each mutated to Gln. The mutant ACDs retained the pH-dependent spectral behavior of the WT-ACD (data not shown). Altogether, the data implicate His-104, which sits at the base of Loop 5/6 (Figure 3.4B), as a hotspot whose conformation, H-bonding capacity, and protonation state strongly affect the stability of the HSPB5-ACD dimer interface.

- **3.3.4 A destabilized dimer interface triggers a large expansion in HSPB5 oligomers**

To uncover consequences of dimer interface stability in HSPB5 oligomer structure, we compared properties of full-length H104Q- and H104K-HSPB5 with WT-HSPB5. Size exclusion chromatography combined with multi-angle light scattering (SEC-MALS) provided information on oligomer size and polydispersity and negative-stain electron microscopy (EM) allowed observation of single oligomeric particles (Figure 3.5). SEC-MALS data of WT-HSPB5 oligomers confirmed previously reported pH dependent changes in oligomeric dimension [2, 13]. At pH 7.5, the molecular weight (Mw) determined at intervals across the elution peak ranged from 440 kDa to 500 kDa. The average Mw of 465 kDa corresponds to the mass of ~24 subunits, consistent with previous reports [14, 15]. At pH 6.5, WT-HSPB5 oligomers elute earlier, with an average Mw of 720 kDa, corresponding to ~36 subunits per oligomer—an increase of 12 subunits on average per oligomer (Figure 3.5A).
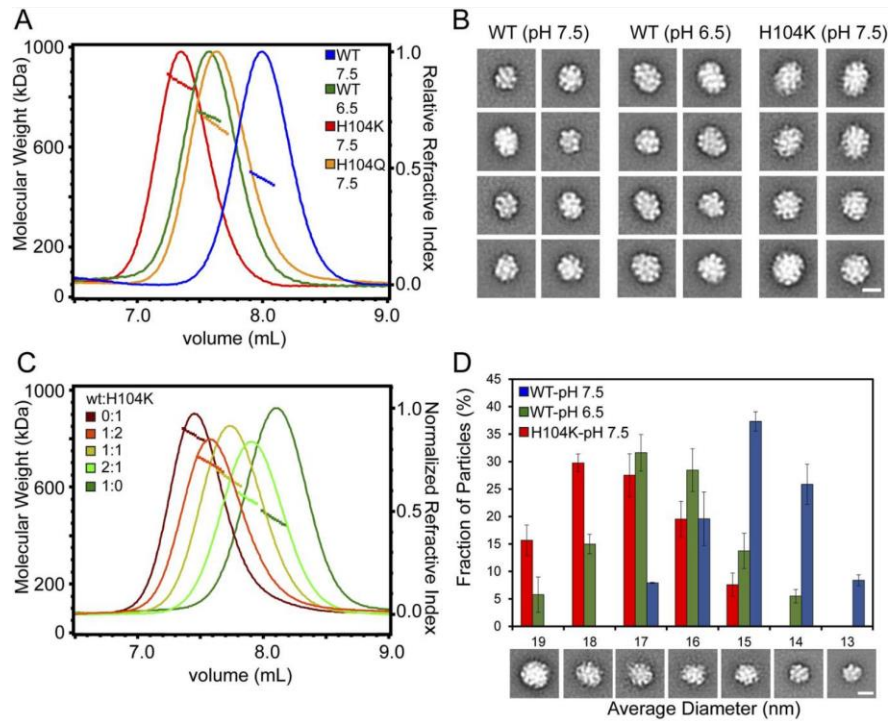
Figure 3.5 Destabilizing the ACD dimer interface via low pH or His-104 mutation triggers large expansion of HSPB5 oligomers. A) SEC-MALS analysis showing protein elution profile (refractive index, right Y-axis) with average M_w (horizontal trace under peak corresponds to left Y-axis) for WT-HSPB5 at pH 7.5 (blue) and pH 6.5 (green), and H104Q-HSPB5 (orange) and H104K-HSPB5 (red) at pH 7.5. B) 2D projection class averages showing representative ensemble of oligomer sizes. C) SEC-MALS analysis showing elution profile and average Mw of mixed oligomers of WT and H104K-HSPB5 incubated together at ratios of 1:0 (green), 2:1 (light green), 1:1 (yellow), 1:2 (orange), and 0:1 (dark red), respectively. D) Histogram of oligomer diameters showing fraction of oligomer particles vs average diameter (nm) for WT at pH 7.5 (blue) and pH 6.5 (green), and H104K at pH 7.5 determined by negative-stain EM 2D classification. Representative 2D class averages corresponding to measured diameter are shown. Experiments were performed in triplicate. Scale bar (lower left image) equals 10 nm.

Negative-stain EM micrographs and single particle images collected on WT-HSPB5 oligomers at pH 7.5 and 6.5 reveal large globular structures at both pHs (Figure 3.6). In 2D projection averages (generated by reference-free alignment of single particle data sets), WT-HSPB5 oligomers are generally spherical and have varied diameters that are on average greater at pH 6.5 than at pH 7.5 (Figure 3.5B, Figure 3.6B). Thus, SEC-MALS and EM measurements reveal an expansion in the hydrodynamic radius, particle dimensions, and number of subunits in WT-HSPB5 oligomers as a function of decreasing pH.
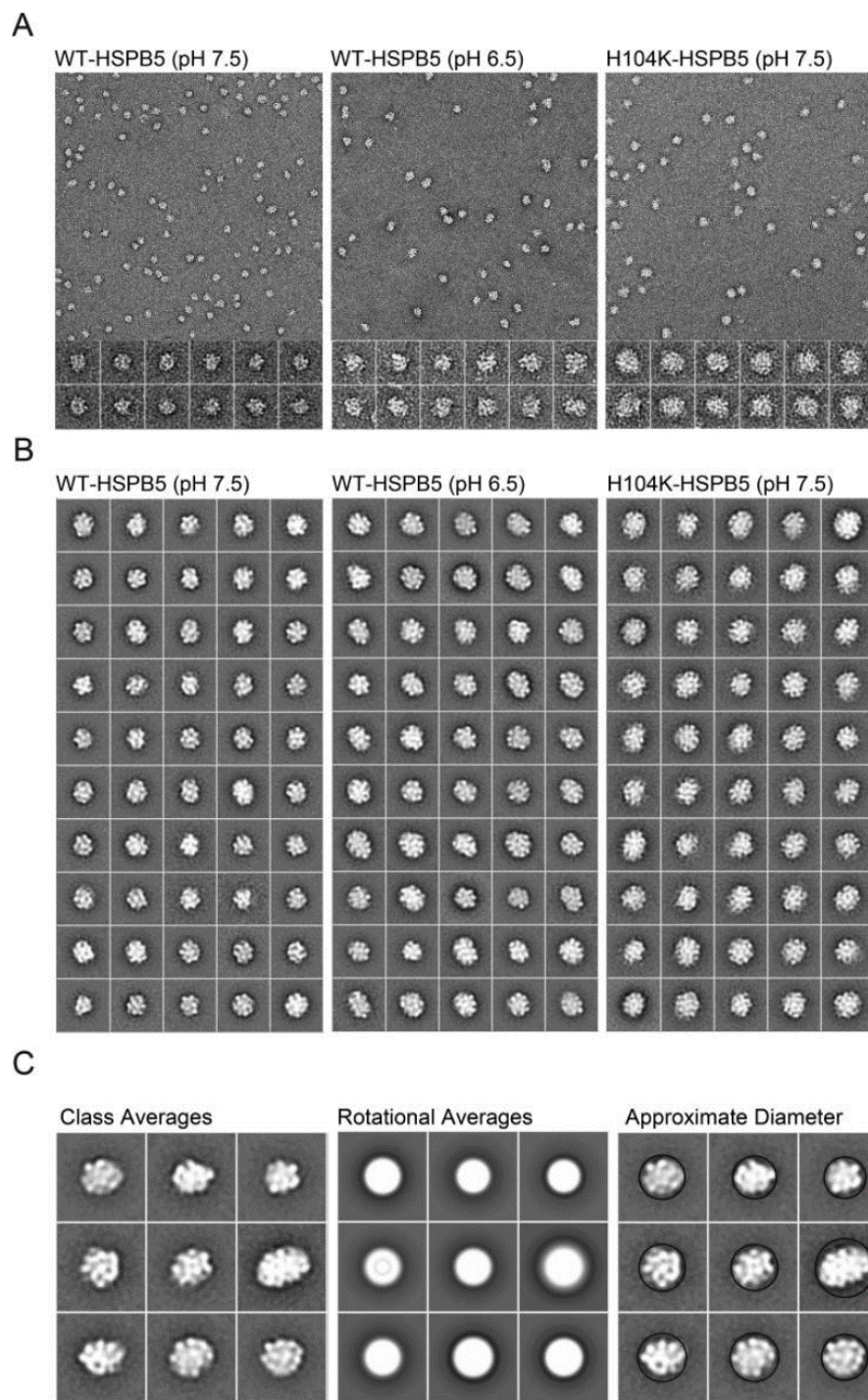
Figure 3.6 EM micrograph images, 2D classification, and particle diameter estimation for WT and H104K HSPB5. A) Representative micrograph images of WT-HSPB5 at pH 7.5 and 6.5 and H104K-HSPB5 at pH 7.5 negatively stained with 0.75% uranyl formate (scale bar equals 20 nm). Example individual particle projections are shown below with scale bar equal to 10 nm. B) 2D reference free class averages for WT-HSPB5 pH 7.5, WT-HSPB5 pH 6.5 and H104K-HSPB5 pH 7.5 from data sets of 5,321, 5713, and 5145 single particles for respectively. Scale bar equals 10 nm. C) Example class averages, corresponding rotational averages and estimated diameter (nm) for HSPB5 oligomers.

To ask if the change in oligomer size observed with pH is a consequence of dimer interface destabilization, the His-104 mutants were analyzed by SEC-MALS and EM at pH 7.5. H104K-HSPB5 forms very large, polydispersed oligomers ranging from 785 to 840 kDa (Figure 3.5A), with an average Mw of 810 kDa (~41 subunits). H104Q-HSPB5 oligomers elute at an intermediate position relative to WT- and H104K-HSPB5. Thus, more subunits are recruited when oligomers are assembled from destabilized dimers. We propose that oligomers composed of H104K-HSPB5 are made predominantly of monomeric units while oligomers composed of H104Q-HSPB5 contain both dimeric and monomeric units. If this model is accurate, we should be able to recapitulate intermediate-sized H104Q-containing oligomers by mixing together WT- and H104K-containing subunits. As shown in Figure 3.5C, the elution position and oligomer mass in mixtures of WT-HSPB5 and H104K-HSPB5 titrate as a function of added H104K-HSPB5 subunits, consistent with a model in which oligomers are formed from both dimeric and monomeric units. WT-HSPB5 oligomers at pH 6.5 have a mass range that corresponds to a 1:2 ratio of WT:H104K subunits, indicating that the pH-dependent oligomeric assemblies likely arise from a combination of monomeric and dimeric subunits.

The results above suggest that H104K-HSPB5 oligomers represent an endpoint in a continuum of oligomer composition and that H104Q- and (pH 6.5) WT-HSPB5 are reflective of species that are favored under differing conditions including stress-induced acidosis. To ask if oligomers composed uniquely or partly of monomeric units have distinct structural features, negative-stain EM images of H104K-HSPB5 at pH 7.5 and WT-HSPB5 at pH 6.5 were collected and analyzed. In a majority of images, defined features, identified as light and dark regions of density, are apparent within the structures, indicating an organized arrangement of subunits. The particles are generally spherical, with some oblong-shaped structures also observed. Quantitative information on the size and distribution of oligomers was obtained by measuring the diameter of circular averages generated for each 2D projection average (Figure 3.6C). Single particles were then binned based on diameter of their corresponding average to generate a distribution (Figure 3.5D). The size distribution derived in this way is consistent with the SEC-MALS analysis: WT-HSPB5 at pH 7.5 has the smallest average diameter, 15 nm, (a range of 13–17 nm), H104K-HSPB5 has the largest, with an average of 17 nm, and WT-HSPB5 at pH 6.5 is intermediate, at 16 nm. Oligomers of WT-HSPB5 at pH 6.5 cover the entire range of diameters measured, between 14 and >18 nm, while the distribution of H104K-HSPB5 is skewed to the largest dimensions, with a majority of particles (>70%) greater than 16 nm. For comparison, the diameter of the WT-HSPB5 cryo-EM model [16] determined similarly from the circular average measures 15 nm, in good agreement with our

89

measurements. Altogether the results reveal that conditions and/or mutations that affect the stability of the antiparallel dimer interface have substantial impact on HSPB5 oligomer size and structure.

- ### 3.3.5 Oligomers with destabilized dimer interfaces are effective holdases that reorganize to bind client proteins

To ascertain the functional and mechanistic consequences of the expanded oligomer structures described above, standard holdase assays in which aggregation of a model client protein is monitored as a function of time in the absence and presence of sHSP were performed. At pH 7.5, H104Q- and H104K HSPB5 are more effective than WT-HSPB5 at delaying formation of large aggregates by two model clients, αLactalbumin (αLac) destabilized by addition of DTT, and alcohol dehydrogenase (ADH) destabilized by addition of DTT and EDTA (Figure 3.7). The results indicate that enhanced holdase activity is associated with destabilization of the dimer interface.
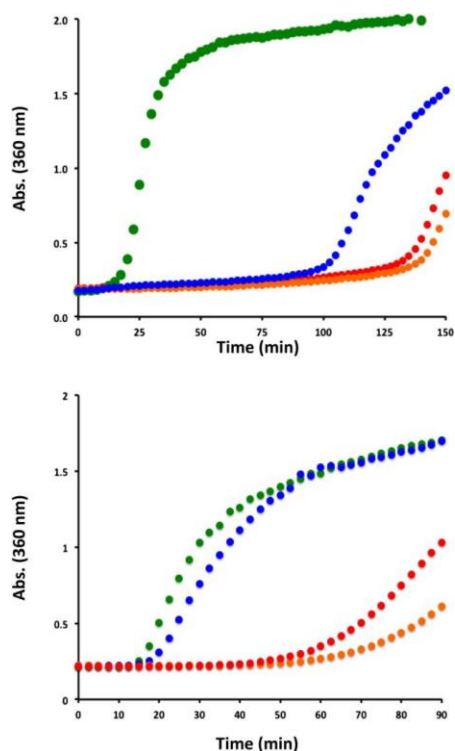
Figure 3.7 His-104 mutants of HSPB5 are effective at delaying the onset of aggregation of a model client protein.

(Top panel) Aggregation of DTT-denatured bovine αLactalbumin at 42°C in the absence (green) and presence of WT-HSPB5 (blue) or HSPB5 mutants H104K (red) and H104Q (orange). Light scattering at 360 nm was used to monitor the DTT-induced aggregation of αLac (600 µM) in the presence and absence of HSPB5 (40 µM). Assays were performed in duplicate and the average scattering curves are shown. (Bottom panel) Aggregation of Yeast Alcohol Dehydrogenase in the presence of EDTA and DTT, at 37°C in the absence (green) and presence of WT-HSPB5 (blue) or HSPB5 mutants H104K (red) and H104Q (orange). Light scattering with 360 nm light was used to monitor ADH (100 µM) aggregation in the presence and absence of HSPB5 (20 µM).

To understand how destabilization of the dimer interface yields more effective holdases, we compared how HSPB5 and the mutants interact with clients. We took advantage of the long delay in αLac aggregation afforded by both the WT and mutant HSPB5 species to attempt to detect sHSP-client interactions. Mixtures of αLac and one of the HSPB5 species were analyzed by SEC-MALS following addition of DTT and before the onset of aggregation (Figure 3.8). Although WT-HSPB5 maintains αLac in a soluble form during the time frame of the experiment, no interaction between the two proteins was detected by SEC or SDS-PAGE, indicating that its holdase function is achieved through highly transient interactions (Figure 3.8A). In contrast, a mixture of αLac and H104K-HSPB5 elutes with a dramatically different profile. SDS-PAGE analysis across the broad peak that elutes between 7.5 and 9.2 ml shows that it contains both proteins (Figure 3.8B). There is a broad range of molecular weights across this peak, from >550 kDa to ~250 kDa. A similar but less dramatic change in the elution profile was obtained for a mixture of αLac and H104Q-HSPB5 (Figure 3.8C). Thus, long-lived complexes are formed between αLac and the H104 mutant HSPB5s, and these are markedly smaller than the oligomers that are populated in the absence of client protein.
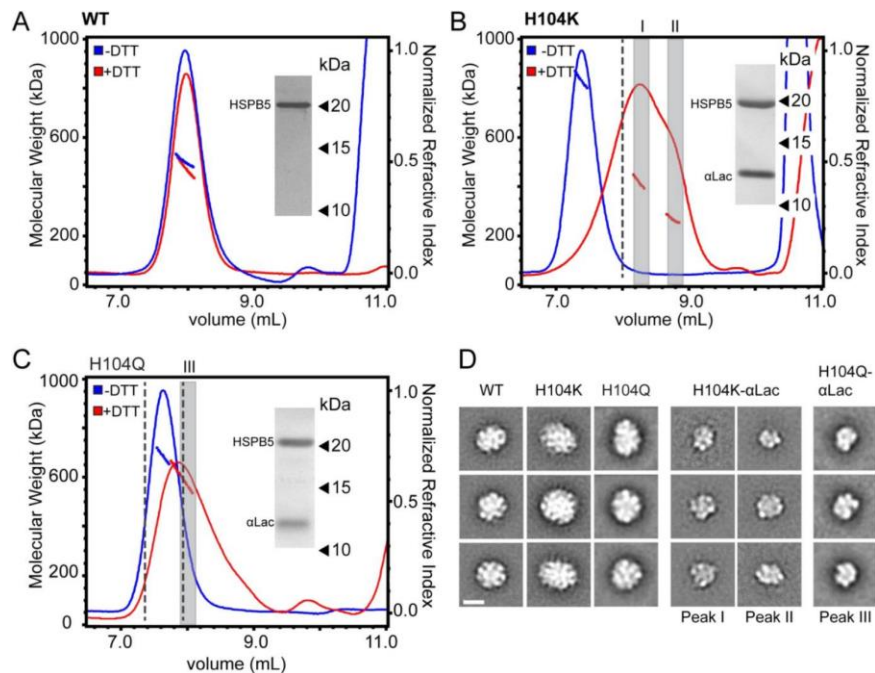
Figure 3.8 H104K- and H104Q-HSPB5 oligomers reorganize into small, long-lived client-bound complexes in the presence of αLac model client protein. A–C) SEC-MALS analysis and corresponding M_w of WT A), H104K B) and H104Q C), HSPB5 oligomers (40 µM in subunit concentration) incubated with αLac (120 µM) in the absence (blue) and presence (red) of 50 mM DTT to destabilize αLac. SDS-PAGE analysis of peak fractions for corresponding HSPB5-αLac incubations with DTT (red trace) is shown (inset). Dashed lines correspond to WT elution at 8 ml and H104K elution at 7.4 ml. D) 2D projection class averages of H104K-

and H104Q-HSPB5-αLac peak fractions corresponding to peaks I, II, and III (gray bars) in B and C are shown with representative averages of WT, H104K-, and H104Q-HSPB5 incubated without αLac substrate for comparison. Scale bar (lower left panel) equals 10 nm.

Negative-stain EM was performed on fractions collected across the peak containing both H104K-HSPB5 (or H104Q-HSPB5) and α-Lac (Figure 3.8D). In micrograph and single particle images, the particles appear intact and there is little background from unbound protein, indicating the mutant HSPB5/αLac complexes remain stable following dilution for EM (Figure 3.9). The particles are much smaller and are structurally distinct from the spherical oligomers observed for WT-, H104Q-, or H104K-HSPB5 on their own. A large single particle data set of fractionated H104K-HSPB5/αLac complex was collected, and 2D projection averages were determined as above. The 2D averages (Figure 3.8D) show clear structural features and reveal that a major structural reorganization occurs in the mutant sHSP upon binding of a model client protein. Among the 2D averages, some smaller spherical oligomers similar to WT-HSPB5 are observed, but the ultra-large (>16 nm) oligomers that predominate in H104K HSPB5 alone are no longer detected. The sizes are highly variable, likely depending on the orientation, stoichiometry, and/or oligomeric state of the complex.

To see if similar HSPB5/αLac complexes form with WT-HSPB5 but do not survive the SEC-MALS experiment, unfractionated samples of mixtures of WT-HSPB5 and α-Lac were analyzed by negative stain EM (data not shown). No smaller species were detected and the spherical oligomers remain unchanged for WT-HSPB5. Overall the results demonstrate that HSPB5 oligomers with destabilized dimer interfaces disassemble and undergo a dramatic reorganization to form stable complexes with a model client protein while the wild-type protein at pH 7.5 does not do so and performs its holdase function via highly transient interactions with client.
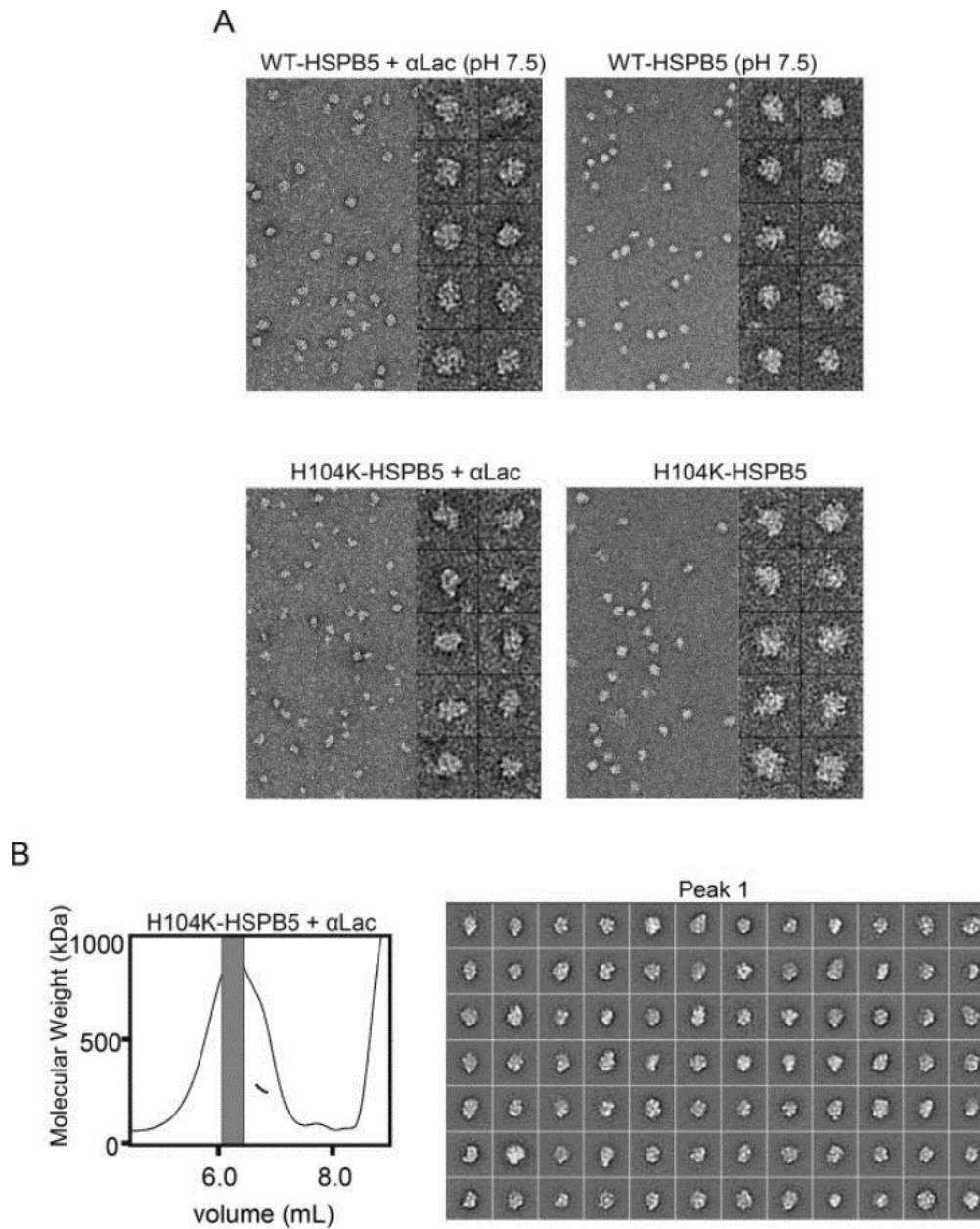
Figure 3.9 EM micrograph images and 2D classification of HSPB5 incubated with αLac. A) Representative micrograph images and single particles of WT-HSPB5 and H104K-HSPB5 incubated with or without αLac substrate and DTT prior to fractionation by SEC-MALS showing the shift in oligomer size only occurs with H104K-HSPB5 and α-Lac. Scale bars equal 20 nm and 10 nm for the micrographs and single particles, respectively. B) Complete set of 2D projection class averages of H104K-HSPB5-αLac isolated in Peak 1 and Peak II following SEC-MALS fractionation. Class averages were obtained from 11,727 particles in fraction I and 9257 particles in fraction II are shown and the scale bars equal 10 nm.

- **3.4 Discussion**

Despite their key roles in maintaining cellular protein solubility under and following stress conditions, the determinants of sHSP structure and function remain ill defined. Stresses such as ischemia and hypoxia are associated with acidosis in which cellular pH can decrease to as low as pH 6.4 [3]. As HSPB5 must function under stress conditions, we sought to investigate effects of pH on its structure and function. sHSPs have three structural regions, each of which plays a role in oligomer assembly. The highly conserved ACD is necessary and sufficient for dimer formation and dimers are thought to be the fundamental building blocks for oligomers. The N- and C-terminal regions appear to drive oligomer assembly, although the details of these interactions are not yet elucidated. We find that HSPB5-ACD dimers dissociate into folded monomers that are favored as the pH decreases. ITC and NMR measurements revealed a modest affinity for the ACD dimer (K_D of 36 µM at pH 7.5, 37°C), with dimers dissociating at a rate of 400 s−1. The long β6+7 strands of two subunits align in an antiparallel fashion to form the dimer interface. This structure with its associated H-bonds might be expected to afford higher affinity. The juxtaposition of Glu-117 and Glu-117′ in the middle of the interface and the positively and negatively charged patches that cross the interface may contribute to the modest affinity and to the dynamics and plasticity we observed in the interface. Dimer affinity decreases 15-fold over 1 pH unit (pH 7.5 to pH 6.5) and this likely corresponds to a similar fold increase in the rate of dissociation at the dimer interface. A pH-dependent destabilization of the HSPB5-ACD dimer interface was inferred from native MS studies performed on oligomers as a function of pH; our results offer a direct confirmation and quantification of this hypothesis [17].

We identified a histidine residue that plays a key role in ACD dimer interface stability. Substitution of His-104 with Gln or Lys decreases dimer stability substantially. NMR spectra reveal that the His-104 ring is in the more unusual of the two possible tautomeric forms, stabilized by serving as an H-bond donor. Analysis of members of the solution structure ensemble and crystal structures with the Loop 5/6-up conformation identifies several backbone carbonyls as potential H-bond acceptors for His-104: His-83, Glu-105, and Glu-106. Alteration of the H-bonding potential or geometry (as in the H104Q mutant) or charge (as in the H104K mutant and low pH) destabilizes the dimer. Among the ten human sHSPs, His-104 is the most conserved His residue, appearing in eight of ten proteins, with the non-H104-containing sHSPs having a Gln (HSPB9) or a Lys (HSPB7) (Figure 1—source data 2). Consistent with a conserved role for His-104, the unusual tautomeric state adopted by His-104 in HSPB5 is also observed for the

analogous histidines in HSPB1 (His-124) and HSPB6 (His-103) (Rajagopal and Klevit, unpublished observation).

Identification of the role of His-104 in dimer stability was unexpected because while there are histidines on the dimer interface, His-104 is not one. His-104 is located at the beginning of Loop 5/6, the loop connecting strands β5 and the dimer interface strand, β6+7 (Figure 4B). NMR relaxation dispersion analysis of the ACD dimer revealed that residues in the dimer interface (116–123) exist in two states consistent with a dimer-monomer equilibrium (Figure 2B). Residues in Loop 5/6 have similar exchange rates suggesting that loop movements and the structural transition may be coupled. However, a rigorous demonstration that the dynamics of the two regions are coupled requires a robust determination of kex values as a function of [ACD] for loop residues as well as interface residues and the data collected did not allow for this determination with sufficiently high confidence. Nevertheless, consistent with this notion, inter-subunit contacts are observed that involve Loop 5/6 residues: His-111 at the apex of Loop 5/6 makes contacts to Arg-120' and Tyr-122' across the dimer interface. These inter-subunit contacts help to position Loop 5/6 in a 'loop up' conformation in the solution structure at pH 7.5 (Figure 1E, Figure 4—figure supplement 1). A majority of residues in Loop 5/6 are charged (H104-E-E-R-Q-D-E-H111) so a possible consequence of His-104 protonation, which sits at the base of the loop, is to alter the conformation or position of Loop 5/6, disrupting inter-subunit contacts involving the loop and shifting the dimer–monomer equilibrium of the HSPB5-ACD. In structures with the 'loop up' conformation, side chains of Arg-107 and Arg-116 are in proximity to His-104; the 'loop down' conformation moves Arg-107 away from His-104 and Glu-106 closer to His-104 (Figure 4—figure supplement 1). In sum, we propose that in both loop conformations His-104 sits at the center of a dynamic network of electrostatic and H-bonding interactions that is responsible for modulating the stability of the dimer interface.

A survey of all 17 available mammalian sHSP-ACD structures (9 HSPB5 [WT and mutants], 3 HSPB1, and 3 HSPB6) reveals that Loop 5/6 is found in two conformations; a 'loop up' conformation as seen in the HSPB5-ACD solution structure and a 'loop down' conformation. In the 'loop up' structures, the details of the interactions between Loop 5/6 residues across the dimer interface vary, again pointing to the plasticity of this region. Nevertheless, the residues corresponding to His-111, Asp-109, and Arg-120 are involved in all cases. Furthermore, although Loop 5/6 contains predominantly polar and/or charged residues, it is remarkably well conserved among the human sHSPs (Figure 1—source data 2). There are several reported examples where Loop 5/6 residues affect the dimer-monomer equilibrium. In HSPB5,

residues His-104, Asp-109, and His-111 have recently been implicated in Cu2+ and Zn2+ binding and the binding of divalent cation appears to destabilize the dimer interface [18]. In HSPB1, which has an almost identical Loop 5/6 sequence to HSPB5, substitution of the two glutamate residues that correspond to HSPB5 Glu-105 and Glu-106 to Ala resulted in monomeric HSPB1-ACD [19]. Also, a Loop 5/6 mutation in HSPB1, R127W (corresponding to Arg107 in HSPB5 numbering) is reported to promote monomer over dimer [20]. In each case, a change in the net charge of Loop 5/6 leads to monomer being more favored. Altogether the observations suggest a model in which properties of Loop 5/6 are coupled to the stability of the dimer interface. It is notable that inheritance of single alleles of D109H-HSPB5 or R127W-HSPB1 is associated with cataract, myofibrillar myopathy, and distal hereditary motor neuropathy [21]. Both mutations alter the net charge of Loop 5/6, implying a critical role for structural and/or dynamic properties of Loop 5/6 in sHSP function.

Moving into the context of full-length HSPB5, we found that decreasing pH or substituting His-104 has dramatic effects on oligomer dimensions and subunit stoichiometry. A continuum of oligomer sizes is observed that trends reciprocally with ACD dimer interface stability. H104K-HSPB5, whose ACD will be predominantly monomeric, assembles into the largest oligomers containing over 40 subunits. While the notion that dimers are the fundamental building blocks of sHSP oligomers may describe the situation under certain conditions, our results indicate that oligomers can also be built from monomeric subunits and from combinations of dimeric and monomeric units and that more monomeric subunits can be incorporated into a given oligomer. This revelation will be important in any future attempts to determine HSPB5 oligomer structures for oligomers larger than the 24-mer previously determined [2, 16].

The His-104 mutants allowed us to ask if and how the dimer interface contributes to holdase function without the confounding complications of comparing aggregation of model denatured client proteins at differing pHs. Both dimer-destabilizing mutations yield an HSPB5 that can delay aggregation of model clients longer than the wild-type protein at pH 7.5. Unexpectedly, the His-104 mutant proteins, which form much larger oligomers than WT-HSPB5, reorganize to form long-lived complexes with a client protein. EM images reveal particles that are markedly smaller and distinct from the mostly spherical sHSP-alone structures. During the time period in which WT-HSPB5 inhibits client protein aggregation, we were unable to detect a complex with the client, either by SEC or by EM. Thus, the mutant sHSPB5 species perform holdase function via a different mechanism from the wild-type protein at pH 7.5. WT HSPB5 acts via weak-and-transient interactions while the mutants act via stronger-and-longer

interactions. Notably, two inherited missense mutations in HSPB1 associated with Charcot-Marie-Tooth syndrome, R127W-HPSB1 (in Loop 5/6) and S135F-HSPB1 (on the dimer interface), engage in stronger, longer-lived interactions with client proteins than the WT-HSPB1, as evidenced from tandem affinity purification [20]. Two client binding modes have been observed in studies of the highly related HSPB4 (αA-crystallin), dubbed 'high capacity' and 'low capacity' based on differing client:sHSP stoichiometries [22]. It remains for future studies to ascertain whether these reflect the species observed and reported here.

Solid-state NMR studies of WT-HSPB5 oligomers at pH 7.5 revealed three types of inter-subunit interactions: (1) ACD-to-ACD (i.e., the dimer interface), (2) C-terminal region-to-ACD, and (3) N-terminal region to either ACD or other N-terminal regions [2]. The findings in the current study indicate that the relative strength and, perhaps, abundance of these interactions can affect not only the size and structure of oligomers but also the way in which client proteins are recognized. Subunit exchange in WT-HSPB5 is orders of magnitude slower than the exchange rate we measured for the dimer-to-monomer transition (10^{-3} s^{-1} vs ca. 10^3 s^{-1}, respectively, at pH 7.5, 37°C; [12]). So, while breaking the dimer interface is not the rate-limiting step in subunit exchange, destabilizing the ACD dimer yields oligomers that can more readily disassemble to form smaller species with clients and these complexes must be more stable than the mutant sHSP oligomers themselves. Long-lived sHSP-client complexes have been detected by SEC for Hsp18.1 from peas, but the complexes formed are larger than those of Hsp18.1 in the absence of client [23, 24]. Hsp26 from yeast also forms larger complexes with client than in the absence [25]. These examples contrast with our findings, which imply that HSPB5 has evolved to perform its holdase function via weak-and-transient interactions and that small perturbations can unleash a second, cryptic mode of client interaction (long-and-strong). The highly charged ACD dimer interface and the proximal Loop 5/6 provide exquisite sensitivity to small changes in electrostatic environment that can be effected by slight changes in pH, temperature, divalent cations, other cellular conditions, and mutations. Of the approximately twenty inherited disease-related missense mutations documented in ACD regions of human sHSPs, more than half are in residues on the dimer interface or in Loop 5/6 and all these involve substitutions of charged residues.

Our original intent was to define how HSPB5 functions under pH conditions associated with stress-induced acidosis. Our results show unequivocally that the dimer interface stability decreases over a physiologically relevant pH range and that mutation (or protonation) of a single histidine residue is sufficient to destabilize the dimer. The His-104 mutants provide several general insights regarding the

modulation of structure and function of sHSPs. First, the stability of an ACD dimer interface relative to other interactions involved in oligomer formation can modulate holdase function. In our study, destabilization of the dimer interface leads to enhanced holdase activity. It remains to be seen if the converse will be true. Second, dimer stability can be modulated by residues other than the dimer interface itself. Such effects are likely achieved through a network of conserved charged residues that ultimately favor or disfavor the dimer over monomer. Third, relatively small changes in pH or single missense mutations are capable of shifting HSPB5 from a weak, transient mode of client interaction to one that involves long-lived co-complexes. We propose that the continuum of oligomeric structures we observe for HSPB5 under differing pH (or mutation) may lead to a continuum of client-binding modes that allow the sHSP to ramp its holdase activity up or down as conditions require. A thorough understanding of the ways in which sHSP structure and activity can be modulated under differing cellular conditions will ultimately provide much needed insights into the cellular functions of this important, but previously intractable class of protein chaperones.

- **3.5 Methods**

- Protein purification and Cloning

HSPB5 and HSPB5-ACD (residues 64-152) were expressed and purified as described previously [9]. Site-directed mutagenesis was performed with Quik-Change mutagenesis kit from Sigma. The growth and purification protocols of mutant proteins were similar to that of wild-type proteins.

- Structure determination of WT-ACD by solution state NMR

Resonances in the NMR spectrum of WT-ACD were previously assigned [9]. To obtain distance restraints from NOES, ^{15}N-edited NOESY and ^{13}C-edited NOESY spectra on aliphatic and aromatic groups were acquired on a 1 mM, ^{13}C, ^{15}N-WT-ACD sample in NMR buffer (50 mM sodium phosphate, pH 7.5100 mM NaCl, 0.1 mM EDTA, and 1 mM PMSF). The spectra were acquired on a Bruker 950 MHz US2 (ultra-shield, ultra-stabilized) spectrometer equipped with Avance III console and a z-gradient, triple resonance cryoprobe (David H Murdock Research Institute in Kannapolis, North Carolina). ^{15}N-edited NOESY and ^{13}C-edited spectra were acquired with a mixing time of 120 ms in 90%H_2O/10%D_2O solution at 22°C and 100% D_2O solution at 37°C, respectively. Data were processed with NMRPipe [26] and analyzed with NMRViewJ [27] and CcpNmr [28]. NOEs were binned into short (3 Å), medium (4 Å), and long-range constraints (5 Å) and input as distance restraints into RosettaOligomer [29]. Intermolecular NOEs in homodimeric proteins are usually obtained from edited/filtered-type NOESY experiments on a mixed

sample containing labeled and unlabeled protein. This method failed in the case of WT-ACD due to signal-to-noise issues. A preliminary structure of the dimer was determined with CS-Rosetta [30] and RosettaDock [31] (see below). The β-sandwich fold was determined from CS-Rosetta using backbone chemical shifts. RosettaDock gave a model of the dimer in the APIII register (where residue R116 from each subunit is across from each other). Using this preliminary model, intra- and inter-molecular NOEs could be parsed out from ^{15}N-edited and ^{13}C-edited NOESY spectra. The Hα-Hα NOEs observed in the ^{13}C-edited NOESY spectra unambiguously confirmed the APII register as the dimer interface (Glu-117-Glu-117' across from each other). Intra- and inter-molecular NOE restraints, ^{1}H-^{15}N RDCs, and all chemical shifts including the backbone and side-chain were input into RosettaOligomer for the final determination of the WT-ACD dimer structure.

^{1}H-^{15}N residual dipolar couplings (RDCs) were measured on a 500-μM protein sample dissolved in 500 μl of NMR buffer containing 10% Pf1 phage obtained from ASLA biotech. IPAP (In-Phase/Anti-Phase) ^{1}H-^{15}N HSQC spectra were acquired in-house on a Bruker Avance III 800 MHz spectrometer equipped with a z-gradient, triple resonance cryoprobe. Spectra were analyzed in NMRView to obtain the values of RDCs. The program PALES [32] was used to calculate RDCs for the different structures published in literature.

- RosettaOligomer

The Rosetta symmetric fold-and-dock protocol can be used to determine the structure of symmetric homodimers. Starting from an extended chain, this protocol simultaneously explores the folding and docking degrees of freedom. It consists of four low-resolution stages of increasing complexity in the energy function, in which symmetric fragment insertions are interleaved with symmetric rigid-body trials. During the low-resolution step, side chains are represented using a single, residue-specific pseudo-atom, positioned at the Cα carbon. Finally, symmetric repacking of the side chains and gradient based minimization of the side chain, rigid body, and backbone degrees of freedom are applied. In this high-resolution step, Rosetta's full-atom energy function is used. The conformational search is largely guided by experimental data, including intra- and inter-molecular NOE distance constraints and RDCs. A penalty term that is proportional to the rmsd between experimental and calculated data was used in Rosetta during the Monte Carlo trials and gradient-based minimization. NOE distances are modeled as atom pair constraints in Rosetta. For a structural model, RDCs are fitted using Levenberg–Marquardt non-linear square fitting algorithm. The orientations of alignment tensor are optimized, while keeping the axial component (Dα) and Rhombic component (R) of the alignment tensor fixed. The values of Dα and R of 21.5 and 0.35, respectively, were estimated from a powder pattern distribution of the RDC

data. A total of 10,000 models are generated, of which 1000 lowest ones are selected for cluster analysis. Ten models with the lowest Rosetta full-atom energy in the best-ranked cluster were selected as the final structural ensemble and deposited in the Protein Databank as PDB 2N0K.

- pH titration and determination of pKR by NMR

^{1}H-^{15}N HSQC-TROSY spectra were acquired on WT-ACD (200 μM) in NMR buffer at pH values 9.3, 8.56, 7.86, 7.44, 7.0, 6.83, 6.7, 6.52, and 6.0 at 22°C on an in-house Avance III 500 MHz spectrometer equipped with a z-gradient, triple resonance probe. The pH of the solution was adjusted by adding small aliquots of 1N HCl or NaOH. The long-range correlations between the ring carbon-bound hydrogens (H^{ε1} and H^{δ2}) and the ring nitrogens (N^{ε2} and N^{δ1}) give information on the tautomeric states of the histidines [33]. These correlations were observed in ^{1}H-^{15}N HSQC spectra using WATERGATE for water suppression and by setting the INEPT delay to an integral multiple of $1/J_{NH}$ where J_{NH} is the value of the single bond N-H coupling constant. pK$_R$ values of histidine residues were determined by following the chemical shifts of H^{ε1}, N^{ε2}, and N^{δ1} atoms as a function of pH. Non-linear regression fitting of chemical shifts vs pH was performed with Prism (GraphPad) using a modified version of the Henderson–Haselbach equation:

$$\delta_{obs} = \frac{\delta_{HA} + \delta_A - 10^{pH - pK_r}}{1 + 10^{pH - pK_r}}$$

δ_{obs} is the observed chemical shift at a specific pH value, and δ_{HA} and δ_A are the chemical shifts in the fully protonated and deprotonated state, respectively.

- Chemical shift perturbations (CSP) due to pH

CSPs ($\Delta\delta$(pH7.5–pH6.5)) were computed as follows:

$$\Delta\delta = 1/2 \left(\sqrt{\left((\Delta HN)^2 + (\Delta N/5)^2 \right)} \right)$$

where $\Delta\delta$ is the chemical shift difference of an amide group at pH 7.5 and 6.5, ΔHN and ΔN are the amide proton and ^{15}N backbone amide chemical shift differences, respectively.

- ^{15}N-CPMG relaxation dispersion experiments

To probe conformational fluctuations in the ms timescale, ^{15}N effective relaxation rates ($R_{2,eff}$ which is the sum of the intrinsic relaxation rate, $R_{02}R20$ and the chemical exchange rate, R_{ex}) were measured for WT-ACD using pulse sequences described in literature [34]. Experiments were performed on 200 and 700 µM samples at 22°C and 37°C at two field strengths, 800 and 600 MHz. The values of v_{cpmg} used were 25, 50, 75, 100, 150, 175, 200, 300, 600, and 1000 Hz. A recycle delay of 2.2 s between scans and a total CPMG delay (T) of 20 ms was used. Spectra were processed and analyzed with NMRPipe, and the fits of intensities vs v_{cpmg} were analyzed with the program, GUARDD [35]. 32 out of 85 observable residues in WT-ACD exhibit values of $R_{2,eff}(\infty)-R_{2,eff}(0) > 8$ s^{-1} at 22°C, where $R_{2,eff}(\infty)$ and $R_{2,eff}(0)$ are the effective relaxation rates at v_{cpmg} values of 25 Hz and 1000 Hz, respectively. Of those, 16 residues could be fit to a two-site exchange model with a reduced $\chi^2 < 10$ and these exhibit two exchange regimes (a) fast exchange (model-2, $k_{ex} \gg \delta\omega$) and (b) slow exchange (model-3, $k_{ex} \ll \delta\omega$). k_{ex} and $\delta\omega$ are the exchange rate and the chemical shift difference between the major and minor state, respectively. In the slow exchange regime, the parameters, pb (the population of the minor state) and $\delta\omega$ can be extracted from the fits in addition to k_{ex}. In the fast exchange regime, only the value of k_{ex} can be extracted from the fits. For estimation of goodness of fits, the target function, χ^2 is determined as follows:

$$\chi^2 = \sum_{all v_{cpmg}} \left(\frac{R_{2,eff}^{obs}(v_{cpmg}) - R_{2,eff}^{Calc}(v_{cpmg})}{\sigma\left(R_{2,eff}^{obs}(v_{cpmg})\right)} \right)^2$$

where $R_{2,eff}^{Calc}$ is the calculated value of the effective relaxation rate, and σ is the experimental uncertainty in observed $R_{2,eff}$ which is estimated from two data sets that are repeat values of v_{cpmg}. In this case, repeat data sets were collected at 25 and 200 Hz. The errors reported in k_{ex}, pb, and $\delta\omega$ values are estimated from 100 Monte Carlo simulations and are reported as the standard deviation of the optimized fit parameter from its 100-element distribution.

- Determination of K_D

The value of the dimer–monomer dissociation equilibrium constant, K_D, was determined with isothermal titration calorimetry (ITC). ITC was performed on a MicroCal iTC$_{200TM}$ Calorimeter at the Analytical Biopharmacy Core, Univ of Washington. WT-ACD samples were dialyzed into 50 mM sodium phosphate, 100 mM NaCl at either pH 7.5 or pH 6.5. 200 µl of 1 mM WT-ACD and 300 µl buffer were placed in the

sample and reference cells, respectively. Forty 1 µl injections were performed and the exothermic heat was measured. Data were fitted using MicroCal Origin software to obtain values of K_D and change in enthalpic heat (ΔH).

- Holdase assays

All holdase assays were performed in duplicate using a 96-well plate reader (BioTek) with PBS solutions at pH 7.5 and 250 µL well volumes. DTT-denatured bovine αLactalbumin (Sigma L6010) was used as a model substrate and light scattering at 360 nm was used to monitor protein aggregation in the presence and absence of WT- and mutant HSPB5 at 42°C. 40 µM sHSP (subunit concentration) was added to 600 µM αLac. Aggregation of αLac was induced by the addition of DTT to final concentrations of 50 mM. Aggregation of the model substrate Yeast Alcohol Dehydrogenase (Sigma A8656) was achieved with the addition of EDTA and DTT to final concentrations of 5 mM at 37°C. Light scattering by aggregates was monitored in the presence and absence of WT- and mutant HSPB5. 20 µM sHSP (subunit concentration) was added to 100 µM Alcohol Dehydrogenase.

- Molecular weight (M_w) determination by SEC-MALS

The M_w of HSPB5 oligomers was determined by separation using a WTC-050S5 SEC column (Wyatt Technology Corporation) with an Akta micro (GE Healthcare) and analysis with a DAWN HELEOS II MALS detector equipped with a WyattQELS DLS, and Optilab rEX differential refractive index detector using ASTRA VI software (Wyatt Technology Corporation). The M_w was determined from the Raleigh ratio calculated by measuring the static light scattering and corresponding protein concentration of a selected peak. Bovine serum albumin served as a calibration standard. Prior to SEC-MALS HSPB5 samples were pre-incubated at 37°C for 30 min at 40 µM monomer concentration in 50 mM sodium phosphate, pH 7.5, 100 mM NaCl, and 1 mM DTT. To examine HSPB5 behavior at pH 6.5, 40 µM of protein was allowed to equilibrate in phosphate buffer (50 mM sodium phosphate, pH 6.5, 100 mM NaCl, and 1 mM DTT) at 37°C for at least 60 min. Substrate binding assays were performed under similar conditions established from αLac holdase assays: HSPB5 (40 µM) was pre-incubated with αLac (240 µM) at 37°C in pH 7.5 buffer for 10 min. DTT was subsequently added to a final concentration of 50 mM to trigger αLac aggregation. After 50 min, the sample was filtered and injected for SEC-MALS analysis and fractionation. Light scattering data and calculations were performed using the ASTRA software package (Wyatt Technology Corporation).

- Negative-stain EM analysis

HSPB5 and HSPB5-αLac samples were diluted to approximately 100–200 nM, applied to a thin carbon-coated copper grid and negatively stained using uranyl formate, pH ~6.0, essentially as described [36]. Micrograph images were collected on a Tecnai T12 transmission electron microscope (FEI) equipped with a LaB$_6$ filament operated at 120 kV. Images were recorded at 50,000X magnification with 2.2 Å/pixel spacing and a 1.0–1.5 µM defocus on a 4k × 4k CCD camera (Gatan). Micrograph images were phase-corrected following CTF estimation and HSPB5 particle projections were selected and excised from micrographs using *EMAN2* [37]. 2D reference-free alignment and classification was performed using *SPIDER* [38] to generate projection averages. For size estimation, rotational averages were generated from class averages using *SPIDER*. The contrast was normalized for all images and the diameter was measured across the rotational average. The averages were grouped according to size, and the total number of single particles for each group was used to obtain the size distribution. Independent data collection and analysis were performed in triplicate to obtain error bars.

- **3.6 References**

1. Kampinga, H.H. and C. Garrido, *HSPBs: small proteins with big implications in human disease.* Int J Biochem Cell Biol, 2012. **44**(10): p. 1706-10.
2. Jehle, S., et al., *N-terminal domain of alphaB-crystallin provides a conformational switch for multimerization and structural heterogeneity.* Proc Natl Acad Sci U S A, 2011. **108**(16): p. 6409-14.
3. McVicar, N., et al., *Quantitative tissue pH measurement during cerebral ischemia using amine and amide concentration-independent detection (AACID) with MRI.* J Cereb Blood Flow Metab, 2014. **34**(4): p. 690-8.
4. Bassnett, S. and G. Duncan, *Direct measurement of pH in the rat lens by ion-sensitive microelectrodes.* Exp Eye Res, 1985. **40**(4): p. 585-90.
5. Mathias, R.T., G. Riquelme, and J.L. Rae, *Cell to cell communication and pH in the frog lens.* J Gen Physiol, 1991. **98**(6): p. 1085-103.
6. Clark, A.R., et al., *Crystal structure of R120G disease mutant of human alphaB-crystallin domain dimer shows closure of a groove.* J Mol Biol, 2011. **408**(1): p. 118-34.
7. Hochberg, G.K., et al., *The structured core domain of alphaB-crystallin can prevent amyloid fibrillation and associated toxicity.* Proc Natl Acad Sci U S A, 2014. **111**(16): p. E1562-70.
8. Hochberg, G.K. and J.L. Benesch, *Dynamical structure of alphaB-crystallin.* Prog Biophys Mol Biol, 2014. **115**(1): p. 11-20.
9. Jehle, S., et al., *alphaB-crystallin: a hybrid solid-state/solution-state NMR investigation reveals structural aspects of the heterogeneous oligomer.* J Mol Biol, 2009. **385**(5): p. 1481-97.
10. Kleckner, I.R. and M.P. Foster, *An introduction to NMR-based approaches for measuring protein dynamics.* Biochim Biophys Acta, 2011. **1814**(8): p. 942-68.
11. Northrup, S.H. and H.P. Erickson, *Kinetics of protein-protein association explained by Brownian dynamics computer simulation.* Proc Natl Acad Sci U S A, 1992. **89**(8): p. 3338-42.
12. Peschek, J., et al., *Regulated structural transitions unleash the chaperone activity of alphaB-crystallin.* Proc Natl Acad Sci U S A, 2013. **110**(40): p. E3780-9.

13. Baldwin, A.J., et al., *Quaternary dynamics of alphaB-crystallin as a direct consequence of localised tertiary fluctuations in the C-terminus.* J Mol Biol, 2011. **413**(2): p. 310-20.

14. Aquilina, J.A., et al., *Polydispersity of a mammalian chaperone: mass spectrometry reveals the population of oligomers in alphaB-crystallin.* Proc Natl Acad Sci U S A, 2003. **100**(19): p. 10611-6.

15. Peschek, J., et al., *The eye lens chaperone alpha-crystallin forms defined globular assemblies.* Proc Natl Acad Sci U S A, 2009. **106**(32): p. 13272-7.

16. Braun, N., et al., *Multiple molecular architectures of the eye lens chaperone alphaB-crystallin elucidated by a triple hybrid approach.* Proc Natl Acad Sci U S A, 2011. **108**(51): p. 20491-6.

17. Baldwin, A.J., et al., *alphaB-crystallin polydispersity is a consequence of unbiased quaternary dynamics.* J Mol Biol, 2011. **413**(2): p. 297-309.

18. Mainz, A., et al., *Structural and mechanistic implications of metal binding in the small heat-shock protein alphaB-crystallin.* J Biol Chem, 2012. **287**(2): p. 1128-38.

19. Baranova, E.V., et al., *Three-dimensional structure of alpha-crystallin domain dimers of human small heat shock proteins HSPB1 and HSPB6.* J Mol Biol, 2011. **411**(1): p. 110-22.

20. Almeida-Souza, L., et al., *Increased monomerization of mutant HSPB1 leads to protein hyperactivity in Charcot-Marie-Tooth neuropathy.* J Biol Chem, 2010. **285**(17): p. 12778-86.

21. Nefedova, V.V., et al., *Physico-chemical properties of R140G and K141Q mutants of human small heat shock protein HspB1 associated with hereditary peripheral neuropathies.* Biochimie, 2013. **95**(8): p. 1582-92.

22. McHaourab, H.S., E.K. Dodson, and H.A. Koteiche, *Mechanism of chaperone function in small heat shock proteins. Two-mode binding of the excited states of T4 lysozyme mutants by alphaA-crystallin.* J Biol Chem, 2002. **277**(43): p. 40557-66.

23. Lee, G.J., et al., *A small heat shock protein stably binds heat-denatured model substrates and can maintain a substrate in a folding-competent state.* EMBO J, 1997. **16**(3): p. 659-71.

24. Stengel, F., et al., *Quaternary dynamics and plasticity underlie small heat shock protein chaperone function.* Proc Natl Acad Sci U S A, 2010. **107**(5): p. 2007-12.

25. Franzmann, T.M., et al., *The activation mechanism of Hsp26 does not require dissociation of the oligomer.* J Mol Biol, 2005. **350**(5): p. 1083-93.

26. Delaglio, F., et al., *NMRPipe: a multidimensional spectral processing system based on UNIX pipes.* J Biomol NMR, 1995. **6**(3): p. 277-93.

27. Johnson, B.A., *Using NMRView to visualize and analyze the NMR spectra of macromolecules.* Methods Mol Biol, 2004. **278**: p. 313-52.

28. Vranken, W.F., et al., *The CCPN data model for NMR spectroscopy: development of a software pipeline.* Proteins, 2005. **59**(4): p. 687-96.

29. Sgourakis, N.G., et al., *Determination of the structures of symmetric protein oligomers from NMR chemical shifts and residual dipolar couplings.* J Am Chem Soc, 2011. **133**(16): p. 6288-98.

30. Vernon, R., et al., *Improved chemical shift based fragment selection for CS-Rosetta using Rosetta3 fragment picker.* J Biomol NMR, 2013. **57**(2): p. 117-27.

31. Schueler-Furman, O., C. Wang, and D. Baker, *Progress in protein-protein docking: atomic resolution predictions in the CAPRI experiment using RosettaDock with an improved treatment of side-chain flexibility.* Proteins, 2005. **60**(2): p. 187-94.

32. Zweckstetter, M., G. Hummer, and A. Bax, *Prediction of charge-induced molecular alignment of biomolecules dissolved in dilute liquid-crystalline phases.* Biophys J, 2004. **86**(6): p. 3444-60.

33. Pelton, J.G., et al., *Tautomeric states of the active-site histidines of phosphorylated and unphosphorylated IIIGlc, a signal-transducing protein from Escherichia coli, using two-dimensional heteronuclear NMR techniques.* Protein Sci, 1993. **2**(4): p. 543-58.

34. Korzhnev, D.M., et al., *Low-populated folding intermediates of Fyn SH3 characterized by relaxation dispersion NMR.* Nature, 2004. **430**(6999): p. 586-90.

35.   Kleckner, I.R. and M.P. Foster, *GUARDD: user-friendly MATLAB software for rigorous analysis of CPMG RD NMR data.* J Biomol NMR, 2012. **52**(1): p. 11-22.

36.   Ohi, M., et al., *Negative Staining and Image Classification - Powerful Tools in Modern Electron Microscopy.* Biol Proced Online, 2004. **6**: p. 23-34.

37.   Tang, G., et al., *EMAN2: an extensible image processing suite for electron microscopy.* J Struct Biol, 2007. **157**(1): p. 38-46.

38.   Shaikh, T.R., et al., *SPIDER image processing for single-particle reconstruction of biological macromolecules from electron micrographs.* Nat. Protocols, 2008. **3**(12): p. 1941-1974.

Chapter 4

Identification of the chaperone binding site in a 2-Cys peroxiredoxin[3]

- **4.1 Abstract**

Two-Cys-peroxiredoxins (2-Cys-Prxs) are ubiquitous and highly abundant proteins endowed with two functions, that of peroxidase and of chaperone. While the peroxidase activity has been extensively studied and characterized, the mechanisms underlying the chaperone function of 2-Cys-Prxs are not so well defined. In this study we used the mitochondrial Prx (mTXNPx) from *Leishmania*, whose chaperone function is crucial for parasite infectivity, to dissect the regions involved in client binding. In collaboration with the Jakob lab, our approach involved the genetic incorporation of a photo-crosslinkable amino acid at various positions of the mTXNPx sequence, followed by *in vivo* crosslinking with client proteins. In this chapter I present the work by the Jakob lab the biochemistry detailing residues that make up the chaperone binding interface as well as describe preliminary data on a high resolution cryo-EM structure of the client bound mTXNPx, where the ordering of the N-terminus is found specifically with client binding. Our preliminary results indicate that temperature-dependent structural rearrangements of the reduced mTXNPx decamer are required for exposure of the client binding site.

- **4.2 Introduction**

Peroxiredoxins (Prxs) are ubiquitous, highly abundant proteins found in every biological kingdom [1]. Best known for their ability to detoxify a variety of different peroxides, peroxidases act as general antioxidant devices, sophisticated regulators of peroxide-dependent cell signaling pathways and thiol oxidases [2]. The catalytic activity of Prx is mediated by an active site cysteine, which reacts with peroxides and undergoes reversible thiol oxidation [3]. Importantly, during peroxide catalysis, 2-Cys-Prxs (from here on abbreviated as Prx) undergo major structural rearrangements and transition between obligate homodimers and higher oligomeric species [4]. Generally, five reduced Prx dimers associate into decamers with ring-like structure [5]. Oxidation and disulfide bond formation results in the dissociation of the decamer into the individual oxidized dimers, while overoxidation of the active site cysteine can lead to the formation of even higher oligomeric structures [6]. These higher oligomeric

---

[3] My contributions to this chapter include the preparation of luciferase bound mTXNPx for negative stain and cryo-EM structure determination. This chapter is currently a work in progress with the goal of publishing a manuscript on both the *in vivo* crosslinking data and cryo-EM structure. Contributions by Ursula Jakob and members of her lab (University of Michigan) are indicated in figure legends.

structures were found to adopt a peroxidase-independent second function as molecular chaperones, which protect cells against stress-induced protein unfolding [7].

In agreement with previous studies, we reported that the mitochondrial 2-Cys Prx of Leishmania (mTXNPx) also adopts two functions, as peroxidase and as molecular chaperone [8, 9]. Reduced, decameric mTXNPx functions as an effective chaperone holdase that protects a wide range of proteins from heat-induced aggregation *in vitro*. Upon return to non-stress conditions, mTXNPx interacts with other chaperones and transfers its client proteins for proper refolding [8]. Activation of the chaperone function of mTXNPx appears to be mediated by heat-induced structural rearrangements of the reduced protein that lead to the exposure of hydrophobic surfaces, which are likely the binding sites for unfolding client proteins. Importantly, expression of this chaperone-inactive mutant variant in mtxnpx-/- deletion strains of leishmania revealed that the lack of Prx's chaperone function causes extensive protein aggregation in parasites at temperatures that reflect the body temperature of mammals, and decreases the survival of the parasites in mammalian hosts [8, 10]

The present study aimed at gaining further insight into the mechanism of chaperone activity of mTXNPx by defining which residues of the protein are involved in client binding. To accomplish this, we constructed several mTXNPx variants harboring the unnatural photo-crosslinkable amino acid p-benzoyl-L-phenylalanine (Bpa) at different positions in the mTXNPx sequence. We then analyzed the mTXNPx muteins which crosslinked with client proteins under protein unfolding heat-shock conditions. Following this approach we could identify five residues with probability of being directly implicated in interaction with client proteins. Furthermore, we were able to obtain a cryo-EM structure of mTXNPx in complex with client, revealing the ordering of N-terminal residues that have not been previously resolved by x-ray crystallography or cryo-EM. The results presented here pinpoint the importance of the heat-induced structural rearrangements necessary for the exposure of the client binding site of mTXNPx as many of the residues found to crosslink with client proteins under heat-stress conditions are found buried in the structure of the resting protein and the quaternary structure of mTXNPx also appears to change under such stress conditions.

- **4.3 Results**

- **4.3.1 Genetic Incorporation of p-benzoyl-L-phenylalanine (Bpa) into mTXNPx**

To identify regions in mTXNPx potentially involved in client binding, we employed an *in vivo* crosslinking technique originally developed by Schultz et al. [11]. We engineered 19 different mTXNPx variants, each

of which harboring one unnatural, UV-crosslinkable amino acid p-benzoyl-L-phenylalanine (Bpa) at defined positions in the protein. Upon exposure to UV light, Bpa acts as zero-length cross-linker. Irreversible crosslinks with client proteins are therefore only expected when the clients come in very close proximity to one of the engineered Bpa residue in mTXNPx. By applying site-specific mutagenesis to mTXNPx, we individually substituted each phenylalanine or tyrosine codon with a TAG amber stop codon (Figure 4.1). We reasoned that mTXNPx would likely tolerate these substitutions since Bpa is a structural analogue of Phe/Tyr.
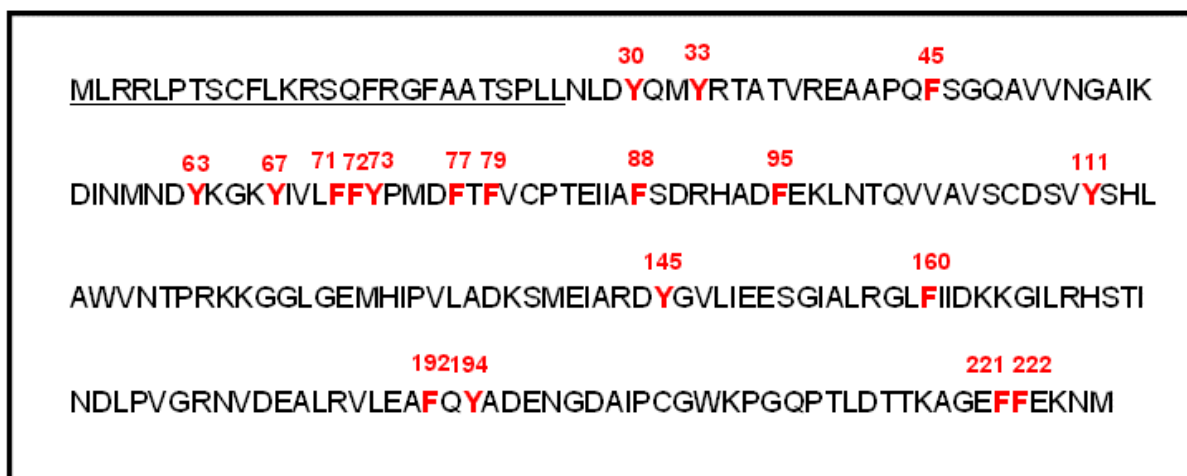
Figure 4.1 Primary structure of mTXNPx showing the residues tested in the crosslinking studies. Highlighted in red are all phenylalanine and tyrosine residues that were genetically substituted by an amber stop codon which allows for the incorporation of Bpa during protein synthesis. Underlined is the mitochondrial import sequence of mTXNPx which is not present in the constructs utilized in this study. This figure was generated by Jakob U (University of Michigan).

Importantly, the 19 substitutions were fairly randomly distributed throughout the amino acid sequence of mTXNPx, potentially increasing our chances to detect residues involved in client binding. We then co-transformed the mutant plasmids together with the aminoacyl-tRNA synthetase/suppressor tRNA pair into E. coli and tested them for *in vivo* Bpa incorporation by growing them in the presence or absence of exogenously added Bpa at 30°C for 3 hours. Subsequently, we determined the expression level of full-length mTXNPx, indicative of successful Bpa incorporation, by western blot analysis using anti-mTXNPx antibodies. We found that the majority of our E. coli strains expressed some amount of the full-length mTXNPx in the presence of Bpa but not in its absence. The expression levels of Y63Bpa, F192Bpa and F194Bpa were reproducibly low, and required prolonged exposure times for detection (Figure 4.2). The F221Bpa and F222Bpa variants, which contain Bpa substitutions only 5 or 4 aa from the C-terminus of mTXNPx, respectively were also detectable in the absence of Bpa making it impossible to determine

whether they contained Bpa. We therefore decided to primarily focus our studies on the remaining 17 mTXNPx mutant variants.
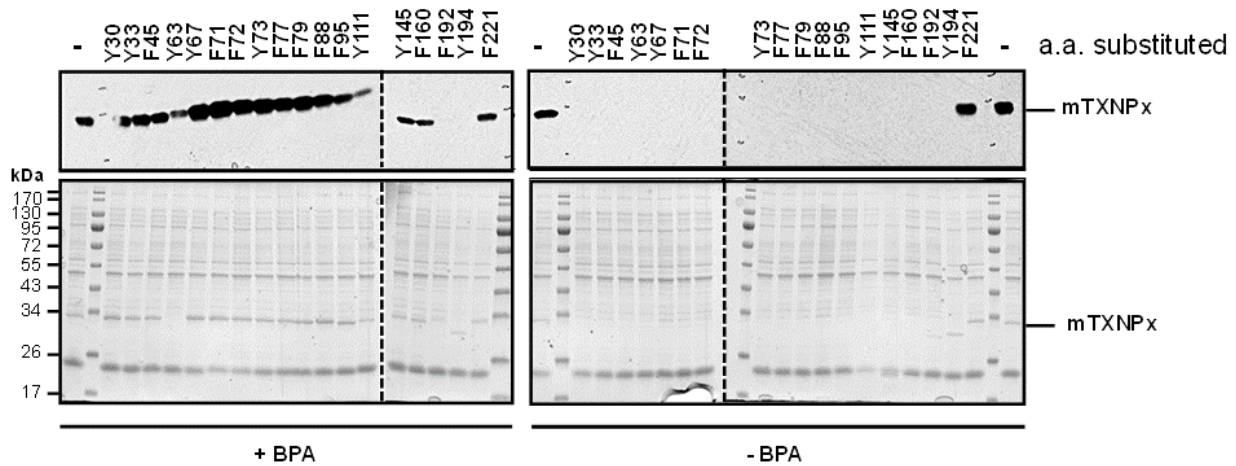
Figure 4.2 Expression levels of mTXNPx in the presence and absence of BPA by western blot. These experiments were performed by Teixeira F (University of Michigan). This figure was generated by Jakob U (University of Michigan).

- **4.3.2 Determination of mTXNPx residues putatively involved *in vivo* in client binding**

Previous in vitro studies revealed that reduced, decameric mTXNPx becomes rapidly activated upon exposure to heat shock temperatures, and forms apparently stable complexes with thermally unfolding client proteins [8]. We therefore reasoned that exposure of our mTXNPx-Bpa expressing E. coli strains to 45°C should fulfill the two requirements; activate reduced mTXNPx and, at the same time, provide a pool of thermally unfolding client proteins that could interact with active mTXNPx.

To test for *in vivo* crosslinking, we then cultivated all of our mTXNPx-Bpa expressing strains as before in Bpa, and either left them at 30°C or shifted them to 45°C for 30 min. After the incubation, we moved the samples onto ice knowing that in vitro complexes between mTXNPx and client proteins are stable at low temperature for extended periods of time [8]. To crosslink any potential clients with mTXNPx, we then subjected the samples to a 10 min exposure to UV light, applied the samples on SDS Page and detected mTXNPx by western blot, using at least two exposure times (short and long) for optimal detection (Figure 4.3). The most prominent band that we detected upon crosslinking in all but one mutant Bpa variant (i.e., Y63Bpa) migrated with twice the molecular weight of mTXNPx, suggesting that it corresponds to a Bpa-linked mTXNPx dimer. In addition, however, a subset of our mTXNPx-Bpa mutant

also showed UV-specific higher molecular weight bands, which became particularly obvious upon exposure to 45°C. These higher migrating bands are likely due to crosslinked complexes between mTXNPx and client proteins (mTXNPx-X) and not due to inter-mTXNPx crosslinks. Given that mTXNPx monomers are arranged in head-to-tail orientation in the dimer, only crosslinks between two monomers within one dimer or between the monomers of neighboring dimers would be expected.
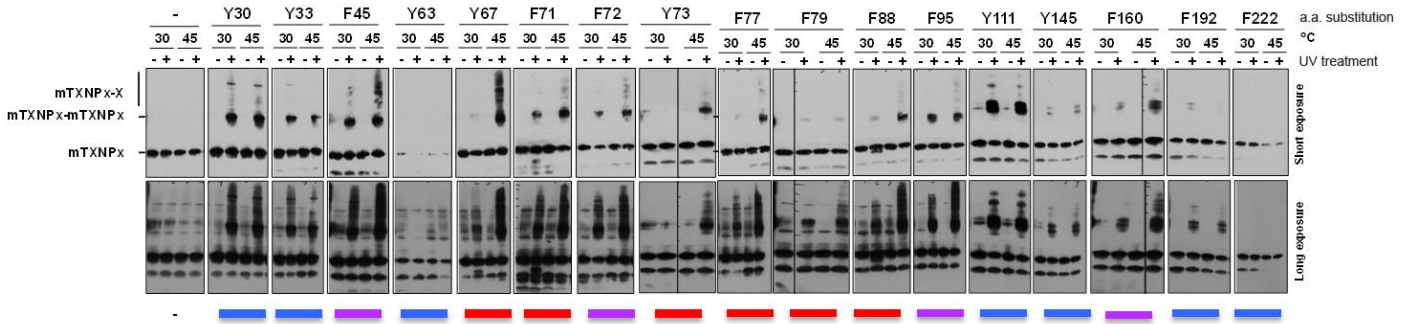
Figure 4.3 Bpa crosslinking of mTXNPx *in vivo*. Escherichia coli expressing mTXNPx variants, in which specific amino acids were substituted by Bpa, were treated either at 30°C or 45°C for 30 min. Upon temperature treatment, cells were transferred to ice and either exposed (+) or not (-) to UV light for 10 min to induce crosslinking. Subsequently, bacteria were lysed and cell extracts analyzed by western blot with an anti-mTXNPx antibody. The two most prominent bands correspond to monomeric (mTXNPx) and dimeric mTXNPx-mTXNPx). Additional bands, seen as a smear, correspond to mTXNPx crosslinked to E. coli proteins (mTXNPx-X). Western blot signals detected at different intervals (short and long exposures) are shown. Wild-type mTXNPx, in which no amino acid was substituted, was used as negative control, and so were Bpa variants not irradiated with UV (-). Here shown is a representative experiment

As can be seen in one representative experiment, by comparing the crosslinking pattern and efficiency of the different mTXNPx mutant variants at 30°C and 45°C, we identified at least three different categories of crosslinks: Group I) Bpa variants, which reveal reproducibly higher migrating bands at 45°C as compared to 30°C (e.g., Y67Bpa); Group II) Bpa mutants, which crosslink similarly to other proteins at both 45°C and 30°C (e.g., Y30Bpa) and Group III) Bpa variants, which do not show any detectable higher migrating smear, suggesting that they do not crosslink with clients (e.g., Y63Bpa) (Figure 4.3, 4.4). While the results with group I) Bpa variants were highly reproducible, some variability in crosslinking efficiency and pattern were observed for group 2 and group 3 Bpa-variants. We therefore decided to score the respective crosslinks in each of the conducted experiments according to their classification, giving a score of "1" to group 1 crosslinks, "0.5" to group 2 crosslinks and "0" to group 3 crosslinks. We classified those amino acids (F67, F71, Y73, F77, F79, F88) with an average score of "1" to be most relevant for temperature-dependent client binding (Figure 4.4, red). We considered all those amino acids (F45, F95, F160, F192, Y194) with an average score of 0.5 < 1 as potential interactors since they revealed temperature-induced increase in crosslinking in at least one or more of our experiments (Figure 4.4,

magenta). Amino acids with a score of < 0.5 were considered as non-binders (Y30, Y33, Y63, Y111, Y145) (Figure 4.4, blue).
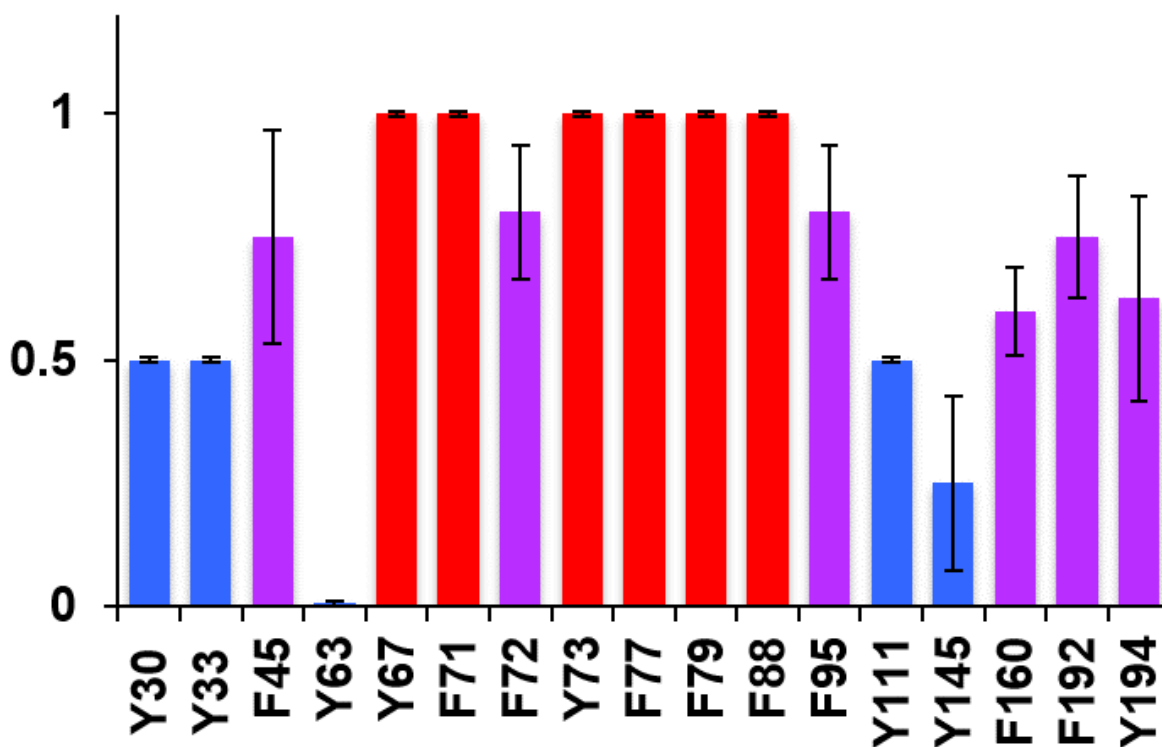
Figure 4.4 Classification of residues involved with mTXNPx client binding. Several independent experiments were conducted as described in A. Here shown are the categorization of each amino acid into binder (red), likely binder (pink), and non-binder (blue), as detailed in the main text, for the several experiments conducted. The normalized final categorization of each amino acid into the 3 classes described above was achieved by attributing to each experiment the following arbitrary numbers: (1) to binders, (0.5) to likely binders and (0) to non-binders and dividing the sum by the number of experiments performed. Based on this, each amino acid that had a score i) > 0.5 was categorized as binder, ii) ≤0.5 and >0.25 were categorized into likely binders and iii) ≤ 0.25 categorized into non-binders.

Crosslinking of group 1 Bpa variants, such as Y73-Bpa or F77-Bpa upon exposure to protein unfolding conditions *in vivo* revealed extensive crosslinking, whereas no higher migrating smear was observed with group 3 Bpa variants, such as the Y111-Bpa mutant. To ascertain that the higher migrating bands observed upon shift to 45°C and crosslinking in group 1 mutants are indeed crosslinks with *in vivo* client proteins and that the lack of crosslinks in group 3 mutants is not due to loss of chaperone function, we purified three representative mTXNPx-Bpa variants (i.e., Y73-Bpa, Y77-Bpa and Y111-Bpa). We then measured their *in vitro* chaperone function (Figure 4.5A) and their in vitro crosslinking behavior (Figure 4.5B). All three purified proteins showed wild-type like chaperone-activity when reduced, excluding that the inability of Y111-Bpa to crosslink with clients is due to lack of chaperone function. Moreover, crosslinking of the three proteins only yielded in the expected monomeric and dimeric mTXNPx species.

These results suggested that the higher migrating species that we observed upon *in vivo* exposure of Y73-Bpa, Y77-Bpa and most likely all other group 1 and 2 mutant variants to 45°C and subsequent UV-crosslinking, are indeed mTXNPx-client complexes.
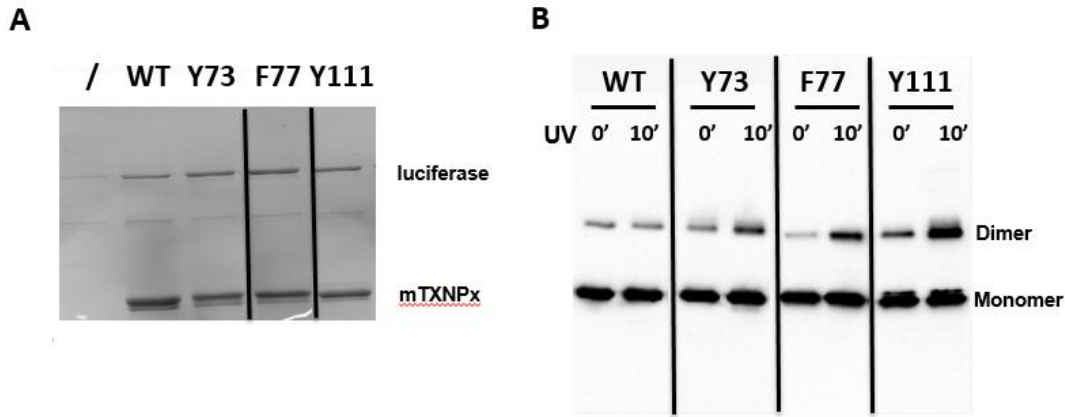
Figure 4.5 Chaperone activity and Oligomeric status of mTXNPx$_{red}$ and mTXNPx$_{ox}$ as assessed by gluteraldeyde mediated cross-linking. A) Chaperone activity was assessed for each Bpa variant, where the presence of luciferase in the soluble fraction indicating protection from heat induced aggregation is identified by SDS-PAGE, B) Increasing concentration of mTXNPx$_{red}$ or mTXNPx$_{ox}$ were incubated in the presence (+) or absence (-) of 40 mM glutaraldehyde at 30 °C for 10 min. The oligomeric status of mTXNPx was assessed by running the samples on reducing SDS-PAGE followed by silver staining.

- ### 4.3.3 Localization of client- mTXNPx interaction sites

To visualize which region(s) of mTXNPx might be involved in client binding, we mapped the three groups of amino acids onto the solved crystal structure of the reduced mTXNPx decamer from *Leishmania brasiliensis* (pdb: 4KB3)(Figure 4.6). For simplification, we focused only on one dimeric unit of the decamer and applied the same color scheme established in our previous figure. We found that some of the amino acids that when substituted to Bpa reproducibly crosslinked with client proteins upon exposure to heat shock conditions (i.e., group 1 amino acids) are in very close proximity to the active site cysteine Cys80 (Figure 4.6). These results made us wonder whether some of the crosslinking products that we observed might involve proteins that form transient disulfide bonds with mTXNPx's active site cysteines before and/or during the process of UV-crosslinking. Formation of an intermolecular disulfide bond would bring the proteins into close contact with Bpa-substituted amino acids close to the active site residue, and hence could cause crosslinking. Indeed, analysis of protein samples prepared from cells expressing the non-crosslinkable wild-type mTXNPx on non-reducing SDS-PAGE revealed a large number of proteins that form reversible disulfide bonds with the protein. However, the pattern and amount of co-migrating proteins appeared to be completely independent of temperature or UV exposure.
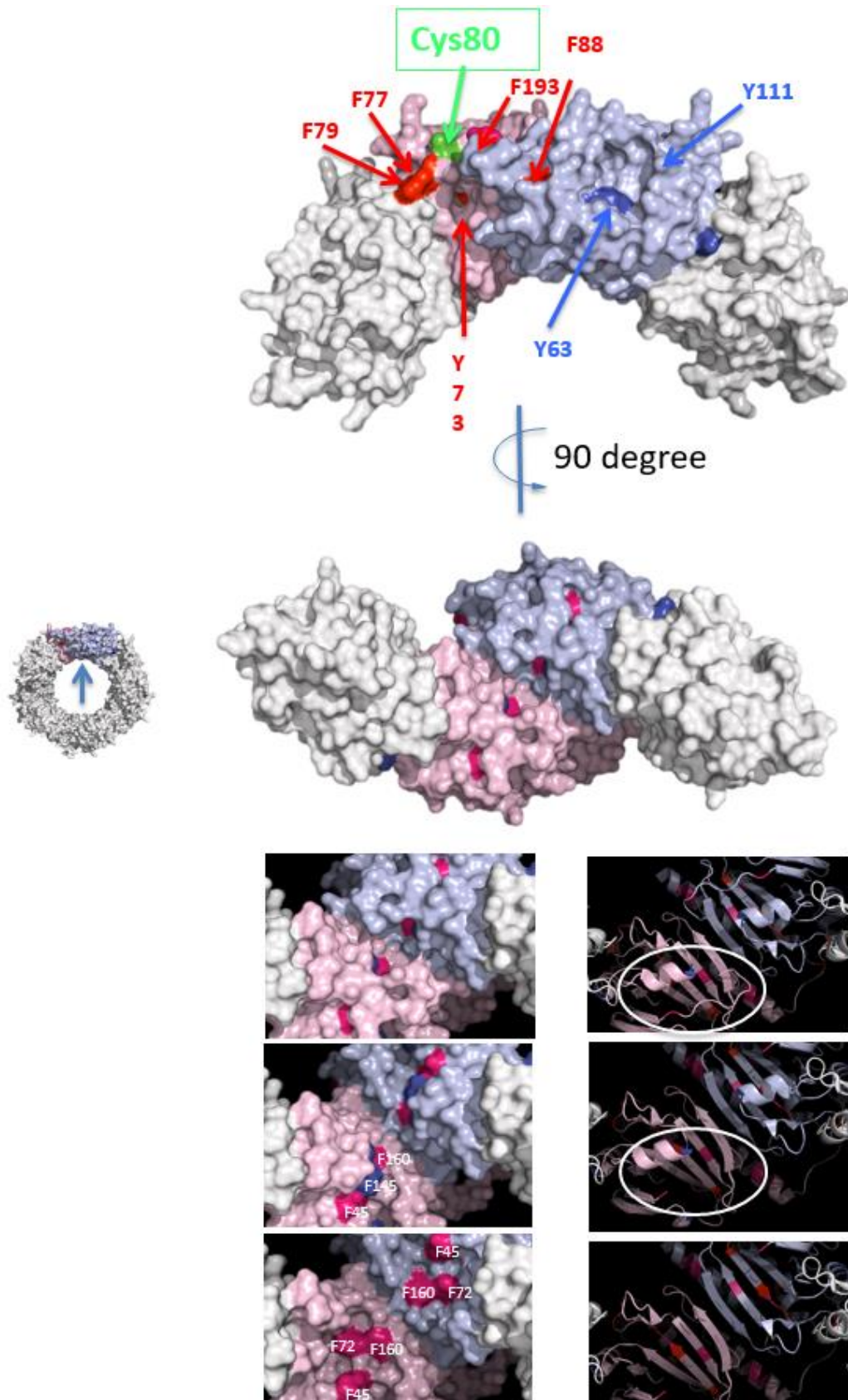
Figure 4.6 Mapping of Bpa-substituted residues in the quaternary structure of mTXNPx. Representation of the quaternary structure of ring-like decameric mTXNPx_red. For simplicity, in this structure one of the composing dimers of the decamer is highlighted while the others are shown in grey. Different views of the selected mTXNPx dimer are presented. Amino acids are colored differentially into binders (red), likely binders (pink) and non-binders (blue), as detailed before, according to their ability to crosslink E. coli proteins. The structure of the mTXNPx homologue from *L. brasiliensis* was used to highlight the residues involved in binding (4KB3) using pymol software. This figure was generated by Jakob U (University of Michigan).

While these results might explain the behavior of Bpa-mutants that revealed similar crosslinking pattern at both 30°C and 45°C (Figure 4.7A), they did not explain our results with Group 1 variants, which were found to crosslink with a specific subset of proteins only upon *in vivo* exposure to 45°C (Figure 4.6, 4.7B). These findings corroborate our conclusion that the interactions that we observe with Group 1 and, most likely also Group 2 residues are not the result of thiol-disulfide exchange reactions but specifically due to interactions between chaperone-activated mTXNPx and thermally unfolding *in vivo* client proteins.
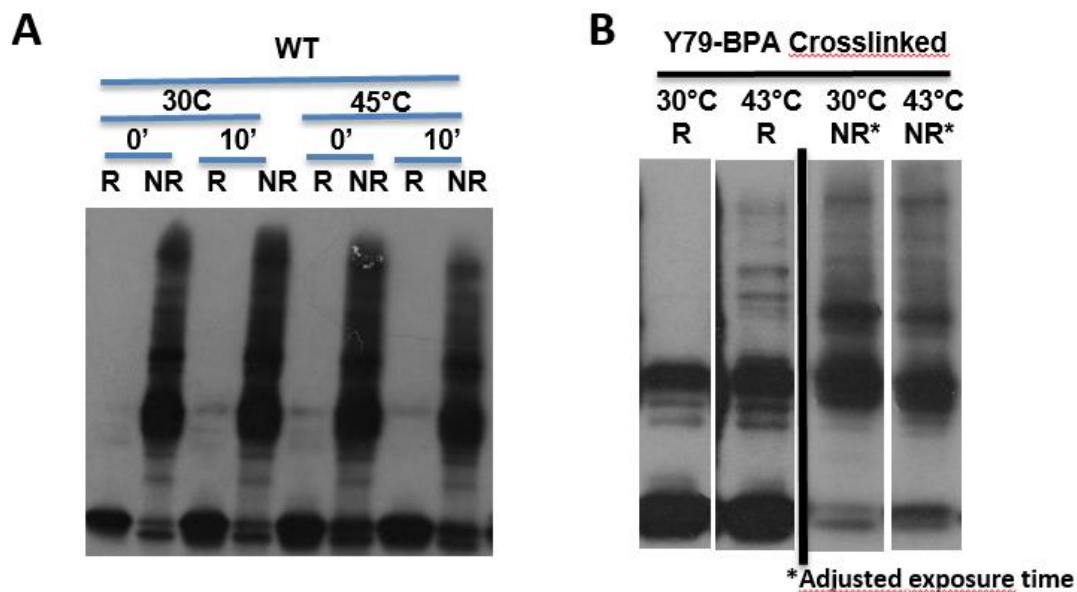
Figure 4.7 Bpa crosslinking of Group 1 variants are specific for client interactions, A) extracts using cells expressing wildtype mTXNPx was run on non-reducing SDS-PAGE showing that disulfide bond formation was not dependent on temperature or UV exposure. B) *in vivo* crosslinking with the Y79-Bpa mTXNPx variant after UV exposure reveals that heat shock under reducing conditions causes specific subsets of unfolding client proteins. These experiments were performed by Teixeira F and the figure was generated by Jakob U (University of Michigan).

Most group 2 crosslinking residues (i.e., F45; F72; F159) were found facing the interior of the decameric structure. This result made sense given that our previous EM studies on mTXNPx:luciferase complexes revealed the presence of electron dense material in the center of mTXNPx's decameric ring structure [8]. However, we were surprised to notice that in the crystal structure of leishmania mTXNPx, which was modeled according to existing structures [12], was highly charged and the crosslinking residues were only partially accessible (Figure 4.6). Closer inspection of the structure revealed that the crosslinking residues were masked by several N-terminal amino acids as well as a short flexible alpha-helix (H4), which appears to interact with and is stabilized by the N-terminus (Figure 4.6, bottom panels, circled). Both regions contribute to the highly charged nature of this surface. Moreover, we determined that H4 also contains one of our few clearly non-binding Group 3 residues (F145), which put this residue in

immediate vicinity to three crosslinking amino acids. Based on these and previous results, which showed that i) tmTXNPx undergoes significant conformational rearrangements upon activation that increase surface hydrophobicity; ii) upon client binding, the N-termini of mTXNPx form spoke-like structures that extend into the interior of the ring structure; and iii) manipulation of the N-termini abolishes chaperone function, we propose that activation and/or client binding likely changes the position of mTXNPx's N-terminus. This rearrangement would affect the stability of the nearby alpha-helix, which, when removed, causes the exposure of an almost contiguous, highly hydrophobic surface, which could serve as the binding site for unfolding proteins in mTXNPx (Figure 4.6).

- **4.3.4 Cryo-EM structure of reduced mTXNPx and mTXNPx:client complexes reveal ordering of the N-terminus in response to client binding**

We further analyzed the mTXNPx-client complex using cryo-EM to analyze the inner ring binding interface and the role of the N-termini. Two samples were prepared with the mTXNPx$_{red}$ decamer treated with heat shock in the presence or absence of luciferase as described previously [8] for the collection of cryo-EM data. 57,683 and 234,808 particles were selected for the mTXNPx$_{red}$ alone and mTXNPx$_{red}$ with luciferase respectively after initial 2D classification using the RELION software package [13]. The remaining selection of particles classified into clear ring structures similar to those observed in negative stain with high resolution features within the decamer ring (Figure 4.8A). Through much optimization of sample purification and preparation, we were able to obtain a cryo-EM dataset of the mTXNPx$_{red}$:luciferase complex with enough substrate occupancy to show that a majority of the top-down views had density in the center of the ring. Both mTXNPx datasets were then refined to yield 3D models estimated at resolutions of 4 Å (Figure 4.8B). Clear densities for the carbon backbone of mTXNPx were resolved and interestingly fits well with the crystal structure of the *Leishmania braziliensis* mTXNPx [12].
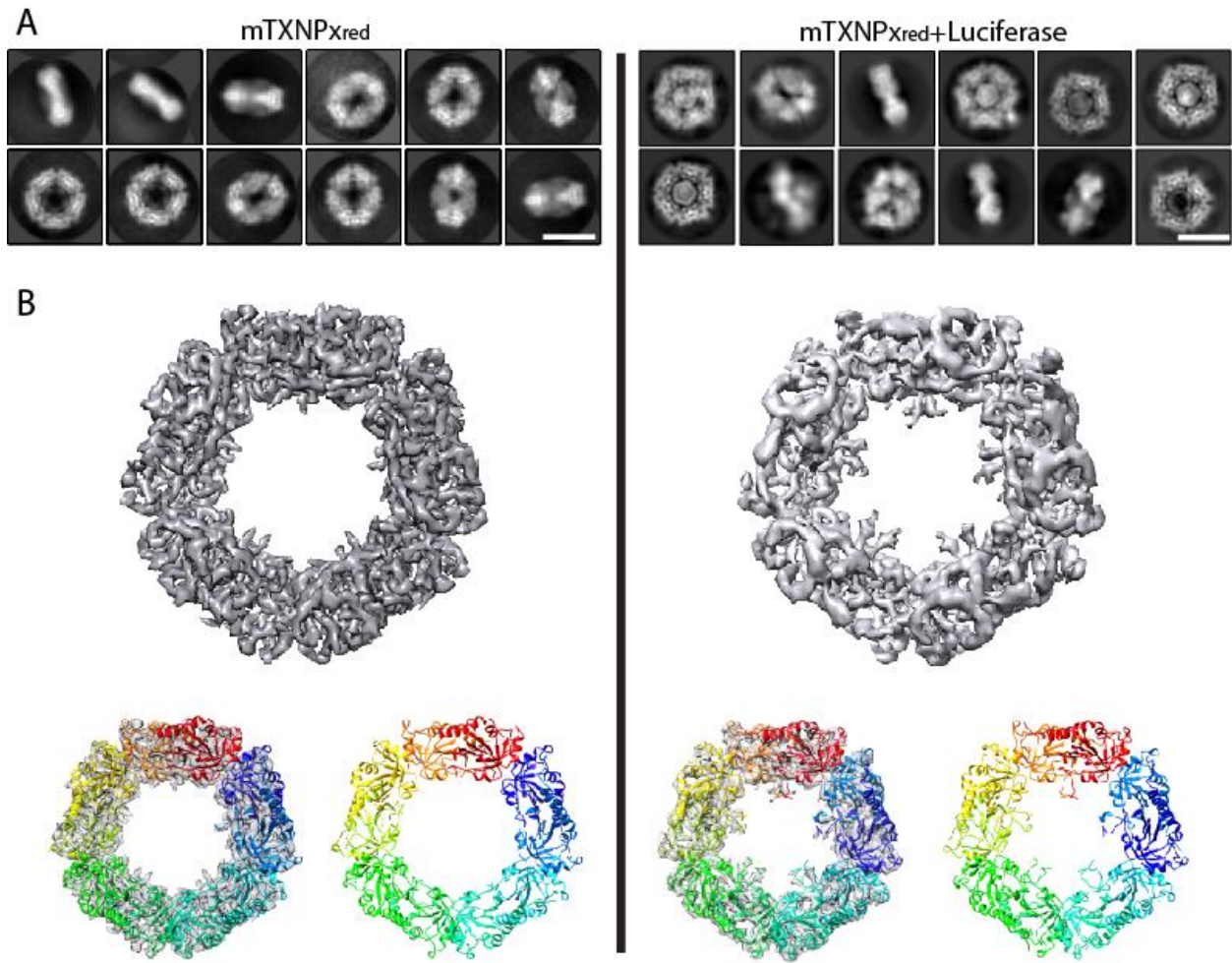
Figure 4.8. Cryo-EM structure of the mTXNPx:luciferase complex compared to the mTXNPx alone. A) reference-free class averages generated by RELION software, comparing heat treated mTXNPx by itself (left) or upon protecting clients from aggregation (right) showing clear protrusions of density into the lumen in the presence of client. Scale bar: 10 nm. B) 3D reconstruction of the mTXNPx and mTXNPx:luciferase complex resolved to 4 Å resolution, a crystal structure of the *Leishmania braziliensis* mTXNPx dimer was used to generate a homology model for the *Leishmania infantum* variant and docked into the EM density (bottom left). Coot and Rosetta software was used to refine the homology model into the mTXNPx:luciferase structure and build the N-terminal residues (bottom right).

One of the most striking features of the 3D map of mTXNPx_red:luciferase was the resolved density within the center of the ring. At higher contour levels, the density in this region becomes weak, most likely due to the disordered nature of the unfolded substrate. Nonetheless, density is present in the lumen of the mTXNPx:luciferase map compared to mTXNPx alone, and we attribute the ordering of these central densities due to client binding since heat shock of the mTXNPx alone did not effectively resolve these residues. Because the crystal structure was solved for the *Leishmania braziliensis* mTXNPx decamer [12], which has 89% sequence identity with *Leishmania infantum* mTXNPx, we generated a homology model based on the previously solved structure for pseudo-atomic modelling into the EM map. Refinement by

Rosetta and Coot shifted the carbon backbone compared with the positions of the Leish crystal structure (Figure 4.9A, top panel). Density present in the center of the mTXNPx:luciferase map allowed us to build additional residues of the N-terminus, previously unresolved in the *Leishmania braziliensis* mTXNPx crystal structure (PDB:4KB3) which begins with alanine 36. We were able to extend the carbon backbone about 6 amino acids (Figure 4.9A), fitting side chain densities for R34, Y33 and Y30, (data not shown). We identify these two tyrosines in the N-terminus as group 3 non-binding residues, making non-specific contacts with non-clients at both high and low temperatures (Figure 4.3). This may be due to how these N-terminal residues are positioned in the central pore where initial contacts with substrates can be made. Because the ordering of these residues is seen only after exposure with client (Figure 4.8), we propose a model where these initial contacts may be important for chaperone activity. Refinement of side chains into the EM density is currently ongoing.

The Prx1 family of 2-cys peroxiredoxins are conserved in the regions of the protein commonly resolved by x-ray crystallography and cryo-EM (Figure 4.9B, 4.9C). Crystal structures from diverse organisms and Prx families, show that the lumen of these Prx structures lack any protruding residues compared to our structure [14-18]. Because of the intrinsic flexibility of the N-terminal regions, it has been difficult to characterize the binding events in the lumen of decameric mTXNPx. A protein BLAST and alignment of various mTXNPx from different species give further aspects for additional study [19]. A comparison between *Leishmania* mTXNPx with other mitochondrial peroxiredoxins show a divergence in the N-terminal region which contains the mitochondrial import sequence [20] (Figure 4.9C). Organisms of a different class of the euglenozoa phylum to which *Leishmania* belong already show divergence in Euglena gracilis, a unicellular algae that does not deal with the stressors of a digenic life cycle. Examining the next closest homologues, PrxII family 2-cys peroxiredoxins, we observe the loss of an N-terminal region after the putative mitochondrial import sequence. In higher eukaryotic phylum including the bovine, mouse and human PrxIII (Figure 4.9C) an extended N-terminus is present for mitochondrial import. Interestingly, the mTXNPx among different Euglenozoa phylum parasites show sequence conservation at the N-terminus (Figure 4.9D). The N-terminus may be important for client binding and holdase activity, as it was observed that the extension of the N-termini with a large His-thrombin tag interferes with its chaperone activity [8]. Thus we propose a model where the N-terminal region is responsible for a mechanism unique to trypanosome parasites of mTXNPx chaperone activity in response to heat stress. Further studies into the N-terminus of these parasitic mTXNPx chaperones are necessary to further understand the mechanism of activation, as well as Prx classes of other species to test whether the loss of N-termini coincides with loss of chaperone activity.
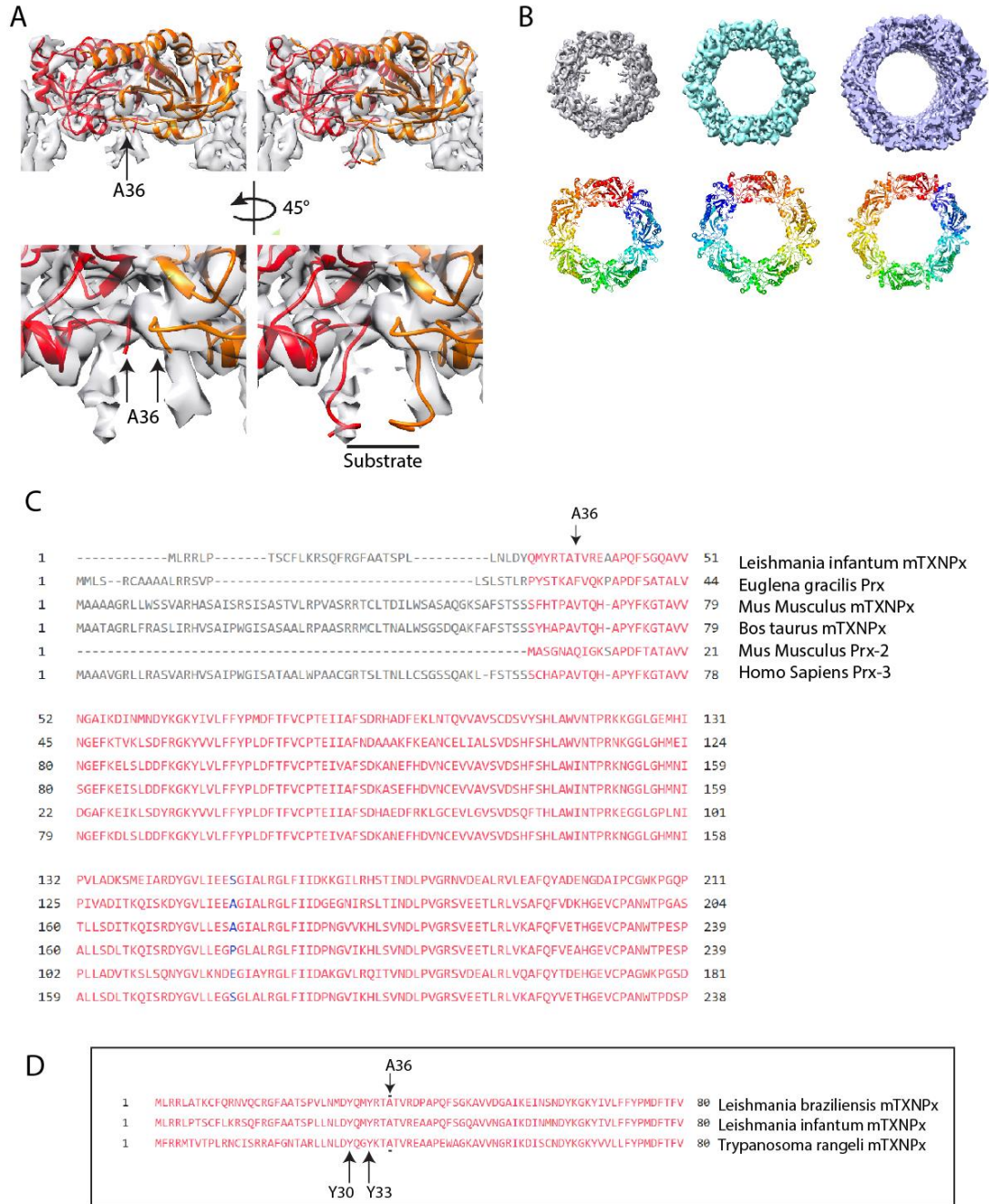
Figure 4.9 mTXNPx activation leads to ordering of its N-terminus upon client binding. A) Zoomed in view of dimer in the mTXNPx:luciferase map with the *Leishmania infantum* homology model before (left panel) and after building in the N-terminus and refinement (right). The A36 residue where the 4KB3 structure starts is positioned perfectly at the protruding densities into the lumen, allowing us to use coot to append 6 a.a. into the densities of the N-terminus subsequent refinement in Rosetta as described in the methods. B) Comparison of our mTXNPx:luciferase structure with various Prx class enzymes solved by cryo-EM and x-ray crystallography demonstrating the lack of center density; top left: our current model, top center: human Prx3 (EMDB: 3233), top right: human Prx3 filament (EMDB: 6309), bottom left: Crithidia fasciculata mTNPx (PDB: 1E2Y), bottom middle Schistosoma masoni Prx1 (PDB: 3ZL5), bottom right bovine Prx3 (PDB: 1ZYE). C) Protein BLAST search of mitochondrial peroxiredoxins reveal sequence conservation in the thioredoxin domains and the majority of the protein. D) Protein BLAST of mTXNPx from different genus of trypanosomatidae show that *Leishmania infantum* relatives possess similar N-termini [19]

- **4.4 Discussion**

Overall, the results shown here represent the first step towards the characterization of the client-binding site in mTXNPx. This study implicated residues belonging to Group I (Y48Bpa, F54Bpa, F63Bpa, F70Bpa, F135Bpa) and to Group II (F20Bpa, Y42Bpa, F46Bpa, F47Bpa, F52Bpa) in mTXNPx client binding. Importantly, since the spacing between the substituted residues (Figure 4.1) is, in some regions, larger than 30 residues, it will be worth conducting additional experiments focusing on residues around the potential client binding site(s). Although preliminary, these results support the idea that residues facing the lumen of mTXNPx ring-like structure might be involved in client binding.

Given how well the *Leishmania braziliensis* mTXNPx decamer crystal structure fits into our *Leishmania infantum* mTXNPx$_{red}$:luciferase map, one possibility is that the client bound structure reflects a state distinct from the 42°C heat stressed decamer (Figure 4.8). The exact nature of the N-terminus interactions with substrate requires further investigation; refinement of residues into the electron density of the cryo-EM map is still in the preliminary stages and further validation is required in order to discern how much of the mTXNPx protein can be resolved from the substrate in the center of the ring (Figure 4.9). The high resolution achieved in this map makes exploring previously uncharacterized regions of both the N- and C- terminus possible. It is at least clear that changes in the N-terminus has occurred due to heat stress. Density is present in the center of these rings when mTXNPx is exposed to conditions where it must protect client, this is especially apparent in the 2D averages (Figure 4.8). Though we were unable to trap the client bound mTXNPx structure in a heat activated conformation exposing the Group I and Group II residues, the N-terminus may still be important for initiating holdase activity, and that further structural arrangements that occur upon heat shock must be made in order to protect clients.

Based on the *in vivo* crosslinking data, the presence of additional client binding sites cannot be disregarded. More importantly, this study highlights the significance of the structural rearrangements that mTXNPx undergoes at high temperatures which likely contribute to the exposure of the client binding site. Interestingly, these rearrangements may even involve the reorganization of the decameric structure of mTXNPx, a model that needs to be further explored. Uncovering the exact nature of such structural rearrangements as well as solving the structure of a chaperone-active form of mTXNPx will be crucial to define the client binding site and therefore constitute the next step of this project.

In a long term perspective, we expect that, by shedding light into the mechanistic aspects of mTXNPx chaperone activity, these findings aid in the development of inhibitors of mTXNPx-client interactions. Inhibition of the chaperone function of mTXNPx is expected to negatively impact on Leishmania survival in their mammalian hosts, and might thus constitute a novel strategy to treat the devastating diseases elicited by these parasites. It will also be interesting to investigate whether this mechanism of sensing heat shock is dependent on the elusive N-terminus and is missing in higher eukaryotes.

- **4.5 Methods**

- Plasmid construction

To express mTXNPx without the mitochondrial import sequence or any additional tags, pET28c6His-THR-TmTXNPx was PCR-amplified using Pfu polymerase and primers

5'-ccgcgcacatatgAATCTGGACTATCAGATGTAC-3' and

5'-gcacatatgTATATCTCCTTCTTAAAGTTAAACAAAATTATTTCT-3'. The PCR product was digested with NdeI (restriction site underlined in the primer) and subsequently re-ligated to originate a plasmid encoding mTXNPx devoid of any tag – pET28cTmTXNPx. The plasmid was further sequenced to ensure that no mutations on mTXNPx ORF had occurred and that the N-terminal 6His-Thr tag had been successfully removed.

- Production of the mTXNPx - p-benzoyl-L-phenylalanine (bpa) variants

For the construction of mTXNPx-Bpa variants, we used a site-directed mutagenesis approach and substituted each phenylalanine or tyrosine codon in the sequence with an amber stop codon (TAG). Following DpnI digest of the parental DNA for 1h at 37 °C and desalting, the PCR product was transformed into E. coli (XL1-Blue strain). Mutant colonies were sequenced and confirmed to carry the desired mutation.

- *In vivo* Bpa-mediated photo-crosslinking

Bpa-mediated crosslinking was performed as previously described [11]. Briefly, E. coli cells (BL21 strain) were co-transformed with a plasmid encoding the respective mTXNPx-Bpa variant (pET28cTmTXNPx-Bpa) and a plasmid encoding the orthogonal aminoacyl-tRNA synthetase/tRNA pair (pEVOL) necessary for Bpa incorporation. Cells were then plated in the presence of appropriate selective drugs and incubated overnight at 30°C. Colonies were scraped off the plates and resuspended in LB medium

(OD600=0.4) containing the adequate combination of antibiotics with or without 1 mM Bpa (Bachem AG, Bubendorf, Switzerland). Cells were then grown at 37 °C for 1h. Afterwards, cells were cooled down to 30 °C and expression of mTXNPx-Bpa variants and the tRNA synthetase/tRNA pair was induced with 10 µM IPTG and 0.1% L-arabinose, respectively. Cells were grown for 3 h at 30ºC, after which they were harvested and resuspended in … buffer using a volume of 100 µl per OD600 of 1.0. Each sample was then subjected to a 30 min incubation at either 30ºC (control) or 45ºC (heat shock), transferred onto ice and exposed to a 10 min UV irradiation (366 nm) using a lamp distance of 2.5 cm. Cells were subsequently lysed using three cycles of sonication and two cycles of freeze-thaw. Total cell extracts were then supplemented with 5x SDS sample loading buffer before analysis by SDS-PAGE. Immunoblotting using polyclonal anti-mTXNPx antibodies was used to visualize mTXNPx and its crosslinking products.

- Differential *in vivo* thiol trapping with NEM

Cells expressing either wild-type mTXNPx or the Bpa-mutants were cultivated in LB as described above. Afterwards, the *in vivo* redox status of mTXNPx was assessed as previously described [8]. Briefly, cells were acidified with trichloroacetic acid (10%) for 30 min on ice. Subsequently, samples were centrifuged (20,000xg 20 min, 4°C) and the precipitated proteins were resuspended in DAB buffer (6 M Urea, 200 mM Tris-HCl pH 8.5, 10 mM EDTA, and 0.5% w/v SDS) +/- 100 mM N-ethylmaleimide (NEM). Upon incubation for 30 min at 25°C, the samples were again precipitated with TCA and separated on SDS-PAGE under reducing or non-reducing conditions and visualized by western blot analysis using a polyclonal anti-mTXNPx antibody

- Preparation of mTXNPx$_{red}$ - client complexes and electron microscopy (EM)

Reduction of mTXNPx was done as previously described [8]. To allow complex formation between chaperone active mTXNPx$_{red}$ (10 µM) and thermally unfolding luciferase (1 µM), the two proteins were incubated for 2 min at room temperature before they were slowly heated from 30°C to 42°C for 10 min [REF]. Samples for negative staining electron microscopy were collected either before or immediately after treatment at 42°C, and centrifuged at 16,100 xg for 30 min at 4°C to remove large aggregates. The supernatant was removed and negatively stained with 0.75% (w/v) uranyl formate (pH 5.5-6.0) on 400-mesh as previously described [21].

Samples for cryo-EM were prepared on C-FLAT holey carbon grids (EMS) in 100mM HEPES buffer pH 7.0 with a Vitrobot (FEI Co.). Data was collected on a Titan Krios microscope (FEI co.) operated at 300 kV on

a K2 direct electron detector with a 1.0 Å pixel size. 8 second exposures with 0.2s/frame rate and a dose of 50 e/Å2 were used in electron counting mode. 5419 Micrographs were collected for the mTXNPx:luciferase dataset and 1406 micrographs were collected for mTXNPx$_{red}$ alone, utilizing Leginon automated data collection software [22]. Micrograph movie files were output and Motioncor2 program was used to perform gain normalization and patch-based motion correction [23], after which Ctffind3 was used to estimate CTF parameters for the corrected micrographs [24]. The DoG picker program was used for automated particle picking generating an initial 394,201 particles for the mTXNPx alone dataset and 653,294 particles for the mTXNPx:luciferase complex [25]. RELION was used to do multiple rounds of reference-free 2D averaging to remove images that did not correspond to mTXNPx particles to result in a final particle count of 57,683 and 234,808 for mTXNPx alone and in complex respectively [13]. Refinement of these particles using the 4KB3 crystal structure converted to mrc format and low pass filtered to 60 Å yielded final structures at 4 Å resolution after B factor sharpening. The *Leishmania infantum* homology model was obtained using SWISS-MODEL [26] and further refinement and modelling makes use of features in coot [27], used to build the N-terminal residues into the structure, as well as EM tools developed in Rosetta by the DiMaio lab for refinement of the carbon backbone [28].

- **4.6 Notes**

I was involved in the work leading up to the data of this chapter, initially characterizing the structure of the mTXNPx:luciferase complex, which has been published in Teixeira, F. Castro, H. Cruz, T. **Tse, E**. Koldewey, P. Southworth, D. R. Tomas, A. M. Jakob, U., Proc Natl Acad Sci U S A, 2015. **112**(7): p. E616-24. Refinement of the cryo-EM data is ongoing and the data presented in this chapter is currently being formatted into a manuscript.

- **4.7 References**

1. Hall, A., P.A. Karplus, and L.B. Poole, *Typical 2-Cys peroxiredoxins--structures, mechanisms and functions.* FEBS J, 2009. **276**(9): p. 2469-77.
2. Chae, H.Z., S.J. Chung, and S.G. Rhee, *Thioredoxin-dependent peroxide reductase from yeast.* J Biol Chem, 1994. **269**(44): p. 27670-8.
3. Winterbourn, C.C., *Reconciling the chemistry and biology of reactive oxygen species.* Nat Chem Biol, 2008. **4**(5): p. 278-86.
4. Hall, A., et al., *Structure-based Insights into the Catalytic Power and Conformational Dexterity of Peroxiredoxins.* Antioxidants & Redox Signaling, 2011. **15**(3): p. 795-815.
5. Barranco-Medina, S., J.J. Lazaro, and K.J. Dietz, *The oligomeric conformation of peroxiredoxins links redox state to function.* FEBS Lett, 2009. **583**(12): p. 1809-16.
6. Sarma, G.N., et al., *Crystal structure of a novel Plasmodium falciparum 1-Cys peroxiredoxin.* J Mol Biol, 2005. **346**(4): p. 1021-34.

7.	Jang, H.H., et al., *Two Enzymes in One: Two Yeast Peroxiredoxins Display Oxidative Stress-Dependent Switching from a Peroxidase to a Molecular Chaperone Function.* Cell, 2004. **117**(5): p. 625-635.

8.	Teixeira, F., et al., *Mitochondrial peroxiredoxin functions as crucial chaperone reservoir in Leishmania infantum.* Proceedings of the National Academy of Sciences of the United States of America, 2015. **112**(7): p. E616-E624.

9.	Castro, H., et al., *Leishmania mitochondrial peroxiredoxin plays a crucial peroxidase-unrelated role during infection: insight into its novel chaperone activity.* PLoS Pathog, 2011. **7**(10): p. e1002325.

10.	Gretes, M.C., L.B. Poole, and P.A. Karplus, *Peroxiredoxins in parasites.* Antioxid Redox Signal, 2012. **17**(4): p. 608-33.

11.	Chin, J.W. and P.G. Schultz, *In vivo photocrosslinking with unnatural amino Acid mutagenesis.* Chembiochem, 2002. **3**(11): p. 1135-7.

12.	Morais, M.A.B., et al., *Calcium and magnesium ions modulate the oligomeric state and function of mitochondrial 2-Cys peroxiredoxins in Leishmania parasites.* J Biol Chem, 2017. **292**(17): p. 7023-7039.

13.	Scheres, S.H.W., *A Bayesian View on Cryo-EM Structure Determination.* Journal of Molecular Biology, 2012. **415**(2): p. 406-418.

14.	Khoshouei, M., et al., *Volta phase plate cryo-EM of the small protein complex Prx3.* Nature Communications, 2016. **7**: p. 10534.

15.	Radjainia, M., et al., *Cryo-Electron Microscopy Structure of Human Peroxiredoxin-3 Filament Reveals the Assembly of a Putative Chaperone.* Structure, 2015. **23**(5): p. 912-920.

16.	Alphey, M.S., et al., *The structure of reduced tryparedoxin peroxidase reveals a decamer and insight into reactivity of 2Cys-peroxiredoxins.* J Mol Biol, 2000. **300**(4): p. 903-16.

17.	Angelucci, F., et al., *Switching between the Alternative Structures and Functions of a 2-Cys Peroxiredoxin, by Site-Directed Mutagenesis.* Journal of Molecular Biology, 2013. **425**(22): p. 4556-4568.

18.	Cao, Z., et al., *Bovine mitochondrial peroxiredoxin III forms a two-ring catenane.* Structure, 2005. **13**(11): p. 1661-4.

19.	Papadopoulos, J.S. and R. Agarwala, *COBALT: constraint-based alignment tool for multiple protein sequences.* Bioinformatics, 2007. **23**(9): p. 1073-9.

20.	Gomes, F., et al., *Proteolytic cleavage by the inner membrane peptidase (IMP) complex or Oct1 peptidase controls the localization of the yeast peroxiredoxin Prx1 to distinct mitochondrial compartments.* J Biol Chem, 2017. **292**(41): p. 17011-17024.

21.	Ohi, M., et al., *Negative Staining and Image Classification - Powerful Tools in Modern Electron Microscopy.* Biol Proced Online, 2004. **6**: p. 23-34.

22.	Suloway, C., et al., *Automated molecular microscopy: the new Leginon system.* Journal of structural biology, 2005. **151**(1): p. 41-60.

23.	Zheng, S., et al., *Anisotropic Correction of Beam-induced Motion for Improved Single-particle Electron Cryo-microscopy.* bioRxiv, 2016.

24.	Rohou, A. and N. Grigorieff, *CTFFIND4: Fast and accurate defocus estimation from electron micrographs.* Journal of Structural Biology, 2015. **192**(2): p. 216-221.

25.	Voss, N.R., et al., *DoG Picker and TiltPicker: software tools to facilitate particle selection in single particle electron microscopy.* Journal of structural biology, 2009. **166**(2): p. 205-213.

26.	Biasini, M., et al., *SWISS-MODEL: modelling protein tertiary and quaternary structure using evolutionary information.* Nucleic Acids Res, 2014. **42**(Web Server issue): p. W252-8.

27.	Emsley, P., et al., *Features and development of Coot.* Acta Crystallogr D Biol Crystallogr, 2010. **66**(Pt 4): p. 486-501.

28.   DiMaio, F., et al., *Atomic-accuracy models from 4.5-A cryo-electron microscopy data with density-guided iterative local refinement.* Nat Methods, 2015. **12**(4): p. 361-365.

Chapter 5

Conclusions and Future directions

- **5.1 Conclusions**

The biochemical decision for client degradation by molecular chaperones is a central question in understanding protein quality control. Because of the implications linking together Hsp70, CHIP and tau, this process is critical to understanding tau homeostasis and neurodegeneration. The repertoire of Hsp70 is vast, in terms of its clientele as well as the co-chaperones diversifying its function, thus studies aiming to characterize structure of these various protein complexes can help us understand how the various Hsp70 conformational states are affected by CHIP and client ubiquitination. Given how structurally different the ADP and ATP states of Hsp70 are and the sparse structural information available on Hsp70:co-chaperone binding, I performed a systematic study on CHIP binding and nucleotide state in context of the full-length proteins, establishing that the ADP conformation of Hsp70 is essential for association for further structural characterization. Studies have shown that increasing affinity of Hsp70 for tau has a direct effect on its turnover, however direct evidence of how Hsp70 directs ubiquitination of client is lacking. Thus, in chapter 1, I characterized CHIP catalyzed ubiquitination events on tau. With assistance from the lab of Rachel Klevit in designing a ubiquitination assay and purification of the E1 and E2 enzymes, I was able to identify the Hsp70 dependent ubiquitination of tau and observed that the ADP conformation of Hsp70 was also important for the efficiency of poly-ubiquitination of tau. We were able to observe evidence of multiple Hsp70 binding events to tau, and how it might be significant in relating the structure of CHIP to the function of chaperone triage of clients. We supported our biochemical observations with help from our collaborators in the lab of Phil Andrews, to obtain MS linkage maps that identify conserved contacts that occur within the Hsp70:CHIP and Hsp70:CHIP tau complexes of our study. Additional support will be provided in the use of cryo-EM as well to corroborate the contacts made in the Hsp70:CHIP complex with the ternary Hsp70:CHIP:tau complex.

Pro-folding decisions balance the other end of proteostasis, and through collaborations I have been fortunate to explore various mechanisms promoting the chaperone activities of Hsp70, sHSPs and Prx. The distribution of oligomeric species makes structural studies on the mechanism of sHsp holdase activity difficult. One global question on sHsp structure lies in how oligomeric holdase chaperones bind to client proteins. Thus, in collaboration with the labs of Jason Gestwicki and Rachel Klevit, two sHsp

family members were used to characterize chaperone activation. We were able to define sHsp activation and use EM to define global changes to sHsp oligomer distribution. We also looked at the distinct rearrangements that occur with client binding.

In chapter 2, in collaboration with the lab of Jason Gestwicki, we characterized the NEF BAG3, a co-chaperone with limited structural information, that has multiple protein binding domains linking it to both Hsp70 and sHsp systems. We found that the structure of Hsp27 oligomers was modulated by the presence of BAG3, disassembling the oligomer by competing with sHsp interactions with IXI motif binding. We further established a direct link between the Hsp70 and sHsp systems and correlate these structural changes to the ability to refold luciferase. In chapter 3, in collaboration with the lab of Rachel Klevit, we analyzed a specific modification to the histidine 104 residue at the interface of the HSPB5 dimer critical for sensing changes in pH. This caused activation of HSPB5 modifying its oligomeric distribution to form larger species when analyzed by electron microscopy and increasing its ability to protect client from aggregation. When we looked at the forms of HSPB5 that engaged with client we saw a surprising result where the sHsp oligomers rearranged into smaller form, another mechanism of a sHsp family member where global rearrangements in its quaternary structure are triggered by some cellular factor such as a BAG3 co-chaperone or pH, and allow for proteostasis to be maintained in the cell.

Another protein chaperone of interest is the peroxiredoxin class of enzymes, discovered as enzymes that protect against oxidative stress it has been discovered that these proteins can also act as molecular chaperones. Aside from the general ability to delay protein aggregation, the mechanism by which Prx switches its function is not understood. Given the abundance of different families of Prx and the homologues that exist among different species, different mechanisms for activation are expected. In chapter 4, in collaboration with the lab of Ursula Jakob, we further characterized the structural role of the mTXNPx ring lumen as a client binding site, whose chaperone activity we previously elucidated as a response to heat stress [1]. Given our initial work in characterizing a novel binding site within the ring of the Prx, we mapped residues facing the lumen of the mTXNPx ring through an *in vivo* crosslinking assay to be close proximity to clients upon heat stress. Furthermore we were able to obtain a high resolution cryo-EM map of the mTXNPx:luciferase complex. Specific for the heat activation and client binding we find an ordering of the N-terminal residues protruding into the ring structure and are working on refining the structure to model more definitively the structure of this region to discern what parts of this density correspond to the N-terminus and what could be interpreted as substrate. We propose a model

where the N-terminus acts to initiate contacts with potential clients which allows for subsequent conformational changes to occur to expose the binding sites identified by *in vivo* crosslinking.

The protein systems I have studied are diverse, but revolve around a central theme of protein quality control. Given the flexible nature of the protein complexes or oligomeric states involved, and the vast dynamics that define the action of chaperone proteins, electron microscopy seems particularly amenable to exploration of these mechanisms of protein quality control. Each case of client:chaperone interaction may prove to have unique structural implications, thus we must exhaust the study of these interactions essential for proteostasis. In so doing we may find generalities of chaperone mechanisms that can help us bridge our studies to an increasing breadth of important client proteins.

- **5.2 Future Directions**

- **5.2.1 Hsp70 and CHIP- the degradation pathways**

Although our biochemical characterization of Hsp70 and CHIP binding give insight towards the conditions required for client ubiquitination to occur, our model still needs more validation and clarification. We proposed that he stalling of Hsp70 folding activity results in or from conditions that push Hsp70 towards its ADP state, allowing the engagement of both TPR domains of CHIP resulting in a 210 kDa complex. Questions remain as to how these conditions originate that would facilitate favoring the ADP state. We can utilize conditions from *in vivo* experiments where Hsp70 can facilitate tau turnover in order to describe tau turnover mechanisms that would explain the *in vivo* phenotype [2, 3]. Chemical modulators that inhibit or Hsp70 ATPase activity may be a key in enhancing the client 'dwell-time' which may promote this ADP specific Hsp70:CHIP complex and tau ubiquitination [4]. Although we used the K71M and T204A Hsp70 mutants to explore the roles of Hsp70 conformation on client ubiquitination, exploring how ATP levels directly affect Hsp70 mediated tau ubiquitinaion would be closer to conditions found *in vivo*, whether there is a balance of ATP and ADP that needs to be made and if there's an inflection point at which Hsp70 is no longer able to efficiently direct client ubiquitination. The question of the nature of client is also just beginning to be explored. Questions of how pathological post-translational modification of tau [5-7] impact this Hsp70 driven ubiquitination could point to new examples of Hsp70 substrate binding and model how tauopathies develop. Using the ubiquitination and binding assay platforms, a wide array of different clients could be tested for Hsp70's role in their triage.

To further analyze the question of whether Hsp70 engagement at both TPR domains is necessary, a CHIP heterodimer mutant would be very informative. It has proven extremely difficult to generate this

heterodimer since the homodimer affinity is so high that even guanadinium chloride or urea treatment of this complex was unable to separate the dimer. Various efforts have been made from affinity purifications mixing homodimers of mutant and wildtype proteins, but the most promising is the dual expression of the two constructs, which must be carefully adjusted in terms of expression levels in order to obtain appreciable levels of heterodimer protein. Efforts are currently needed to validate the formation of a heterodimer aside from the observation that the protein managed to pass the tandem affinity purification scheme.

Another elusive topic is the possibility of multiple Hsp70 binding events on a tau molecule. Observations have been made for multiple DnaK binding events to substrate [8], which required the role of the bacterial Hsp40 homologue DnaJ. One report used σ^{32} heat shock transcription factor as a substrate which is rapidly degraded during bacterial steady state growth, giving one example of the possible role of multiple chaperone binding events facilitating protein turnover [9]. In order to validate this part of our model for Hsp70, efforts must be made to establish conditions that could favor multi-valent Hsp70 binding. Conditions that could result in increased high molecular weight crosslinked species for instance can be explored. Currently we have generated tau deletion mutants that target putative Hsp70 binding sites [3]. Though binding of the complex is diminished in these mutants, it is still difficult to ascertain the stoichiometry of the species contained in our SEC peaks by MALS and Mw_{avg} calculations. Another ambitious project relies on FRET between Hsp70 molecules. With the controls to prove that tau binding with Hsp70 would be stronger than Hsp70 dimer formation, the formation of a FRET pair in the presence of tau would be indicative of multiple binding of Hsp70.

Hsc70 which has had several structural characterizations are conflicted in the dominant structure of the Hsp70:CHIP complex in solution. Whether or not the two proteins are tethered in loose flexible conformations or if there are important contacts that are made between Hsp70 and CHIP are still unclear without a high resolution structural model of the complex. Resolving the DC4 crosslinked structure will be helpful since the MS crosslink identification will provide much additional information about the complex formation [10]. However, because the crosslinks are made at random there is a fundamental limit on the resolution achievable. To aid in the development of linkage maps, work in the lab of Phil Andrews aim to develop shorter DC4 variant crosslinkers, as well as the development of heavy and light isotope crosslinked complexes which can be mixed and then used to generate a quantitiative comparison of crosslinks. The resolution of the non-crosslinked Hsp70:CHIP complex as well as

additional biochemistry on the binding interface of Hsp70 and CHIP must be made to validate our proposed model.

- ### 5.2.2 sHsp systems – HSPB5 and Hsp27

Efforts to elucidate the structural arrangement of the oligomeric sHsp proteins are ongoing and [11, 12]. Previous attempts to obtain a 3D structure of HSPB5 utilized a symmetric 24-mer model, with the rationale that symmetry with 24 subunits would assemble with a small subset of variations in the building blocks [13]. Although extensive efforts were made to sort the heterogeneous dataset, and crosslinking and various structural approaches were utilized to generate this model, we still do not have atomic resolution to really understand the behavior of the variable N-terminii or C-terminal IXI/V motifs. I have been trying to sort out a cryo-EM dataset of a similar size to the previous study mentioned, but collected on a microscope operated at a higher voltage and utilizing a direct detector camera. We have noticed that while it is possible to sort out highly symmetric particles with features similar to the previous tetrahedral 24-mer model, the resolution shows no improvement. When we try to sort the particles into smaller subsets we have had some success at improving the resolution with fewer particles, illustrating that part of the issue is in the classification process (data not shown). Nonetheless a larger dataset will be combined with more extensive 3D classification of the particles until we can find subsets of particles that are truly of the same conformation. Work on resolving the structures of HSPB5 oligomers will be carried out in collaboration with the Rachel Klevit lab.

With advancements in microscope and detector technology as well as automation of data collection, other examples of activation and client binding of sHsp seem lucrative targets. In the case of HSPB5, our studies in the activation by pH and structural rearrangements that arise from client binding show unique structural characteristics for important chemistry in sHsp activity [14]. The oligomeric structures seen in our negative stain EM analysis, with a high throughput setup for cryo-EM, couldn't be more difficult to process than trying to sort the heterogeneity of the HSPB5. Recently other groups have also reported structural rearrangements into smaller oligomers in response to client binding and holdase activity [15]. The rearrangements we observed for Hsp27 are also of interest, recently in collaboration with Rebecca Freilich from the Gestwicki lab at UCSF we observed that the presence of tau was enough to cause oligomer rearrangements causing Hsp27 particles to become smaller, similar to our study with BAG3, only now with the involvement of a client protein. Other interesting structural forms of sHsps are also emerging, for instance deletions of certain domains in Hsp27 causing unique the formation of long filamentous structures. Exploring the enormous variety of structure in the sHsp family may have been a

daunting question as heterogeneity would be a serious limitation for any structural determination technique. However, with the ability to screen for these unique morphologies as was done in chapters 2 and 3 for sHsps and the continuing development of cryo-EM technology we may be entering a phase where the throughput of cryo-EM makes it worth at least trying to see if we can classify any interesting structures from these sHsp molecules to further investigate their chaperone function.

- **5.2.3 mTXNPx and Prx chaperones**

The *Leishmania infantum* mTXNPx structure remains an ongoing project on the refinement of the 3D structure of the mTXNPx:luciferase complex. The high resolution of the structure is rare to be solved by EM, and we are able to resolve features that indicate client binding and chaperone activity. We are investigating the role of the N-terminal sequence in the binding of client proteins, this region is already shown to be crucial as modifications to make it too long have blocked clients from entering and the protein fails to protect clients from aggregation [1, 16]. We have noticed that the sequence conservation is limited in this region, however it is high among other parasites of the same phylum, suggesting a role unique to these organisms and their life cycles [16]. Understanding how these chaperone functions work in these parasites will allow us to specifically target them to impair their survival, to develop inhibitors for mTXNPx that will treat devastating diseases.

Other Prx proteins also are interesting since they also adopt decameric ring structures, their chaperone functions have been characterized in a variety of contexts, including pH and over-oxidizing conditions and have resulted in the formation of high molecular weight species [17, 18]. Focus has been placed on the C-termini of Prx proteins, on the outside of the ring or filament. It will be interesting to examine the chaperone activities of other classes of Prx to see if the chaperone mechanism is preserved among 2-cys-peroxiredoxins. Regardless of the type of chaperone mechanism, identifying and understanding the structural rearrangements that occur for chaperone activation remains paramount. With the unique functional shift of these peroxidases to chaperone activity it is very interesting that cells have evolved multiple functions in various protein systems, such as Hsp70 dual functions as a foldase and also in facilitating client degradation, and Prx proteins which handle oxidative stress until other stressors kick in their chaperone holdase functions all within the same protein.

- **5.2.4 Use of EM for structure determination**

Various efforts are being made to push the capabilities of cryo-EM, the ability to freeze almost any protein particle for visualization makes it powerful tool in accessing structural information contained in a vast variety of protein complexes. EM is becoming a higher throughput technique, with advancements in automated data collection and speed up of computational processing is being pushed constantly [19-21]. This will allow for tackling any chaperone chemistry despite the possible issue of flexibility and heterogeneity, one needs only embrace the technology to push past these issues. Though there are many exciting developments in EM, two examples are presented for their potential application to chaperone protein chemistry especially for the study of smaller or more dynamic protein complexes: the phase plate and the stochastic gradient descent algorithm for generating initial models *ab initio*.

The phase plate is a technology that promises improvement of contrast for small molecules, improving the ability to align particles by improving signal and thus hopefully not have to sacrifice high resolution information [22]. Alignment of particles, or determining the pose, relies on low resolution information, which we can obtain by taking a heavily defocused image. But in so doing we lose higher spatial frequency information and lower the resolution of our map. If we try to take an image too close to focus we lose the low resolution frequencies and our particles become very difficult to see, with low signal we have high resolution information and noise, none of which can aid us in assignment of the projection's actual pose [23].

Despite advances in sample preparation and detectors, electron scattering events from proteins is still limited by radiation damage, which result in poor contrast between protein and vitreous ice [19]. Thus, classical approaches to obtaining contrast have been to take advantage of the physics of electron image formation in the imperfect contrast transfer, or 'contrast transfer function' (CTF) due to aberrations characteristic of every electron microscope [24]. This causes phase contrast in the scattered electron wave from the proteins to generate variations in amplitudes, or intensities at the detector level. It is common practice to therefore obtain images out of focus and correct for the microscope aberrations in order to correct or translate the phase contrast (CTF correction) [23]. A phase plate, situated in the diffraction plane, can cause a shift in the electron wave such that after the wave is diffracted from the sample, containing the weak phase contrast from the proteins of interest, the phase shifts basically become amplitude shifts producing detectable contrast near focus instead of relying on microscope aberrations. Greatly boosting the contrast of particles allow alignment of smaller particles, where before there was too little signal [22, 25]. In practice there are still limitations to the resolution achievable but

recently a hybrid approach where images are acquired closer to focus rather than at focus and CTF correction is still carried out resulted in reconstructions with resolutions better than 3 Å. [26]

The initial model problem is another issue that In order to assign a pose to a given 2D projection one must have an initial 3D model from which to produce projections at various poses to compare the correlations, referred to as the initial model problem [27]. Various methods have been developed to solve this issue, such as using random blob models to compare with 2D reference-free class averages to bootstrap refinement of pose [28]. More recently algorithms utilizing the raw data and stochastic gradient descent (SGD) to obtain models for a cryo-EM dataset *ab initio* [21]. SGD basically utilizes an iterative method to approximate gradient descent optimization to minimize an objective function, used in a wide variety of computing applications such as machine learning. SGD optimization is a fast process where each iteration takes random subsets of the EM dataset to calculate the gradient of the objective function, eventually converging to a local optima, for instance minimizing the error in cross correlations between the particles and projections to assign their pose. What this ultimately allows is a robust method of generating an ab initio model that is consistent with the experimental data, without any prior knowledge of the structure. This promises to be a valuable tool in both discovery and validation of structure.

Finally, an issue that plagues many endeavors in structural biology lies in the inherent structural heterogeneity that is required for proteins to fulfill their biochemical functions, a major hurdle to many of the cryo-EM projects in this thesis. For example, the flexibility of the Hsp70 C-terminus allows for a wide range of conformational states of the Hsp70:CHIP complex, making it difficult to determine whether a given 2D projection represents a particular orientation or a different conformation altogether [29]. One method used to deal with sample heterogeneity is the use of chemical crosslinking to limit the number of conformations a protein complex can adapt in solution. The development of compounds that can be used for crosslinking as well as the identification of crosslinks via mass spectrometry is a rapidly developing field where more efficient as well as shorter crosslinkers are becoming available [30]. There are challenges with using these crosslinkers in the determination of high resolution structures by cryo-EM, namely that lysine or cysteine reactive compounds will non-specifically crosslink to different amino acids in different particles, thus when trying to reach beyond the 10 Å resolution regime these crosslink moieties will provide an additional level of heterogeneity. However, in the case where the flexibility of the protein conformations are apparent at the level of quaternary structure, as was the case with the Hsp70:CHIP complex, chemical crosslinking provides a valuable tool in stabilizing low energy states of

the complex reducing the overall number of conformations allowing determination of a number of 3D structures in solution. Using these low-resolution EM maps, one can obtain information about protein component orientation or relative positioning of the component proteins. Future work involves pushing the achievable resolution on crosslinked complexes to allow increased confidence in quaternary structure determination. Some efforts have already been carried out on chaperone complexes [31, 32]. The use of shorter length or amino acid specific crosslinking may provide ways to allow stabilization of both quaternary/tertiary structure as well as higher resolution secondary structure [30, 33].

The problem of sample preparation for cryo-EM remains one of the slowest progressing aspects limiting the achievable resolution of the protein structure. In the case of HSPB5, which exists as a distribution of oligomers where crosslinking does not isolate any specific oligomer, it has proven very challenging to obtain high resolution information [34]. One hopes for serendipity in discovering mutations or post-translational modifications at the level of protein engineering to cause stabilization of certain states of the protein sample. In one of our experiments with HSPB5, mixing WT and H104K molecules shifts the oligomer distribution depending on their ratio (Chapter 4) [35]. Unfortunately, the problem of the overall heterogeneity and distribution remains. Thus, other methods must be considered to change the properties of the protein to obtain a smaller subset of conformations. The process of protein purification under different buffer conditions and analysis of changes by SEC has been classically used to optimize the same protein for cryo-EM [36, 37]. In addition, use of different detergent or amphipol molecule additives have allowed improvement of sample preparation, but success has mainly lied in the case of membrane proteins where these molecules in solution bind to the transmembrane domains of these proteins [36]. The use of these additives in solution would also cause changes in the solution and surface properties as the sample undergoes vitrification, which may protect the protein from denaturing or unfolding at the air-water interface [38]. In my hands, I have observed the effects of these additives to allow us to resolve particles where previously there were none, as with the Hsp70:CHIP complex, which may attest to the air-water interface denaturation events. Changing the surface properties of solution have also allowed samples such as peroxiredoxin to adapt many more conformations in solution. Though this process of cryo-EM sample preparation remains one of trial-and-error, much like in crystallography, various techniques for optimization exist to attempt to obtain a better image of the protein particles. The goal is to exhaust both the developments of both sample preparation, data acquisition and processing and use the throughput of EM to obtain large datasets and computationally sort through the conformational heterogeneity.

- **5.3 References**

1.   Teixeira, F., et al., *Mitochondrial peroxiredoxin functions as crucial chaperone reservoir in Leishmania infantum.* Proceedings of the National Academy of Sciences of the United States of America, 2015. **112**(7): p. E616-E624.
2.   Fontaine, S.N., et al., *The active Hsc70/tau complex can be exploited to enhance tau turnover without damaging microtubule dynamics.* Hum Mol Genet, 2015. **24**(14): p. 3971-81.
3.   Jinwal, U.K., et al., *Imbalance of Hsp70 family variants fosters tau accumulation.* FASEB J, 2013. **27**(4): p. 1450-9.
4.   Young, Z.T., et al., *Stabilizing the Hsp70-Tau Complex Promotes Turnover in Models of Tauopathy.* Cell Chem Biol, 2016. **23**(8): p. 992-1001.
5.   Cook, C., et al., *Acetylation of the KXGS motifs in tau is a critical determinant in modulation of tau aggregation and clearance.* Hum Mol Genet, 2014. **23**(1): p. 104-16.
6.   Shahpasand, K., et al., *Regulation of mitochondrial transport and inter-microtubule spacing by tau phosphorylation at the sites hyperphosphorylated in Alzheimer's disease.* J Neurosci, 2012. **32**(7): p. 2430-41.
7.   Cripps, D., et al., *Alzheimer disease-specific conformation of hyperphosphorylated paired helical filament-Tau is polyubiquitinated through Lys-48, Lys-11, and Lys-6 ubiquitin conjugation.* J Biol Chem, 2006. **281**(16): p. 10825-38.
8.   Zuiderweg, E.R., L.E. Hightower, and J.E. Gestwicki, *The remarkable multivalency of the Hsp70 chaperones.* Cell Stress Chaperones, 2017. **22**(2): p. 173-189.
9.   Noguchi, A., et al., *DnaJ-promoted binding of DnaK to multiple sites on sigma32 in the presence of ATP.* J Bacteriol, 2014. **196**(9): p. 1694-703.
10.   Clifford-Nunn, B., H.D. Showalter, and P.C. Andrews, *Quaternary diamines as mass spectrometry cleavable crosslinkers for protein interactions.* J Am Soc Mass Spectrom, 2012. **23**(2): p. 201-12.
11.   Delbecq, S.P. and R.E. Klevit, *One size does not fit all: the oligomeric states of alphaB crystallin.* FEBS Lett, 2013. **587**(8): p. 1073-80.
12.   Carra, S., et al., *The growing world of small heat shock proteins: from structure to functions.* Cell Stress Chaperones, 2017. **22**(4): p. 601-611.
13.   Braun, N., et al., *Multiple molecular architectures of the eye lens chaperone alphaB-crystallin elucidated by a triple hybrid approach.* Proc Natl Acad Sci U S A, 2011. **108**(51): p. 20491-6.
14.   Rajagopal, P., et al., *A conserved histidine modulates HSPB5 structure to trigger chaperone activity in response to stress-related acidosis.* Elife, 2015. **4**.
15.   Mymrikov, E.V., et al., *The Chaperone Activity and Substrate Spectrum of Human Small Heat Shock Proteins.* J Biol Chem, 2017. **292**(2): p. 672-684.
16.   Castro, H., et al., *Leishmania mitochondrial peroxiredoxin plays a crucial peroxidase-unrelated role during infection: insight into its novel chaperone activity.* PLoS Pathog, 2011. **7**(10): p. e1002325.
17.   Jang, H.H., et al., *Two Enzymes in One: Two Yeast Peroxiredoxins Display Oxidative Stress-Dependent Switching from a Peroxidase to a Molecular Chaperone Function.* Cell, 2004. **117**(5): p. 625-635.
18.   Radjainia, M., et al., *Cryo-Electron Microscopy Structure of Human Peroxiredoxin-3 Filament Reveals the Assembly of a Putative Chaperone.* Structure, 2015. **23**(5): p. 912-920.
19.   Suloway, C., et al., *Automated molecular microscopy: the new Leginon system.* Journal of structural biology, 2005. **151**(1): p. 41-60.
20.   Kimanius, D., et al., *Accelerated cryo-EM structure determination with parallelisation using GPUs in RELION-2.* Elife, 2016. **5**.

21. Punjani, A., et al., *cryoSPARC: algorithms for rapid unsupervised cryo-EM structure determination.* Nat Methods, 2017. **14**(3): p. 290-296.

22. Danev, R., et al., *Volta potential phase plate for in-focus phase contrast transmission electron microscopy.* Proc Natl Acad Sci U S A, 2014. **111**(44): p. 15635-40.

23. Penczek, P.A., *Image restoration in cryo-electron microscopy.* Methods Enzymol, 2010. **482**: p. 35-72.

24. Wade, R.H., *A brief look at imaging and contrast transfer* Ultramicroscopy, 1992. **46**: p. 145-156

25. Khoshouei, M., et al., *Volta phase plate cryo-EM of the small protein complex Prx3.* Nature Communications, 2016. **7**: p. 10534.

26. Danev, R., D. Tegunov, and W. Baumeister, *Using the Volta phase plate with defocus for cryo-EM single particle analysis.* eLife, 2017. **6**: p. e23006.

27. Penczek, P.A., *Chapter One - Fundamentals of Three-Dimensional Reconstruction from Projections*, in *Methods in Enzymology*, J.J. Grant, Editor. 2010, Academic Press. p. 1-33.

28. Tang, G., et al., *EMAN2: an extensible image processing suite for electron microscopy.* J Struct Biol, 2007. **157**(1): p. 38-46.

29. Smith, M.C., et al., The E3 ubiquitin ligase CHIP and the molecular chaperone Hsc70 form a dynamic, tethered complex. Biochemistry, 2013. 52(32): p. 5354-64.

30. Clifford-Nunn, B., H.D. Showalter, and P.C. Andrews, Quaternary diamines as mass spectrometry cleavable crosslinkers for protein interactions. J Am Soc Mass Spectrom, 2012. 23(2): p. 201-12.

31. Kirschke, E., et al., Glucocorticoid receptor function regulated by coordinated action of the Hsp90 and Hsp70 chaperone cycles. Cell, 2014. 157(7): p. 1685-97.

32. Alvira, S., et al., Structural characterization of the substrate transfer mechanism in Hsp70/Hsp90 folding machinery mediated by Hop. Nat Commun, 2014. 5: p. 5484.

33. Chin, J.W. and P.G. Schultz, In vivo photocrosslinking with unnatural amino Acid mutagenesis. Chembiochem, 2002. 3(11): p. 1135-7.

34. Braun, N., et al., Multiple molecular architectures of the eye lens chaperone alphaB-crystallin elucidated by a triple hybrid approach. Proc Natl Acad Sci U S A, 2011. 108(51): p. 20491-6.

35. Rajagopal, P., et al., A conserved histidine modulates HSPB5 structure to trigger chaperone activity in response to stress-related acidosis. Elife, 2015. 4.

36. Liao, M., et al., Structure of the TRPV1 ion channel determined by electron cryo-microscopy. Nature, 2013. 504(7478): p. 107-12.

37. Liao, M., et al., Single particle electron cryo-microscopy of a mammalian ion channel. Curr Opin Struct Biol, 2014. 27: p. 1-7.

38. Glaeser, R.M. and B.G. Han, Opinion: hazards faced by macromolecules when confined to thin aqueous films. Biophys Rep, 2017. 3(1): p. 1-7.